Sanjay Yadav · Naveen Garg ·
Shankar G. Aggarwal ·
Shiv Kumar Jaiswal · Harish Kumar ·
Venu Gopal Achanta   *Editors*

Recent Advances in Metrology

Select Proceedings of AdMet 2022

🦅 Springer

Lecture Notes in Mechanical Engineering

Sanjay Yadav · Naveen Garg ·
Shankar G. Aggarwal · Shiv Kumar Jaiswal ·
Harish Kumar · Venu Gopal Achanta
Editors

Recent Advances in Metrology

Select Proceedings of AdMet 2022

Editors
Sanjay Yadav
CSIR-National Physical Laboratory
New Delhi, India

Naveen Garg
CSIR-National Physical Laboratory
New Delhi, India

Shankar G. Aggarwal
CSIR-National Physical Laboratory
New Delhi, India

Shiv Kumar Jaiswal
CSIR-National Physical Laboratory
New Delhi, India

Harish Kumar
Department of Mechanical Engineering
National Institute of Technology Delhi
New Delhi, India

Venu Gopal Achanta
CSIR-National Physical Laboratory
New Delhi, India

Preface

This book presents proceedings of the 11th International Conference on "Advances in Metrology" AdMet 2022 organized by CSIR-National Physical Laboratory from 24 to 26 August 2022 New Delhi, India. The book highlights and discusses the technological developments and advances in the areas of physico-mechanical metrology, electrical metrology, environmental sciences, sensor technology, advance materials for industrial application, automation, traceability in measurements and quality control. It provides significant advanced technological information to metrologists, scientists, engineers, academicians and students from research institutes and industrial sector to explore the future research and development in the areas of sensors, advance materials, measurement, and quality improvement. The main objectives of AdMet 2022 were to provide a healthy platform for metrologists, technocrats, researchers, and students of various National Metrology Institutes, laboratories and institutions to participate and share their knowledge and experiences and foster national and international collaborations across the globe in various fields of metrology. The book serves as a valuable reference for science and engineering graduates and postgraduates, researchers, policy-makers, and entrepreneurs for a better understanding about the art of measurements and personnel engaged in conformity assessment, quality system management, calibration and testing and quality control in all sectors of industry.

The response to the call for papers had been overwhelming from all over India. AdMet 2022 proved to be an enlightening experience with several eminent keynote and invited speakers and two Pre-admet Workshops were also organized on 22 and 23 August 2022. The event consisted of invited talks, technical sessions, paper presentations, poster presentations and discussions with eminent speakers on various topics in the field of metrology. This book is a compilation of some of the research papers presented at the conference by various researchers all across the country.

We express our earnest gratitude to all the eminent keynote speakers, authors, and the participants who made AdMet 2022 and successful and memorable event. We

also express our gratitude and appreciation to all the eminent reviewers who have helped us to maintain the high quality of manuscripts included in the proceedings. We are highly grateful to the entire Springer team for their support and cooperation in bringing this book.

New Delhi, India   Sanjay Yadav
                                                                                    Naveen Garg
                                                                      Shankar G. Aggarwal
                                                                        Shiv Kumar Jaiswal
                                                                                   Harish Kumar
                                                                      Venu Gopal Achanta

Contents

About the Editors

Sanjay Yadav born in 1962, obtained his master degree in science (M.Sc.) in 1985 and Ph.D. degree in Physics in 1990. He is Former Chief Scientist and Head, Physico Mechanical Metrology Division of NPL and also Former Professor, Faculty of Physical Sciences, Academy of Scientific and Innovative Research (AcSIR), HRDG, Ghaziabad. Presently, he is working as the Editor-in-Chief (EIC) of the MAPAN: The *Journal of Metrology Society of India*. He is also Vice President of Metrology Society of India (MS), New Delhi as well as Vice President of Ultrasonic Society of India (USI), New Delhi. He had taught 'Advanced Measurement Techniques and Metrology' course, taken practical classes and supervising graduate, master and Ph.D. students since 2011 to 2022. He is the recipient of research scholarships from Ministry of Home Affairs, India (1986); CSIR, India (1988); Col. G. N. Bajpayee Award of Institution of Engineers, India (1989); Commendation Certificates from Haryana Government (1991 and 1992); JICA Fellowship of JAPAN (1998), Commendation Certificates from SASO, Saudi Arabia (2003); three Appreciation Certificates from Director, NPL (2005); Managing Editor, MAPAN (2006–2014); nominated as Member of APMP Technical Committee of Mass Related Quantities (TCM), Australia (2013–2019); Nominated as Country Representative in APMP, China (2019); Member, National Advisory Committee, NCERT, Delhi (2019); Members, Testing and Calibration Advisory Committee, BIS (2019, 2020 and 2021), Certified NABL Assessor as per ISO/IEC 17025:2017, very recently received a prestigious International award i.e. APMP Award for Developing Economies, China (2020), Governing Council Member of Fluid Controls Research Institute (FCRI), Palghat (2022), and Member of several Committees of International Measurement Confederation (IMEKO) including Governing Council since 2018. He has significantly contributed in the field of pressure metrology, biomedical instrumentation, ultrasonic transducers and instrumentation systems. His current research interests include research and developmental activities in physico mechanical measurements; establishment, realization, maintenance and up-gradation of national pressure and vacuum standards; dissemination of national practical pressure scale to users through apex level calibration, training and consultancy services; inter-laboratory comparisons, proficiency testing programme and key comparisons, implementation of

Quality System in the laboratory as per ISO/IEC 17025 standard and Finite Element Analysis (FEA) and Monte Carlo Simulations for pressure balances. He has published more than 450 research papers in the national and international journals of repute and conferences, edited 20 books, 14 patents and copyrights, supervised eight Ph.Ds. (another five in waiting), drafted several projects, scientific and technical reports, documents and policy papers.

Naveen Garg is Senior Principal Scientist and Head, Acoustics and Vibration Standards in CSIR-National Physical Laboratory, New Delhi, working in the field of sound and vibration since the past 19 years. He is Mechanical Engineer specializing in machine design, vibrations and acoustics, measurement science and working in development and upgradation of primary standards of sound pressure and vibration amplitude and R&D in Applied Acoustics. He has done his Doctorate in mechanical engineering from Delhi Technological University, Delhi, and M.Tech. in Machine Design from Indian Institute of Technology (IIT) Delhi. He has been Managing Editor of *MAPAN-Journal of Metrology Society of India* published by Springer and reviewer of many international journals and has enormously contributed towards evaluation, analysis and control of noise pollution.

Shankar G. Aggarwal is working at CSIR-NPL as Senior Principal Scientist (Professor (AcSIR)) from 2009, and his current research focus is "metrology for national ambient air quality standards (NAAQS)" in which he involves in preparation of gas standards and PM2.5/PM10 samplers and their calibration work, gas monitoring and analysis, etc. Before joining to NPL he has been working in Taiwan and Japan as postdoc for ~10 years. So far he has been published > 110 papers in international journals, six patents, supervised six Ph.D. thesis and given > 100 talks including talks in ~15 different countries. He was the fellow of Japan Society for the Promotion of Science, JSPS (2005–2007), Recipient of CITAC award—2013, NABL assessor of ISO/IEC 17025:2017 and ISO 17034:2016, Associate Editor of Mapan-JMSI and *Asian Journal of Atmospheric Environment*, member of BIPM GAWG Task Group on Particulate Matter Comparison, member of APMP Focus Group on Climate Change and Clean Air (FG-CCCA), etc.

Shiv Kumar Jaiswal obtained his B.E. (Electrical Engineering), M.Tech. (Electrical Engineering) and Ph.D. (Fluid Flow) degrees in 1994, 1996 and 2016 respectively. He is currently working as a Senior Principal Scientist and Head—Fluid Flow Metrology Section of CSIR-National Physical Laboratory (NPLI), New Delhi. He has more than 25 years of research, industrial and academic experience. He has been active Researcher in the field of electrical and fluid flow metrology. He has worked as Guest Researcher for one year in Quantum Electrical Metrology Division of National Institute of Standards and Technology (NIST), Gaithersburg, USA, during year 2006–2007. He is Member of several committees of Bureau of Indian Standards (BIS), National Accreditation Board for Testing and Calibration Laboratories (NABL), Legal Metrology Department, Central Ground Water Authority, APMP

Technical Committee for Fluid Flow (TCFF), International Measurement Confederation (IMEKO), etc. He has authored more than 59 publications in peer-reviewed journals, conferences, and book chapters. He is Managing Editor of *MAPAN—Journal of Metrology Society of India* and Vice President, Metrology Society of India.

Harish Kumar is currently working as Associate Professor and Dean Academic at the National Institute of Technology (NIT), Delhi. With more than 20 years of research and academic experience, he is an active researcher in the area of mechanical measurement and metrology. He served as Scientist at the National Physical Laboratory, India, for more than a decade, and as Guest Researcher at the National Institute of Standards and Technology, USA, in 2016. He has authored more than 150 publications in peer-reviewed journals and conference proceedings. He is an active reviewer for many prominent journals on measurement, metrology, and related areas and is Associate Editor of the *MAPAN-Journal of Metrology Society of India*, published by Springer.

Venu Gopal Achanta is a Noted Physicist, Nanophotonics expert, Metrologist and Science Leader, who joined CSIR-NPL as its Director in June 2021. He also held responsibility of another esteemed CSIR laboratory, i.e., CSIR-IGIB, New Delhi during April–December 2022. He did his M.Sc. in Physics from Central University Hyderabad. He obtained Ph.D. in Physics from TIFR in 2000 for his work on Exciton dynamics in low-dimensional semiconductors. In 2006, he was awarded Ph.D. in Electronics Engineering from Tokyo University for work on design and demonstration of an ultrafast all-optical switch. He joined TIFR as faculty in 2004 where he is a Professor (H) since 2018. His research interests include classical and quantum information processing with dipolar emitters like quantum dots embedded in photonic and nanophotonic structures, single photon metrology, dissemination of apex metrological traceability through world-class measurement standards, BNDs, skill development in the country, and strengthening the national quality infrastructure for the overall economic growth of the country.

Characterization of Atmospheric Carbonaceous Species in PM$_{10}$ over Darjeeling, an Eastern Himalayan Region of India

Akansha Rai, A. Chatterjee, T. K. Mandal, and S. K. Sharma

Abstract Carbonaceous aerosol (CAs) pollution is a significant cause of the deterioration of the susceptible Himalayan region, which profoundly affects climate change. In this study, we examined the winter-time pollution load of carbonaceous species [Organic Carbon (OC), Elemental Carbon (EC), Water-Soluble Organic Carbon (WSOC), Water-Soluble Ionic Species (WSIS), Primary Organic Carbon (POC), Secondary Organic Carbon (SOC), and Total Carbonaceous Aerosols (TCAs)] of PM$_{10}$ over a semi-urban high-altitude site of Darjeeling (27.041° N, 88.266° E, 2200 m above mean sea level (AMSL); an eastern Himalayan region), India, from January to February 2019. During winter, the PM$_{10}$ concentration (μg m^{-3}) was found to be 52 $\pm$ 18, which comprises 24% of CAs, 30% of WSIS, and 8% of sea salts. The secondary aerosols contribute about 79% to WSIS and 24% to PM$_{10}$. The average concentration of WSIS was observed in the order of SO$_4^{2-}$ > NH$_4^+$ > NO$_3^-$ > Na$^+$ > K$^+$ = Ca^{+2} > Cl$^-$ > Mg^{+2} > F$^-$, respectively. Lower ECR (Effective Carbon Ratio) suggests a reduction in the number of scatterings CAs and possibly an increase in the absorbing CAs. The mean OC/EC ratio (2.04 $\pm$ 0.37), K$^+$/OC (0.11 $\pm$ 0.04), and their good correlations of 0.77 and 0.74, respectively, suggested fuel combustion (biomass burning and fossil fuels) as the major contributing source in Eastern Himalayas. In addition, a high WSOC/OC ratio (0.74 $\pm$ 0.22) implied the formation of secondary aerosols and the presence of aged aerosols. The trajectory analysis showed that the air masses mainly originated from the IGP region, Nepal, and the local region of the sampling site.

A. Rai (✉) · T. K. Mandal · S. K. Sharma
CSIR-National Physical Laboratory, Dr. K. S. Krishnan Road, New Delhi 110012, India
e-mail: akansha.npl19j@acsir.res.in; akansharai.may@gmail.com

Academy of Scientific and Innovative Research (AcSIR), Ghaziabad 201002, India

T. K. Mandal
e-mail: tuhin.npl@nic.in

S. K. Sharma
e-mail: sudhir.npl@nic.in

A. Chatterjee
Environmental Science Section, Bose Institute, Saltlake, Kolkata 700091, India
e-mail: abhijit.boseinst@gmail.com

1 Introduction

Globally, air pollution is the most common environmental contributor to premature death. There are several air pollutants, each with their chemical composition, reaction behaviors, emissions, environmental permanence, capacity to be transported, and eventual influence on the quality of air and human well-being [1, 2]. Due to its detrimental impacts on atmospheric chemistry, quality of air, reduced vision, the Earth's radiation budget, and human health, particulate matter (PM) has a substantial impact [3, 4]. Because they have implications for pollution problems, improvements in our understanding of atmospheric aerosols are an essential study concern [5]. Recently, organic and elemental carbon, denoted as OC and EC, comprises most of the carbonaceous aerosols (CAs) and has received the most attention. EC is a by-product of the partial combustion of fuels (fossil fuels (FFC) and biomass (BB)) from human-made sources [6, 7]. Primary organic carbon (POC) and secondary organic carbon (SOC) are other components of OC. POC is emitted from anthropogenic or biogenic sources. On the other hand, with in-situ reactions of POC, SOC is formed. Water-soluble organic carbon (WSOC) can either come from primary emissions or be created by a chain reaction of organic compounds in the atmosphere while they are transported. It significantly affects hygroscopic characteristics, radiative forcing, and cloud condensation nuclei (CCN) [8–10]. In urbanized climates, water-soluble ionic species (WSIS) constitute a significant fraction of 50–70% mass of $PM_{2.5}$ [11]. Additionally, due to their aerosol hygroscopicity, secondary inorganic ions (NO_3^-, SO_4^{2-}, and NH_4^+), essential components of WSIS, could worsen a decrease in visibility and lead to the formation of a haze [12].

The study of airborne particles over the Himalayan region is of utmost importance since the ecosystem of that region is seriously threatened by various environmental pollutants. Due to high vehicular traffic because of tourists, biomass burning for cooking, and fuelwood burning for heating, play a significant role in loading anthropogenic aerosols over the Himalayan region [13–15]. Due to their relatively longer lifetime (several days to weeks), PM and its species often disperse far from their site of origin [7, 16]. Limited studies were conducted earlier on the physicochemical characterization of aerosols over the eastern Himalayas. They did not enlighten the possible sources of pollutants/aerosols from long-range regions [14, 17]. Thus, it is crucial to examine the pollutant concentrations, chemical characteristics, temporal fluctuations, and the impact of WSIS in the atmosphere over the eastern Himalayas of India.

Fig. 1 Map of PM$_{10}$ sampling site in the Eastern Himalayan region of India (*Source* Google Earth)

2 Site Description

In this study, the sampling was performed at Darjeeling, a well-known hill station over the eastern Himalayas, for tourists. The sampling location is close to the Indo-Gangetic Plain (IGP), located ~50 km with a dense population with substantial aerosol mass loadings. The sampling site was located inside the Bose Institute (27.01° N, 88.15° E) at an altitude of 2200 m above mean sea level (AMSL), as shown in Fig. 1. Around the sample site, and there are numerous tea processing facilities and gardens that occupy 17,500 acres of land [14, 15]. Darjeeling Himalayan Railway (Toy Train) is a world heritage site UN (United Nations) which still runs on coal. The seasonal variations of aerosols produce subsequent signatures on the different physicochemical characteristics of aerosols [7].

3 Methodology

3.1 Sample Collection

For the collection of PM$_{10}$ samples ($n = 25$), a respirable dust sampler (RDS) was used during the sampling period (January–February 2019). On the building's rooftop, 15 m above ground level (AGL), the sampler was placed on the Bose Institute campus. For 24 h, ambient air was filtered through 20×25 cm^2 PALLFLEX quartz microfiber filters at a flow rate of 1.2 m^3 min^{-1} (flow accuracy: $\pm 2\%$). The standard protocol was followed for PM$_{10}$ sampling using a Sartorius microbalance (resolution: ± 10 µg). After the samples were collected, the filters were placed in a deep freezer and stored at a temperature of –20 °C until analysis.

3.2 Chemical Analysis

OC and EC analysis: Using an OC/EC carbon analyzer (Model: DRI 2001A, CA, USA), a punch of 0.536 cm^2 of PM$_{10}$ filter was used to determine OC and EC concentrations by following the IMPROVE-A carbon protocol. The thermal-optical analysis is the method-defined for the analyzer based on the successive oxidation of OC and EC at different temperatures. A previous publication has discussed the details regarding the operating procedure, calibration, and calibration standards [7].

Water-Soluble Organic Carbon (WSOC) analysis: Using a Shimadzu TOC analyzer, a punch of 3.79 cm^2 of PM$_{10}$ filter was used to determine WSOC concentration. The filter was cut in 20 ml of deionized water (resistivity: 18.2 MΩ cm), sonicated for 30 min and filtered using a nylon membrane. Its working principle is based on catalytic-oxidation combustion of carbonaceous compounds at 680 °C. The details regarding these methods have been discussed elsewhere [7].

Water-Soluble Ionic Species (WSIS) analysis: The collected PM$_{10}$ samples were analyzed for WSIC using Ion Chromatography (IC Model: Metrohm 930 Compact IC Flex, USA). The left filtered extract (10 ml) from WSOC analysis was used to estimate ionic species. The cations and anions were measured using a 930 Compact IC Flex (Metrohm, Switzerland) system equipped with a Metrosep C4150/4.0 and ASRS-4MN columns, respectively. The details regarding these methods have been discussed in [18].

3.3 Air Mass Trajectory Analysis

In the Himalayan region, Hybrid Single-Particle Lagrangian Integrated Trajectory Model (HYSPLIT) trajectory models are crucial for examining the movement of pollutants, long-term passage patterns, and probable local sources of PM$_{10}$ [15, 19]. The air parcel back trajectories were downloaded for the sampling days for 500 m AGL. In order to estimate backward trajectories using the isentropic model calculation approach, three days (i.e., 72 h) were chosen because PM$_{10}$ can travel a great distance. The geographical area of air parcels approaching a receptor site is created by the backward trajectory analysis, which generates enormous sets of trajectories [4, 20].

Cluster Analysis: Using Ward's hierarchical technique, cluster analysis is employed to integrate all air mass trajectories into discrete transport groups arriving at the sampling location. The Euclidean distance was applied to identify the coordinates as variables of the distance between two trajectories and calculated using Eq. 1 to examine the direction of air masses [21, 22]:

$$d_{ij} = \sqrt{\sum_{k=1}^{p} \left(\left(x_i(k) - x_j(k)\right)^2 + \left(y_i(k) - y_j(k)\right)^2 \right)}, \tag{1}$$

where p denotes the point in p-dimensional space, X_i and Y_i are denoted to the location of trajectory 1. X_j and Y_j are denoted to the location of trajectory 2. The 'eye ball' method was used to identify the appropriate cluster number by analyzing the disparities between the mean trajectories data [7, 21].

Concentration Weighted Trajectory (CWT) Method: The relative importance of probable source locations and their spatial distribution are determined using the CWT approach [15]. To calculate trajectory-weighted concentrations (WCWT), the geographical magnitude of the air mass trajectories determines how the total area occupied by the back trajectories is fragmented into a series of grid cells concerning its pollutant concentrations, as given in Eq. 2 [7, 21, 22]:

$$C_{ij} = \frac{1}{\sum_{k=1}^{N} \tau_{ijk}} \sum_{k=1}^{N} c_k \tau_{ijk}, \tag{2}$$

C_{ij} denotes the mean concentration weighted in particular (i, j)th cell,
k denotes the trajectory's index,
N represents the overall number of trajectories,
C_k is the pollutant concentration measured during the entry of trajectory k, and
τ_{ijk} denotes the time spent in the (i, j)th cell by trajectory k.

4 Result and Discussion

4.1 Mass Concentration of PM$_{10}$

The average winter-time concentration of PM$_{10}$ was observed as $52 \pm 18 \, \mu g \, m^{-3}$ with a range of 21–$89 \, \mu g \, m^{-3}$ at Darjeeling. Table 1 shows the statistical overview of PM$_{10}$ with a 34.5% coefficient of variation during the winter. The monthly average concentration of PM$_{10}$ was found to be comparatively lower in the month of January ($43 \pm 11 \, \mu g \, m^{-3}$) and higher in February ($59 \pm 20 \, \mu g \, m^{-3}$). Similar observations were reported by [23] at Pohara ($51.8 \pm 18.9 \, \mu g \, m^{-3}$) in the North-Western Himalayas, [20] at Nainital ($39 \pm 10 \, \mu g \, m^{-3}$), Central Himalayas, [17] at Mohal-Kullu ($51 \pm 16 \, \mu g \, m^{-3}$), Western Himalayas.

Table 1 PM$_{10}$ statistical overview

Number of samples (n)	25
Average concentration ($\mu g\ m^{-3}$)	52
Standard deviation	18
Standard error	4
Median ($\mu g\ m^{-3}$)	50
Range ($\mu g\ m^{-3}$)	21–89
Minimum concentration ($\mu g\ m^{-3}$)	21
Maximum concentration ($\mu g\ m^{-3}$)	89
Confidence level (95%)	7
Coefficient of variation (%)	34.5

4.2 Carbonaceous Species (OC, EC, and WSOC) and Effective Carbon Ratio (ECR) in PM$_{10}$

The average winter-time concentrations of carbonaceous species (OC, EC, POC, SOC, TCAs, and WSOC) of PM$_{10}$ with maxima, minima, and median are summarized in Table 2. High concentration of OC ($5.4 \pm 2.0\ \mu g\ m^{-3}$), EC ($2.7 \pm 1.0\ \mu g\ m^{-3}$), and WSOC ($3.8 \pm 1.3\ \mu g\ m^{-3}$) was observed (in Fig. 2), which ranges from 2.1– 12.3 $\mu g\ m^{-3}$, 1.4–5.3 $\mu g\ m^{-3}$, and 0.2–7.5 $\mu g\ m^{-3}$, respectively that might be due to local burning activities during the study period. The average concentration of carbonaceous aerosols (TCAs = OC × 1.6 + EC) was $11.4 \pm 4.1\ \mu g\ m^{-3}$ and contributed around ~22% to PM$_{10}$. The POC and SOC were also computed using the EC tracer approach, which contributes 35 and 65% to OC, whereas WSOC contributes 70% to OC. The higher fraction of WSOC in the total OC indicated the aged nature of the carbonaceous aerosols. The substantial concentrations of CAs could be attributed to the enhanced impact of firewood burning for space heating, steady meteorological conditions, and open burning that led to the deposition of pollutants in the lower atmosphere.

The effective carbon ratio (ECR) indicates a link between CAs and climate change, taking into account the absorption properties of POC, which can be calculated as: ECR = SOC/POC + EC. The average winter-time ECR was estimated as 0.32 ± 0.16, which varied from 0.01 to 0.6. According to [24], ECR values less than 0.30 indicate low SOC concentrations, implying a decrease in the quantity of scattering CAs and maybe an upsurge in the absorbing type of CAs.

4.3 Waters-Soluble Ionic Species (WSIS) in PM$_{10}$

The average winter-time concentrations of WSIS (Na$^+$, K$^+$, Mg^{2+}, Ca^{2+}, F$^-$, Cl$^-$, NH$_4^+$, NO$_3^-$ and SO$_4^{2-}$) of PM$_{10}$ with maxima, minima, and median are summarized in Table 2. The average winter sum of WSIS (ΣWSIS) concentration (15.5 $\pm$

Table 2 Average concentrations of carbonaceous and ionic constituents (in $\mu g\ m^{-3}$) of PM$_{10}$ at Darjeeling

Species	Average ($n = 25$)	Min	Max	Median
OC	5.4 ± 2.0	2.1	12.3	5.1
EC	2.7 ± 1.0	1.4	5.3	2.5
POC	3.6 ± 1.3	1.8	6.9	3.3
SOC	1.9 ± 1.1	0.1	5.4	2.0
TCAs	11.4 ± 4.1	4.7	25.0	10.4
WSOC	3.8 ± 1.3	0.2	7.5	3.9
Na$^+$	1.4 ± 0.7	0.1	4.0	1.4
K$^+$	0.6 ± 0.4	0.1	1.8	0.6
Mg^{2+}	0.1 ± 0.1	0.01	0.5	0.1
Ca^{2+}	0.6 ± 0.3	0.1	1.5	0.6
F$^-$	0.04 ± 0.1	0.01	0.2	0.02
Cl$^-$	0.4 ± 0.2	0.02	0.9	0.3
NH$_4^+$	4.0 ± 4.1	0.3	16.0	3.2
NO$_3^-$	2.4 ± 2.5	0.4	11.7	1.7
SO$_4^{2-}$	5.9 ± 5.2	0.5	19.7	5.2

$\pm$ Standard Deviation
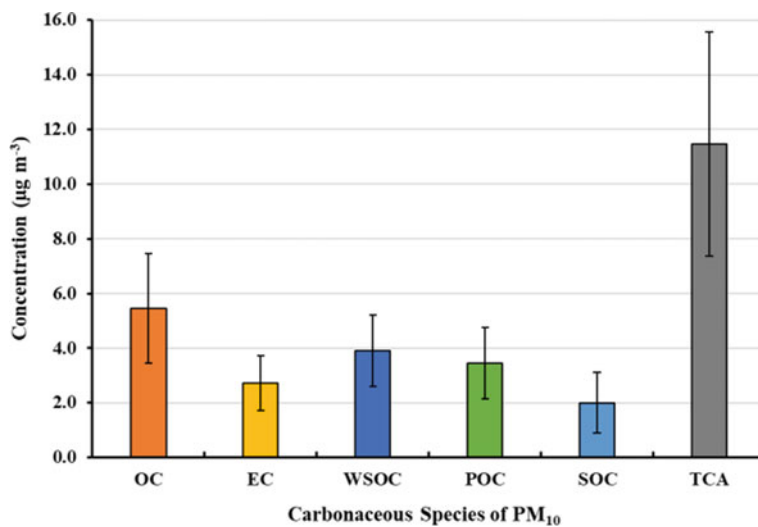
Fig. 2 Mass concentration of carbonaceous species of PM$_{10}$

12.2 μg m^{-3}) contributed nearly 30% to PM$_{10}$. In terms of concentration, SO$_4{}^{2-}$, NO$_3{}^{-}$, and Cl^{-} were the most prevalent anions, whereas NH$_4{}^{+}$, Na^{+}, and K^{+} were the most prevalent cations. Based on winter average percentage contribution, the trend of most dominant ions was found to be in the order of SO$_4{}^{2-}$ (38%) > NH$_4{}^{+}$ (26%) > NO$_3{}^{-}$ (16%) > Na^{+} (9%) > K^{+} (4%) = Ca^{+2} (4%) > Cl^{-} (2%) > Mg^{+2} (1%) > F^{-} (0.2%). A marker for secondary inorganic aerosols (SIA) is sulphate-nitrate ammonium (SNA) which contributes around 24% of the PM$_{10}$ concentration and 79% to WSIC. Only ~8% of sea salts were reported during the winter season. The charge balance of ionic species showed a good correlation of 0.79, as shown in Fig. 3f.

4.4 Diagnostic Ratios and Scatter Plots

The diagnostic ratios of PM$_{10}$ species (OC, EC, SOC, and WSOC) aid in determining the formation and removals processes of secondary organic aerosols (SOA), the aging of atmospheric aerosols, and the emission of CAs (Fig. 3a–c). The ratio of OC/EC suggests the origin of aerosols emitted from various sources, both locally produced and transported. In this study, the ratio of OC/EC ranged from 1.31 to 2.61, with an average of 2.04 $\pm$ 0.37 and a good correlation of 0.77. This indicates that fossil fuel combustion (FFC) is influenced mainly by tourist vehicles and local biomass burning (BB), as well as over the IGP region. Aerosols produced by BB and FFC can be identified using the ratios of K^{+} with OC and EC. The ratio of K^{+}/OC varied from 0.04–0.21 for BB and agricultural residue burning, which shows a good correlation of 0.74 (Fig. 3d). Similarly, relatively high K^{+}/EC ratios were recorded for BB with a range of 0.06–0.53 and a significant correlation of 0.52 (Fig. 3e). On the other hand, WSOC/OC ratio can also be used as a tracer for emission sources, strength, and SOA contribution. In the present study, the ratio of WSOC/OC varied from 0.08 to 0.94, with an average ratio of 0.72 $\pm$ 0.19 and a significant correlation of 0.66. In the atmosphere, the photochemical oxidation reactions of volatile organic compounds (VOCs) through the gas-phase conversion are generally responsible for the high WSOC/OC ratio, i.e., through SOA formation. The obtained results indicate the emissions from FFC, widespread BB practices, and the production of SOC due to carbonaceous species transported from the surrounding IGP region.

4.5 Air Mass Backward Trajectory

Backward trajectory analysis is a conventional technique for identifying the location, airflow, and transport of aerosols imposing severe pollution load in the Himalayan region [15, 19]. In Fig. 4a, the 500 m trajectories originated from different regions in Nepal, the north-western regions of India, the Thar desert, central highlands, the semi-arid region, the IGP region, and Bhutan, demonstrating that the near-surface flows are chaotic in nature [7]. The medium-range transport was observed with heavy
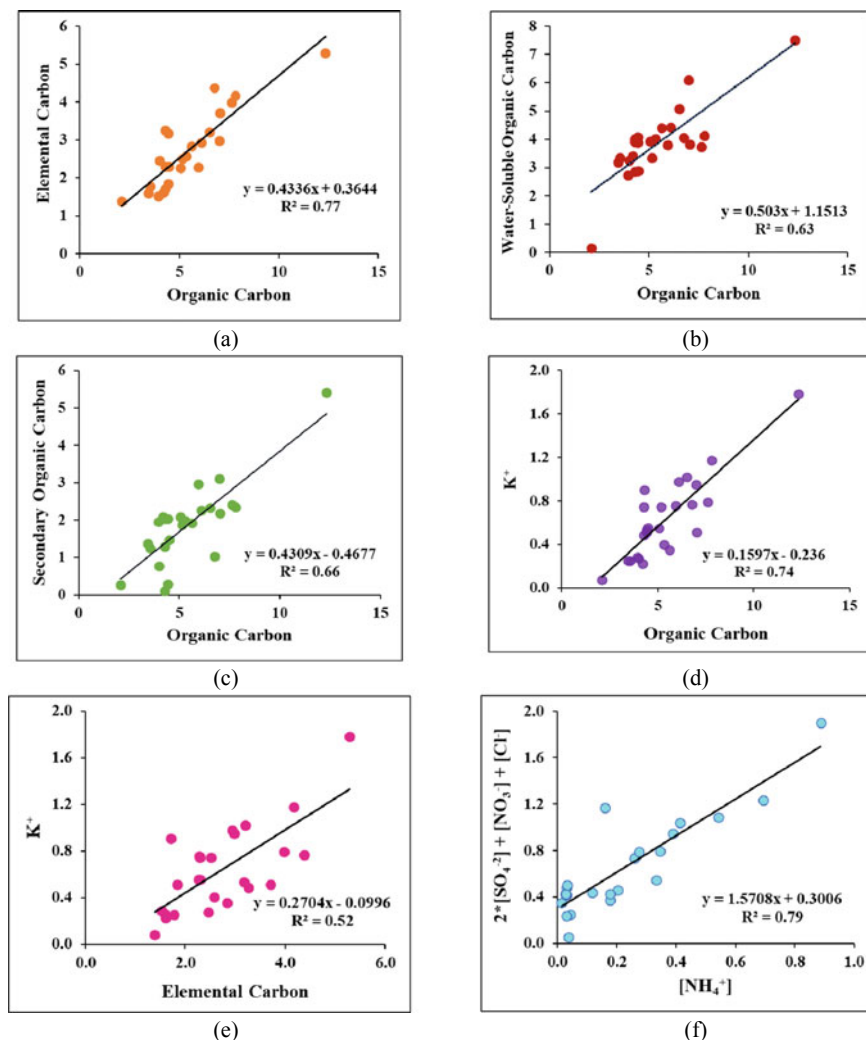
Fig. 3 Scatter plots of species of PM$_{10}$ **a** OC with EC **b** OC with WSOC **c** OC with SOC **d** K$^+$ with OC **e** K$^+$ with EC **f** ionic charge balance

air mass loading at the IGP region. Whereas the long-distant passage of pollutants was observed from the north-western region, passing over China and approaching the receptor site.

Cluster Analysis of PM$_{10}$: Cluster analysis was performed at an altitude of 500 m AGL to limit the impacts of surface friction and to simulate breezes in the lower boundary layer. The trajectory numbers of trajectories after clustering from different directions are depicted in Fig. 4b. Cluster 1 (orange color) belongs to short-range transport,
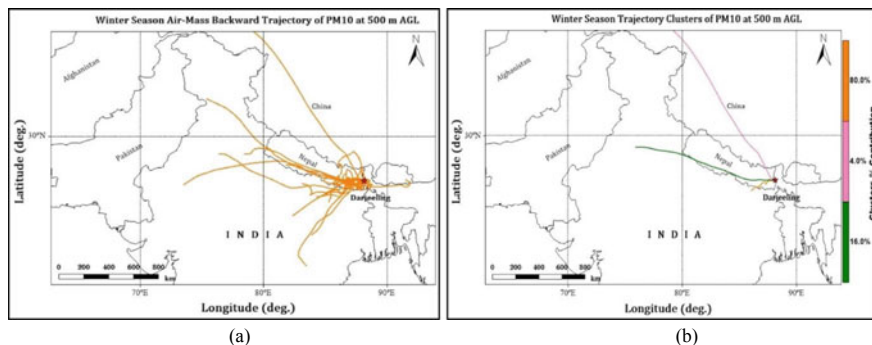
Fig. 4 Air-mass backward trajectory (**a**) and cluster analysis (**b**) of PM$_{10}$ during the winter season at 500 m AGL over Darjeeling

which accounts for 80% of air mass trajectory originating from the local and lowers IGP region, which is the most polluted belt in India. Cluster 2 (green color) belongs to medium-range transport, which accounts for 16% of air mass trajectory originating from the Thar desert and passing through Nepal and the IGP region towards the receptor site. In contrast, cluster 3 (pink colour) represented the long-distant passage of air masses (accounting for 4% of the total) from the north-western pathway passing over China. The short-distant trajectories were observed to correspond to the slow-moving parcel of air masses. On the other hand, highly long pathways indicate strong flows, which significantly impact the quality of the atmosphere differently [15, 25].

CWT Analysis of PM$_{10}$ along with its species (OC, EC, TCA, POC, SOC, WSOC, SIA): The WCWT were applied to identify the influence of the probable sources by aggregating apportionment numbers for each source and evaluating the pollution level associated with various trajectories. In Fig. 5a, the local area, lower IGP region, and Nepal contribute to higher concentration (WCWT values) of PM$_{10}$, and low concentration was observed in the IGP region of India. From the observed results of winter-time PM$_{10}$ and its carbonaceous species, it was found that these species might be generated by incomplete burning of fuel and wood at low temperatures, which are employed to combat chill—owing to the trapping of coarse particulates in the fog and calm breeze, a persistent thermal inversion with constrained dispersion forms at ground level.

The higher concentration of OC (Fig. 5b) and reconstructed POC (Fig. 5d) was observed in local and Nepal regions, which may contribute to fungal spores, plant debris, and biomass burning activities. The long-distant pathway of TCA through the prevailing westerly wind was assessed over Nepal, and local areas (Fig. 5e). Whereas EC (Fig. 5c) and SIA (Fig. 5g) concentrations were increased from the IGP region to Nepal and near the receptor site, which might contribute to the emissions from the vehicular exhaust and secondary aerosols. Higher concentrations of SOC (Fig. 5f) and WSOC (Fig. 5h) over the sampling area and Nepal region showed the emissions from the secondary aerosol formation, as reported by [10].
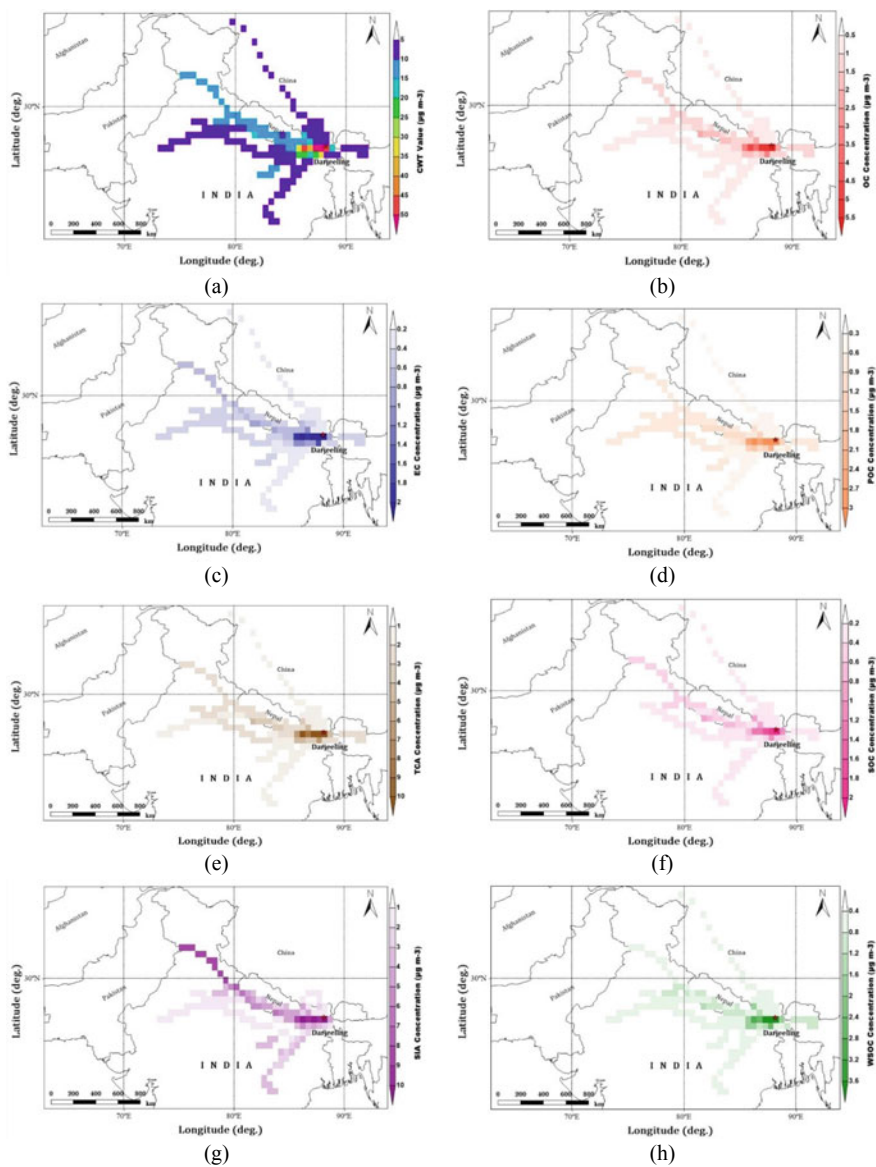
Fig. 5 CWT plots of **a** PM$_{10}$, **b** OC, **c** EC, **d** POC, **e** TCA, **f** SOC, **g** SIA, **h** WSOC (μg m^{-3}) during the winter season at 500 m AGL over Darjeeling

Similar results were also observed by [26, 27] in Nainital and Dhulikhel (Nepal), which showed that the accumulation of IGP aerosols and polluted continental air mass consisting of dust and smoke was prevalent during the winter seasons. [28] reported on the complexities of OC sources such as burning, pollen, tiny soil minerals, and mechanisms of secondary organic compounds. Because the pollutants from the suburban areas cannot reach the mountaintop during the winter, the boundary layer stays below Darjeeling (2.2 km), and the atmosphere remains relatively pristine [14]. So, in the winter, there are also fewer human activities involving tourists, which contributes to the local production of CAs.

5 Conclusion

The winter-time aerosols of PM_{10} have been studied at a high-altitude site (Darjeeling) in the eastern Himalayan region of India. The mean concentration (μg m^{-3}) of winter-time PM_{10} was 52 ± 18, close to NAAQS and WHO limits.

- In this study, the winter-time concentrations ($\mu g\ m^{-3}$) of OC (5.4 ± 2.0), EC (2.7 ± 1.0), and WSOC (3.8 ± 1.3) were observed due to the increasing influence of burning wood for domestic purposes, outdoor BB, and steady air conditions.
- WSOC contributes 70% to OC, indicating the aging nature of the CAs. The average winter-time concentration ($\mu g\ m^{-3}$) of CAs was 11.4 ± 4.1, contributing around ~22% to PM_{10}.
- A lower effective carbon ratio (0.32) suggests a reduction in the number of scatterings CAs and possibly an increase in the absorbing CAs.
- The average winter-time concentration ($\mu g\ m^{-3}$) of WSIC was observed as 15.5 ± 12.2, contributing nearly 30% to PM_{10}. SIA contributes around 24% of the PM_{10} concentration and 79% to WSIC.
- A major effect of BB, FFC, and SA as an origin of carbonaceous species over the eastern Himalayan region was revealed by the diagnostic ratios and linear regression analysis of OC with EC, WSOC with OC, K^+ with OC, and EC. These variables were also positively correlated with carbonaceous components.

Based on cluster analysis, 80% of air mass was short-range (local and lower IGP region), 16% was medium-range transport (the Thar desert and passing through Nepal and the IGP region), and 4% was long-range transport of air masses (north-western route passing over China). CWT analysis showed that carbonaceous species traveled from Nepal and the IGP region apart from local emissions.

The present study showed a significant implication for the Himalayan region because the deposition of CAs over Darjeeling, a high-altitude location, is a matter of concern from the human well-being perspective and fragile ecology across the Indian Himalayas. Therefore, it is crucial to reduce the key contributors to PM_{10} and CAs over the Himalayan region (automobile pollution, FFC, and BB) by implementing effective and efficient waste management techniques, etc. Therefore, this study can

aid the stakeholders and policymakers in understanding the characteristics of PM$_{10}$ for the Himalayan region.

References

1. Akasha H, Ghaffarpasand O, Pope F (2021) Climate change and air pollution. K4D helpdesk report
2. Marina-Montes C, Pérez-Arribas LV, Anzano J, Cáceres JO (2020) Local and remote sources of airborne suspended particulate matter in the antarctic region. Atmosphere 11(4):373
3. Buchunde P, Safai PD, Mukherjee S, Leena PP, Singh D, Meena GS, Pandithurai G (2019) Characterization of particulate matter at a high-altitude site in southwest India: impact of dust episodes. J Earth Syst Sci 128(8):237
4. Sharma SK, Mandal TK (2017) Chemical composition of fine mode particulate matter (PM2. 5) in an urban area of Delhi, India and its source apportionment. Urban Clim 21:106–122
5. Moretti S, Salmatonidis A, Querol X, Tassone A, Andreoli V, Bencardino M, Naccarato A (2020) Contribution of volcanic and fumarolic emission to the aerosol in marine atmosphere in the central Mediterranean sea: results from Med-Oceanor 2017 cruise campaign. Atmosphere 11(2):149
6. Kontuľ I, Kaizer J, Ješkovský M, Steier P, Povinec PP (2020) Radiocarbon analysis of carbonaceous aerosols in Bratislava, Slovakia. J Environ Radioact 218:106221
7. Rai A, Mukherjee S, Choudhary N, Ghosh A, Chatterjee A, Mandal TK, Kotnala RK (2021) Seasonal transport pathway and sources of carbonaceous aerosols at an urban site of eastern Himalaya. Aerosol Sci Eng 5(3):318–343
8. Dinoi A, Cesari D, Marinoni A, Bonasoni P, Riccio A, Chianese E, Tirimberio G, Naccarato A, Sprovieri F, Andreoli V, Moretti S, Gulli D, Calidonna CR, Ammascato I, Contini D (2017) Intercomparison of carbon content in PM$_{2.5}$ and PM$_{10}$ collected at five measurement sites in southern Italy. Atmosphere 8(12):243
9. Panicker AS, Kumar VA, Raju MP, Pandithurai G, Safai PD, Beig G, Das S (2021) CCN activation of carbonaceous aerosols from different combustion emissions sources: a laboratory study. Atmos Res 248:105252
10. Jin Y, Yan C, Sullivan AP, Liu Y, Wang X, Dong H, Chen S, Zeng L, Collett JL Jr, Zheng M (2020) Significant contribution of primary sources to water-soluble organic carbon during Spring in Beijing, China. Atmosphere 11(4):395
11. Bamotra S, Kaushal D, Yadav S, Tandon A (2022) Variations in the concentration, source activity, and atmospheric processing of PM2. 5-associated water-soluble ionic species over Jammu, India. Environ Monit Assess 194(9):1–18
12. Zhao X, Huang Y, Han F, Touseef B, Song Z, Zhao X, Bandna B (2022) The seasonal characterization and source analysis of water-soluble inorganic ions in PM$_{2.5}$ in Fuxin, northeast China. Environ Forensics 1–12
13. Adak A, Chatterjee A, Singh AK, Sarkar C, Ghosh S, Raha S (2013) Atmospheric fine mode particulates at eastern Himalaya, India: role of meteorology, long-range transport, and local anthropogenic sources. Aerosol Air Qual Res 14(1):440–450

14. Sarkar C, Roy A, Chatterjee A, Ghosh SK, Raha S (2019) Factors controlling the long-term (2009–2015) trend of $PM_{2.5}$ and black carbon aerosols at eastern Himalaya, India. Sci Total Environ 656:280–296
15. Rai A, Mukherjee S, Chatterjee A, Choudhary N, Kotnala G, Mandal TK, Sharma SK (2020) Seasonal variation of OC, EC, and WSOC of PM_{10} and their CWT analysis over the eastern Himalaya. Aerosol Sci Eng 4(1):26–40
16. Joshi H, Naja M, Gupta T (2020) In-situ measurements of aerosols from the high-altitude location in the Central Himalayas. In: Measurement, analysis, and remediation of environmental pollutants. Springer, Singapore, pp 59–89
17. Choudhary N, Srivastava P, Dutta M, Mukherjee S, Rai A, Kuniyal JC, Sharma SK. Seasonal characteristics, sources and pollution pathways of PM_{10} at high altitudes Himalayas of India. Aerosol Air Qual Res 22:220092
18. Ahmed M, Bhuyan P, Sarkar S, Hoque RR (2022) Seven-year study of monsoonal rainwater chemistry over the mid-Brahmaputra plain, India: assessment of trends and source regions of soluble ions. Environ Sci Pollut Res 29(17):25276–25295
19. Kulshrestha U, Kumar B (2014) Airmass trajectories and long-range transport of pollutants: a review of wet deposition scenario in South Asia. Adv Meteorol
20. Sharma SK, Choudhary N, Kotnala G, Das D, Mukherjee S, Ghosh A, Mandal TK (2020) Winter-time carbonaceous species and trace metals in PM_{10} in Darjeeling: a high altitude town in the eastern Himalayas. Urban Clim 34:100668
21. Chen Y, Xie S, Luo B (2018) Seasonal variations of transport pathways and potential sources of $PM_{2.5}$ in Chengdu, China (2012–2013). Front Environ Sci Eng 12(1):12
22. Li Y, Zhao W, Fu J, Liu Z, Li C, Zhang J, He C, Wang K (2020) Joint governance regions and major prevention periods of $PM_{2.5}$ pollution in China based on wavelet analysis and concentration—weighted trajectory. Sustainability 12(5):2019
23. Kaushal D, Kumar A, Yadav S, Tandon A, Attri AK (2018) Winter-time carbonaceous aerosols over the Dhauladhar region of North-Western Himalayas. Environ Sci Pollut Res 25(8):8044–8056
24. Ramírez O, de la Campa AS, de la Rosa J (2018) Characteristics and temporal variations of organic and elemental carbon aerosols in a high–altitude, tropical Latin American megacity. Atmos Res 210:110–122
25. Yang W, Wang G, Bi C (2017) Analysis of long-range transport effects on $PM_{2.5}$ during a short severe haze in Beijing, China. Aerosol Air Qual Res 17:1610–1622
26. Dumka UC, Kaskaoutis DG (2014) In-situ measurements of aerosol properties and estimates of radiative forcing efficiency over Gangetic-Himalayan region during the GVAX field campaign. Atmos Environ 94:96–105
27. Tripathee L, Kang S, Chen P, Bhattarai H, Guo J, Shrestha KL, Sharma CM, Ghimire PS, Huang J (2021) Water-soluble organic and inorganic nitrogen in ambient aerosols over the Himalayan middle hills: seasonality, sources, and transport pathways. Atmos Res 250:105376
28. Li C, Yan F, Kang S, Yan C, Hu Z, Chen P, Gao S, Zhang C, He C, Kaspari S, Stubbins A (2020) Carbonaceous matter in the atmosphere and glaciers of the Himalayas and the Tibetan plateau: an investigative review. Environ Int 146:106281

Establishment of Sound Impedance Tube Facility at CSIR-National Physical Laboratory, New Delhi, India

C. Gautam and N. Garg

Abstract The paper discusses about the Sound Impedance Tube facility for evaluation of sound absorption characteristics of acoustical materials at CSIR-National Physical Laboratory, New Delhi, the National Metrology Institute (NMI) of India. The facility has been recently revived and brought under the Quality Management System as per ISO 17025:2017 and traceable to the national standards to the Sound Pressure Level. The paper reports methodology and measurement uncertainty in the evaluation of the sound absorption characteristics of acoustical materials as per ISO 10534-2: 1998. The revived facility traceable to the national standards of sound pressure level is instrumental in design and development of building acoustic materials for noise management and control.

Keywords Sound impedance tube · Sound absorption characteristics · Acoustical materials and sound impedance

1   Introduction

Sound Impedance tube transfer function method is widely used in laboratory experimentation especially when one can't afford the costly Reverberation chambers. The sound impedance tube uses a small size of sample for measurement of the sound absorption characteristics. It is a conventional method to measure sound absorption characteristics, reflection coefficients and acoustic impedance [1]. A variety of materials with PU films with different diameters and different frequency ranges have been measured using the sound impedance tube [1]. There are two types of sound impedance tube methods: one is two-microphone transfer function method and other one is standing wave method. Several studies revealed that the two-microphone based transfer function method is quicker and provides absorption coefficient curve,

C. Gautam (✉) · N. Garg
CSIR-National Physical Laboratory, New Delhi 110012, India
e-mail: c.gautam@nplindia.org

Academy of Scientific and Innovative Research (AcSIR), Ghaziabad 201002, India

whereas, in the standing wave method, single values for discrete sinusoidal frequencies are obtained [2]. Sound absorption properties in textile industries are more popular for investigating the nanofibers and microfiber materials through sound impedance tube [3]. The textile's acoustical properties in the range of 1000–4000 Hz frequency range had been reported in studies using the sound impedance tube [3]. Some studies reported the high sound absorption properties of natural fibers such as ramie, flax and jute fibers and their composites by the two-microphone based transfer function method and compared their results with synthetic fibers and their composites [4]. In some studies, four different excitation signals (white noise, pink noise, linear sine sweep and exponential sine sweep) were used with two microphone transfer function method to investigate the acoustical properties of melamine foam with 25 mm thickness and 60 mm diameter [5]. Also, some studies reported the Sound absorption characteristics, reflection factor and acoustical impedance ratio of 40 mm thick and 44 mm thick acoustical foam were analyzed in the frequency range of 200–1600 Hz [6]. It is obvious that sound impedance tube facility is widely used for routine measurements and is instrumental in design and development of acoustical materials for noise control. The present study discusses about the recently revived Sound Impedance Tube facility at CSIR-National Physical Laboratory, New Delhi.

2 Sound Impedance Tube

Sound impedance tube consists of Sound impedance AFD1000 Base Module Set (801022.5 Speaker Module, Amplifier, 971024.1, ¼ in. microphones), DAQ system, AFD1000 Absorption Tube with 30 and 100 mm diameter and Measurement of sound absorption Coefficient AFD 1000—AcoustiTube® Analysis Software AFD 1001. The testing samples are inserted in between the specified location of the sound impedance tube. The sample size and impedance tube size are selected as per the frequency requirement. A loudspeaker in the tube then emits precisely quantified sound in the form of plane waves, and the microphones measure the sound pressure level at specific locations along the length of the tube. The software then calculates the normal incident acoustic properties of the material based on frequency response functions measured. Figures 1 and 2 show the pictorial view of the sound impedance tube facility at CSIR-NPL, New Delhi. The facility has been brought under the Quality Management system as per ISO 17025:2017 recently and also the testing services are provided to the customers in the measurement frequency range of 50–6600 Hz.
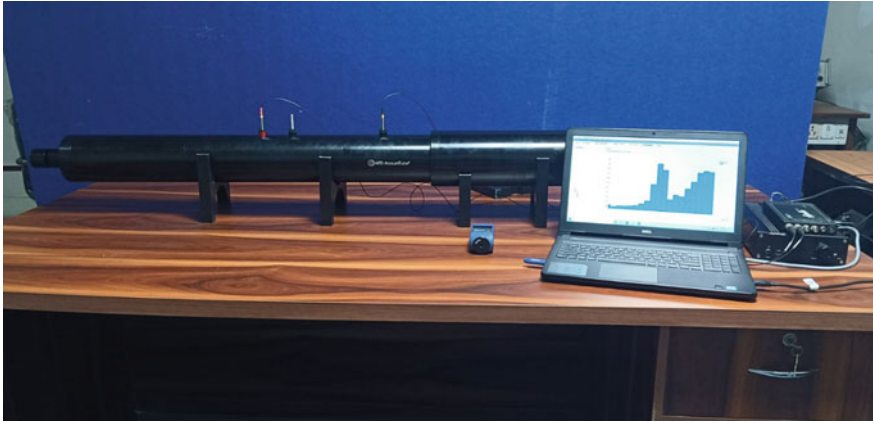
Fig. 1 Sound impedance tube for measurement of sound absorption characteristics in lower frequency range

Fig. 2 Sound impedance tube for measurement of sound absorption characteristics in higher frequency range

The Transfer function, H_{12} is calculated by placing the microphones at their original position and interchanging the microphone positions. Equations (1) and (2) determined to calculate the transfer function measured by the microphone interchange method [7].

$$H_{12} = |H_{12}|e^{j\varnothing} = H_r + jH_i \tag{1}$$

$$H_{12} = \frac{e^{jk_0 x_2} + re^{-jk_0 x_2}}{e^{jk_0 x_1} + re^{-jk_0 x_1}} \tag{2}$$

Sound pressure reflection factor is the amplitude of the reflected wave that of the incident wave in the reference plane for a plane wave at normal incidence. Normal incidence reflection factor is determined by Eq. (3) [7].

$$r = |r|e^{j\varnothing_r} = r_r + jr_i = \frac{H_{12} - H_1}{H_R - H_{12}}e^{2jk_0x_1} \tag{3}$$

where H_r: real part of H_{12}; H_i: imaginary part of H_{12}; r_r: real component; r_i: imaginary component; x_1: distance between sample and the further microphone location; x_2: distance between sample and first microphone; $\varnothing_r$: phase angle of normal incidence reflection factor; H_1: transfer function for the incident wave; H_R: transfer function for the reflected wave; k_0: complex wave number. Sound absorption coefficient at normal incidence Eq. (4) is the ratio of sound power entering to the test object to the incident sound power for a plane wave at normal incidence [7].

$$\alpha = 1 - |r|^2 = 1 - r_r^2 - r_i^2 \tag{4}$$

Specific acoustic impedance ratio and specific acoustic admittance ratio Eqs. (5) and (6) [7]

$$Z/\rho c_0 = R/\rho c_0 + jX/\rho c_0 = (1 + r)/(1 - r) \tag{5}$$

$$G\rho c_0 = g\rho c_0 - jb\rho c_0 = \rho c_0/Z \tag{6}$$

where R and X is the real and imaginary component of acoustic impedance; g and b is the real and imaginary component of acoustic admittance; Z is the acoustic impedance; G is the acoustic admittance; ρc_0 is the characteristic impedance.

3 Case Study

The commercially available Pine Wood Board Panel, PET (Polyethylene Terephthalate) Acoustic Board and Glasswool of size 30 and 100 mm diameter were used to measure the sound absorption properties by sound impedance tube method as per ISO 10534-2: 1998 [7]. Figure 3 shows the pictorial view of the 100 mm samples of pine wood board, glasswool and PET acoustic panel. The 30 mm sample size was used for doing sound absorption measurements in 150–6600 Hz frequency range, whereas 100 mm sample size was used for 50–500 Hz frequency range measurement in the sound impedance tube. The two-microphone transfer function method was used to do measurements in the range of 50–6600 Hz.

Table 1 shows the parameters of sound impedance tube and sound absorption and impedance characteristics were calculated and the correction for boundary absorption was applied.

Fig. 3 Pine wood board, glasswool and PET acoustic panel (100 mm diameter)

Table 1 Sound impedance tube parameters

Sl. No.	Sample size (mm)	Frequency range (Hz)	Distance between two microphone (mm)	Distance between microphone and sample (mm)
1	100	50–500	300	500
2	30	150–1250	120	180
3	30	900–6600	20	80

3.1 Sound Absorption Characteristics

Pine Wood Board, PET acoustical panel and glasswool samples acoustical characteristics such as Noise Reduction Coefficient (NRC), Sound Absorption Average (SAA) and Weighted Sound Absorption Coefficient (α_w) were measured by the two-microphone transfer function method in sound impedance tube facility in the frequency range of 50–6600 Hz.

Figure 4 describes the sound absorption characteristics of pine wood board, PET acoustic panel and glasswool in 50–6600 Hz frequency range. Sound Absorption Characteristics of all three samples in 1/3rd octave band frequency range.

Pine wood board's NRC 0.50, SAA 0.50 and α_w 0.35(H) were determined in 1/3rd octave frequency band whereas PET acoustical panel's NRC 0.45, SAA 0.46 and α_w 0.35(LH) were observed in 1/3rd octave frequency band. The glasswool's acoustical characteristics like NRC 0.62, SAA 0.63 and α_w 0.55(H) were determined at 1/3rd octave band frequency range.

Figure 5 shows the real part of sound impedance properties, whereas Fig. 6 shows the imaginary part of sound impedance properties of pine wood board, PET acoustical panel and glasswool in the sound impedance tube. Figures 7 and 8 show the sound reflection characteristics in terms of real and imaginary part with 50–6600 Hz frequency range.
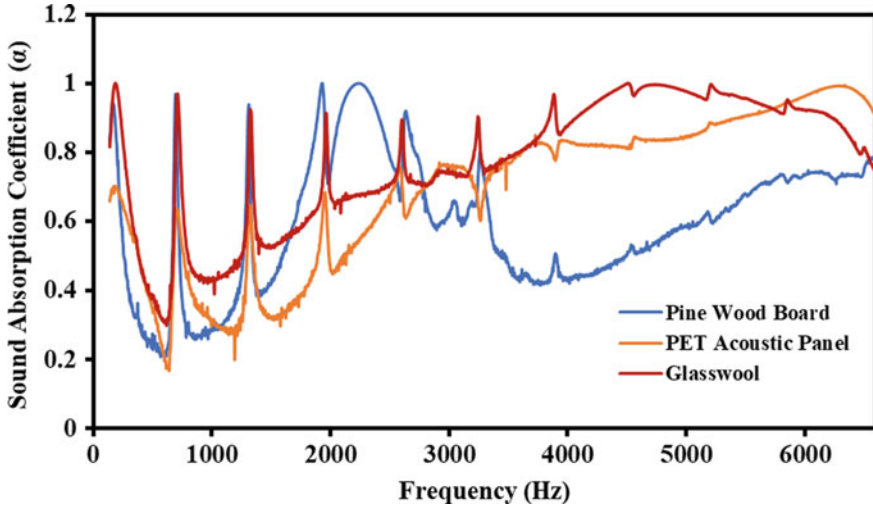
Fig. 4 Sound absorption coefficient of Pine wood board, PET acoustic panel and glasswool in 50–6600 Hz frequency range
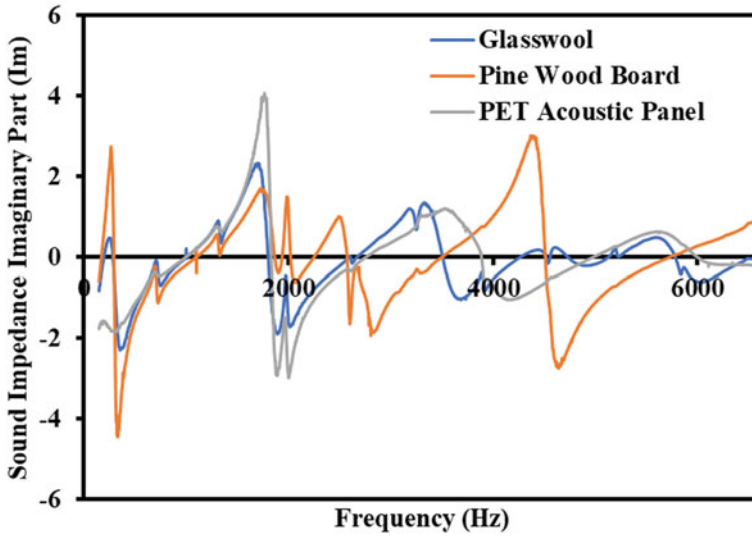
Fig. 5 Sound impedance characteristics (real part) of pine wood board, PET acoustic panel and glasswool in 50–6600 Hz frequency range
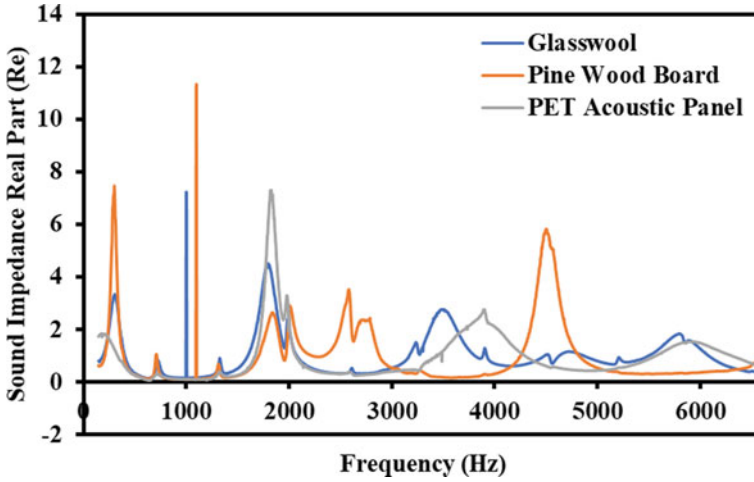
Fig. 6 Sound impedance characteristics (imaginary part) of pine wood board, PET acoustic panel and glasswool in 50–6600 Hz frequency range
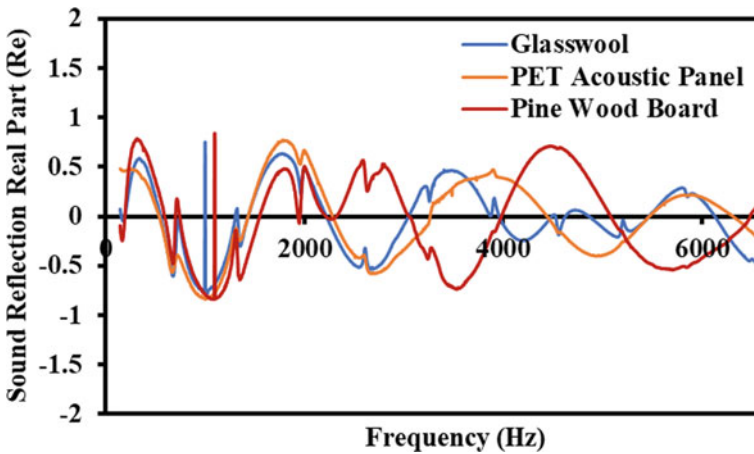
Fig. 7 Sound reflection characteristics (real part) of pine wood board, PET acoustic panel and glasswool in 50–6600 Hz frequency range

3.2 Measurement Uncertainty Evaluation

The sound impedance tube facility of CSIR-National Physical Laboratory, New Delhi provides the evaluation of sound absorption coefficient with the highest levels of accuracy and precision due to its traceability to the National standards of sound pressure level realized at CSIR-NPL, New Delhi. The quarter inch microphones, and
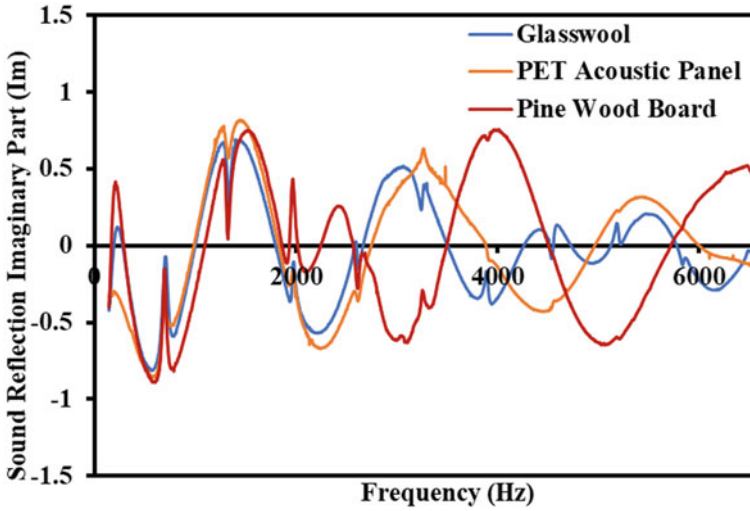
Fig. 8 Sound reflection characteristics (imaginary part) of pine wood board, PET acoustic panel and glasswool in 50–6600 Hz frequency range

the DAQ system (Make: SINUS Messtechnik GmbH) are calibrated using the multi-function acoustic calibrator, which in turn calibrated using the reference standard, LS2P microphone calibrated by primary reciprocity method in the frequency range of 31.5 Hz–8 kHz.

While testing the sound absorption characteristics, high Signal to Noise Ratio, microphone mismatch correction factor, phase mismatch and spatial averaging is accounted to reduce the measurement uncertainty. Table 2 shows the uncertainty budget of the sound impedance tube with a coverage factor of $k = 2$ as per the *Guide to the Expression of Uncertainty in Measurement* [8], that corresponds to a confidence level of approximately 95% in the testing result. The quality checks with the reference sample are conducted periodically to understand the deviations if any in the sound absorption characteristics.

Table 2 Measurement uncertainty (in %) in the evaluation of sound absorption characteristics by sound impedance tube facility

Description of influencing components	$50 \leq f \leq 200$ Hz	$200 \leq f < 1000$ Hz	$1000 \leq f < 3150$ Hz	$3150 \leq f \leq 6600$ Hz
Sound calibrator calibration	0.2	0.2	0.2	0.2
Error in calibration factor used for amplitude and phase mismatch between the microphones	0.81	0.5	0.5	0.81
Error in microphone amplitude calibration and analyzer	0.57	0.57	0.57	0.57
Error in correction for microphone mismatch	0.92	0.57	0.57	0.92
Analyzer non linearity and A/D conversion, signal-to-noise ratio	0.81	0.8	0.8	0.81
environmental conditions in tube	0.81	0.8	0.8	0.81
Error in correction for tube attenuation	0.75	0.5	0.5	0.75
Bias error (time aliasing, amplitude and phase mismatch)	0.92	0.8	0.8	0.92
Accuracy of transfer function	0.89	0.69	0.69	0.89
Speciment mounting, shape and size considerations	0.92	0.92	0.92	0.92
Residual effects including the spatial averaging, finite impedance of microphone, offset from acoustic centre, distortion and hum in loudspeaker, frequency, vibration isolation and resonance modes	1.15	0.75	0.75	1.15
Random effect in repeat measurements	0.57	0.37	0.44	0.39
Expanded uncertainty (in %) ($k = 2$, 95% confidence level)	6.0	5.0	5.0	6.0

4 Conclusion

The paper reports about the revived sound impedance tube facility at CSIR- National Physical Laboratory, New Delhi for evaluation of sound absorption characteristics of small size of acoustical materials with highest level of accuracy and precision. The measurement uncertainty of $\pm 6\%$ ($k = 2$, 95% C.I) is evaluated in the frequency range of 50–6600 Hz. The paper presents the case study of various acoustical materials such as Pine Wood Board, PET acoustical panel and Glasswool. The sound impedance tube facility serves as a good substitute to the Reverberation chamber utilizing a smaller sample size of diameter 30 and 100 mm for determination of sound absorption characteristics. However, future studies in this regard shall focus on the comparison of sound impedance tube measurements with the Reverberation chamber method for ascertaining the accuracy and correlation of sound absorption characteristics measured by the two methodologies.

References

1. Hasan K (2014) An assessment of the performance of impedance tube method. Noise Control Eng J 62(4):264–274
2. Mia S, Jambrosic K, Horvat M (2008) A comparison of two methods for measuring the sound absorption coefficient using impedance tubes. In: 2008 50th International symposium ELMAR, vol 1. IEEE, pp 321–324
3. Na Y, Agnhage T, Cho G (2012) Sound absorption of multiple layers of nanofiber webs and the comparison of measuring methods for sound absorption coefficients. Fibers Polym 13(10):1348–1352
4. Yang WD, Li Y (2012) Sound absorption performance of natural fibers and their composites. Sci China Technol Sci 55(8):2278–2283
5. Corredor-Bedoya AC, Acuña B, Serpa AL, Masiero B (2021) Effect of the excitation signal type on the absorption coefficient measurement using the impedance tube. Appl Acoust 171:107659
6. Ďuriš R, Labašová E (2021) The design of an impedance tube and testing of sound absorption coefficient of selected materials. IOP Conf Ser: Mater Sci Eng 1050(1):012003
7. ISO 10534-2 (1998) Acoustics—determination of sound absorption coefficient and impedance in impedance tubes, Part 2: Transfer-function method
8. JCGM 100:2008. Evaluation of measurement data—guide to the expression of uncertainty in measurement

Timing Accuracy for Internet of Things and Industry 4.0 Applications: Technologies and Research Trends

Deepak Sharma, Divya S Yadav, Bharath Vattikonda, and Ashish Agarwal

Abstract With the advent of time sensitive innovative applications under the Internet of Things and Industry 4.0 landscape, timing accuracy requirements have become crucial. Many current areas, like telecommunications, smart grids, the stock market, intelligent sensors ecosystems, etc., require timing accuracies in milliseconds to microseconds. The upcoming applications will require even more precise timing synchronization. For time synchronization, industrial applications are considering various approaches based on satellite or network-oriented techniques. These techniques are unique in terms of their functioning and pose unique challenges regarding their applicability. For example, Global Navigation Satellite System (GNSS) based time synchronization can provide nanosecond-level accuracy; however, the accessibility of satellite signals in indoor and other scenarios is a challenge. Distributed systems, like sensor networks, vehicular ad-hoc networks, distributed clouds, and many smart technologies under the umbrella of Industry 4.0, pose their unique challenges for time synchronization. The paper presents timing accuracy requirements for different application scenarios and discusses the suitability of available timing technologies to support them. It discusses the applicability and constraints of different technological solutions and explores new research directions in the area.

Keywords Timing accuracy · Time synchronization · Internet of Things (IoT) · Industry 4.0

D. Sharma (✉) · D. S. Yadav · B. Vattikonda · A. Agarwal
CSIR-National Physical Laboratory, New Delhi 110012, India
e-mail: deepak.sharma@nplindia.org

D. Sharma · B. Vattikonda · A. Agarwal
Academy of Scientific and Innovative Research (AcSIR), Ghaziabad 201002, India

1 Introduction

Internet of Things (IoT) technologies are becoming ubiquitous in modern days life [1, 2]. Timing accuracies are crucial for many IoT applications and the Industry 4.0 landscape. From steam power machines to the invention of electricity and information technology, time synchronization is still one of the most critical aspects of the industrial revolutions [3, 4]. Time synchronization requirement varies with application scenarios. The precision requirement for telecommunication applications' time synchronization varies from millisecond to nanosecond [5], e.g., ± 65 to 240 ns for 5G wireless communication. In a smart power grid, ± 1 microsecond traceability is required as per IEEE standards. Different applications require different types of precise timing, e.g., few applications require absolute timing, while other applications require relative timing [4]. There are many driving applications considering future industrial automation, e.g., synchronization among robotics systems with distributed computing and cloud; wireless sensor nodes synchronization; wireless synchronization for drone technology [6]. Timing is critical for applications like smart transportation, smart power grids, financial systems, and medical applications like telesurgery [7]. Further, as IoT applications are ubiquitous, the mass scale deployments require better timing accuracies with minimizing cost, weight, size and power consumption of the devices. As widely used inexpensive clocks drift due to various factors, the time synchronization is crucial for correct operations and correlating information from multiple devices. This motivates for developing innovative timing technologies to support noble solution in IoT and Industry 4.0 landscape.

The manuscript presents timing accuracy aspects for IoT and Industry 4.0 landscape. It discusses timing accuracy aspects for different application domains. It explains time transfer technologies and time traceability aspects. It highlights timing technology selection criteria under different scenarios and explores key research directions in the area. The work, covering both technological advancements and the application aspects of timing technologies, is highly relevant for formulating innovative solutions in the area.

The manuscript covers timing accuracy aspects in IoT and Industry 4.0 landscape in Sect. 2. In Sect. 3, time transfer technologies are discussed. Section 4 covers timing technology selection under different application scenarios. The research trends in the area are discussed in Sect. 5 and the manuscript is concluded in Sect. 6.

2 Timing Accuracy in IoT and Industry 4.0

As industries have evolved over time, the timing accuracy requirements have become more stringent (Fig. 1). Industry 4.0 considers cyber physical systems approach, interfacing physical and digital worlds, with the capability of real-time information exchange and decision making [8]. Industry 4.0 introduces an advanced automation
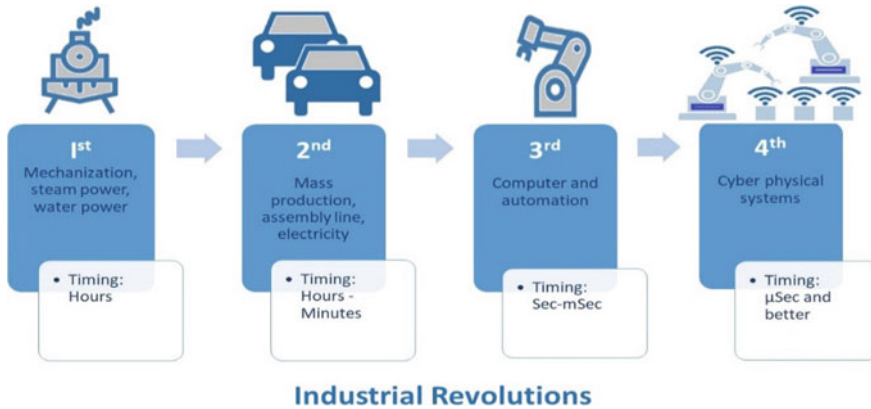
Fig. 1 Increase in accurate timing requirements with Industrial Revolutions

level that requires more accurate time synchronization. Considering the application/domain specific requirements (e.g., industrial automation (1 µs–1 ms), wireless communication (200 ns–12.8 µs), smart grids (1 µs–100 ms)), a suitable time synchronization technology is considered based on satellite or terrestrial technologies [9] such as Network Time Protocol (NTP), Precision Time Protocol (PTP), Generalized Precision Time Protocol (gPTP), Precision Transparent Clock Protocol (PTCP), Synchronous Ethernet (SyncE) and White Rabbit (WR).

The Internet of thing landscape is based on connected devices with communication, computations and sensing/actuating capabilities. Time synchronization is required for the correct operation of IoT networks involving efficient spectrum usage, coordinated communications and data acquisition from different sensors [10]. In Wireless Sensor Networks (WSN), time synchronization is required for many operations, e.g., correlating different reports, duty cycling and channel access scheduling, time-division multiple-access (TDMA) scheduling, data fusion/aggregation, real-time monitoring and actuation [11]. IoT is widely used in various real-time applications such as smart homes, smart security solutions, smart healthcare, smart wearables, transportation, renewable energy, etc. Each node/device in the IoT architecture generally contains a local clock. There are many parameters which affect the accuracy of clocks such as humidity, temperature, pressure, aging, voltage, and vibration [7]. On the other hand, network, software and hardware parameters may affect the time accuracy/offset of IoT devices. The local clock of IoT devices are synchronized with other more stable clocks for accurate timing. Time synchronization strategy for IoT devices is an exciting research area [12, 13]. Adequate time synchronization accuracy can help in achieving energy-efficient, reliable and low-latency communication networks in IoT infrastructure [10]. The IoT devices can improve their timing accuracy by getting a more accurate time using technologies based on network timing, RF based timing and or satellite based timing (Fig. 2). These techniques are discussed in next section.
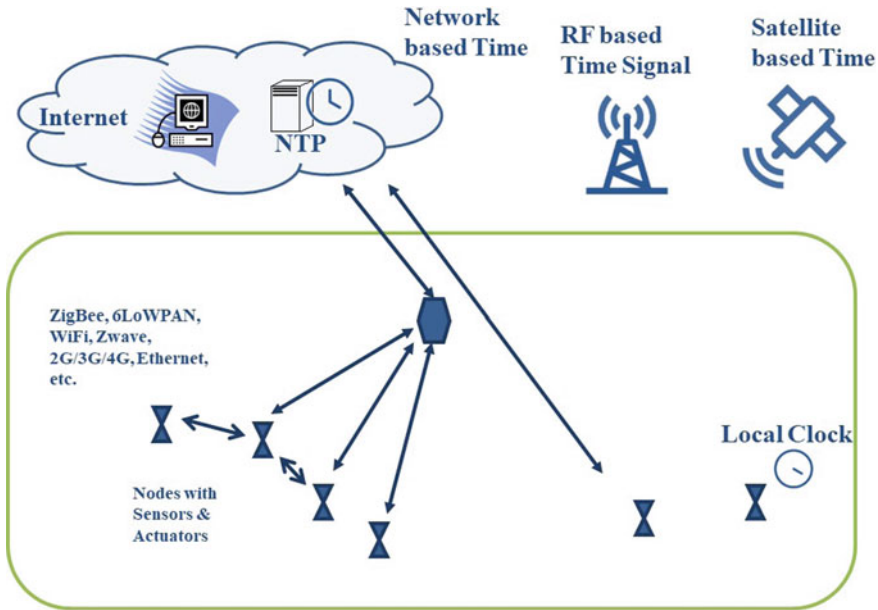
Fig. 2 Timing technologies for IoT landscape

3 Time Transfer Technologies

Metrological traceability is based an unbroken calibration chain to a reference, where each calibration has a documented measurement uncertainty. In time and frequency metrology, the usual reference is Coordinated Universal Time (UTC) or its official realization UTC(k) [14]. Time signals transmitted by satellites and network time servers, can be utilized for metrological traceability. Traceability to a stable time reference helps in maintaining timing accuracy at end devices. In Cyber Physical System landscape synchronization of low cost devices and communication infrastructure is crucial. The key solutions for time synchronization and traceability are generally based on satellites based and/or terrestrial technologies based approaches [5, 9, 15].

3.1 Terrestrial Technologies

Network Time Protocol (NTP) is a widely used time synchronization technique for computer networks (Internet) based devices with a time accuracy limitation of around 100 ms. Precision Time Protocol (PTP) is another network based time transfer mechanism with time accuracy within 10 microseconds. However, PTP requires dedicated LAN/fiber connectivity. Time transfer through telephone (PSTN) line has also

Table 1 Time transfer technologies: terrestrial technologies

Time transfer technique	Accuracy	Details	Limitations
NTP	<100 ms	Data packet based time transfer in the Internet/networks	Millisecond accuracy
Telephone line based	≤10 ms	Telephone lines (PSTN) based	Millisecond accuracy
PTP	≤10 µs	Based on data packets communication on a dedicated link	Requires dedicated connectivity; hardware support
gPTP	≤1 µs	IEEE 802.1AS; specified for time sensitive wired and wireless network	Limited to seven Hops, requires specialized hardware
PTCP	≤1 µs	Based on PTP	Requires specialized hardware on switches and nodes
SyncE	~±4.6 ppm	Ethernet based, end to end reliable exchange	Physical layer operation, Distribute only frequency
White rabbit (WR)	Sub nano second	Deterministic delivery of a packet	Costly, require to support PTP and SyncE
Long wave radio (low frequency)	100 ms	Based on long-wave radio (low frequency) signals	Available in a few countries

been explored with time accuracy within 10 ms. Low frequency ground waves are also used for time dissemination in many countries, e.g., DCF77 by PTB. Further, there are other technologies like Generalized Precision Time Protocol (gPTP), Precision Transparent Clock Protocol (PTCP), Synchronous Ethernet (SyncE) and White Rabbit (WR).Table 1 shows a brief comparison of these key time transfer technologies.

3.2 Satellite Based Technologies

Satellite based time transfer techniques include Common-View/All-in-View Global Navigational Satellite (CVGNSS/AVGNSS) and Two-Way Satellite Time and Frequency Transfer (TWSTFT) (Fig. 3). The CVGNSS/AVGNSS techniques can attain accuracy within ten nanoseconds by processing the common-view data from reception of satellite signals. Two-Way Satellite Time and Frequency Transfer (TWSTFT), involving expensive two-way communication infrastructure and a leased link with a geostationary satellite, can provide a time accuracy within 1 ns.
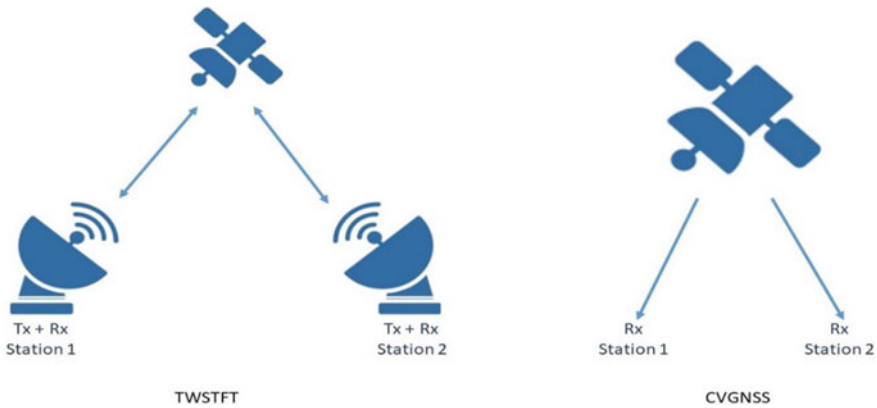
Fig. 3 CVGNS and TWSTFT methods of time transfer

Table 2 Time transfer technologies: satellite based technologies

Time transfer technique	Accuracy (ns)	Details	Limitations
CVGNSS/AVGNSS	≤ 10	Based on microwave signals received from navigational satellites	Common-view data processing
TWSTFT	<1	Based on leased link on geostationary satellite	Expensive; requires huge infrastructure

For achieving high timing accuracy at the users' end, satellites signal based disciplined oscillator may be considered. A GPS disciplined clock's synchronization uncertainty may vary from ~10 ns to ~1 μs [14]. NIST (USA)'s disciplined clock (NISTDC) service considers common-view measurement to lock the user's clock to UTC (NIST) with uncertainty ~10 ns. Table 2 shows a brief comparison of key satellite based time transfer technologies.

4 Technology Selection Under Different Application Scenarios

Different applications have different precise timing requirements. Many applications do not require absolute time or time traceable to Coordinated Universal Time (UTC) and their actual requirement is to measure accurately the time elapsed between events, e.g., heart rate monitors [4]. An accurate local clock can serve the purpose in such cases. However, other applications like global reference clocks require absolute time. There are applications with distributed devices/applications having a shared notion of time intervals. Absolute timing requirements are less stringent in many
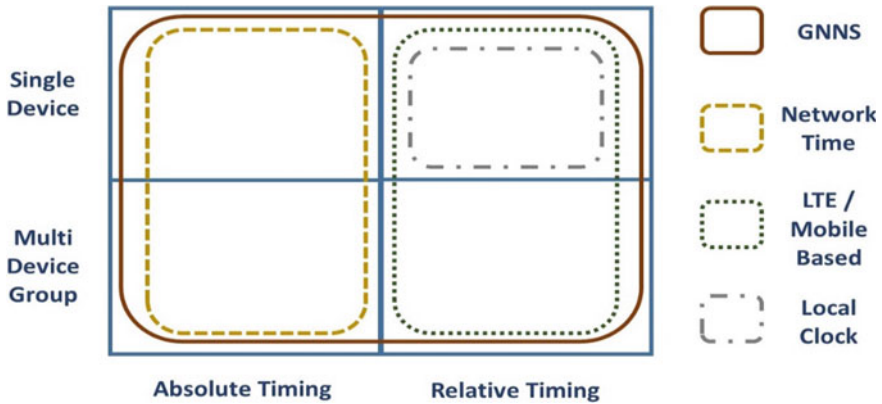
Fig. 4 Technology suitability for different timing requirements

distributed precise timing applications like media equipment (e.g., microphones) synchronization in the broadcast industry requiring microseconds of accuracy [5]. Another example is smart electricity grids considering phasor measurement units. Further, for many distributed applications absolute timing is a necessity, e.g., financial/stock trading. Considering higher accuracies, GNSS based time synchronization may be suited for such cases.

Figure 4 shows the consideration of different timing solutions for different timing requirements. Each timing solutions have some associated limitations, e.g., drifting of local clocks, unobstructed sky view requirement for GNSS-based solutions, etc. A practical approach could be to consider a hybrid solution with combining multiple approaches.

5 Research Trends

Along with Industrial landscape evolution through Industry 4.0, there is a rise of diverse timing aware innovative applications like Smart Power Grids; Smart Transportation; Medical applications like telesurgery; Telecom systems; Financial systems like Stock Markets; Augmented/Virtual reality; Synchronization among robotics systems with distributed computing and cloud; Wireless sensor nodes synchronization; Wireless synchronization for drone technology; Scientific applications, etc.

Timing accuracy research directions are spread across the timing traceability chain. The NIST technical Note 1867 [7] on Time-Aware Applications, Computers, and Communication Systems (TAACCS) highlights six key R&D areas, viz., clock and oscillator designs; transfer methods for time and frequency; timing usage in communications and networking systems; architecture of hardware and software; design environments; design of applications. Considering large scale deployment

requirements in IoT landscape, the clocks and oscillator designs require consideration of increasing accuracy with minimizing cost, weight, size and power consumption. For example, Quartz crystal oscillators are inexpensive with low accuracy (10^{-5}–10^{-4}) and the Cesium oscillators are very accurate (10^{-13}–10^{-12}) and highly expensive. Developing techniques for ensembling low cost oscillators and operating conditions compensation are interesting research directions in the area. The key research directions in time and frequency transfer methods are cost-effective and power-aware methods for networks; interdisciplinary approach like combining GNSS with network based timing; GNSS signal quality and reliability aspects; security technology for time transfer methods. Under time-aware networks and communications, key research areas are timing in network equipment hardware; time-controlled and time-aware networks; Time Sensitive Networking; timing aspects related to time sensitive applications under cloud computing and network visualization; synchronizing databases, distributed applications; time augmentation in routing protocols; time support of latency control, wireless spectrum and bandwidth utilization. Timing support for applications require consideration of predicable execution times (precision timed machines), predictable processor designs, time-aware hardware mechanisms and languages; timing interface hardware support; issues of scale; development of stable ultra-low-power local time references; cross-IoT-network synchronization, distributed computing issues. Other research directions are platform independent design environments with system timing and exploring potential improvements in applications using time-aware techniques. Considering real-time and delay sensitive aspects in today's computer applications, time synchronization is considered as the fourth dimension in data center along with computers, storage and network [16]. In massive scale distributed databases, PTP based solution can improve database transaction timing performance over NTP based approach.

The low cost sensor nodes in WSN are limited in resources (e.g., energy, bandwidth, hardware) and face various challenges like energy-efficiency, networking, etc. Many synchronization protocols are proposed for WSN scenarios with microseconds level precision [17]. Synchronization is required in vehicular ad-hoc networks (VANETs) for communicating time-critical vehicle messages from connected and automated vehicles for various applications related to road safety [18]. Time-critical machine-type communication (cMTC) requires the distribution of accurate time reference for a potential application like industrial automation [19]. Standards and products for Time Sensitive Networks (TSN) are considered to support real-time application requirements, which often require less than 1 microsecond time synchronization [20]. In TSN, the synchronization is separable from other functionalities. The Precision Time Protocol (IEEE Standard 1588) is generally considered for clocks synchronization in the network; however, other algorithms may be considered based on application.

In terms of other new research directions for time synchronization in IoT, researchers considered a visible light-based approach and achieved an average synchronization error of 1.3 timer ticks (32 μs per clock tick) [21]. Hybsync [22], a UWB communication and multisensor-based approach, can achieve clock synchronization in nanosecond-level and centimeter-level positioning. It can work under

GNNS-denied conditions and support 10+ nodes. Timing aspects for IoT devices exploiting remote servers and cloud services is another interesting area. Rinaldi et al. [23] present a comparison of time awareness of different cloud services. Security and trust aspects in timing technologies is another interesting research direction. Margaria and Vesco [24] present trusted satellite based synchronization for Industry 4.0 covering attack vectors analysis. The time synchronization research in upcoming communication technologies like 5G [25, 26] and 6G [27, 28] is another important area. Software-based synchronization (e.g., NTP) provides implementation flexibility; However, improving their performance to match hardware-based solutions is another exciting research direction in the area.

6 Conclusion

Timing accuracy is essential for IoT and Industry 4.0 operations. With the emergence of novel applications, timing accuracy requirements are becoming more stringent and there is a need for innovative solutions for time synchronization. The work presents the timing technologies landscape for IoT and Industry 4.0 applications. The diverse timing technologies are discussed and timing technology selection aspects for different application requirements are covered in detail. The research trends in the area are highlighted, which show that timing accuracy improvements require multidisciplinary R&D across the timing traceability chain, i.e., precise time realization, maintenance and dissemination. Further, improving timing accuracy, stability, and/or reliability could help in developing compelling new or enhanced applications.

References

1. Gubbi J et al (2013) Internet of Things (IoT): a vision, architectural elements, and future directions. Futur Gener Comput Syst 29(7):1645–1660
2. Khan WZ et al (2020) Industrial internet of things: recent advances, enabling technologies and open challenges. Comput Electr Eng 81:106522
3. Gerekli İ, Çelik TZ, Bozkurt İ (2021) Industry 4.0 and smart production. TEM J 10(2):799–805
4. Drazen Drinic CM (2018) Accurate timing for the IoT
5. Aswal DK (2020) Metrology for inclusive growth of India. Springer Nature
6. Gore RN et al (2020) Clock synchronization in future industrial networks: applications, challenges, and directions. In: 2020 AEIT international annual conference (AEIT). IEEE
7. Weiss M et al (2015) Time-aware applications, computers, and communication systems (TAACCS)
8. Varshney A et al (2021) Challenges in sensors technology for industry 4.0 for futuristic metrological applications. MAPAN 36(2):215–226
9. Puttnies H et al (2020) Estimators for time synchronization—survey, analysis, and outlook. IoT 1(2):398–435
10. Tirado-Andrés F, Rozas A, Araujo A (2019) A methodology for choosing time synchronization strategies for wireless IoT networks. Sensors 19(16):3476

11. Djenouri D, Bagaa M (2014) Synchronization protocols and implementation issues in wireless sensor networks: a review. IEEE Syst J 10(2):617–627
12. Yiğitler H, Badihi B, Jäntti R (2020) Overview of time synchronization for IoT deployments: clock discipline algorithms and protocols. Sensors 20(20):5928
13. Mani SK et al (2018) An architecture for IoT clock synchronization. In: Proceedings of the 8th international conference on the internet of things
14. Matsakis D, Levine J, Lombardi M (2018) Metrological and legal traceability of time signals. In: Proceedings of the 49th annual precise time and time interval systems and applications meeting
15. Lévesque M, Tipper D (2016) A survey of clock synchronization over packet-switched networks. IEEE Commun Surv Tutor 18(4):2926–2947
16. NVIDIA (2021) Precision timing for the next wave of data center applications. https://www.nvidia.com/content/dam/en-zz/Solutions/gtcf21/networking/data-processing-unit/gtc-fall-21-networking-overall-dpu-technical-overview-firefly.pdf. Accessed 06–11–2022
17. Sundararaman B, Buy U, Kshemkalyani AD (2005) Clock synchronization for wireless sensor networks: a survey. Ad Hoc Netw 3(3):281–323
18. Hasan KF et al (2018) Time synchronization in vehicular ad-hoc networks: a survey on theory and practice. Veh Commun 14:39–51
19. Mahmood A et al (2019) Time synchronization in 5G wireless edge: requirements and solutions for critical-MTC. IEEE Commun Mag 57(12):45–51
20. Finn N (2018) Introduction to time-sensitive networking. IEEE Commun Stand Mag 2(2):22–28
21. Guo X et al (2016) PSync: visible light-based time synchronization for Internet of Things (IoT). In: IEEE INFOCOM 2016—the 35th annual IEEE international conference on computer communications. IEEE
22. Lei P et al (2021) Hybsync: nanosecond wireless position and clock synchronization based on UWB communication with multisensors. J Sens 2021
23. Rinaldi S et al (2019) Are cloud services aware of time? An experimental analysis oriented to industry 4.0. in 2019 In: IEEE international symposium on precision clock synchronization for measurement, control, and communication (ISPCS). IEEE
24. Margaria D, Vesco A (2021) Trusted GNSS-based time synchronization for Industry 4.0 applications. Appl Sci 11(18):8288
25. Lin J-C (2018) Synchronization requirements for 5G: an overview of standards and specifications for cellular networks. IEEE Veh Technol Mag 13(3):91–99
26. Striffler T, Michailow N, Bahr M (2019) Time-sensitive networking in 5th generation cellular networks-current state and open topics. In: 2019 IEEE 2nd 5G world forum (5GWF). IEEE
27. Mahmood NH et al (2022) A functional architecture for 6G special purpose industrial IoT networks. IEEE Trans Ind Inform
28. Yeh C et al (2022) Perspectives on 6G wireless communications. ICT Express

Effect of Continuous NIR Exposure on the Absorbance Studies of Glucose Solutions at Physiological Levels

Deepshikha Yadav, Manjri Singh, Surinder P. Singh, and P. K. Dubey

Abstract Non-invasive glucose monitoring is the need of the hour due to steep rise in diabetic patients worldwide. Monitoring of glucose level at regular interval is important for preventing the diabetes related complications. Several non-invasive methods Raman, MIR, NIR, photo acoustic, bio impedance and fluorescence spectroscopy, polarimetry, microwave assisted monitoring etc. have been explored for this purpose. However, none of the techniques have achieved accuracies that are suitable for clinical use. NIR spectroscopy is a popular technique which is being extensively employed for the development of a non-invasive glucose measurement device. However, the NIR spectra is prone to variations due to changes in temperature, machine drift, time drift, water content etc. and seem dominant because of extremely low level of absorption variation in glucose. In the present study, the variations in the glucose absorbance at 960 nm as a result of consecutive measurements are demonstrated. The study reveals that there is a decrease in the glucose absorbance because consecutive measurements cause long exposure of sample to NIR and hence the heating of the solutions which results in a rise in temperature. The absorbance at a wavelength of 960 nm is affected by temperature because it corresponds to OH stretching vibrations and the OH groups of sugars are sensitive to temperature. The results also reveal that even at 1 °C variation in the temperature of a 100 mg/dl glucose solution leads to a decrease in the glucose absorbance from 0.00301 to 0.00150 (δ_{abs} = 1.52×10^{-3}). Even this small variation in the absorbance can cause large errors in the prediction of glucose concentrations. Therefore, for device fabrication using NIR spectroscopy temperature variations must be taken into consideration to improve the accuracy of glucose predictions.

Keywords Non-invasive · NIR spectroscopy · Temperature · Absorption · Glucose

D. Yadav (✉) · M. Singh · S. P. Singh · P. K. Dubey
CSIR-National Physical Laboratory, Dr. K.S. Krishnan Marg, New Delhi 110012, India
e-mail: deepshikha.yadav93@gmail.com

Academy of Scientific and Innovative Research (AcSIR), Ghaziabad 201002, India

1   Introduction

Diabetes is a chronic metabolic disorder which leads to high blood sugar levels in the body as a result of insulin dysfunction [1]. According to the International Diabetes Federation (IDF) approximately, 537 million adults are suffering from diabetes worldwide aged between 20 and 79 years. The global mortality rates are 6.7 million [2]. Tight glycemic control is essential to prevent complications like retinopathy, cardiovascular disorders, stroke, neuropathy, nephropathy etc. [3]. Currently, the blood glucose measurement is performed by glucometers which are based on the electrochemical method of sensing. This requires blood sampling for precise measurement of blood glucose levels [4]. The invasive mode of measurement is not suitable for frequent blood glucose monitoring.

Therefore, non-invasive glucose sensing techniques like, near infrared spectroscopy, Raman spectroscopy, mid-infrared spectroscopy, polarimetry, and fluorescence spectroscopy are slowly gaining momentum as alternatives for blood glucose measurements. Non-invasive glucose sensing using near infrared spectroscopy is a popular technique which has been extensively explored. Inspite of the growing popularity of this technique there are certain shortcomings which heavily influence the measurement of glucose. Owing to the low glucose absorption throughout the NIR, the signal to noise ratio is poor [5]. Besides, the temperature variations, water content, and scattering properties of the tissue heavily distort the spectra of glucose [6].

Temperature is an important parameter to be considered for non-invasive measurements using NIR spectroscopy because, the absorption of water is largely influenced by variations in the temperature. It is a well-known fact that in regions where the absorption of water is strong, the S/N is poor [7]. Given, the significant percentage of water (up to 60%) content that makes up the human body, it is critical to consider its impact on the NIR spectra of glucose. The repeated exposure of glucose solutions to NIR light may cause the solution to heat up which leads to obvious temperature changes. These temperature variations result in a variation in the glucose absorbance [8]. In fact, studies have shown that even a variation of 1 °C lead to significant error in prediction of glucose concentration [6]. Therefore, studying the variations in glucose spectra due to continuous exposure to NIR light is necessary for the development of a non-invasive device. As per literature there are few studies on studying the effect of continuous scanning of glucose solutions leading to continuous exposure to NIR light resulting in temperature fluctuations.

In the present study, we have corroborated the heating effect due to continuous exposure of NIR light to glucose solutions using three different methodologies, namely, the temperature dependent scanning, kinetic study and average δ (δ_{avg}) studies. All the results reveal that the continuous scanning leads to steady decrease in glucose absorbance due to heating effect and the ultimate rise in temperature.

2 Materials and Methodology

Glucose powder was procured from Sigma Aldrich. For the studies, different concentrations of glucose solutions were prepared including, 60, 100, 140, 160, 180 and 500 mg/dl covering the hypoglycemic, normoglycemic and hyperglycemic ranges. Five consecutive scans of the different glucose solutions were recorded in a Cary-5000 UV-Vis-NIR spectrophotometer, having spectral bandwidth from 175 to 3300 nm. The temperature at the start of the first scan was recorded. The temperature at the end of five consecutive scans was also recorded.

Kinetics study: Furthermore, kinetics study was also performed to evaluate the time dependent variation in glucose absorbance at 960 nm wavelength for a duration of 15 min for glucose concentrations of 150, 200 and 250 mg/dl.

Average δ studies: In order to study this variation in glucose absorbance at 960 nm, we evaluated the average δ value (difference), of absorbance at 860 and 960 nm for glucose concentrations of 350, 380, 400, 440, 470 and 500 mg/dl. Such high concentrations were taken to observe a significant variation in the average delta values. The readings were taken after an interval of 2 min after each scan, up to a duration of 10 min.

3 Results and Discussion

3.1 Glucose Absorbance Variations Due to Continuous Exposure to NIR Light

For determining the effect of continuous exposure to NIR light on glucose absorbance. Different concentrations of glucose solutions covering the hypoglycemic, normoglycemic and hyperglycemic ranges, i.e. 60, 100, 140, 160, 180 and 500 mg/dl were prepared and their NIR spectra were recorded. The temperature of the solutions before scanning was recorded and then the cycle was set for taking 5 consecutive scans of the solutions. After the scanning was complete the solutions were removed from the instrument and their temperature was recorded again. It was observed that there was a steady decrease in the glucose absorbance at 960 nm due to the consecutive scanning with an average rise of 1 °C in the temperature of the solutions after scanning as shown in Fig. 1.

This rise in temperature may be attributed to the heating of the solutions as a result of repeated scanning which results in a rise in the temperature and a decrease in the absorbance of the glucose solution. This heating effect is a result of continuous exposure to the NIR light [4]. For a solution of 100 mg/dl, there is a change of the order of 1.52×10^{-3} in the glucose absorbance which can result in significant errors in the prediction of glucose concentration through NIR spectroscopy. Further, the
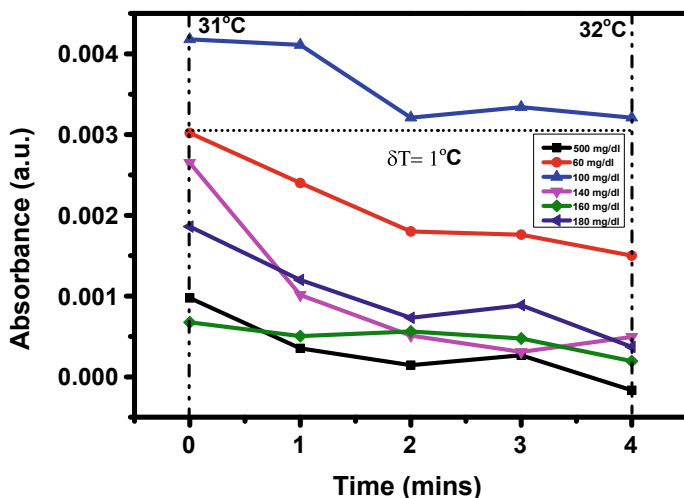
Fig. 1 Variation in glucose absorbance due to continuous exposure to NIR light

wavelength 960 nm is particularly sensitive to temperature fluctuations because of the sensitivity of the OH groups towards temperature.

3.2 Kinetics Study

Different concentrations of glucose solutions i.e. 150, 200 and 250 mg/dl were prepared and subjected to kinetics studies to corroborate the results of the previous study. The study was performed at 960 nm wavelength to observe the variations in the glucose absorbance with time for a period of 15 min. A steady decrease in the glucose absorbance was observed with time up to a period of 5 min which corroborates the results of the previous study where the repeated scanning of the glucose solutions led to a steady decrease in the glucose absorbance for five consecutive scans which adds up to a period of five minutes because each scan takes about a minute to complete. Further, after a period of 5 min, a saturation in the glucose absorbance is obtained which continues for the rest of the time duration as shown in Fig. 2. This decrease in glucose absorbance is attributed to the heating of the glucose solutions as a result of the consecutive scanning due to prolonged exposure to NIR light as discussed above.
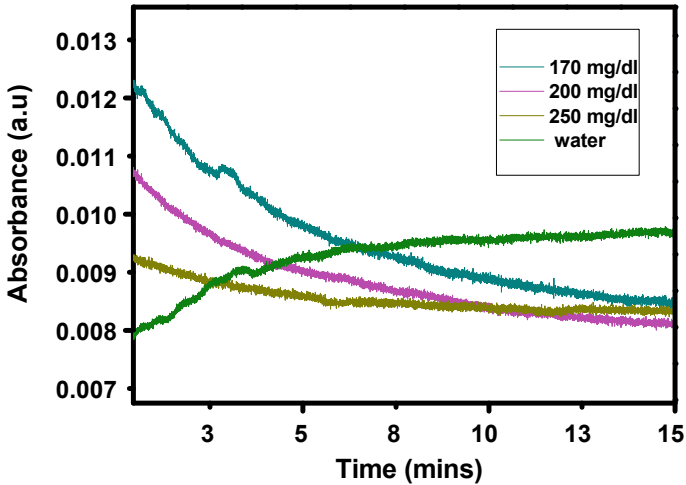
Fig. 2 Kinetics study of different glucose solutions at 960 nm, scanning for 15 min

3.3   Average Δ (δ_{avg}) Studies

To study the average magnitude of the variation in the glucose absorbance with continuous exposure to NIR light, solutions of different glucose concentrations i.e. 350, 380, 400, 440, 470 and 500 mg/dl were prepared and their NIR spectra were recorded. The spectra were recorded in such a way that after the completion of one scan the solution was kept in the cuvette holder of the UV-Vis-NIR spectrophotometer for a period of 2 min. The same process was repeated up to a duration of 10 min for each concentration. Then, the average difference in the absorbance values at 860 and 960 nm (δ_{avg}) for all scans up to a period of 10 min was evaluated for each concentration. There was a steady decrease in the absorbance with time corroborating the results above due to continuous exposure to NIR light, accompanied with an increase in the δ_{avg} value with an increase in the glucose concentration as shown in Fig. 3.
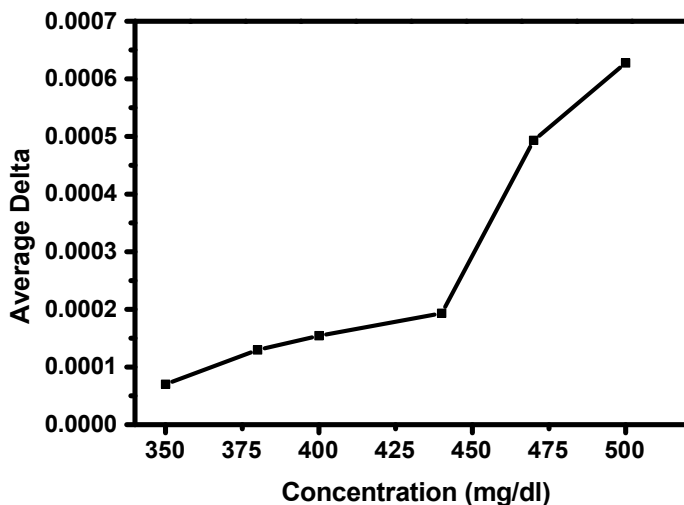
Fig. 3 Average δ values of different glucose solutions between 860 and 960 nm for consecutive scanning up to 10 min

4 Conclusion

In the present study, the effect of continuous exposure to NIR light on the NIR spectra of glucose solutions has been studied using three different methodologies. All the three studies reveal a steady decrease in the glucose absorbance as a result of consecutive scanning. This may be attributed to the continuous exposure of glucose solutions to NIR light resulting in heating effect leading to a rise in the initial temperature of the solution. As discussed above, water absorption is strongly influenced by temperature variations. This is a critical point when undertaking the spectroscopic studies of the biological systems which are largely composed of water. The main aim of this study was to study the influence of temperature variations in the NIR spectra of glucose solutions. This is because, temperature fluctuations may result in large prediction errors in the non-invasive determination of glucose concentrations using NIR spectroscopy. Therefore, for the development of a non-invasive device using NIR spectroscopy, the temperature induced variations in the spectra must not be neglected and must be taken into consideration for better predictions of glucose concentrations.

Conflicts of Interest The authors declare no conflicts of interests in the above research work.

References

1. American Diabetes Association (2010) Diagnosis and classification of diabetes mellitus. Diabetes Care 33(Supplement_1):S62–S69
2. https://idf.org/aboutdiabetes/what-is-diabetes/facts-figures.html
3. Deshpande AD, Harris-Hayes M, Schootman M (2008) Epidemiology of diabetes and diabetes-related complications. Phys Ther 88(11):1254–1264
4. Yoo EH, Lee SY (2010) Glucose biosensors: an overview of use in clinical practice. Sensors 10(5):4558–4576
5. Goodarzi M, Sharma S, Ramon H, Saeys W (2015) Multivariate calibration of NIR spectroscopic sensors for continuous glucose monitoring. TrAC Trends Anal Chem 67:147–158
6. Cui H, An L, Chen W, Xu K (2005) Quantitative effect of temperature to the absorbance of aqueous glucose in wavelength range from 1200nm to 1700nm. Opt Express 13(18):6887–6891
7. Jensen PS, Bak J, Andersson-Engels S (2003) Influence of temperature on water and aqueous glucose absorption spectra in the near-and mid-infrared regions at physiologically relevant temperatures. Appl Spectrosc 57(1):28–36
8. Bazar G, Kovacs Z, Tsenkova R (2016) Evaluating spectral signals to identify spectral error. PLoS One 11(1):e0146249

Accuracy in Object Detection by Using Deep Learning Method

Divya Sirala and Kuldeep Singh Nagla

Abstract Accuracy and Precision measurement of an object in a complex environment for mobile robot applications is an important task. In a complex environment it is difficult to identify similar objects, such as chairs, tables, furniture and other objects available. Different methods are available to identify such objects, but high accuracy and precision are not easily achievable. This paper presents MobileNet with Vision Transformer for identification of objects in complex environments. Several experiments have been conducted for indoor environments where 94.3% accuracy is achieved for indoor environment with the implementation of MobileNet with Vision Transformer model.

Keywords MobileNet · Vision transformer · Mobile robot · Accuracy and precision measurement

1 Introduction

For Mobile Robots, the process of object detection is an important task as it is what helps the autonomous robot to detect hurdles and react to its environment to navigate without the help or involvement of humans. Object Detection and Recognition method using deep learning is important as to verify new theories and methods for solving the various detection problem of general complex environment because of the accuracy and speed of the methods. There are many approaches of object detection for mobile robots like laser-based detection, camera-based detection, deep learning-based detection, etc. However, Deep Learning has recently become quite popular because of its superior accuracy when taught on massive amounts of data.

D. Sirala (✉) · K. S. Nagla
Dr. B. R. Ambedkar, National Institute of Technology, Jalandhar, India
e-mail: divyasirala@gmail.com

There are many Machine Learning and Deep learning based algorithms used for Object Detection and Recognition, such as Convolution Neural Networks (CNNs), Support Vector Machine (SVM), Regional Convolutional Neural Networks (R-CNNS), You Only Look Once (YOLO) etc., it becomes crucial to select the appropriate algorithm for Mobile Robot Object Detection which should solve the problem regarding speed, accuracy response time and input data used to train and test the model.

MobileNet model is used for object detection with custom dataset. To build MobileNet a light deep learning model with depthwise convolutions was created, which are faster compared to other CNN architectures. Due to its smaller size and low latency, MobileNet outperforms other Deep Learning methods for object detection.

The proposed method describes an efficient network architecture using MobileNet with an additional Vision Transformer layer to be trained on a Custom Dataset of indoor environment. By means of high accuracy and efficient computing, ViT models surpass CNNs by roughly four times [1]. With the demonstration of experiments to detect certain objects present in the indoor environment, the factors determining the efficacy of the suggested model in comparison to a traditional model of MobileNet method for object detection are Accuracy, Precision, f1-Score, Confusion Matrix and Losses.

1.1   MobileNet

The depthwise separable convolutions, a type of factorized convolutions that factorize a conventional convolution into a depthwise convolution as well as a 1×1 convolutional known as a point-wise convolution, are the foundation of the MobileNet model. Using depthwise convolution, MobileNet applies a single filter to each input channel. The outputs of the depthwise convolution are combined using a 1×1 convolution after the pointwise convolution.

In one step, a conventional convolution filter mixes inputs to invent a fresh set of outputs. This is divided into two layers by the depthwise separable convolution: a layer for combining and a layer for filtering. The computations and model size are significantly decreased because of this factorization. Figure 1 [2] illustrates the factorization of a conventional convolution into a depthwise and a 1×1 pointwise convolution.

1.2   Vision Transformer

Recently, there has been an increased interest in Vision Transformers (ViTs) in computer vision research. The introduction of self-attention for visuals is a key component of ViT's ideation resulting in self-attention. The ViT model predicts the label for use with a classifier head and represents an input picture as a sequence of

(a) **Regular Convolutional Filters**

(b) **Depthwise Filters**

(c) 1x1 Convolutional Filters called Pointwise Convolution
in the context of Depthwise Separable Convolution
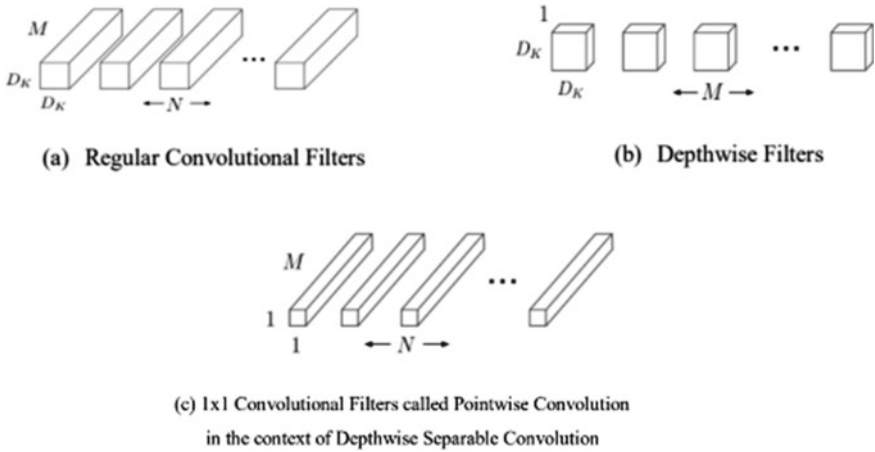
Fig. 1 The standard convolutional filters in (**a**) are replaced by two layers –depthwise convolution in (**b**) and pointwise convolution in (**c**) to build a depthwise separable filter [2]

image patches, like order of word representations used when employing transformers to text [1]. ViT exhibits exceptional performance when given the necessary duties to execute and is well-versed in large data. With very few computational needs, it can render contemporary CNN uses. These transformers have a good success rate for NLP models and are now utilized on photos for image recognition applications.

ViT divides the pictures into visual tokens while CNN uses the pixels as arrays. The visual transformer separates the pictures into fixed-size patches properly integrate each one, and then provides the transformer encoder with the spatial embedding as input. After each block, residual connections are offered which enable components to move directly across the network without going through non-linear activations. When classifying images, the classification head is implemented by the MLP layer. It uses a single linear layer for fine-tuning and a single hidden layer for pre-training. Vision Transformer in computer vision uses multi-head self-attention (Fig. 2).

Without the necessity for image-specific biases [3].

The transformer encoder processes the positional embedding patches that the model creates from the pictures in order to comprehend the local and global aspects of the image. ViT requires less training time and has a better accuracy rate on a big dataset.
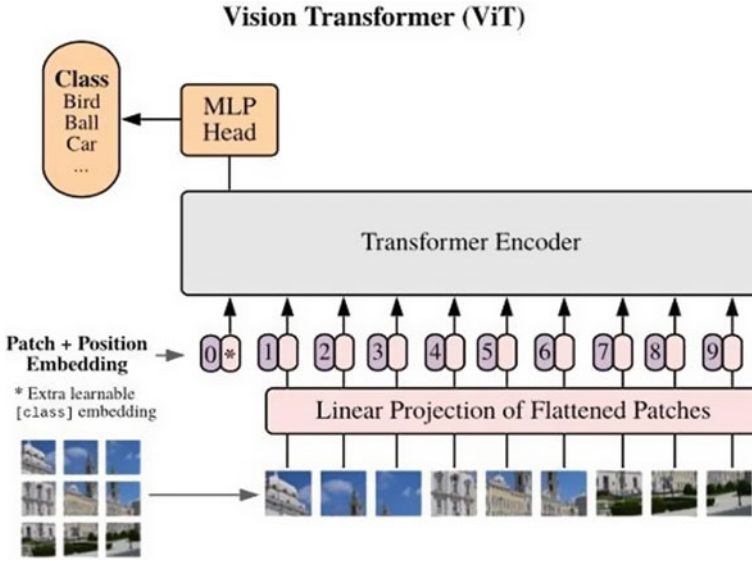
Fig. 2 Vision transformer architecture [3]

2 Experimental Setup

Dataset Preparation: The Dataset was created for five different objects: Almirah, Table, Chair, Bag and Bottle in an indoor environment. This dataset was used to train and test both the networks with eighty percent of images used for training and twenty percent used for validation, i.e., testing the trained models. To generate a large variety of data, different backgrounds, textures and rotations were done using Data Augmentation (Fig. 3).

Object detection models including convolutions and transformers can do better with a few data augmentation that can help the model learn more rigorously and reduce bias which increases the performance of the model. Here image rotation and image protection are applied to fifty percentages of the total input data.

2.1 MobileNet Model

In the implementation of MobileNet, considering a pre-trained MobileNet model from tensor flow, and here training and testing the algorithm on a custom dataset. The top layer of the pertained MobileNet model will be removed, with softmax being used as the classifier for activation. It is a very huge network, so it's not required to train all layers of the model. By freezing the trainable parameters of the original model, the efficiency of the network increases. And few layers on top of this model
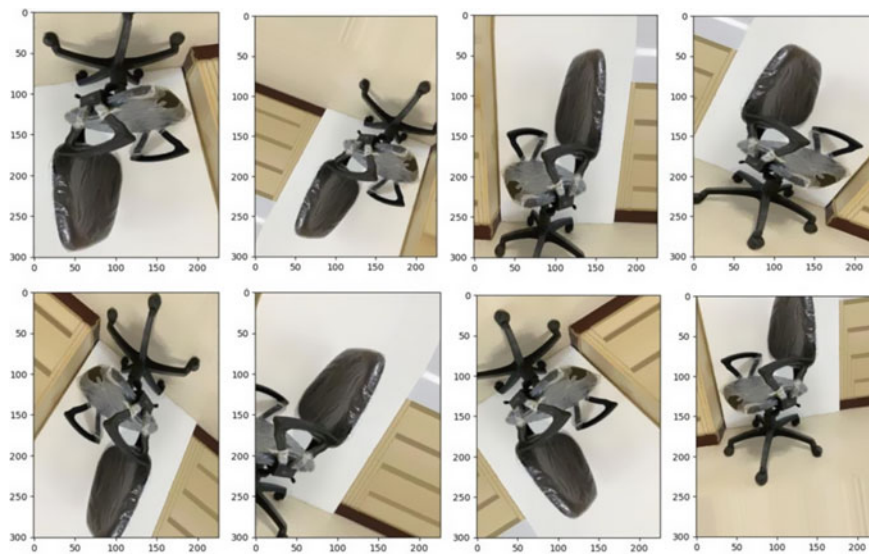
Fig. 3 Data augmentation

are added, which need to be trained. In a deep neural network, ReLU [5] is typically employed as an activation function for the hidden layers, by leveraging the activation of the penultimate layer to learn the weight parameters of the ReLU classification layer by backpropagation [4].

Flow Chart of MobileNet
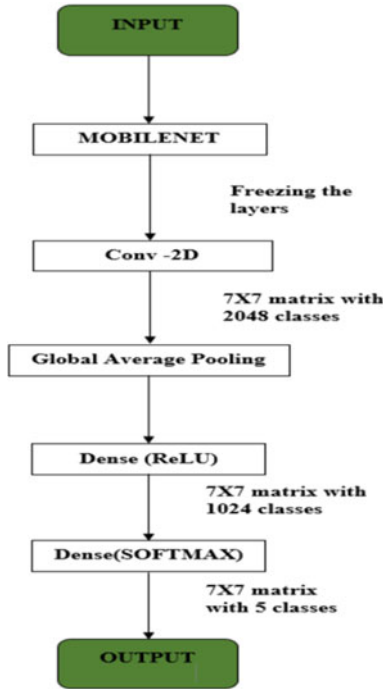
2.2 MobileNet ViT Model

Hyper parameters and image pixels are important for implementation of the model. For the input images of size 256 × 256, a rescaling of the images is done to reduce patch size [6]. A 2D convolution layer is added to perform convolution twice on the same image. MobileNet uses depthwise convolution layer followed by batch normalization and fully convolution layers. After repeating the step nine the layer normalization is done which makes the image suitable to enter the transformer block.

Flow Chart of Proposed Method **Block Diagram of ViT Block**
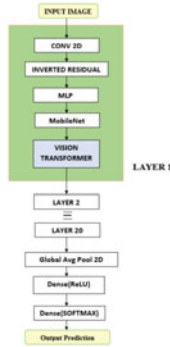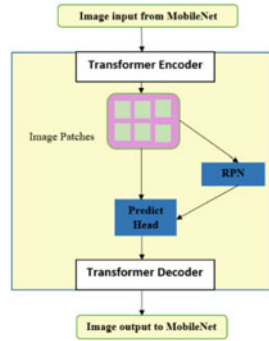
The multi-head attention vision transformer layer is added, which is a part of a single hidden layer, to make the network dense and more accurate these layers are connected twenty times. After execution of all hidden layers with attention layer, a layer of global average pooling before dense layer is added making the model trainable for five image classes. The Transformer Encoder creates image patches, which are flattened constructing "Patch Embeddings," which are lower-dimensional linear embeddings. These sequences are given positional embeddings to preserve the positional information, for detecting anomalies on the frames. The trainable class encoding output from the MLP is simply piled on top of the trainable class output images, completing the classification process [7].

3 Results and Discussion

After the models have been trained on the custom dataset, the performance evaluation metrics are used to measure the performance of the network. These metrics include precision, recall, f1-score, accuracy and confusion matrix that are used to gain valuable information about the performance of algorithms and to perform comparative analysis (Figs. 4 and 5).

For MobileNet model the training and validation accuracy for all the epochs is calculated (see Fig. 6) where the overall accuracy of the model is 65% for Training and 55% for Validation, which makes the model less accurate. The confidence percentage which shows the true positive for chair class object is 94% (see Fig. 7). For Bag class the confidence value is 93%, but for other classes like, the false positive is 25%, making the model less accurate for detection. The evaluation parameters are mentioned in Table 1 with precision, accuracy, recall and f1-score. For all the classes in the dataset, the accuracy is observed to be 61.7% using conventional MobileNet model on custom dataset (Figs. 9, 10, 11).

Fig. 4 Accuracy versus epochs graph for MobileNet
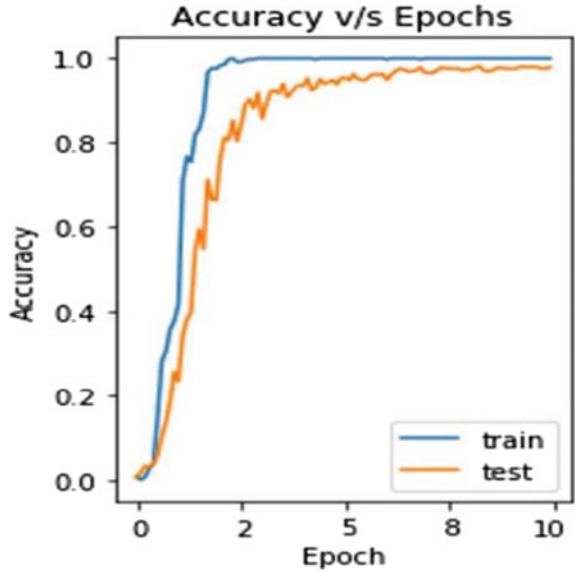
Fig. 5 Loss versus Epochs graph for MobileNet
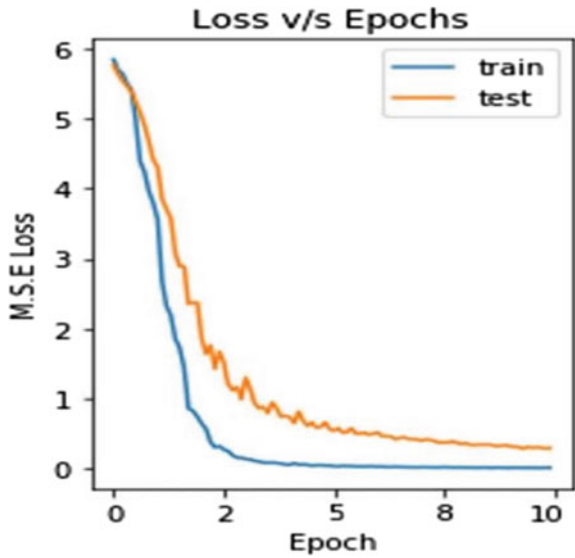
The training and validation accuracies of MobileNet ViT model overlap over 10 epochs (see Fig. 8), with 95% accuracy for training and validation datasets. This increase in accuracy, results in a less erroneous network, result of adding layers of Vision Transformer in the MobileNet network. For the chair class, the true positive value is 94%. Similarly, for class table, the true positive value is 96%. The true positive values are higher, and the false positive values are least, minimizing the
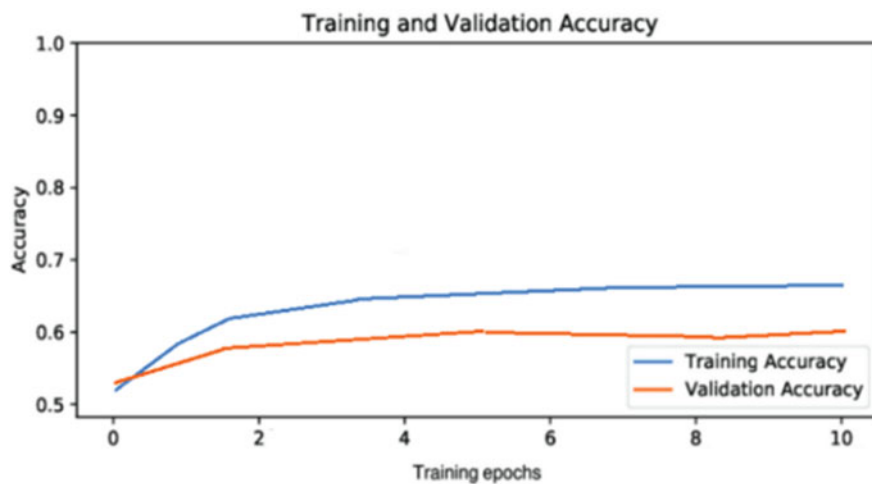
Fig. 6 Training and validation accuracy for MobileNet
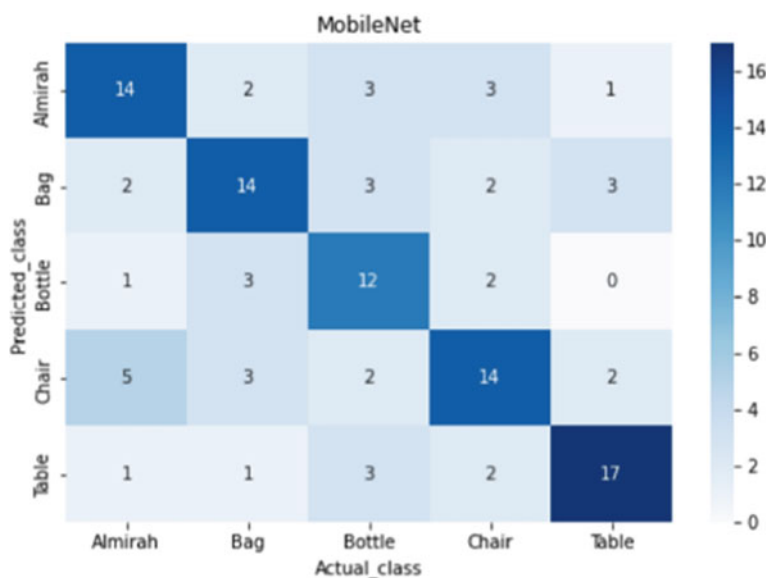
Fig. 7 Confusion matrix

error index of this network. The overall accuracy is 94.3% (see Table 2) using Vision Transformer with MobileNet.

Table 1 Evaluation matrix for MobileNet model

	Precision	Recall	F1-score	Support
Almirah	0.608696	0.608696	0.608696	23.000000
Bag	0.583333	0.608696	0.595745	23.000000
Bottle	0.666667	0.521739	0.585366	23.000000
Chair	0.538462	0.608696	0.571429	23.000000
Table	0.708333	0.739130	0.723404	23.000000
accuracy	0.617391	0.617391	0.617391	0.617391
macro avg	0.621098	0.617391	0.616928	115.000000
weighted avg	0.621098	0.617391	0.616928	115.000000

Fig. 8 Accuracy versus epochs graph for MobileNet ViT
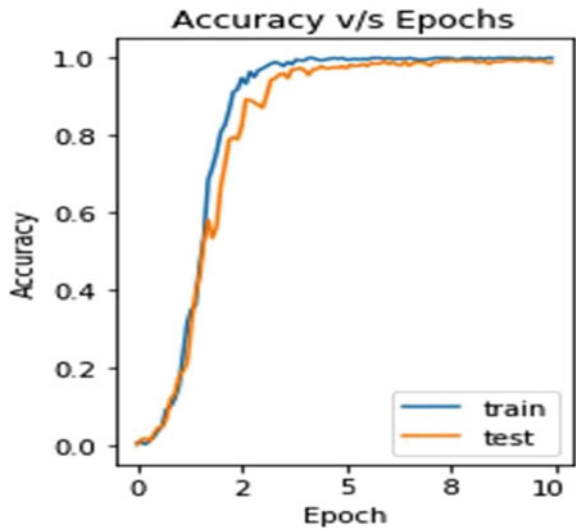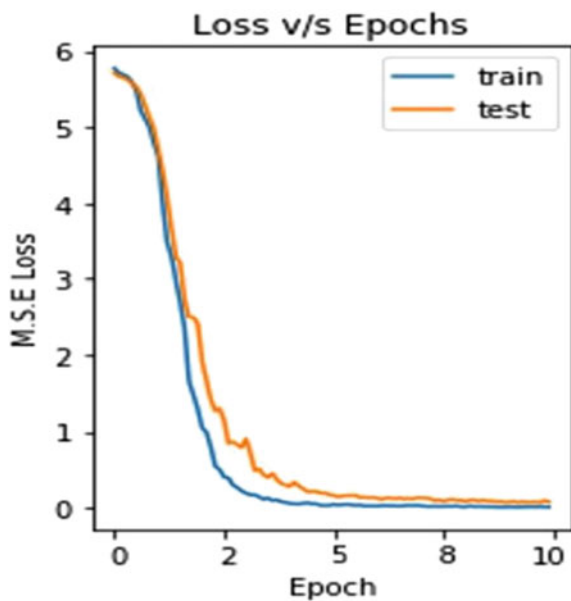
Fig. 9 Loss versus epochs graph
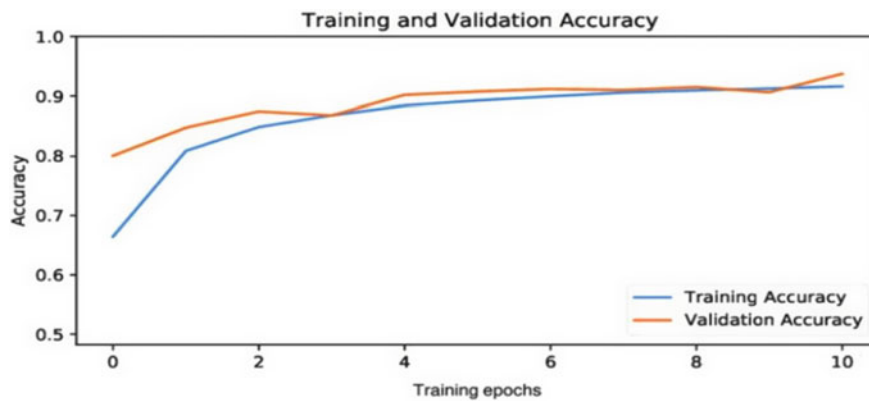
Fig. 10 Training and validation accuracy
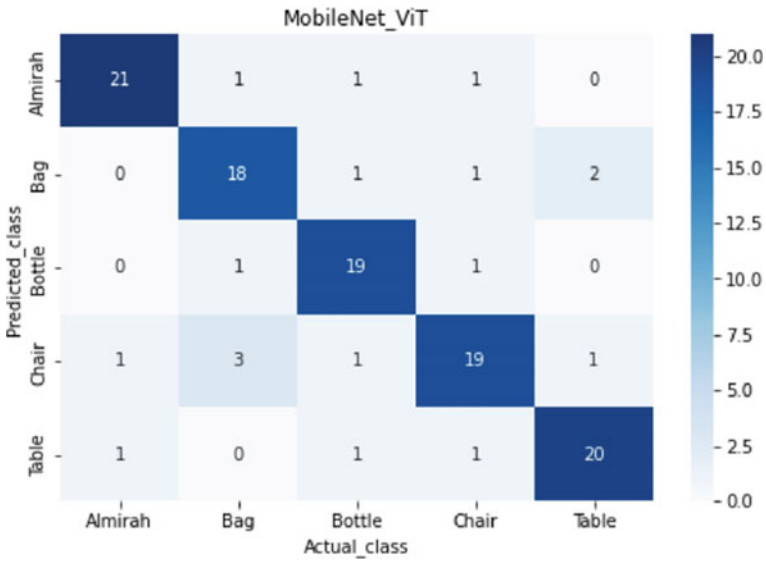
Fig. 11 Confusion matrix for MobileNet ViT model

Table 2 Evaluation Matrix for MobileNet ViT

	Precision	Recall	F1-score	Support
Almirah	0.875000	0.913043	0.893617	23.000000
Bag	0.818182	0.782609	0.800000	23.000000
Bottle	0.904762	0.826087	0.863636	23.000000
Chair	0.760000	0.826087	0.791667	23.000000
Table	0.869565	0.869565	0.869565	23.000000
accuracy	0.943478	0.943478	0.943478	0.943478
macro avg	0.845502	0.843478	0.843697	115.000000
weighted avg	0.845502	0.843478	0.843697	115.000000

4   Conclusion

After observing the Evaluation metrices values of both the models, it can be concluded that the overall accuracy of conventional MobileNet model on custom dataset is 61.7% (see Table 1), whereas the accuracy of MobileNet model with Vision Transformer reaches 94.3% (see Table 2) for the same custom dataset. Thus making MobileNet ViT a suitable model for object detection for mobile robot applications. A conventional MobileNet used for object detection becomes a deep network with multiple layers, making it more complex and time consuming. Adding a layer of Vision Transformer in the MobileNet algorithm, gives a vast difference in the network

output. The vision transformer which is based on the concept of self-attention, outperforms existing transformer models while being faster than most competitive CNNs like MobileNet, shown by extensive experiments on object detection in Laboratory.

The use of Vision Transformer to counter convolutional network helped the network use "self- attention" to focus on key object segments in the image, reduce computationally intensive operations, and provide better results as the positional deployment helped the network learn about the various image segments and the relevance of their position, which was not possible in convolutional network. The transformer network also has a better operational capability than the conventional model. A conventional MobileNet used for object detection becomes a deep network with multiple layers, making it more complex and time consuming. Adding a layer of Vision Transformer in the MobileNet algorithm, gives a vast difference in the network output. The vision transformer which is based on the concept of self-attention, outperforms existing transformer models while being faster than most competitive CNNs like MobileNet, shown by extensive experiments on object detection in Laboratory.

References

1. Beal J et al (2020) Toward transformer-based object detection. arXiv:2012.09958
2. Adarsh P et al (2020) Yolo v3-tiny: object detection and recognition using one stage improved model. In: 6th international conference on advanced computing and communication systems (ICACCS). IEEE, pp 687–694
3. Hui J (2018) Homepage. https://jonathan-hui.medium.com/ssd-object-detection-single-shot-multibox-detector-for-real-time-processing. Last accessed 14 Mar 2018
4. Agarap AFM (2019) Deep learning using rectified linear units (ReLU)
5. Ioffe S, Szegedy C (2015) Batch normalization: accelerating deep network training by reducing internal covariate shift. arXiv preprint arXiv:1502.03167
6. Chorowski JK et al (2015) Attention-based models for speech recognition. In: Advances in neural information processing systems, pp 577–585
7. Mehta S, Rastegari M (2021) MobileViT: light-weight, general-purpose, and mobile-friendly vision transformer 2021 ICLR 2022 conference

Metrological Controls and Performance Studies on a Liquefied Natural Gas Dispenser

K. Suresh, K. G. Jayesh, and G. Sundaravadivel

Abstract The requirement of metrological controls and performance tests stems from either the intended or potential use of measuring instruments in activities where the quality of measurement is of public concern. Such uses may be identified as the measurement of quantities related to specified classes of objects, commodities, phenomena, materials, or conditions. Performances of Liquefied Natural Gas Dispensers are critical because of their potential use in commerce, especially where custody transfer is involved. At an auto LNG dispensing station, LNG is stored and dispensed as automotive fuel to motor vehicles. Billing is done based on the quantity measured by the dispenser. Any potential error in measurement will lead to losses to the public. Tests were conducted as per general guidelines of OIML R117 (OIML R 117-1:2019 (E), Dynamic measuring systems for liquids other than water, 2019), Dynamic measuring systems for liquids other than water. This paper focuses on the model approval studies, metrological controls and performance tests on a LNG dispenser along with discussions and interpretations of results (OIML R 117-1:2019 (E), Dynamic measuring systems for liquids other than water, 2019; ISO/IEC 17,025, General requirements for the competence of testing and calibration laboratories, 2017; ISO/TS 21,748, Guide to the use of repeatability, reproducibility, and trueness estimates in measurement uncertainty estimation; Certificate number FCRI/WFL/T/2021/75 issued by Fluid Control Research Institute).

Keywords LNG dispenser · OIMLR117 · Model approval · Metrological controls

1 Introduction

Fuel dispensers are devices for supplying and quantifying LNG directly to vehicles that use LNG for fuel instead of petrol or diesel. As a standard, a flow meter is used to confirm the accurate transfer of LNG. To ensure that the liquid is cold enough to be delivered, the dispensers use a recirculation circuit that is linked to the flow

K. Suresh (✉) · K. G. Jayesh · G. Sundaravadivel
Fluid Control Research Institute, Kerala 678623, India
e-mail: k.suresh@fcriindia.com

meter. The circuit closes once the flow meter is cooled sufficiently, beginning the delivery of LNG. As the receiving vehicles need to vent the excess vapor from their supply tank, a vapor return line connecting to the LNG dispenser is used. In the LNG dispenser configuration, the vapor return will be measured to correct the total LNG measurement for this amount.

Liquefied natural gas (LNG) is natural gas that has been cooled to a liquid state, at about $-162°$ Fahrenheit, for shipping and storage. The volume of natural gas in its liquid state is about 600 times smaller than its volume in its gaseous state.

According to the policy of the Ministry of Petroleum and Natural Gas, the share of natural gas in the Indian economy is estimated to increase from the current 6.3 to 15% by 2030. In order to facilitate that, the policy proposes setting up of LNG terminals of 100 MMTPA capacity by 2030, and regasification capacity of 100 MMTPA by 2040, allowing free marketing and sale of LNG.

With the government's plan of setting up more than 1,000 LNG stations across the country, LNG as a transport fuel would not only reduce air and noise pollution levels but also have a greater commercial advantage in comparison to the prices of other petroleum products like diesel and petrol.

The decision for governments to recognize LNG measuring systems is made easier by the fact that detailed guidance exists in the International Organization of Legal Metrology OIML R 117-2019 [1] for LNG measurements. Section 5.11 of OIML R 117-1 2019 [1] outlines the requirements to follow for both industrial LNG transactions and those with fuel dispensers.

LNG dispensers play a significant role in measuring the use of sustainable and environment-friendly LNG for motor vehicle transportation. Model approval of LNG dispensers is mandatory because of their potential use in commerce, especially where custody transfer is involved.

During the model approval program, the metrological and technical characteristics of the model are studied after taking into account the possible incidence of influence factors and their effect on metrological and technical characteristics. The general behavior of the model, that is to say, its robustness, reliability, and susceptibility to fraudulent use are studied.

2 Methodology

The design and operation of an LNG measuring system shall ensure that the product in the liquid flow meter remains in a liquid state during the measurement. LNG delivery systems shall indicate the quantity delivered in terms of mass. Supplemental information may include energy unit quantity. LNG fuel dispensers for direct selling to the public shall have a minimum measured quantity not exceeding 20 kg. The minimum height for the figures of the resettable quantity indicator is 10 mm. The minimum height for the unit price is 4 mm [1].

When only one nozzle can be used during delivery, and after the nozzle has been replaced, the next delivery shall be inhibited until the corresponding indicating device

has been reset to zero. When two or more nozzles can be used simultaneously or alternately, and after the utilized nozzles have been replaced, the next delivery shall be inhibited until the indicating device has been reset to zero. Moreover, by design, the provisions in measuring systems intended to deliver liquids, no means shall be provided by which any measured liquid can be diverted downstream of the meter. However, two or more delivery outlets may be permanently installed and operated simultaneously or alternately provided so that any diversion of flow to other than the intended receiving receptacle(s) cannot be readily accomplished [1].

When the flow is not interrupted during the failure of the principal power supply device, the measuring system shall be provided with a means to safeguard all measuring functions during that failure. When the flow is interrupted during the failure of the principal power supply device, data contained at the moment of the failure shall be saved and shall be available for (on-demand) display on an indicating device subject to legal metrology control during a period of at least 15 min, to permit the conclusion of the current transaction.

In addition, electronic fuel dispensers shall be designed such that an interrupted delivery cannot be continued after the power supply has been re-established if the power failure has lasted more than 15 s.

For LNG fuel dispensers, the quantity-indicating device and its printing device, if provided, shall comply with the zero-setting device for the quantity-indicating device. A quantity-indicating device may be provided with an ancillary device for setting the indication to zero either by manual operation or by means of an automatic system. Once the zeroing operation has begun, it shall be impossible for the quantity-indicating device to show a result different from that of the measurement which has just been made, until the zeroing operation has been completed. Indicating devices on fuel dispensers and electronic measuring systems shall not be capable of being reset to zero during measurement. On analog indicating devices, the residual indication after return to zero shall not be more than half the minimum specified quantity deviation. On digital indicating devices, the quantity indication after return to zero shall be zero without any ambiguity [1].

When it is necessary to cool the delivery path of the LNG prior to making a delivery (to prevent vaporization of the liquid), the measuring system may include a circuit, downstream of the meter, to allow for the recirculation of the product. Such circuits shall be equipped with a suitable means to indicate when there is a product flowing through the circuit. If the flow is detected in this circuit before or during delivery, the delivery shall not be started or shall be terminated. If the piping/hose downstream of the meter of an LNG system is not designed to remain filled between transactions, the system shall employ a means to automatically account for the quantity of product required to fill the piping/hose downstream of the meter prior to starting a transaction.

The calculator that indicates the total mass of the transaction may reset to a negative value (buyer credit) compensating for the mass of LNG that is missing from the hose during normal transaction conditions, prior to commencing the transaction, reset to zero before the transaction commences, but after the hose has been filled, or suppress the advancement of the indication until the piping/hose is charged and

start the transaction at zero at that time. The manufacturer shall specify the operating conditions required for the correction device to ensure the stated accuracy. A suitable correction device can be a flow meter in the vapor return line. There shall not be an ability to flow liquid between the delivery tank and the receiving tank through the vapor return line. If it is possible for liquid to enter the gas return line, provisions shall be made to detect this and stop the transaction.

For LNG fuel dispensers, any connection between the vapor space of the storage tank and that of the receiving tank is prohibited during the transaction unless the system is equipped with a vapor return correction device [1].

Testing of the LNG Dispenser was carried out in two stages. As part of initial verification, certification of the dispenser was carried out with a water medium which differs from the liquid the dispenser is intended to measure; comparative tests with these two liquids shall also be carried out to determine the maximum permissible errors on this verification [1, 7].

Whatever the number and location of the stages and whatever are the tests, it must be possible to conclude that the measuring system, installed at the site of use, fulfills all applicable requirements under rated operating conditions. The Auto LNG Dispenser was tested at cryogenic conditions with liquid nitrogen as a flow medium at the site [1, 7].

3 About Flow Laboratory

The flow Laboratory at FCRI, established in 1989, has been providing technical consultancy, research, training, testing, calibration, and flow measurement for clients across the globe. Activities of the water flow laboratory are calibration and testing of flow products including flow meters, valves, water meters, pumps, and firefighting equipments. Static gravimetric method as per ISO 4185 [3] is adopted here for the measurement of flow rate (Fig. 1).
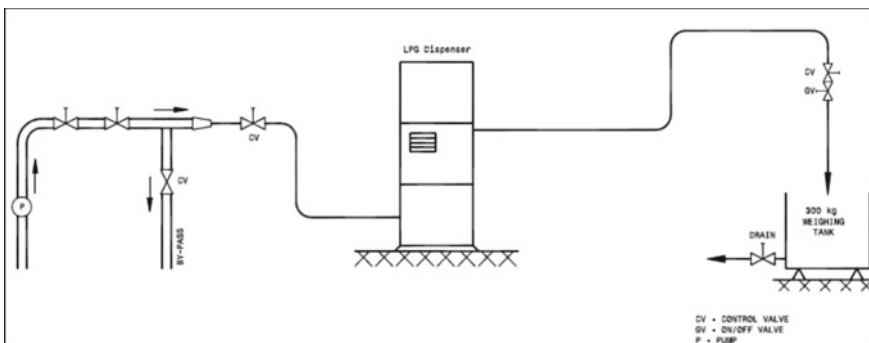
Fig. 1 Schematic of test setup of the dispenser at the laboratory

The dispenser to be tested was installed in the standard test line of the Water Flow Laboratory. The required flow was provided using pumps. The "Standing start and stop" method was employed for the test. Universal Counter was used to determine the time of collection of water. The upstream pressure of the dispenser was measured using a precision pressure gauge and the density of the working fluid was determined using an online density meter.

The line was flooded and entrapped air cleared using circuit air bleeds. Direct pumping was employed to obtain higher flow rates. The flow rate was adjusted using the downstream control valve. When flow conditions had stabilized, the actual flow rate was determined by collecting water for a measured time interval in the weighing system.

The time of collection was determined by a high-precision counter, which was triggered by a photo switch-timer blade arrangement attached to the diverter. The collection time, differential pressure, line temperature and line pressure also were recorded. The actual flow rate, actual mass, and % of error were then computed as given in the sample calculation. This procedure was repeated for the other flow rates covering the entire flow range. A set of five readings were taken at each flow rate for repeatability estimation (Fig. 2).

Fig. 2 Dispenser under test at the laboratory

4 Tests Conducted on the Dispenser

4.1 Test to Check the Functioning of the Flow Meter and to Make Initial Adjustments

Initially, the dispenser was assembled to the test line and the air vented from the test lines and the dispenser. The flow was started through the dispenser at a medium flow rate and a higher flow rate to check whether the dispenser is functioning smoothly.

4.2 Accuracy Test Before Endurance Test

After sufficient warm-up, the accuracy of the dispenser was determined at six different flow rates which are distributed over the measuring range at regular intervals.

$$\% \text{ Accuracy in mass} = \frac{(\text{Mi} - \text{Ma}) \times 100}{\text{Ma}}$$

where "Mi" is the indicated mass by the dispenser and, "Ma" actual mass measured by the gravimetric system. At each flow rate, the accuracy in indicated mass was determined at least three times independently. The repeatability was checked at different flow rates within the flow range specified. The minimum flow rate at which the accuracy test was conducted was 19 lpm and the maximum was 190 lpm, covering the span of the dispenser.

4.3 Durability Tests

A durability test was carried out at above 80% of the maximum flow rate ($Q_{max} = 190$ lpm) of the dispenser. Here the continuous flow is given through the dispenser to check the wear and tear of the flow meter and any drift occurring during the run. During the endurance tests, accuracy is also determined periodically to check at what point the equipment failed.

4.4 Accuracy Test After Durability Test

As per OIML R117 [1], an accuracy test should succeed the durability testing. The deviations between the errors determined before and after the durability test shall remain within the limits specified as in OIML R 117—i.e. 1.5% of the measured

quantity, without any adjustment or correction. The Repeatability of the mass flow meter shall be within 1% of the measured quantity.

4.5　Minimum Measured Quantity Test

A Minimum Measured Quantity deviation test was conducted to determine the absolute value of the maximum permissible error for the minimum measured quantity. In measuring systems intended for delivery operations, this smallest quantity is referred to as the minimum delivery; in those intended for receiving operations, it is referred to as the minimum receipt. The accuracy test was conducted by collecting the minimum measured quantity specified by the manufacturer (20 kg).

4.6　Flow Disturbance Test

A flow disturbance test was conducted to determine the effect of abrupt pressure variations on the accuracy of the dispenser. The interruption test was performed three times at the maximum flow rate. The test volume shall be at least the volume delivered in one minute at Q_{max}. Using the nozzle valve, the liquid flow was started and stopped abruptly five times during the same measurement. These stops were made at various intervals.

4.7　Verification of Dispenser at Manufacturers Site

The dispenser was verified at the manufacturer's premises using Liquid Nitrogen as a flow medium. The verification was conducted using the gravimetric method. Here LNG is pumped through the dispenser and collected in a closed fuel tank placed above a weigh scale. The initial mass of the empty fuel tank was recorded and after the run, the final mass was noted. The difference in mass gives the actual LNG passed through the dispenser. The accuracy is calculated by comparing the indicated mass by the dispenser to the actual mass collected in the weighing system (Fig. 3).

5　Results and Discussion

LNG dispensers are equipped with Coriolis mass flow meters which measure mass flow rate. Since the cost of fuel is expressed per unit mass, the use of a Coriolis meter eliminates the need to determine the LNG density in the calculation. This avoids the uncertainty associated with density measurement (Fig. 4).

Fig. 3 Test at site with liquid nitrogen
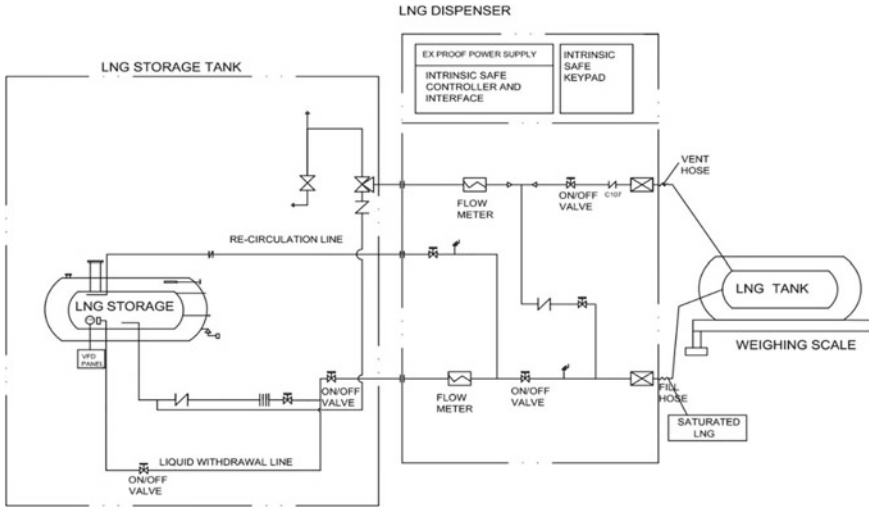
Fig. 4 Dispenser under test with liquid nitrogen

Accuracy and repeatability were verified before and after the durability test. A durability test was conducted on the dispenser for a cumulative time period of hundred hours at a flow rate between 145 and 155 lpm. The accuracy obtained was within the specified limits of $\pm 0.15\%$ [1, 5–7] of the rate as claimed by the manufacturer. The

repeatability obtained was better than 0.05%, which is within the limits specified in OIML R 117. The stable performance of the meter, and the accuracy and repeatability of the measurements, are evidence of the general suitability of mass flow meter technology for cryogenic applications. Although the LN2 measurements were less accurate than with water, the flow meter meets the requirements of OIML recommendations. Flow meter manufacturers provided technical data in product specification sheets specifying the zero stability and mass or volume flow measurement accuracy. For the flow rates considered in this paper, the accuracy of flow meters stated is typically at around 0.15% and repeatability better than 0.05%. These values are typically stated for ambient water flow conditions. In addition, temperature and pressure sensitivities on the measurement accuracy are also specified. The dispenser was tested at liquid nitrogen without changing any parameters in the flow meters. Manufacturers recommend mitigating the temperature and pressure effects on measurement uncertainty by zeroing in the process at cryogenic conditions. The accuracy obtained during the test in liquid nitrogen was 0.8% [7]. The results indicate that the calibration results are within the manufacturer's specifications as given by product data sheets and user manuals. Proper zeroing in cryogenic conditions will be challenging even if carefully following the manufacturer's instructions and as one depends on the insulation capability of a cryogenic installation. The results have indicated that a calibration taken at room temperature with water, with some loss of accuracy, be transferred to liquid nitrogen at cryogenic conditions. The cryogenic tests were conducted using liquid nitrogen at a temperature around -193 °C and LNG operating temperatures are around -160 °C. It would therefore seem reasonable to assume that the liquid nitrogen calibration can be transferred to LNG [2]. The similar properties of LN2 and LNG mean that an LN2 calibration shall be transferable to LNG. However, precautions should be taken for the sub-cooling and insulation required to avoid bubble nucleation due to heat leakage to the flowing stream.

References

1. OIML R 117–1 (2019) (E)—Dynamic measuring systems for liquids other than water
2. Costa FO, Pope JG, Gillis KA (2020) Modeling temperature effects on a Coriolis mass flowmeter. Flow Measure Instrum J
3. ISO/IEC 17025 (2017) General requirements for the competence of testing and calibration laboratories
4. ISO 4185:1980 (1980) Measurement of liquid flow in closed conduits—weighing methods, 1st edn

5. ISO/IEC Guide 98–3 (1995) Uncertainty of measurement Part 3: Guide to the expression of uncertainty in measurement. GUM
6. ISO/TS 21748. Guide to the use of repeatability, reproducibility, and trueness estimates in measurement uncertainty estimation
7. Certificate number FCRI/WFL/T/2021/75 issued by Fluid Control Research Institute

Intermediate Checks: Ensure Confidence in Validity of Measurement Results

K. Arulselvi and S. M. Saraswathi

Abstract According to the definition, calibration refers to the procedures with which comparison is carried out between the results of a measuring instrument or a measuring system and the corresponding values in the measurement standard. It includes evaluation of measurement uncertainty and providing measurement traceability to SI units. Calibration is carried out in a periodic time cycle referred as a calibration interval, which is expected to ensure the reliability of the equipment performance. In order to confirm the equipment performance and maintain confidence in the measurement carried out, intermediate checks in between calibrations shall be performed as per documented procedure. Intermediate checks are the best monitoring system in between the calibration interval for identifying any drift or change in the performance of the equipment. The ISO/IEC 17,025:2017 (1) standard requirement is that 'when intermediate checks are necessary to maintain confidence in the performance of the equipment these checks shall be carried out' and 'when' mentioned in the requirement is the selection of periodicity for performing intermediate checks based on the significance of applications. Discovering an equipment which is out of calibration (beyond tolerance limits) has a high potential value which would result in reducing the risks like financial risk, consumer risk etc. The sooner the equipment is identified as out of tolerance, the lesser the risks associated with the measurements. The purpose of this paper is to provide the details about the importance of the intermediate checks, plan and perform intermediate checks, analyze the results and maintain the records. It is hoped that the intermediate checks on measuring and test equipment will be given more importance and carried out for the equipment which requires calibration to minimize the risks involved in performing measurements.

K. Arulselvi (✉) · S. M. Saraswathi
Electronics Test & Development Centre, Ministry of Electronics & Information Technology, STQC Directorate, Thiruvanmiyur, Chennai 600 041, India
e-mail: arulselvi@stqc.gov.in

1   Introduction

Periodic calibrations are performed on measuring and Test Equipment for the purpose of evaluation of measurement uncertainty and to provide metrological traceability to SI units. The purpose is to control the measurement errors and uncertainties to acceptable levels, defined by the tolerance limits of parameters under calibration as per the manufacturer's specification. A calibration is valid only at the time of implementation and immediately after calibration the status is affected due to the reasons like extreme temperature conditions, high operating hours (continuous operation), dirt and moisture conditions and any vibration during transportation etc. and hence the confidence of the user would be decreased. The continuous and frequent monitoring of the equipment performance may provide or enhance the confidence of the user of the equipment. The periodicity of these checks may vary depending on the purpose, applications and parameters included in the equipment or standard. For some applications, this may be daily or before use every time. An intermediate check is a periodic quality check performed to maintain confidence in the calibration status in between calibrations. These checks are one of the calibration quality control activity that is implemented internally and the data shall be recorded and results of intermediate checks are analysed using the laboratory statistical techniques documented in the procedure. This process can easily identify the errors or any significant drift in the performance of the measuring and test equipment. The importance of intermediate checks and the procedure to implement the intermediate checks are discussed in this paper.

2   Purpose

2.1   Why to Perform Intermediate Checks

- Necessary to maintain confidence in the performance of the measuring and test equipment in between calibrations.
- To monitor the validity of measurement results, if the results are within the acceptable limits or if any significant drift occurred.
- To ensure the equipment performance is as required by the user for its fitness for purpose.
- To minimize or eliminate the risks which would lead to false accept or false reject in the manufacturing field due to inaccurate (wrong) measurements.
- Intermediate checks are required by the International Standard ISO/IEC 17025:2017 (1) under the clauses 6.4.2, 6.4.10 & 7.7.1. Clause 6.4.10 states that when intermediate checks are necessary to maintain confidence in the performance of the equipment, these checks shall be carried out according to a procedure.

2.2 When to Perform Intermediate Checks

- If intermediate check plan is available for each equipment and standard, the same shall be followed (The intermediate check plan shall be modified every year based on the results of the previous intermediate check and performance for each equipment, by monitoring the trends of the deviations).
- If any failures during measurement or any significant deviations are observed in the performance of the equipment, unplanned intermediate checks shall be carried out and the results shall be analysed and recorded based on which the frequency of checks shall be altered.
- When the results are suspected and if they deviate more than usual, and when they are not caused by the work or device under calibration, intermediate checks shall be carried out.

3 Procedure

3.1 Equipment Record/Equipment History

The user of the equipment or the laboratory personnel is responsible for the correctness and condition of the equipment. In order to confirm the proper conditions of the laboratory equipment, equipment records shall be maintained by the user of the equipment with the details of calibration plan, maintenance plan and intermediate plan for every year. The calibration record or history shall consist of an unbroken sequence of calibration results with respect to parameters calibrated, tolerances used, procedure followed, standards used for calibration and the results for the same shall be recorded. The equipment record shall be prepared and maintained according to the accepted norms considering the manufacturer's instructions and also the standard ISO/IEC 17025:2017 (1) requirements by the trained and authorized laboratory personnel. For all the parameters in the equipment, traceability details shall be available to the national or international standards. The calibration agency shall not be changed often in order to maintain traceability as far as possible because to have control over the performance of the equipment and to maintain consistency in the values of uncertainty in measurement. The drift for the value of the parameter has to be calculated after every calibration from the calibration certificate and also the intermediate check results also to be compared with the results given in the calibration certificate. The trend in the deviation of values from the calibration certificates with the intermediate check values shall be analysed and recorded.

3.2 Steps Involved in Performing Intermediate Checks

- Establish a process to check the performance of the equipment and standards which includes the intermediate check plan at regular intervals and results of the same.
- Select the parameters, range and points for the equipment under intermediate check which are required for effective performance of the equipment and have a major impact on the measurements.
- Based on the parameters and range select the equipment or standard to be used for comparison or check. The equipment used for check shall be better than or equal to the tolerance limits of the equipment which requires intermediate check (at least with equal or better resolution and with better accuracy). If the checks are performed with lower accuracy standards, the expected result or purpose will not be achieved.
- Define the acceptance criteria for evaluation of the results which would confirm the status of the performance of the equipment. The acceptance criteria shall be decided and/or approved by the authorized person in the management system.
- Use control charts for each parameter of the equipment to verify and monitor the measurement results. This will identify the changes in the results and the drift rate of the parameters which will be useful for further process of intermediate checks.
- If the changes observed are found to be out of the limits set by the acceptance levels, take appropriate actions to control or minimize the impact on the quality of measurements or validity of calibration.

3.3 Case Study

An example of typical behavior of a DMM, 6½ Digits taken from the results of the calibration certificate are given in the table for AC and DC voltage of 0.9 V in 1.0V range when calibrated using Multifunction calibrator. The difference in the values varies in both + and − sides and the trend of error would not increase or decrease in any direction. It shows the inherent behavior of the instrument and hence continuous monitoring is required for any type of equipment used for measurement (Figs. 1, 2 and Tables 1 and 2).

(1) DC Voltage Range: 1 V

   Calibration Point: 0.9 V
   Initial measurement: 0.899992 V

(B) AC Voltage Range: 1 V

   Calibration Point: 0.9 V @ 50 Hz
   Initial measurement: 0.899616 V @ 50 Hz
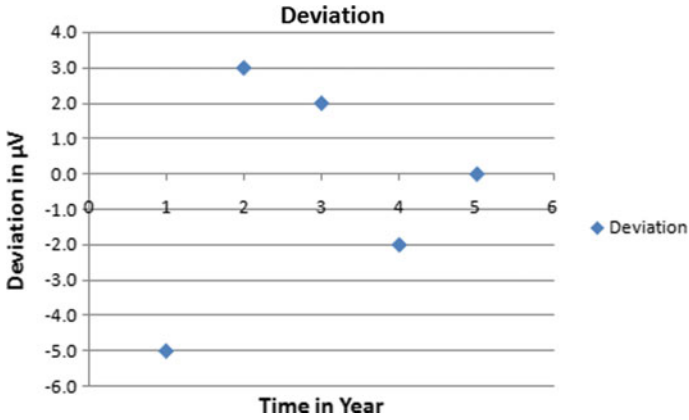
Fig. 1 Voltage deviation chart

Table 1 DC voltage variation

Time in year	Observed value (V)	Deviation in μV
2016	0.899987	−5.0
2017	0.899995	3.0
2018	0.899994	2.0
2020	0.89999	−2.0
2022	0.899992	0.0

The behavior of the measuring equipment and standard is unpredictable and the results are uncontrolled. Monitoring the performance in between calibration would help the user to have more confidence and any changes in the performance would be identified at the early stage and necessary action could be taken appropriately.
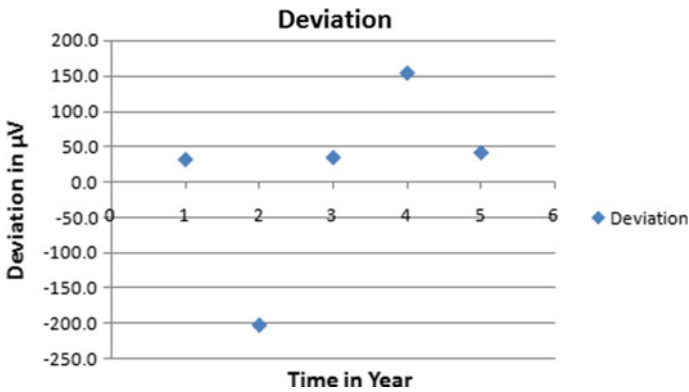
Fig. 2 Voltage deviation chart

Table 2 AC voltage variation

Time in year	Observed value (V)	Deviation in μV
2016	0.899648	32.2
2017	0.899413	−203.0
2018	0.899651	35.0
2020	0.899771	155.0
2022	0.899658	42.0

4 Results

The intermediate check plan and the completion records including analysis of the intermediate checks shall be kept along with the equipment record or history. This will help in finalizing the calibration periodicity and provide confidence to the user about the performance of the equipment.

5 Conclusion

All measurements are critical and severity varies based on their applications. Any manufacturing plant needs to be absolutely confident that the products produced by them are working within the tolerance limit for a specified period of time. If the items are in doubt or with out of tolerance limits, the consequences can be disastrous, and the risks involved are unidentifiable. Hence any manufacturing plant or service organization like calibration and test laboratories shall have a maintenance plan and quality check activity which include intermediate checks on the equipment and standard used for measurement activity. The results of the intermediate checks can be used as a tool or evidence for confirming the calibration intervals and if required to adjust the calibration periodicity. Being the requirement of the international standard ISO/IEC 17025: 2017, the intermediate checks shall be carried out not only for the benefit of the organization in the area of technical and quality management but also enhances economical benefits [1–5].

References

1. ISO/IEC 17025 (2017) General requirements for the competence of testing and calibration Laboratories
2. ILAC-P10:07/2020 ILAC policy on metrological traceability of measurement results

3. ILAC-G24 (2007) Guidelines for the determination of calibration intervals of measuring instruments
4. Ensuring the validity of results by intermediate checks in the field of mass measurements by Adriana Vâlcu, Adela Calin in the XXII World Congress of the International Measurement Confederation (IMEKO 2018)
5. Calibration Interval Controls Measurement Reliability, NCSL Workshop & Symposium 1999, Authors : R.Subburaj, K.Arulselvi, A.Yegnanathan

Comparison of Texture, Shape, and Combined Feature Vectors for Classification of Breast Ultrasound Images

Kriti, S. P. S. Narula, Surneet Kaur, and Ravinder Agarwal

Abstract The most prevalent malignancy nowadays in women is breast cancer. Breast cancer risk factors include changes in lifestyle, hormonal changes, genetic mutations, radiation therapy, and alcohol consumption. Ultrasound is the predominantly used mode of examination due to its portability, low cost, and lack of ionising radiation. Despite these benefits, the quality of ultrasound images can be lowered by the presence of speckle noise and low contrast. With the advancement of computer technology, medical image processing techniques, and artificial intelligence-based algorithms, numerous opportunities for the research community to investigate the potential of computer-aided diagnosis (CAD) for the classification of breast abnormalities using ultrasound images have arisen. Tissue-specific features must be computed during medical image characterisation; e.g., when analysing breast abnormalities, the texture, as well as the shape of the tumour region, are considered important for diagnostic purposes. As a result, the current study compared the performance of texture, shape, and combined feature vectors on a total of 110 breast ultrasound images collected from a scan centre in Patiala. The results of the experiments show that the PCA-SVM classifier achieves an overall accuracy of 93.9% using feature vectors containing texture features (computed using 2D Gabor wavelet transform) combined with shape features. Radiologists can use the proposed CAD system to verify their diagnosis in the course of their regular medical procedures.

Kriti (✉)
DIT University, Dehradun 248009, Uttarakhand, India
e-mail: kriti.23gm@gmail.com

S. P. S. Narula · S. Kaur
Modern Laboratory and Scan Centre, Patiala 147001, Punjab, India

R. Agarwal
Thapar Institute of Engineering and Technology, Patiala 147001, Punjab, India

1   Introduction

Cancer occurs when cellular changes in the body result in the uncontrolled growth of cells, thus forming tissue masses called tumours [1]. These tumours can either be cancerous (malignant) or non-cancerous (benign). The benign tumour cells grow more slowly, do not invade other bodily regions, and are more differentiable. Other healthy body tissues may become infected by the cancerous tumour cells. Through the lymph system or bloodstream, these cells often travel to other parts of the body resulting in the formation of new tumours. This process is known as metastasis [1]. Breast cancer develops in the breast cells beginning either in the breast lobules or the ducts. It has become a notable health concern nowadays as it is being majorly diagnosed in women all over the world [2]. World Health Organisation (WHO) reports that approximately 2.3 million women worldwide will be diagnosed with breast cancer by 2020 [3]. Annually, at least one lakh new cases of breast cancer are reported by the Indian Council of Medical Research (ICMR). For women in the U.S.A, it was estimated that in the year 2019, a total of 268,600 new cases of breast cancer would be diagnosed [4]. These facts are alarming and indicate that breast cancer is prevalent not only in India but also globally. In the year 2017, India had the highest mortality rate for breast cancer globally. Even though high mortality rates have been associated with breast cancer, significant improvement in the possibility of surviving can be witnessed if detection is made at the onset of the disease [5–7]. For diagnosing breast diseases, various methods of imaging like mammography, ultrasound (US), digital breast tomosynthesis (DBT), computed tomography (CT), magnetic resonance imaging (MRI), etc. have popularly been used, however, CT, MRI, DBT are costly modalities and in case of CT and DBT, the patients are exposed to ionising radiations therefore, to cater to the need of general population in India, mammography and ultrasound are commonly used as screening tools [6–11]. Mammography is however not suitable for patients like pregnant women due to the use of ionising radiations and also sometimes false-negatives are obtained with mammography due to the effect of high breast density in younger women. The advantages of ultrasound over other modalities are (a) absence of ionising radiations, (b) low cost, (c) non-invasive nature, (d) ease of availability, and (e) ability to differentiate between cystic and solid tumours [11]. Due to speckle noise, the resolution of the ultrasound image is affected resulting in difficulty in the detection of small lesions thus making the interpretation difficult [12]. As technology, image processing techniques, and artificial intelligence algorithms have become increasingly advanced, researchers have been able to explore the potential of computer-aided diagnosis (CAD) to classify breast abnormalities based on medical scans. The tissue-specific features need to be computed during the characterisation of medical images, e.g. for the analysis of breast abnormalities, the shape and texture information of the tumour is considered important hence, the CAD systems should be designed based on both texture and morphological features exhibited by the tumours [13–26].

Daoud et al. [13] utilised an SVM-based decision fusion method to classify breast tumours, reporting an accuracy of 98.2%. An analysis of 110 images was conducted

to determine texture and shape features. The morphological characteristics were calculated utilising the whole tumour, whereas the grey level co-occurrence matrix (GLCM)-based texture features were computed using several non-overlapping ROIs. The minimal-redundancy-maximal relevance (mRMR) and backward selection techniques were then used on each feature set. The study used individual textural and morphological criteria to categorise the tumours, and the final tumour class was decided using decision fusion.

Moon et al. [24] used 249 ultrasound images of malignant tumours for classifying them into metastatic and non-metastatic cancer. The images were first pre-processed using a sigmoid filter and gradient magnitude filter. Using a level set approach of segmentation, the tumour patches were recovered from the filtered images. Using the patches, textural and morphological characteristics were taken from the tumour photocomputeds. Backward feature selection was used to create an ideal feature set, which was then given to the logistic regression (LR) classifier, which reported an accuracy of 75.1%.

A collection of 2050 breast ultrasound images were utilised by Gomez-Flores et al. [25] to differentiate between benign and malignant tumours. Using multiple-resolution images acquired by the Ranklet transform, the authors calculated auto-mutual information-based texture characteristics. The SVM classifier received the generated feature set after that and reported an area under the curve (AUC) value of 0.82.

167 breast ultrasound images were utilised by Bhusri et al. [26] in their study to categorise breast lesions as benign or malignant using a combination of several texture and shape characteristics computed using ROIs derived from the images. Texture features have been calculated by using different statistical techniques. According to the results, the authors' method of combining morphological information with first-order statistics (FOS) using an SVM classifier yielded the maximum accuracy of 89.6%.

Using a combination set of texture and shape characteristics, Liao et al. [17] classified breast tumours from 321 ultrasound images. Although the morphological characteristics were calculated using sonographic data, the texture features were computed using spatial grey level dependency (SGLD) matrices. The merged feature set was fed to several classifiers, including SVM, ANN, and k-nearest neighbour (kNN), and the authors reported a maximum accuracy of 86.92% using SVM classifier.

The purpose of the current work is to evaluate the effectiveness of several feature vectors for categorising breast tumours based on findings from earlier studies.

2 Materials and Methods

In the current study, a series of experiments have been performed for classifying breast tumours using different feature vectors containing texture, shape, and a combination of these features. In Fig. 1, the design process for the proposed CAD system is depicted.
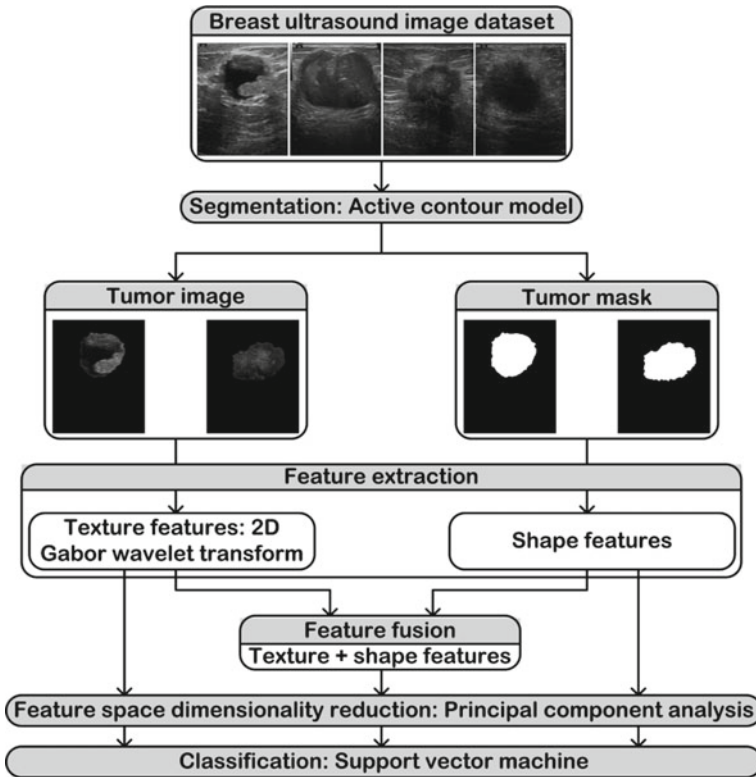
Fig. 1 The design process for the proposed CAD system stem

2.1 Dataset Description

The ultrasound images in this study's experimental analysis were gathered from Patiala's Modern Laboratory and Scan Center between December 2016 and September 2018. For inclusion, the images have been selected in collaboration with the participating radiologist based upon the following criterion, (i) Out of the multiple images of the same tumour, only one has been included. (ii) The size of the tumour region should be at least 800 pixels for computing reliable statistics. (iii) The images should not contain any artifacts. (iv) The images having annotations to point out certain features have not been included. The final dataset has a total of 110 images comprising 60 benign and 50 malignant cases.

2.2 Segmentation

The active contour method and its variants have been a popular choice for segmenting breast ultrasound images [15, 18, 27–30]. In the current work, breast tumours were segmented using the Chan and Vese active contour approach [31]. This method was typically used to segment objects that did not have well-defined boundaries and for which the classical active contour model was not applicable. This model is based on level sets that evolve iteratively to minimise an energy function. The model begins with an initial contour that evolves according to the level set method and stops on the desired boundaries of the foreground region. The user-provided parameters are (i) the initial level set function (mask) which represents the initial contour that evolves towards desired boundaries of the foreground and (ii) the length parameter that represents the number of iterations which are different for all images depending on the size of the tumour to be detected. The algorithm's stopping condition is to maximise the overlap between the contours marked by the radiologist and the segmented tumour contour.

2.3 Feature Extraction

In CAD systems, the feature extraction stage makes use of the visual data that has been captured in an image and transforms it into what is known as features or attributes. These attributes include either morphological information, such as shape or colour information, or intensity distribution information, such as texture features. Radiologists use the shape and texture information present in the image to characterise tumours in breast tissue ultrasound imaging. [13, 32–36].

Texture Features. The distribution of grey levels in an image is quantified using texture information. The methods for computing texture characteristics can be broadly divided into three categories: (i) statistical methods, (ii) methods based on spatial filtering, and (iii) methods based on transform decomposition.

By translating the image under study into the frequency domain, the transform domain methods are utilised to capture the texture information at various scales and orientations. In the present work, a transform domain-based method namely 2D Gabor wavelet transform (2D-GWT) has been used. Several Gabor functions, which are created by performing a sequence of dilation and shifting operations on the mother wavelet, are used to process the images. As a result, a collection of frequency- and orientation-selective filters is obtained and utilised to process the images [37, 38]. In the present work, 3 scales (0, 1, 2) and seven orientations (22.5º, 45º, 67.5º, 90º, 112.5º, 135º, and 157.5º) have been used to create a group of 21 filters that are then convolved with the segmented tumour images to produce 21 feature images for each segmented tumour image. Two texture descriptors, mean and standard deviation, have been computed from the resulting feature images, yielding a total of 42 Gabor-based features.

Shape Features. It has been well established that shape and margin information is prominent for the differentiation of breast tumours [39]. While malignant tumours have an ill-defined margin, benign tumours have a smooth and well-defined margin. Accordingly, different shape features namely area, perimeter, equivalent diameter, convex area, length of the major and minor axis, Euler number, solidity, and circularity [15], etc. have been computed in the present work.

2.4 Feature Space Dimensionality Reduction

Some of the features in the computed feature set might be correlated with one another and ineffective for identifying benign and malignant tumours [15]. In the present work, principal component analysis (PCA) has been used to reduce the dimensionality of the input feature space thus finding the optimal principal components (PCs) useful for classification tasks [15, 40–42].

2.5 Classification

The SVM is a kernel-based classifier used popularly for tasks involving the classification of medical images [13, 15, 17, 25, 26, 43–49]. A hyper-plane is employed in this classifier to divide the instances into distinct classes in the feature space. The hyper-plane is chosen in a way that maximises the distance between the two classes. The SVM classifier is a popular choice because it can handle linear data as well as non-linearly distributed data. The problems having a non-linear distribution of data are handled by mapping the non-linear data into linear data in a higher dimensionality space by making use of kernel functions. LibSVM library has been used for implementation in the current study, and the Gaussian radial basis function (GRBF) kernel is used for data mapping [50].

3   Results and Discussion

Table 1 displays the findings of the experiments performed in the current study for categorising breast tumours.

  As observed from the results shown in Table 1, using a mix of texture and shape features, the maximum accuracy is attained. It is also worth noting that in the case of all three feature sets, the same number of benign cases are being classified correctly however, the detection of malignant tumours starts to increase from texture to shape to combined feature set cases. These results are indicative of the fact that shape features combined with texture features are useful for clearly identifying malignant

Table 1 The findings of the experiments performed in the current study for categorising breast tumours

Feature set (No. of PCs)	CM			Accuracy (%)	ICA_B (%)	ICA_M (%)
		B	M			
Texture features (6)	B	17	1	75.7	94.4	53.3
	M	7	8			
Shape features (5)	B	17	1	84.8	94.4	73.3
	M	4	11			
Texture + shape features (11)	B	17	1	93.9	94.4	93.3
	M	1	14			

Note PCs: Principal components, B: Benign class, M: Malignant class, CM: Confusion matrix, ICA: Individual class accuracy

tumours. The combined feature set achieves an overall accuracy of 93.9% for differentiating between benign and malignant tumours with only 2 testing instances being misclassified.

4 Conclusion

The visual analysis of ultrasound scans is very subjective, which has led to a rise in the use of CAD system designs for categorising breast ultrasound images during the past few decades. The authors of the current study use ultrasound images obtained with the assistance of radiologists at a nearby scan centre in Patiala to try to create a computer-aided design (CAD) system for differentiating between breast tumours. The experiments have been conducted on the segmented tumour images extracted using Chan-Vese active contour segmentation algorithm. The texture and morphological feature sets were then tested individually and in a combined fashion using SVM classifier. The findings show that combining textural and morphological features yields the best classification accuracy, thus indicating the usefulness of both texture and shape information of tumours in differentiating between breast tumour types.

References

1. Ganesan K, Acharya UR, Chua CK, Min LC, Abraham TK, Ng KH (2013) Computer-aided breast cancer detection using mammograms: a review. IEEE Rev Biomed Eng 6:77–98
2. Karimi B, Krzyzak A (2014) Computer-aided system for automatic classification of suspicious lesions in breast ultrasound images. In: Rutkowski I et al (eds) ICAISC 2014, vol 8468. Springer, Cham, pp 131–142
3. World health organization (2021) Breast cancer, https://www.who.int/news-room/fact-sheets/detail/breast-cancer. Last accessed 22 July 2022

4. Indian Council of Medical Research (2018) Consensus document for management of breast cancer. Available online: http://www.icmr.nic.in/guide/cancer/Breast_Cancer.pdf. Last accessed 22 July 2022

5. Anderson BO, Braun S, Lim S, Smith RA, Taplin S, Thomas DB (2003) Early detection of breast cancer in countries with limited resources. Breast J 9:S51–S59

6. Chamberlain J, Rogers P, Price JL, Ginks S, Nathan BE, Burn I (1975) Validity of clinical examination and mammography as screening tests for breast cancer. The Lancet 306(7943):1026–1030

7. Berg WA, Blume JD, Cormack JB, Mendelson EB, Lehrer D, Bohm-Velez M, Pisano ED, Jong RA, Evans WP, Morton MJ, Mahoney MC, Larsen LH, Barr RG, Farria DM, Marques HS, Boparai K (2008) Combined screening with ultrasound and mammography vs mammography alone in women at elevated risk of breast cancer. J Am Med Assoc 299(18):2151–2163

8. Bazzocchi M, Mazzarella F, Frate CD, Girometti F, Zuiani C (2007) CAD systems for mammography: a real opportunity? a review of the literature. La Radiol Med 112(3):329–353

9. Burgess MD, O'Neal EL (2019) Breast ultrasound for the evaluation of benign breast disease. Curr Radiol Rep. https://doi.org/10.1007/s40134-019-0316-x

10. Gardezi SJS, Elazab A, Lei B, Wang T (2019) Breast cancer detection and diagnosis using mammographic data: systematic review. J Med Internet Res 21(7):e14464

11. Velez N, Earnest DE, Staren ED (2000) Diagnostic and interventional ultrasound for breast disease. Am J Surg 180:284–287

12. Burckhardt CB (1978) Speckle in ultrasound B-mode scans. IEEE Trans Sonics Ultrasonics SU-25 (1):1–6

13. Daoud MI, Bdair TM, Al-Najar M, Alazral R (2016) A fusion based approach for breast ultrasound image classification using multiple-ROI texture and morphological analyses. Comput Math Methods Med 2016:1–12

14. Drukker K, Gruszauskas NP, Sennett CA, Giger ML (2008) Breast US computer-aided diagnosis workstation: performance with a large clinical diagnostic population. Radiology 248(2):392–397

15. Kriti, Virmani J, Agarwal R (2019) Effect of despeckle filtering on classification of breast tumors using ultrasound images. Biocybern Biomed Eng 39:563–560

16. Lee JH, Seong YK, Chang CH, Ko EY, Cho BH, Ku J, Woo KG (2013) Computer aided lesion diagnosis in B-mode ultrasound by border irregularity and multiple sonographic features. In: Novak CL, Aylward S (eds) Medical imaging 2013: computer-aided diagnosis, vol 8670. SPIE, pp 430–436

17. Liao R, Wan T, Qin Z (2011) Classification of benign and malignant breast tumors in ultrasound images based on multiple sonographic and textural features. In: 3rd international conference on intelligent human-machine systems and cybernetics. IEEE, Hangzhou, China, pp 71–74

18. Marcomini KD, Caneiro AAO, Schiabel H (2014) Development of a computer tool to detect and classify nodule in ultrasound breast images. In: Aylward S, Hadjiiski LM (eds) Medical imaging 2014: computer-aided diagnosis, vol 9035, SPIE, pp 440–448

19. Marcomini KD, Carneiro AAO, Schiabel H (2016) Application of artificial neural network models in segmentation and classification of nodules in breast ultrasound digital images. Int J Biomed Imag. https://doi.org/10.1155/2016/7987212

20. Menon RV, Raha P, Kothari S, Chakraborty S (2015) Automated detection and classification of mass from breast ultrasound images. In: 5th national conference on computer vision, pattern recognition, image processing and graphics. IEEE, Patna, India, pp 1–4

21. Moon WK, Huang YS, Lo CM, Huang CS, Bae MS, Kim WH, Chen JH, Chang RF (2015) Computer-aided diagnosis for distinguishing between triple-negative breast cancer and fibroadenomas based on ultrasound texture features. Med Phys 42(6):3024–3035

22. Nemat H, Fehri H, Ahmadinejad N, Fragi AF, Gooya A (2018) Classification of breast lesions in ultrasonography using sparse logistic regression and morphology-based texture features. Med Phys 45(9):4112–4124

23. Prabusankarlal KM, Thirumoorthy P, Manavalan R (2015) Assessment of combined textural and morphological features for diagnosis of breast masses in ultrasound. HCIS 5:12–28

24. Moon WK, Chen IL, Yi A, Bae MS, Shin SU, Chang RF (2018) Computer-aided prediction model for axillary lymph node metastasis in breast cancer using tumor using morphological and textural features on ultrasound. Comput Methods Programs Biomed 162:129–137
25. Gomez-Flores W, Rodriguez-Cristina A, de Albequerque PWC (2019) Texture analysis based on auto-mutual information for classifying breast lesions with ultrasound. Ultrasound Med Biol 45(8):2213–2225
26. Bhusri S, Jain S, Virmani J (2016) Breast lesions classification using the amalgamation of morphological and texture features. Int J Pharma Bio Sci 7(2):(B):617–624
27. Cai L, Wang Y (2013) A phase-based active contour model for segmentation of breast ultrasound images. In: 6th international conference on biomedical engineering and informatics. IEEE, Hangzhou, China, pp 91–95
28. Liu Z, Zhang L, Ren H, Kim JY (2013) A robust region-based active contour model with point classification for ultrasound breast lesion segmentation. In: Novak CL, Aylward S (eds) Medical imaging 2013: computer-aided diagnosis, vol 8670. SPIE, pp 437–444
29. Prabhakar T, Poonguzhali S (2014) Feature based active contour method for automatic detection of breast lesions in ultrasound images. Appl Mech Mater 573:471–476
30. Daoud MI, Baba MM, Awwad F, Al-Najjar M, Tarawneh ES (2012) Accurate segmentation of breast tumors in ultrasound images using a custom-made active contour model and signal-to-noise variations. In: 8th international conference on signal image technology and internet based systems. IEEE, Sorrento, Italy, pp 137–141
31. Chan TF, Vese LA (2001) Active contours without edges. IEEE Trans Image Process 10(2):266–277
32. Gruszauskas NP, Drukker K, Giger ML, Sennett CA, Pesce LL (2008) Performance of breast ultrasound computer-aided diagnosis dependence on image selection. Acad Radiol 15(10):1234–1245
33. Takemura A, Shimizu A, Hamamoto K (2010) Discrimination of breast tumors in ultrasonic images using an ensemble classifier based on the AdaBoost algorithm with feature selection. IEEE Trans Med Imaging 29(3):598–609
34. Zakeri FS, Behnam H, Ahmadinejad N (2012) Classification of benign and malignant breast masses based on shape and texture features in sonography images. J Med Syst 36(3):1621–1627
35. Verma K, Singh BK, Tripathi P, Thoke AS (2015) Review of feature selection algorithms for breast cancer ultrasound images. In: Barbucha B et al (eds) New trends in intelligent information and database systems, vol 598. Springer, Cham, pp 23–32
36. Cristerna AR, Guerrero-Cedillo CP, Donati-Olvera GA, Gomez-Flores W, Pereira WCA (2017) Study of the impact of image processing approaches on segmentation and classification of breast lesions on ultrasound. In: 14th International conference on electrical engineering, computer science and automatic control. IEEE, Mexico pp 299–317
37. Virmani J, Kumar V, Kalra N, Khandelwal N (2013) Prediction of liver cirrhosis based on multiresolution texture descriptors from B-mode ultrasound. Int J Converg Comput 1(1):19–37
38. Kriti, Virmani J, Thakur S (2016) Application of statistical features for breast tissue density classification. In: Awad A, Hassaballah M (eds) Image feature detectors and descriptors, vol 30. Springer, Cham, pp 411–435
39. Chang RF, Wu WJ, Moon WK, Chen DR (2005) Automatic ultrasound segmentation and morphology based diagnosis of solid breast tumors. Breast Cancer Res Treat 89(2):179–185
40. Virmani J, Kumar V, Kalra N, Khandelwal N (2013) PCA-SVM based CAD system for focal liver lesions using B-mode ultrasound images. Def Sci J 64(5):478–486
41. Virmani J, Kumar V, Kalra N, Khandelwal N (2013) A comparative study of computer-aided classification systems for focal hepatic lesions from B-mode ultrasound. J Med Eng Technol 37(4):292–306
42. Wang JS, Chiang WC, Hsu YL, Yang YTC (2013) ECG arrhythmia classification using a probabilistic neural network with a feature reduction method. Neurocomputing 116:38–45
43. Sharma S, Khanna P (2015) Computer-aided diagnosis of malignant mammograms using Zernike moments and SVM. J Digit Imaging 28(1):77–90

44. Kaucha DP, Prasad PWC, Alsadoon A, Elchouemi A, Sreedharan S (2017) Early detection of lung cancer using SVM classifier in biomedical image processing. In: IEEE international conference on power, control, signals and instrumentation engineering. IEEE, Chennai, India, pp 3143–3148

45. Sengan S, Priya V, Syed Musthafa A, Ravi L, Palani S, Subramaniyaswamy V (2020) A fuzzy based high-resolution multi-view deep CNN for breast cancer diagnosis through SVM classifier on visual analysis. J Intell Fuzzy Syst 39(6):8573–8586

46. Garcia-Floriano A, Ferreira- Santiago A, Camacho-Nieto O, Yznez-Marquez C (2019) A machine learning approach to medical image classification: detecting age-related macular degeneration in fundus images. Comput Electr Eng 75:218–229

47. Mall PK, Singh PK, Yadav D (2019) GLCM-based feature extraction and medical image classification using machine learning techniques. In: 2019 IEEE conference on information and communication technology. IEEE, Allahabad, India, pp 1–6

48. Wei M, Wu X, Zhu J, Liu P, Luo Y, Zheng L, Du Y (2019) Multiple feature-fusion for ultrasound breast image classification of benign and malignant. In: 4th International conference on image vision and computing. IEEE, Xiamen, China, pp 474–478

49. Shia WC, Chen DR (2021) Classification of malignant tumors in breast ultrasound using a pre-trained deep residual network model and support vector machine. Comput Med Imaging Graph 87:101829. https://doi.org/10.1016/j.compmedimag.2020.101829

50. Chang CC, Lin CJ (2011) LIBSVM: a library for support vector machines. ACM Trans Intell Syst Technol 2(3):1–27

Investigations on Sound Absorption Properties of Perforated Designed Panels for the Selective Frequency Absorption

Kuldeep Meena, Kirti Soni, Girija Moona, and Mahavir Singh

Abstract Due to rapid industrialization and urbanization, noise pollution emerges as one of the serious threats to human beings. Noise is countered by sound-absorbing materials in the buildings and other places. In this study sound absorption properties of pinewood-based high-density fiberboard (HDF) perforated ceiling panels have been investigated. Perforated panels have been selected because they can counter the noise in specific low frequency ranges. The panels of different specific drilled hole sizes and perforation ratios have been studied to see the influence of these parameters on sound absorption characteristics. Further, an attempt has been done to enhance the sound absorption bandwidth by inserting a porous material behind the perforated panels. The experiments for the measurement of sound absorption coefficients (alpha) have been done by the Reverberation Chamber method as per ISO 8285-1987. The main aim of this study is to optimize different parameters and design a structure for the ceiling panel that can provide an efficient, economical noise reduction solution for confidential speech privacy by reducing echoes and long reverberation inside rooms.

Keywords Noise · Sound absorbing materials · Frequency · Perforation · Reverberation chamber

K. Meena · G. Moona · M. Singh
CSIR-National Physical Laboratory, Dr K. S. Krishnan Marg, New Delhi 110012, India
e-mail: moonag@nplindia.org

K. Meena · K. Soni · G. Moona · M. Singh
Academy of Scientific and Innovative Research (AcSIR), Ghaziabad 201002, India

K. Soni (✉)
CSIR-Advanced Materials and Processes Research Institute (AMPRI), Bhopal 462026, India
e-mail: soniks@ampri.res.in

1 Introduction

A noisy environment negatively impacts human life as well as other species by interfering in different ways such as disturbing normal sleeping time irritates. Moreover, continuous regular exposure to high-intensity sound can cause some serious problems such as hearing impairment, hypertension, and ischemic heart disease [1]. The living spaces such as building nearby to heavily trafficked roads are highly prone to noise pollution from vehicles. Noise in hospitals is also a big worry as it disturbs the sleeping and rest time of patients and can become the cause of their (inpatient and working staff) high-stress levels; can further create a possibility of medical error [2–4]. Therefore, noise is a big threat and it must be controlled to enhance the quality and working efficiency of daily routine life.

The application of sound-absorbing materials is one of the widely accepted techniques used to reduce noise in living spaces by reducing echoes and reverberations; thus creating an acoustically pleasing environment. Hence, acoustical treatment of living spaces is a useful tool to create a healthy and peaceful working environment inside the home/office that enhances productivity. Further due to rising environmental awareness, it is important to produce eco-friendly and cost-effective sound-absorbing material [5, 6]. Porous materials, resonant absorbers, and perforated panels are the main types of sound-absorbing materials that are familiar and used for acoustical treatment. Porous absorbing materials are efficient at mid to higher frequencies while resonator and perforated panels absorb sound in the lower frequency but with limited bandwidth. The resonating panels that contain tiny holes are referred to as perforated absorbers. They could tune the resonance frequency to a particular need in room acoustics for reducing the reverberation time in a particular frequency range [7]. They are widely used in the interior of buildings e.g. ceilings and roofs. The research work on perforated panels for acoustic purposes begin in 1947 when a scientist named Bolt suggested that perforated plates can be used for sound-absorbing purposes. The structure of these panels (plates) can be considered (or is a type of) as multiple parallel compositions of Helmholtz resonators [8]. Researchers investigated these types of panels and found that the major factors that influence acoustic properties are panel thickness, aperture size, perforated rate, and pore depth, of these perforated panels [9, 10]. The experimental study [11] about the wooden decorative perforated panels revealed that the sound absorption properties could be improved when a suitable perforated panel cavity depth was used, up to a certain extent. In another study, Hou et al. [12] discussed various factors linked to the wooden perforated panel which influences the sound absorption properties. Maa carried out more research work on perforated and porous materials [13] especially focused on the micro-perforated panels, and revealed that when holes are drilled with smaller diameters sound absorption increases. Further, scientists had approached the prediction of the sound absorption coefficient of acoustically designed perforated panels with a porous layer backing [14]. Perforated panels provide selective absorption features by optimizing different parameters [9]. Generally, panel absorbers are manufactured by utilizing non-porous materials such as plasterboards, metallic sheets, and aluminum.

Fig. 1 The perforated panels with different specific hole diameters **a** d = 2 mm and P = 2.2% **b** d = 6 mm and P = 4.4% **c** d = 9 mm and P = 6%

Therefore, rationally selecting parameters can effectively improve the sound absorption coefficients of wooden perforated panels if they are optimized in a better way [15]. However, a lot of early research work focused on the sound absorption properties investigation of metal-based or gypsum perforated panels mainly [16], and the systematic studies on wooden-based perforated panels have not been investigated yet to the best of our knowledge. In this study, pinewood-based MDF was used due to the sustainability, biodegradability and eco-friendly nature of wood. The influence of two structural parameters aperture size, and perforation ratio studied. The influence of the back air cavity and porous backing below the wooden perforated panels have been investigated experimentally. The influence on the resonance frequency and bandwidth was analyzed based on the experimental results.

2 Materials and Methods

2.1 Testing Materials/Test Samples Specifications

Different pinewood-based panels of fixed thickness and density have been selected for the acoustic properties investigations. Testing specimens were cut out and processed into three different perforation ratios of 2.2, 4.4, and 20% with circular holes having diameters of 3 mm, 6 mm and 9 mm. The panels has been shown in Fig. 1, while thickness and density were fixed at 16 mm and 700 kg/m^3. The drilled holes were in circular patterns as per the design considerations [17]. These manufactured perforated panels are investigated in the reverberation chamber method for acoustical analysis and all materials were provided by Anutone Acoustics Limited, Bengaluru (Table 1).

2.2 Method and Measurements

The sound absorption properties are usually expressed by the term "sound absorption coefficient" also denoted by alpha which is the ratio of reflected and incident

Table 1 Description of the test samples

Sample no	Hole diameter (mm)	Hole pattern	Perforation ratio (%)
1	3	Circular	2.20
2	6	Circular	4.40
3	9	Circular	6

wave intensities and "noise reduction coefficient" (NRC) which is the average of alpha values at four different frequencies. In this reported work sound absorption coefficient measurement has been done by the Reverberation Chamber method as per ISO standards. In this method a white noise signal has been generated in the chamber then decay of sound has been obtained with and without sample. For the calculation of SAC and NRC; the reverberation time with and without samples that are R_{t0} and R_t are required, apart from these chambers volume and sample testing area are also required parameters. A more detailed theory of the experiment and alpha measurement has been given in our previous work [18]. The sample manufactured from pinewood were tested in different conditions: firstly, attached to a rigid wall, secondly at a certain layer of air below the samples and thirdly after placing a porous layer material below perforated samples. For each configuration sound absorption coefficient values were measured successively up to the frequency of 4 kHz.

3   Results and Discussions

3.1   Selection of Materials and Panel Designing Parameters

The pinewood-based acoustic panels with multiple diameter holes and with different perforation rates were analyzed, from the acoustical point of view. However, aesthetic considerations of the panels have also been taken. The circular holes were designed within the panel for acoustic purposes and also perforation rates are limited up to a maximum of 5% because of the mechanical strength of the panels. The drilled holes of 3 mm, 6 mm, and 9 mm diameters and the perforation rates of the panels set up at 2.2, 4.4 and 5% were selected for the acoustical analysis. Greater diameter holes are generally not liked by architectural designers unless it becomes an element of the interior design, thus maximum hole diameter was selected at 9 mm, also too fewer diameters are difficult to obtain. However, medium diameter holes are acceptable, if covered with acoustically transparent fabric [19]. The less visible perforations were obtained with dense perforations and smaller diameter circular holes, this further helps to make the panel more monolithic. The thickness of the typically perforated panels ranges between 5 to 15 mm; in this study thickness of all panels was selected at 16 mm due to acoustical and mechanical reasons. The enhanced sound absorption performance can be obtained by the procedure of combining the membrane or panel absorber with porous materials and so this is even worth considering. Therefore, the

next approach in this section is the selection of a porous material layer for the back of the perforated panel. All the panels have been tested inside a reverberation chamber at the back air cavity of 300 mm.

3.2 Sound Absorption Process in Perforated Panel Absorbers

The wooden perforated panel and back air cavity space both combined work like a Helmholtz resonator [20–22]. This system has two communicating volumes one is called the neck and the other is a cavity, which is equivalent to a mass-spring mechanical system where the neck behave like a mass and the air space behaves like a spring (Fig. 2).

The sound absorption phenomena of the perforated panels can be understood by the Helmholtz principle, where the tiny holes in the panel represent the neck of the resonator, while the space in between the wall and panel constitutes a cavity as shown in the figure. When sound waves strike the panel, the air inside the neck i.e. the mass is forced back into the air cavity. As a result, the air inside the cavity is forced to be compressed and like a spring it reacts by expanding and causing the incoming air to push out. Thus air is driven outside with a certain velocity, this goes a little beyond the neck. Hence, the air inside the cavity becomes rarefied and recalls inside other air restarting the cycle. This mass-spring action can significantly absorb a good amount of acoustic energy, which is changed into the air swing. It is pointed out that this phenomenon happens particularly in a specific frequency range that is resonance frequency, at which the maximal sound absorption occurred. Therefore, the sound absorption properties of such a system are influenced by the neck and cavities volumes. The Changes in volumes of these two (neck and cavity) determine amounts of absorption and the frequency around which maximum sound absorption occurs i.e. absorption peak could be adjusted.

Fig. 2 Longitudinal section of a Helmholtz resonator (left) and a system made of perforated panel and wall (right)
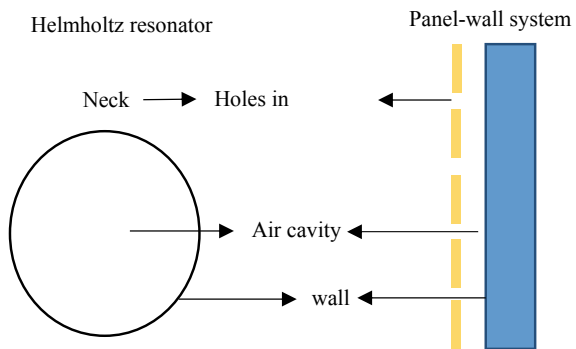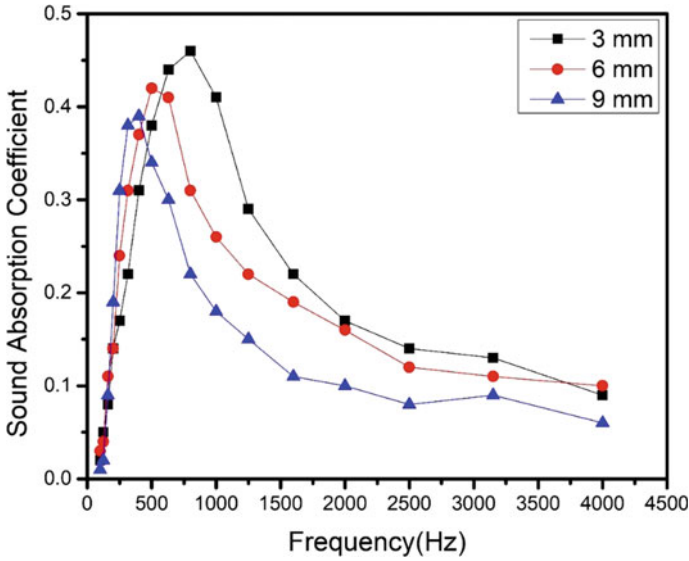
Fig. 3 Influence of hole size on sound absorption of wood panels

3.3   Influence of Hole Diameter

The designed wood-based panels with perforation meet the general sound absorption characteristics, and the maxima of absorption peaks mainly occurred in the low to mid-frequency range [23, 24]. Figure 3, shows the absorption coefficient values obtained by the reverberation chamber method of the wooden perforated panels, having three different configurations that are hole diameters are 3 mm, 6 mm, and 9 mm, while the thickness is 16 mm, the density of 700 kg/m³, perforation rates are 2.2 remained constant. During this variation in circular holes' diameter of panels, the perforations ratio was constant by reducing the number of holes. The resonance frequencies are 800 Hz, 500 Hz, and 400 Hz respectively for the different holes' diameters of 3 mm, 6 mm and 9 mm.

A point can be noted that as the hole size increases the resonance frequency is decreased (from 800 to 400 Hz), and the resonance absorption coefficient or maxima of absorption also decreases (from 0.46 to 0.39). Therefore, according to these results, the drilled hole size has a significant effect on the resonance absorption peak and resonance frequency of the perforated panels.

3.4   Influence of Perforation Ratio

Figure 4, shows the absorption behavior of three different perforation ratio wood panels, the perforation rates were at 2.2, 4.4, and 5% while thicknesses are 16 mm,

density 700 kg/m^3 and hole size 3 mm were fixed. Remember, this time perforation ratio is varied and in the previous case, hole diameters were varied. This variation in perforation ratios was obtained by increasing the number of holes and reducing the separation distance between the adjacent holes. The resonance frequencies of the perforated panels are 400, 500, and 630 Hz, for the panel perforation ratio of 2.2%, 4.4% and 5% respectively. The curve obtained for these panels shows that the sound absorption coefficient peak values decreased from 0.52 to 0.44 and 0.37. This point can be noted that the perforation rate has a significant role in the resonance absorption peak of the perforated plates and the size of the resonant frequency. The acoustic resistance is inversely proportional to the perforation rate. According to the perforated plate resonance frequencies formula [25], when other parameters (the rear pore depth, pore diameter, and thickness) are constant, the perforation rate is proportional to the resonance frequencies of the perforated panels.

When the perforated rate is increased from 2.2% to 5%, the resonance absorption frequency increases from 400 to 630 Hz, and the resonant frequency moves in the direction of a higher frequency but simultaneously a decrease has also been noted in maximum absorption peak value. When the aperture size of the circular holes was fixed at a constant value, an increment in the perforation rate leads to a decrease in the hole spacing and an increase in the number of holes on the specimens of the same area.
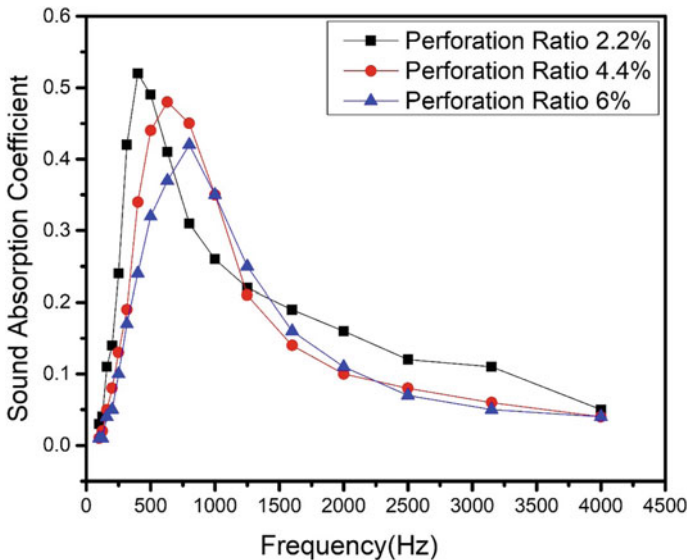
Fig. 4 Influence of perforation ratio on sound absorption of wood panels

3.5 *Influence of Porous Material Backing*

The sound absorption performance of the perforated panel majorly depends upon the design and type of layout of the perforations, which can be considered as a group of multiple parallel Helmholtz resonators. When the frequency of the incident sound wave towards the panel is similar to its resonance frequency, the air within and nearby the small perforations generates intense vibrations and reduces a significant amount of sound wave energy by frictional forces in the backed porous layer behind the perforated panels.

The porous recycled fiber-based polyester nonwoven wool was inserted below the perforated panel. These type of textile nonwoven structures are used as infilling materials due to their lightweight and provides acoustic comfort due to fiber interlocking as these fibers act as a frictional element. This insertion of porous material behind the sample results in enhanced and widened absorption results, as shown in Fig. 5. This might be due to the increased resistance provided to the approaching sound wave towards the installed panel inside the reverberation chamber by the porous layer. This new combination of both perforated panels and porous layer has wide bandwidth absorption properties compared to the without gluing perforated panels [26]. As the porous material is already a good absorber at higher frequencies, the addition of porous material with a perforated panel increases the resultant resistance [27].
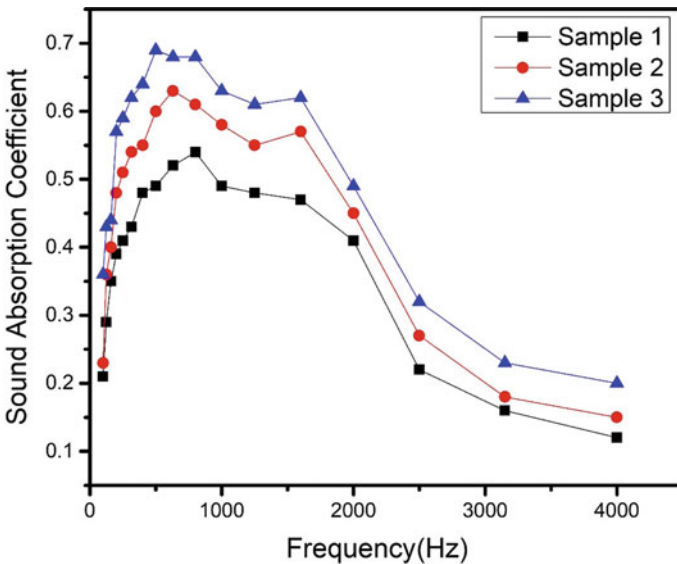
Fig. 5 Wooden perforated panel sample 1, sample 2, and sample 3 backed with polyester fiber-based nonwoven wool (porous material)

4 Conclusions

The designed wooden perforated panels have been studied for sound absorption properties experimentally by the reverberation chamber method and the influence of different parameters has been covered in the study. The following conclusion can be drawn from this study:

(1) When hole size is reduced to a lower diameter then the absorption coefficient peak value increases and the resonance frequency moves towards the lower frequency side, but the sound absorption bandwidth becomes narrower. It has to be noted that all other parameters remain constant.

(2) The increment in the perforation rate causes the absorption peak value to decrease, the location of the resonance frequency to move towards the direction of a higher frequency, and the sound absorption bandwidth to become wider to some extent

(3) Insertion of the recycled polyester fiber-based nonwoven porous layer behind the panels widened absorption bandwidth.

Therefore, this study revealed the practicability of wooden perforated panels and promotion of their use instead of gypsum panels due to their eco-friendly nature. This study will be useful for the engineers in the designing of auditoriums, recording rooms, theatres, studios, hospitals, offices, classes rooms etc. Thus a perforated designing structure of a perforated panel required optimized or preferred conditions of perforation rate, backing porous material etc. Further studies can be done to investigate the influence of air space between perforated facing and backing porous material.

References

1. Shi LL (2014) Laboratory study of the noise annoyance of the low frequency noise. Phd thesis, Zhejiang University
2. Peng L, Song B, Wang J, Wang D (2015) Mechanic and acoustic properties of the sound-absorbing material made from natural fiber and polyester. Adv Mater Sci Eng 2015, Article ID 274913, p 5
3. Yang WD, Li Y (2012) Sound absorption performance of natural fibers and their composites. Sci China Tech Sci 55:2278. https://doi.org/10.1007/s11431-012-4943-1
4. Aaron JN, Carlisle CC, Carskadon MA, Meyer TJ, Hill NS, Millman RP (1996) Environmental noise as a cause of sleep disruption in an intermediate respiratory care unit. Sleep 19:707–710
5. Topf M (1985) Noise-induced stress in hospital patients: coping and non-auditory health outcomes. J Hum Stress 11:125–134
6. Topf M, Dillon E (1988) Noise-induced stress as a predictor of burnout in critical care nurses. Heart Lung 17:567–574
7. Kłosak AK (2020) Design, simulations and experimental research in the process of development of sound absorbing perforated ceiling tile. Appl Acoust 161:107185
8. Bolt RH (1947) On the design of perforated facings for acoustic materials. J Acoust Soc Am 19:917–921

9. Zulkifli R, Azharim CH (2011) Perforated plate backing with coconut fiber as sound absorber for low and mid-range frequencies. Key Eng Mater 462–463:1284–1289
10. Lee YY et al (2005) Sound absorption of a finite flexible micro-perforated panel backed by an air cavity. J Sound Vib 287(1):227–243
11. Zhong XZ et al (2008) Wood perforated decorative sound absorption plate and its application. J Sound Technol Equip Appl 8:27–30
12. Hou QQ et al (2010) Research on influence factors of absorption performance for wooden perforated panels. Adv Mater Res 113–116(1):959–1963
13. Maa DY (1998) Potential of microperforated panel absorber. J Acoust Soc Am 104:2861–2866
14. Morse PM, Bolt RH (1944) Sound waves in rooms. Rev Mod Phys 16:69
15. Peng L (2017) Sound absorption and insulation functional composites. In Fan M, Fu F (eds) Advanced high strength natural fibre composites in construction. Woodhead Publishing, pp 333–373
16. Putra A et al (2015) Utilizing hollow-structured bamboo as natural sound absorber. Arch Acoust 40(4):601–608
17. Hou QQ, Yu HP, Wang JM, Guo MH (2010) Research on influence factors of absorption performance for wooden perforated panels. In: Advanced materials research, vol 113–116. Trans Tech Publications, Ltd., pp 1959–1963
18. Meena K, Singh M, Soni K, Nair AS (2022) Influences of various parameters on sound absorption properties of vetiver grass fiber-based developed composite material. 60(5):422–429
19. Ingard U, Bolt RH (1951) Absorption characteristics of acoustic material with perforated facings. J Acoust Soc Am 23:533–540
20. Fasold V, Veres E (1998) Sound protection and room acoustics in practice: design examples and building solutions (German). Verlag fürBauwesen, Berlin, Germany
21. Rossing TD (ed) (2007) Springer handbook of acoustics. Springer, Würzburg, Germany
22. Everest FA, Pohlmann KC (2009) Master handbook of acoustics, 5th edn. McGraw-Hill, USA
23. Xie S, Yang S, Yang C, Wang D (2020) Sound absorption performance of a filled honeycomb composite structure. Appl Acoust 162
24. Zhao L, Lin TR (2022) A turned double-layer microperforated panel for low frequency sound absorption in enclosures with limited cavity space. Appl Acoust 188:108594
25. Peng L, Liu M, Wang D, Song B (2018) Sound absorption properties of wooden perforated plates. Wood Res 63:559–572
26. Thomas WA, Hurst CJ (1976) Acoustic performance of a stretched membrane and porous blanket combination. J Acoust Soc Am 59(5):1071–1076
27. Davern WA (1977) Perforated facings backed with porous materials as sound absorber-an experimental study. Appl Acous 10:85–112

Parametric Study of Factors Affecting Sound Absorption Characteristics of Acoustical Materials

N. Garg and C. Gautam

Abstract The paper reports the parametric sensitivity of the factors affecting the sound absorption characteristics of the acoustical materials tested in the reverberation chambers. The various factors affecting the sound absorption characteristics such as air-gap, thickness, bulk density, porosity, tortuosity and air flow resistivity have been discussed based on the previous studies. The study also reports some of the recently developed acoustical sound absorbing materials having higher sound absorption characteristics for noise control applications.

Keywords Sound absorption · Sound absorption coefficient · Acoustical materials

1   Introduction

The sound absorption coefficient of a material is defined as the fraction of the incident sound energy absorbed by it. It depends upon the nature of the material, frequency of the sound waves and the angle at which the sound waves strike the surface of the material and is measured at frequencies of 100–5000 Hz. There are numerous sound absorbing materials that can be used for acoustical treatment of buildings, dwellings, offices, theatres, halls and auditoriums. The choice of a suitable absorbent material depends, however, upon the requirements of the low or middle frequency acoustical treatment, durability, maintainability and availability of the material. The majority of the sound absorbing materials are either fibrous or porous in nature, Fibrous materials are in the form of boards or tiles while porous materials are in the form of tiles, blankets and resin-bonded slabs. Acoustic tiles are available in various textures and resin-bonded mineral or glass wool is available in the form of semi-rigid slabs, mats, etc. The cavity of Helmholtz resonators is also typical sound absorber used in auditoria or noisy rooms in a narrow region of the low frequency band. The use of wedge-shaped fibrous materials is extensively used for constructing anechoic chambers [1]. There had been numerous studies in the past on reverberation chambers

N. Garg (✉) · C. Gautam
CSIR-National Physical Laboratory, New Delhi 110 012, India
e-mail: ngarg@nplindia.org

method and sound impedance tube method that had analyzed the parametric analysis of the factors affecting the sound absorption characteristics of the various acoustical materials. However, the reverberation chamber method has proved to be the best method having lesser uncertainty and employing a larger specimen size for evaluating the random incidence sound absorption coefficient. A proper understanding of the factors affecting sound absorption characteristics and mounting considerations shall be indispensable in the design and development of better acoustical materials for noise control.

2 Mounting Considerations

The mountings test specimens during sound absorption tests as recommended by ASTM E795-16 standard as follows [2]:

- Type A Mounting-Test specimen laid directly against the test surface
- Type B Mounting-Test specimen cemented to gypsum board and laid directly against the test surface
- Type C Mounting-Test specimen comprising sound absorptive material behind a perforated, expanded, open facing or other porous material
- Type D Mounting-Test specimen mounted on wood furring stripes
- Type E Mounting-Test specimen mounted with an air space behind it
- Type F Mounting-Test specimen mounted with an air space behind it
- Type G Mounting-Test specimen is a drapery, window shade, or blind hung parallel to the test surface
- Type H Mounting-Test specimen is a drapery suspended away from any vertical surface Type I Mounting-The specimen is a spray- or trowel-applied material on an acoustically hard substrate
- Type J Mounting- The specimen is a sound absorbing unit or set of sound absorbing units
- Type K Mounting-Test specimen is an office screen
- Type L Mounting-This mounting is for use with concrete blocks or block-like specimen that are normally assembled using mortar
- Type M Mounting-Test specimen is theatre seats

Type C, D, E, and G Mountings are further designated by a numerical suffix which indicates the distance (in millimeters from the specimen to the test surface rounded to the nearest integral multiple of 5 mm. For example, a Type E-400 mounting is a plenum mounting in which the face of the test specimen is 400 mm away from the test surface. In case of G mounting, the test specimen shall be drapery, window shade, or window blind hung parallel to the test surface. The suffix of the mounting designation shall be the distance from the test surface to the centreline of the hangers rounded to the nearest integral multiple of 5 mm. The preferred distance between the centreline of the hangers and the test surface is 75 mm. In the case of Type J Mounting, the test specimen shall be a sound absorbing unit or

set of sound absorbing units that are directly attached to or hanging from a ceiling, wall or other room surface. If the units are suspended flat panels (baffles), and an installation pattern is not specified, it is recommended that the following panel size and arrangement be tested. The total absorptive area (all exposed surfaces) of the sound absorbing units shall be at least 10 m^2. The distance between any sound absorbing unit and any reflective surface (other than the test surface), rotating vane or diffuser panel shall be consistent with the requirements of Test Method C423. The measured sound absorption is in square meters per unit or Sabins per unit [2]. The analysis of the observations made for different mounting considerations is shown in Figs. 1 and 2. The following observations associated with various mounting considerations as presented by Sharma and Singal [1] are as follows [1]:

- With increasing thickness, the absorption coefficient of porous soft materials at any frequency increases and for a slab of thickness 100 mm of mineral wool, the absorption coefficient attains a maximum value at 500 Hz which is maintained more or less uniformly at higher frequencies also.
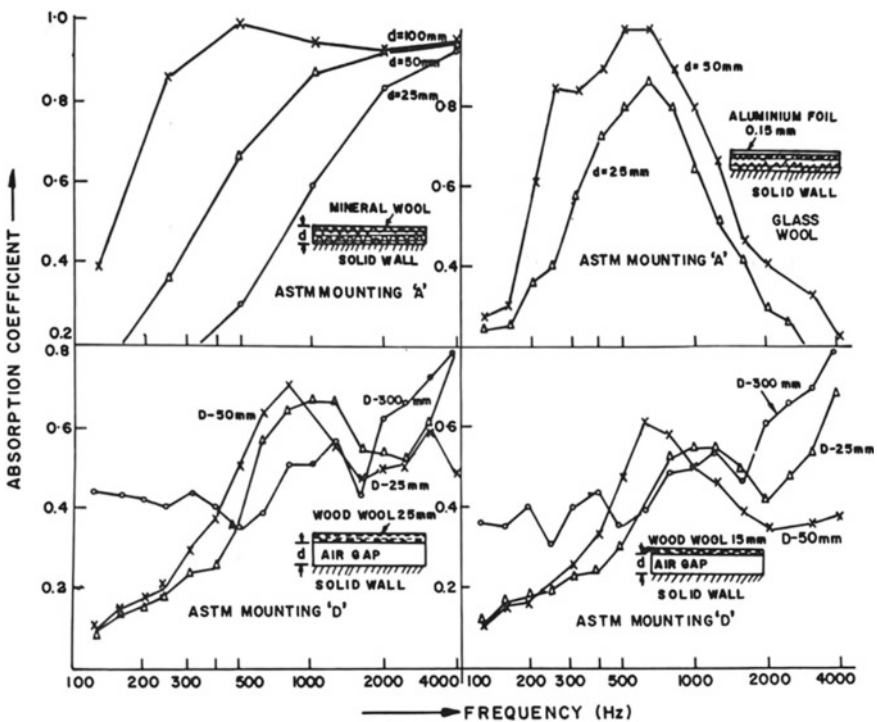
Fig. 1 Sound absorption characteristics of absorptive material in ASTM mountings A and D [1]
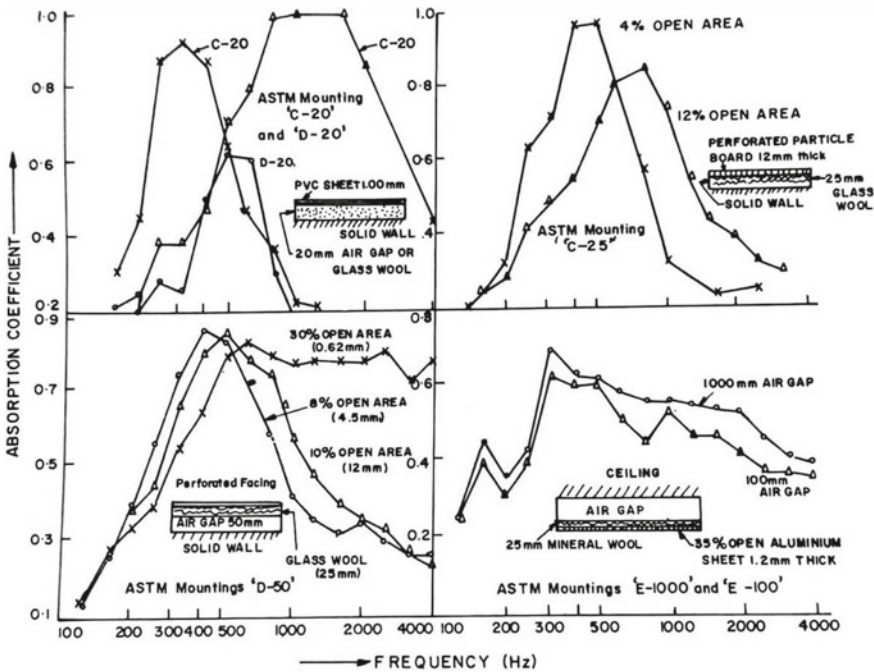
Fig. 2 Sound absorption characteristics of absorptive material in ASTM mountings C, D and E [1]

- With air-gap between the porous absorption material and the solid wall backing, the absorbing material and the solid wall backing, the absorption coefficient becomes more or less uniform in the mid frequency range 500–2000 Hz.
- The addition of the air-gap between the paneled absorbing material and the solid wall increases the maximum absorption coefficient while the increase in the open area in this situation not only shifts the resonance frequency but for a certain percentage of the open area (perforated 30%), absorption coefficient becomes uniformly high over a wider frequency range [1].

3 Edge Effect in Sound Absorption

The diffraction from the edges at low frequencies causes reflected waves to diffract that produces edge effect whereby more sound absorption occurs near the edges of an absorber than its centre. Thus, the wave diffraction at the edges of the specimen causes the sound absorption coefficient greater than unity. The amount by which the absorber's effective area increases is proportional to the ratio of the perimeter of the edges to the area of the absorber. The effect increases with decreasing frequency, decreasing specimen size and increasing aspect ratio [3–5].

4 Parametric Study

The parametric sensitivity of the various factors affecting the sound absorption characteristics of acoustical materials are enlisted in Table 1 based on exhaustive literature surveys of various previous studies carried out in this field [6–13]. It may be noted that several factors such as perforation of the material, air-gap behind the absorptive material, thickness and density of the absorptive material, airflow resistivity etc. play a vital role in determining the sound absorption characteristics. The diffusivity characteristics of the reverberation chamber are also an important aspect in the determination of the sound absorption characteristics.

Table 2 describes the details of some of the sandwich constructions tested and observed to show higher sound absorption characteristics in the entire measurement frequency range. The sandwich constructions in many cases show enhanced sound absorption coefficient as shown in Fig. 3.

5 Conclusions

The paper reports the parametric sensitivity of the factors affecting the sound absorption characteristics of the acoustical materials while these are tested in the Reverberation chambers. The various factors affecting the sound absorption characteristics such as air-gap, thickness, bulk density, porosity, tortuosity and air flow resistivity etc. have been highlighted in the study that has a significant role in determining the sound absorption characteristics in the entire measurement frequency range. The study shows the application of sandwich absorptive materials showing enhanced sound absorption characteristics that can be used widely for noise control applications. Future studies shall focus on the parametric sensitivity analysis of all the factors affecting the sound absorption characteristics using the analytical and experimental evaluation.

Table 1 Effects of various parameters of acoustical materials on sound absorption characteristics [6–13]

Parameter	Basic definition	Effect on sound absorption characteristics
Bulk density	Total mass of the porous material per unit volume	• As the density increases, the sound absorption coefficient shifts to the higher frequency range • In case fibers are too densely packed, it reduces porosity that restricts sound waves to penetrate the absorber [6, 7]
Thickness	Thickness plays a pivotal role at lower frequencies	• The thicker the absorber, the more the low frequency components can be absorbed • The peak absorption of an absorber is indicated by equivalent quarter wavelength. The material thickness should be a quarter of the wave length of the sound wave to be an effective absorber [6, 7]
Porosity	Relative fraction, by volume of the air contained within a porous material	• Value ranges between 0 and 1 for porous materials • Some studies reported that for natural fibers, the sound absorption coefficient increased as porosity is decreased [8]
Airflow resistivity	Resistivity of a material against airflow is a measure of sound to be dissipated inside sound absorbing material	• Airflow resistivity has an inverse relation to air permeability • Moreover, as the airflow resistivity of the material increases, then it is difficult for sound waves to enter the material. Hence, sound absorption shows a significant decrease [9–11]
Tortuosity	It is a dimensionless structural parameter that shows the influence of the internal pore structure on the macroscopic velocity of fluid flow through a porous material	• According to Mamtaz, the more tortuous the material, the greater the sound absorption [12] • Higher tortuosity implies the pores are very curly causing higher interaction between sound and fibers of materials resulting in higher dissipation [13]
Air-gap	Air-gap improves absorption at lower frequencies	• Sound absorption shifts to the lower region by increasing the depth of back cavity [9]

Table 2 Description of sound absorptive materials of higher sound absorption characteristics

S1	Woodwool Fiber cement composite panel with rockwool padding of 50 mm, 48 kg/m^3 density
S2	Perforated composite metal alloy sheet filled with 50 mm thick glasswool of 48 kg/m^3 density
S3	12.5 mm thick gypsum board with a geometric array of 3 mm square perforations (total 9% perforation) and 50 mm thick rockwool (48 kg/m^3 density) filled with 1.5 mm thick gypsum backing
S4	Hexagonal Stretch Ceiling with 12 mm HDF boards, LED in between and 25 mm thick mineral wool HDF boards in between having 47 mm and 60.5 mm air-gaps maintained with 0.17 mm HDF board and acoustic fabric
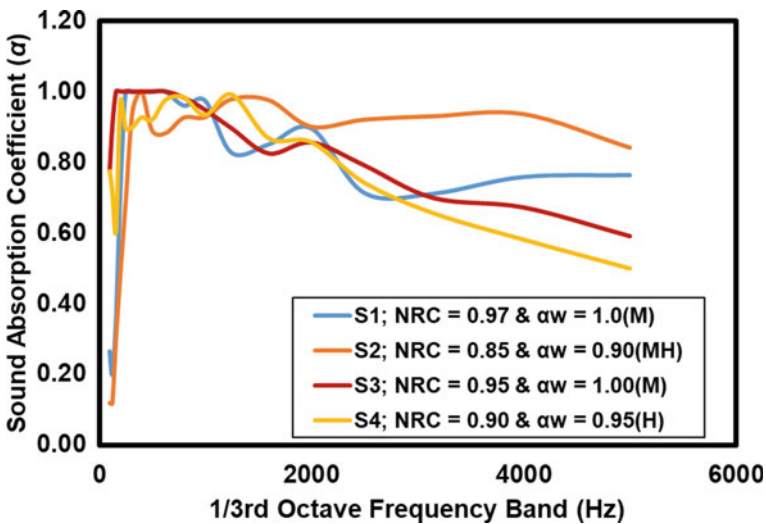
Fig. 3 Sound absorption coefficient of various sandwich acoustical materials of higher sound absorption characteristics tested in Reverberation chambers

References

1. Singal SP, Sharma O (1987) Acoustics of buildings part ii: materials and their characterization. Res Ind 32:14–24
2. ASTM E795-16, Standard practices for mounting test specimens during sound absorption tests
3. McGrory M, Cirac DC, Gaussen O, Cabrera D (2012) Sound absorption coefficient measurement: re-examining the relationship between impedance tube and reverberant room methods. In: Proceedings of acoustics 2012, 21–23 November 2012. Australian Acoustical Society, Fremantle
4. Bartle TW (1981) Effect of absorber geometry on apparent sound absorption coefficients as measured in a reverberation chamber. J Acoust Soc Am 69:1065–1074
5. Honeycutt R (2020) Progress on calculating edge effect of acoustical absorption. Audioxpress. https://audioxpress.com

6. Dunne R, Desai D, Sadiku R (2017) A review of the factors that influence sound absorption and the available empirical models for fibrous materials. Acoust Aust 45:453–469
7. Lim ZY, Putra A, Nor MJM, Yaakob MY (2018) Sound absorption performance of natural kenaf fibres. Appl Acoust 130:107–114
8. Fouladi MH, Nassir MH, Ghassem M, Shamel M, Peng SY, Wen SY, Xin PZ, Nor MJM (2013) Utilizing Malaysian natural fibers as sound absorber. In: Modeling and measurement methods for acoustic waves and for acoustic microdevices. Intech, pp 161–170
9. Hassan T, Jamshaid H, Mishra R, Khan MQ, Pteru M, Tichy M, Muller M (2021) Factors affecting acoustic properties of natural-fiber-based materials and composites: a review. Textiles 1:55–85
10. Czigany T (2006) Special manufacturing and characteristics of basalt fiber reinforced hybrid polypropylene composites: mechanical properties and acoustic emission study. Compos Sci Technol 66:3210–3220
11. Cherradi Y, Rosca IC, Cerbu C, Kebir H, Guendouz A, Benyoucef M (2021) Acoustic properties for composite materials reinforced on alfa and wood fibers. Appl Acoust 174:107759
12. Mamtaz H, Fouladi MH, Al-Atabi M, Namasivayam SN (2016) Acoustic absorption of natural fiber composites. J Eng. https://doi.org/10.1155/2016/5836107
13. Raj M, Fatima S, Tandon N (2020) Recycled materials as a potential replacement to synthetic sound absorbers: a study on denim shoddy and waste jute fibers. Appl Acoust 159:107070

Precise and Secure Time Dissemination Through White Rabbit Network Based Optical Fibre Link

Neelam, M. P. Olaniya, Sumit Kushwah, and S. Panja

Abstract Precise transfer of time and frequency signals is an indispensable activity in the field of time and frequency metrology. Accurate time is a critical requirement for various fields, e.g., navigation, telecommunication and finance sectors along with many technological applications and advanced scientific research. Satellite based time transfer methods fulfil the requirements of accurate time for most of these applications but vulnerability to jamming and spoofing of satellite signals are big concerns for many of the critical applications. Optical fibre-based time transfer techniques provide excellent options for transferring precise and secure time over a distance of several hundreds of kilometers. The present work describes the establishment of an optical fibre link at CSIR-National Physical Laboratory, India utilising White Rabbit Precision Time Protocol (WR-PTP) for precise and accurate transfer of time and frequency signals from a reference atomic clock. White Rabbit (WR) technique includes several advanced features, e.g., synchronous ethernet, precision time protocol, digital dual mixer time difference etc. for measuring as well as compensating link delays very accurately and provides time synchronisation within sub-nanosecond uncertainty. In order to enhance the accuracy and stability of the optical fibre link, a feedback loop has been utilised for estimating as well as compensating dynamic phase variation, which arises due to ambient temperature variation around the link.

Keywords Time & frequency · Time transfer · Synchronisation · White Rabbit · Optical fibre

Neelam · M. P. Olaniya · S. Kushwah · S. Panja (✉)
CSIR-National Physical Laboratory, Dr. K. S. Krishnan Marg, New Delhi 110012, India
e-mail: panjas@nplindia.org

Neelam · S. Panja
Academy of Scientific and Innovative Research (AcSIR), Ghaziabad 201002, India

103

1 Introduction

Time or clock synchronisation is the only activity which solves the problem/ requirement of common notion of time for advanced scientific research and daily life applications such as navigation, banking, defense, power grid management, telecommunications, meteorology *etc*. The requirement of accurate time for the proper functioning of different applications varies from milliseconds to picoseconds or better. Usually designated laboratories from different countries, e.g., NationalMeasurement Institutes (NMIs) are given responsibility to realise and maintain their local time very accurately and keep it traceable to the international reference time realised by International Bureau of Weights and Measure (BIPM) through the weighted average of large numbers of atomic clocks (~500 atomic clocks). The reference time generated at BIPM is called Universal Coordinate Time (UTC) [1]. UTC is not a physical clock, but it is a 'paper clock' and the relative performances of each contributing clocks along with all other information are published through the weekly (*UTC-rapid*) and monthly (*Circular-T*) bulletin of BIPM. [2]. Along with maintenance of accurate time, NMIs have a responsibility to transfer time to different organisations or technological sectors for fulfilling their requirement with desired level of accuracy.

CSIR-National Physical Laboratory (CSIR-NPL) is the NMI of India and realises local universal coordinated time. i.e., UTC (NPLI) with a timescale consisting of an ensemble of Cesium atomic clocks, Hydrogen Maser and other measuring devices. Indian Standard Time (IST) is realised by adding 5 h 30 min to UTC (NPLI). There are several research and development activities in progress for transferring accurate time or synchronising clocks for providing common reference time to different organisations or sectors across the country. Some of the most commonly used network-based time transfer methods are (i) Network time protocol (NTP) and (ii) Precision time protocol (PTP). However, for transferring time and frequency signal very accurately over very long distances, satellite-based time transfer methods, e.g., Common View and All in View Global Navigation Satellite System (CVGNSS and AVGNSS) or Two-way satellite time and frequency transfer (TWSTFT) are used [3]. Optical fibre-based time transfer methods provide most secure options along with the highest level of accuracy in time transfer. The present article discusses about establishment and analysis of White RabbitPrecision Time Protocol (WRPTP) [4, 5] based optical fibre link for transferring time with sub-nanoseconds accuracy. White Rabbit (WR) time synchronisation technique is an ethernet based time transfer technique which uses optical fibres as a physical media for transferring time to remotely located clocks.

It is very well known that the fundamental unit of a clock is an oscillator and a counter which counts the oscillations of that oscillator. In most cases, quartz crystal oscillators are used as a local oscillators in the clock. Some of the improved versions of quartz crystal oscillators are oven-controlled crystal oscillators (OCXO) and temperature-compensated crystal oscillators (TCXO). The resonance frequency of these crystals depends on its shape and size. Its frequency is sensitive to environmental conditions like temperature, humidity, pressure and mechanical vibrations.

White Rabbit devices also use the quartz oscillator as its internal oscillator for generating frequency signals. To increase the stability and accuracy of these internal local oscillators, it must be locked to some external reference clock having higher accuracy and stability *e. g.,* Cs or Rb atomic clocks. WR devices can be locked to an external reference clock through 10 MHz and 1 PPS (one pulse per second) signals or can also be operated in the absence of any external reference clock signal, in that case, its oscillator run freely. The WR devices are called as 'Grandmaster' when they are driven by an external reference signal (10 MHz and 1 PPS) while they are called as 'Master' when their oscillators run freely. In WR network, a hierarchy is followed in the Master-Slave sequence (Fig. 1). WR device act as master when it sends synchronisation messages to the nodes that are lower in hierarchy and acts as slave when they receive synchronisation message from the nodes that are higher in the hierarchy. Grandmaster is acting as 'Master' in hierarchy for both nodes namely Node1 and Node2 in Fig. 1. While Node1, and Node2 are slaves for Grandmaster. Once, these nodes synchronise their time with reference clock with the help of Grandmaster, they can synchronise the nodes in lower hierarchy and act as master. Here (Fig. 1), Node2 acts as a master for Node3. Same process continues, till all the nodes in the WR network, synchronise their time and frequency with reference atomic clock.

To synchronise the frequency or achieve syntonisation of the internal oscillators of the Nodes in the WR network, synchronous ethernet (Sync-E) [6] technique is followed. Through this technique, clock signals are sent to slave node by encoding data from the master node. At slave node, with the help of clock-data recovery circuit, data is separated from the clock signal and phase locked loop (PLL) is used to lock the internal oscillator with the recovered clock signal. This process continued to

Fig. 1 Schematic diagram of White Rabbit-Network
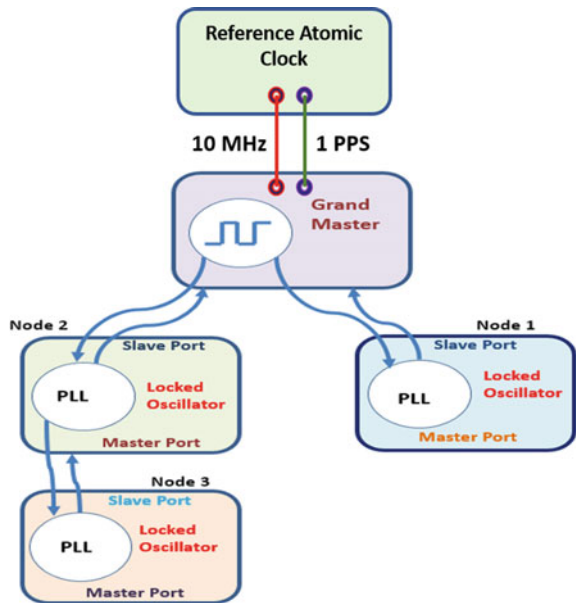
achieve frequency synchronization in the whole WR-network. In this way, frequency is transferred and syntonisation is achieved. After frequency syntonisation, the next step comes to achieve time synchronization in the WR network.

For achieving time synchronisation between the two clocks, the most fundamental requirement is to estimate the link delays and clock offset between them. WR technique follows two–way communication for estimating link delays and clock offsets. It implements wavelength division multiplexing (WDM) for transferring and receiving data through a single strand of optical fibres at different communication wavelength. So, asymmetry arises due to difference in length of optical fibres used separately for transmitting and receiving data during two–way communication can be avoided. The expanses of optical fibres also reduced by 50% by using WDM [7] technique. WR technique estimates the asymmetry in link delays arising due to the different communication wavelengths and considered this delay during time synchronisation process.

This technique estimates link delay between the clocks in two steps:

(1) Coarse link delay

Coarse link delay is estimated by following well known standard protocol called precision time protocol (PTP). During this process, timestamps of transmitting and receiving data at the Master and Slave port are exchanged between master and slave to find out one way link delay from master to slave and clock offset between them. But the limitation of PTP is that it cannot record timestamps with better than the resolution of 1 cycle, which is 8 nsec. The frequency of an oscillator is 125 MHz which is used to timestamp the events. To synchronise clocks with better than nanoseconds accuracy, fine link delay must be estimated.

(2) Fine link delay

Digital dual mixer time difference (DDMTD) [8] technique is used for measuring the phase offset between transmitted and recovered clock signals with sub-nanosecond uncertainty. During this process, firstly frequency of the transmitted and recovered clocks is down-converted by mixing the signal with a slightly lower frequency signal and filtering out the higher frequency component part. Since the frequency has been down-converted, the same phase difference in terms of time offset can be measured with better accuracy. In this way, a fine delay is estimated.

After compensating the total link delay i.e., coarse, and fine delay together, time synchronisation with better than nsec accuracy is achieved within the WR network [9].

In our studies at CSIR-National Physical Laboratory (CSIR-NPL), we have used White Rabbit Lite Embedded Nodes (WRLEN) for establishing WR network based optical fibre link for transferring time with better than nsec accuracy. The impediments associated with WRLEN has been discussed briefly and after that solution of these problems have also been discussed.

Impediments associated with WRLEN based optical fibre links

- When WRLEN is configured in Grand-Master mode, it locks its oscillator with a reference signal (10 MHz and 1 PPS). But, every time, when it is locked, it shows a different time offset between the reference clock and WRLEN 1 PPS signal in the range of a few nanoseconds. Once it locks, this time offset remains the same throughout its operation.
- WRLENs have been found temperature sensitive [10].
- The WRLENs fixed transmission, reception, and asymmetric delay need to be estimated for transceivers operating at other than communication wavelength 1490/1310 nm. At this communication wavelength, WRLENs phase compensation algorithm work properly. The variation in time offset measurement with temperature variation around optical fibres by ~30°C was not noticeable for 10 km long optical fibres. But, when transceivers of other wavelength are used, the variation in time offset with temperature variation around optical fibres are considerable.

To solve all the above-mentioned problems and transfer precise time with better than nanosecond accuracy, a feedback optical fibre along with a phase and frequency offset generator can be incorporated in the WR link to compensate for phase variations and also to improve the stability of the optical fibre link.

2 Experimental Setup

White Rabbit Lite Embedded Nodes (WRLEN, Seven Solutions) and pair of 30 km long single mode optical fibre spools have been utilised for establishing 30 km long time transfer link and the pictorial representation of the experimental setup has been shown in Fig. 2. Bidirectional small form factor pluggable transceivers operating at wavelength 1550/1310 nm have been used for transmitting and receiving data through the single strand of optical fibres. It is important to mention here that, the transmitting wavelength, i.e., 1550 nm for this SFPis different from the default transmitting wavelength, i.e., 1490 nm for which TX, RX and alpha values have been set in White Rabbit nodes. WRLENs follow White Rabbit Precision Time Protocol (WRPTP) and use these parameters during the estimation and compensation of the phase variations that arise due to temperature variations around optical fibres. At 1550/1310 nm wavelength, variation in time offset is noticeable with the temperature variation around optical fibres of length 30 km. Cs atomic clock(5071A, Hewlett Packard) is used for configuring WRLEN1 in Grandmaster mode by providing 10 MHz and 1 PPS signal through a high-resolution phase and frequency offset generator (HROG-10. Spectra-Dynamics). Time interval counters (TIC, 53230A, Keysight) have been used for measuring time offset between two clocks. A specially designed heating chamber has been utilised for varying the temperature around the optical fibres in a controlled manner.

To compensate for the phase variations that arise due to temperature variation around the optical fibres, and enhance the stability and accuracy of the optical fibre
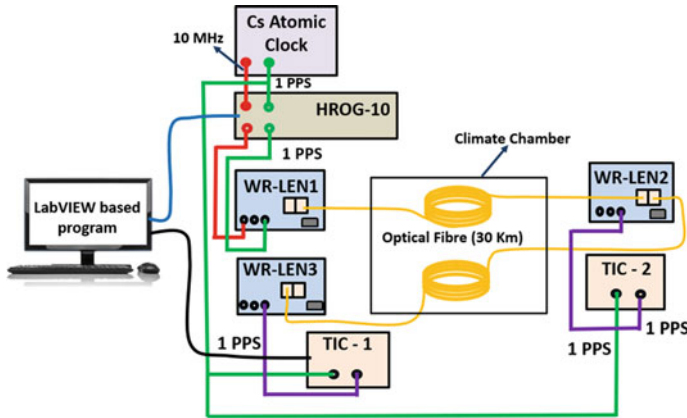
Fig. 2 Schematic diagram of the experimental setup for transferring precise time over 30 km long WR network based optical fibre link

link, TIC and HROG-10 have been interfaced and integrated with a graphical user interface (GUI). The algorithm has been developed to estimate phase variations that arises at remotely located clock (WRLEN2) from the time offset measurement recorded through TIC-1 at central location between Cs atomic clock and WRLEN3. The estimated amount of phase variation is introduced utilising HROG-10 to compensate phase variations arising at remotely located clock (WRLEN2) in real time.

3 Results and Discussion

This section presents the analysis of the time offset variation with the temperature variation around optical fibres (30 km) without introducing phase compensation and with introduction of phase compensation respectively. Firstly, time offset variation at remotely located clock WRLEN2 has been recorded without utilising feedback optical fibre loop and without introducing phase corrections. It has been observed that there is fixed time offset ~58.3 nsec between Cs atomic clock and WRLEN2 at room temperature (24°C), which arises during locking of WRLEN1 with Cs atomic clock. After that temperature around optical fibres has been varied by ~30 °C in steps of 15 °C. The variation in time offset was measured to be ~250 ps with the temperature variation around optical fibres by 30 °C (Fig. 3).

In order to minimise the phase variations arises due to temperature variations around the optical fibres, feedback optical fibre link between WRLEN2 and WRLEN3 has been utilised to measure the variations arising due to temperature variation. The measurement in time offset between Cs atomic clock and WRLEN3 shows the twice phase variations value arises due to temperature variations at the
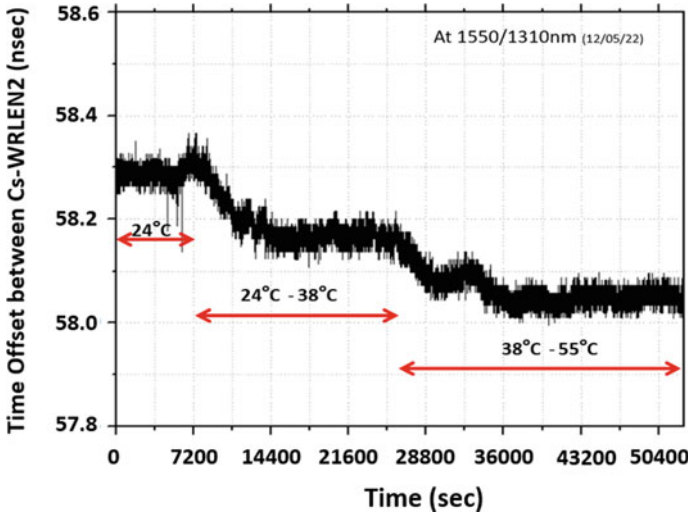
Fig. 3 Time offset variation between Cs atomic clock and WRLEN2 with temperature variation around optical fibres (30 km)

remotely located clock. So, half of the value of total phase variation, measured at central location between Cs atomic clock and WRLEN3, is fed to the HROG-10 to compensate phase variations at remotely located clock WRLEN2.

The time offset variations after introducing required phase corrections have been shown in Fig. 4. The peak-to-peak fluctuation in time offset between Cs atomic clock and WRLEN2 is within 150 ps.

We can see (Fig. 5) that nearly 200 ps phase variations have been compensated and the stability of the link has been enhanced.

Frequency and time stability of the established optical fibre link have been estimated by calculating modified Allan deviation and Time deviation. The value of modified Allan deviation is reaching 1.22 e^{-15} at integration time of 16,384 s and the minimum value of time deviation is 2.34 ps at integration time of 32 s (Fig. 6).

4   Conclusions

A 30 km long WR–PTP based optical fibre link has been established for transferring precise and secure time with better than nanoseconds accuracy. After introducing active phase compensation, the time synchronisation uncertainty remains within 150 ps even under varying temperature conditions (~35 °C) and frequency stability of the time transfer link is reaching 10^{-15} within several hours of integration time.
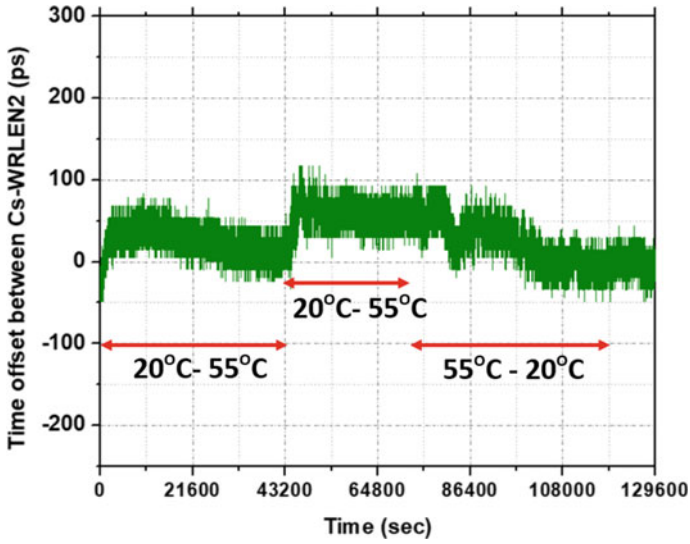
Fig. 4 Time offset variation under varying temperature conditions (by 35 °C around optical fibres), between Cs atomic clock and WRLEN2 after introducing phase corrections for 30 km long optical fibres
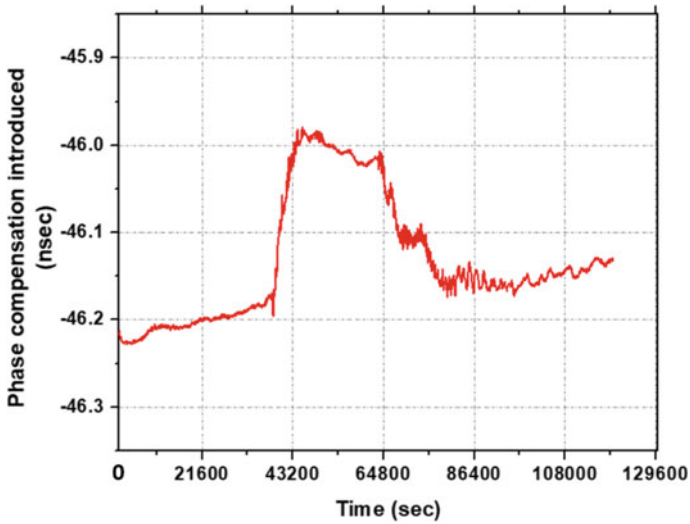
Fig. 5 Amount of phase corrections (in terms of Time offset) introduced for compensating phase variations arises at the remote location due to temperature variations around 30 km long optical fibres
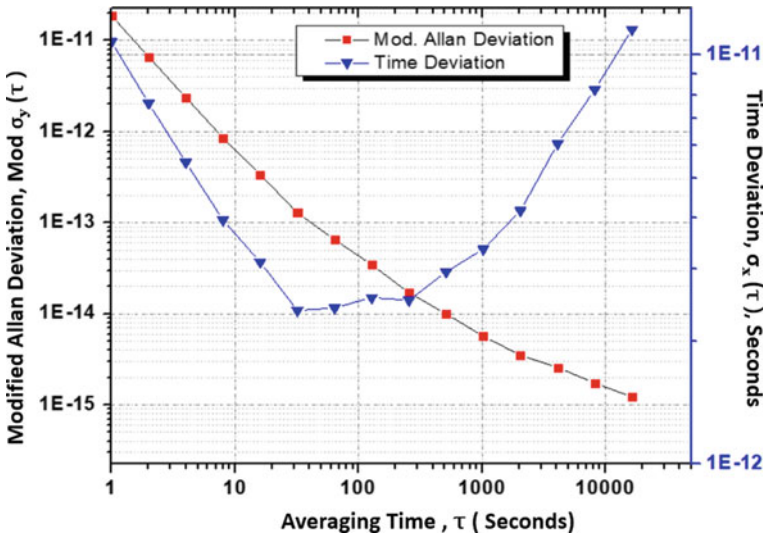
Fig. 6 Frequency and time stability of the 30 km long phase stabilised optical fibre-based time transfer link

References

1. Panfilo G (2016) The coordinated universal time. IEEE Instrum Meas Mag 19(3):28–33
2. Petit G et al (2012) UTCr: a rapid realization of UTC. 2012 European Frequency and Time Forum, pp 24–27. https://doi.org/10.1109/EFTF.2012.6502326
3. Aswal DK (ed) (2020) Metrology for inclusive growth of India. Springer Nature
4. White Rabbit project website, http://www.ohwr.org/projects/white-rabbit/wiki
5. Dierikx EF et al (2016) White rabbit precision time protocol on long-distance fiber links. IEEE Trans Ultrason Ferroelectr Freq Control 63(7):945–952. https://doi.org/10.1109/TUFFC.2016.2518122
6. Hann K, Jobert S, Rodrigues S (2012) Synchronous ethernet to transport frequency and phase/time. IEEE Commun Mag 50(8):152–160. https://doi.org/10.1109/MCOM.2012.6257542
7. Bergano NS, Davidson CR (1996) Wavelength division multiplexing in long-haul transmission systems. J Lightwave Technol 14:1299–1308
8. Moreira P, Alvarez P, Serrano J, Darwezeh I, Wlostowski T (2010) Digital dual mixer time difference for sub-nanosecond time synchronization in Ethernet. In: 2010 IEEE IFCS, pp 449–453, August 2010. https://doi.org/10.1109/FREQ.2010.5556289
9. Neelam, Olaniya MP, Rathore H, Sharma L, Roy A, De S, Panja S. Precise time synchronization and clock comparison through a white rabbit network-based optical fiber link. https://doi.org/10.1029/2020RS007232
10. Neelam, Rathore HK, Sharma L, Roy A, Olaniya MP, De S, Panja S. Studies on temperature sensitivity of a white rabbit network-based time transfer link. https://doi.org/10.1007/s12647-021-00461-1

Variation of Atmospheric Boundary Layer Height and Application of Forward Selection Technique during Diwali

Nishant Kumar, Kirti Soni, and Ravinder Agarwal

Abstract During the Diwali festival in the Delhi region, the Atmospheric Boundary Layer (ABL) height is examined in relation to pollution (caused by firecrackers) and climatic conditions. Air quality, ABL height, and Ventilation Coefficient (VC) have all been studied over the past four years as a result of firecracker use. By employing a forward selection technique, we have determined the most important factors that influence the ABL's height. The primary goal of this study is to discover the air pollution parameter that has the greatest impact on the ABL height. SOund Detection And Ranging (SODAR) has become a key tool for the continuous monitoring of ABL height. On Diwali in 2014–2017, the daily average ABL height was 300, 660, 308, and 263 m, respectively. These year's heights were about 25, 15, and 6% lower than the comparable Pre-Diwali days in 2014, 2016, and 2017, respectively; nevertheless, they were 15% higher in 2015. Mean comparisons and correlations show that the burning of firecrackers on Diwali contributes significantly to the amount of particulate matter and gaseous pollutants in the atmosphere. Using a forward selection strategy to choose the most influential parameters, the strongest correlations between meteorological variables and pollution concentrations were found. Temperature, relative humidity, wind speed, NO_2, and SO_2 input variables were selected based on their importance in 2014–2017 using a forward selection technique.

Keywords Air quality · Atmospheric boundary layer · Diwali · Firecrackers · Air pollution · SODAR structure · Forward selection technique

N. Kumar · K. Soni
Water Resources Management and Rural Technologies Division, CSIR—Advanced Materials and Process Research, Bhopal, India

N. Kumar · R. Agarwal (✉)
Electrical and Instrumentation Engineering Department, Thapar Institute of Engineering and Technology, Patiala, Punjab, India
e-mail: ravinder_eeed@thapar.edu

1 Introduction

Diwali is the most important and big festival, celebrated all over India. During the festival, firecrackers create a lot of pollution in the environment resulting decrease in Atmospheric Boundary Layer (ABL) height and causing negative effects on human health [1–3]. Diwali is celebrated in the winter months of October/November with the bursting of firecrackers, it has created a health hazard for human beings [4]. Uses of bulk firecrackers emit a large number of pollutants into the atmosphere. The concentrations of SO_2 and NO_2, as well as particulate matter such as PM_{10} and $PM_{2.5}$, have been found about 2–6 times higher during Diwali day and next to Diwali day, when compared with the respective concentration of normal day [5, 6].

Lead, magnesium, salt, nitrate and nitrite are some of the compounds included in firecrackers. These chemicals have an adverse influence on the environment and on human health. This high level of pollutants, which is 8–9 times higher than the statutory norm [7] lingers in the air for around 5–10 days after the event. It has been noted that the firing of firecrackers contributes to a significant level of NO_x and SO_2 emissions [5]. There has been a six-year reduction in life expectancy in Delhi owing to Delhi's air pollution [8]. This is due to an increase in automobile, industrial, as well as firecrackers pollution. The number of respiratory illness cases and pollution-related morbidity and death has also increased [9]. Deaths in Delhi due to particulate matter rose by 2.25% between 1995 and 2015, according to a study by Maji et al. [10]. Seven places in Delhi, including the Council of Scientific and Industrial Research—National Physical Laboratory (CSIR-NPL) New Delhi, have been investigated by Kotnala et al. [11] during the Diwali season (for the year 2017). This has prompted us to investigate how short-term changes in air quality might have a negative influence on the environment (such as a maximum concentration of $PM_{2.5}$ 903 g/m^3 and a lowest concentration of 140 g/m^3) during the event.

The ABL height is an important parameter in weather and climate modelling. The ABL is the lowest part of the atmosphere extending from the ground level to a few hundred metres in the troposphere. The ABL height controls the vertical mixing, concentration, and transformation of the atmospheric pollutants and affects the gases in the lower atmosphere. Air quality measurements are directly related to the ABL and it is an important factor in the formation and dissipation of atmospheric pollutants [12–14]. There are several instruments for the measurement of the ABL height like Balloon, RASS, Radiosonde, LIDAR, etc. According to the working principle of the instruments, these are divided into two categories in-situ system and remote sensing system. In this study, the ABL height is measured with SOund Detection And Ranging (SODAR). It is a real-time remote sensing device used to measure the ABL height in real-time. SODAR is a significant instrument that shows how the atmosphere of the ABL is different [14–16].

Studies on air pollution have shown that there are direct correlations between the amount of air pollution and the height of the ABL [1, 17]. The ABL height measured by SODAR can be used as a diagnostic tool for managing air quality. For example, the SODAR structure at different levels of pollution, such as good air quality, bad air

quality, or the worst air quality, can be used to find out which area has the best, worst, or most polluted air. The Ventilation Coefficient (VC) may also be used to determine how much pollution a certain region can take [18]. A SODAR technique has made a big difference in meteorology studies of air pollution, and the data is used in models to predict how pollution will spread [19]. Du et al. [1] found that $PM_{2.5}$, PM_1, and PM_{10} concentrations have a negative relationship with ABL Height. Mahalakshmi et al. [17] used ABL and wind speed in different seasons to calculate the VC and found that it plays a big part in how pollutants move around. Tang et al. [19] found that the ABL Height is the most important factor in how atmospheric particles move around.

It is necessary to investigate and analyse the air quality and ABL height during the Diwali festival in Delhi and the North Capital Region (NCR) to understand how firecracker activity affects these variables. Diwali celebration in Delhi is a unique opportunity to study the impact of a certain parameter on ABL Height. For the past four years, this study will provide useful information about the urban air quality in Delhi throughout the Diwali time (2014–2017). Particulate Matter ($PM_{2.5}$), trace gases (NO_2, SO_2, and CO), and daily and temporal data on ABL height, wind speed, relative humidity, and temperature were all taken into account during the investigation, as were pre- and post-five-day periods under various pollution loading settings.

2 Data Collection and Methodology

2.1 Study Location and Its Meteorological Condition

The study location of Delhi is at the intersection of 77.12° E longitude and 28.64° N latitude. As per the topography, Delhi is located on the western fringes of the Indo-Gangetic Plains. The climate of Delhi experiences extremes of weather due to its geological location [20]. Delhi is the capital of India and the big metropolitan city having a population around 27 million. The climate of Delhi has been influenced by land position, temperature variation from maximum 48 °C in summer to minimum 5 °C in winter [2, 20].

2.2 Measurement of ABL, Meteorological Parameters, and Pollutants

With a carrier frequency of 2.25 kHz, a vertical resolution of 20 m, and a vertical range of 40–3000 m, the Monostatic SODAR has been constantly operating for 5 decades in Delhi [15, 16]. One sound cycle (T&R) is completed at every 6 s with 100 ms pulse duration, electrical transmitting power up to 50 watts and acoustic power of 10 watts. The SODAR antenna is a parabolic dish 1.22 m in diameter and

the beam width is 150. In SODAR highly directional short bursts of acoustic signals are transmitted into the atmosphere and these signals are reflected back due to inhomogeneity in the atmosphere [21, 22]. To estimate an online echogram representation of ABL dynamics based on these reflected signals, the SODAR antenna receives and processes them. The turbulence in the lower atmosphere is captured in the form of SODAR echograms. SODAR sensitivity becomes poor in the daytime as compared to the night time, due to prevailing ambient noise which decreases its probing range. For determining ABL during the daytime, when the plumes are not capped by a stable layer, it establishes the basis of a Holzworth model using radiosonde data for Delhi [22, 23]. The meteorological and concentrations of pollutants data are taken from the Central Pollution Control Board (CPCB) www.cpcb.nic.in.

2.3 *Ventilation Coefficient (VC)*

The VC is an atmospheric dispersion value which gives an indication of the air quality and pollution potential, i.e., the capability of the atmosphere to dilute and disperse the pollutants over a location [24]. It is calculated by the product of ABL height (mixing height) and the average wind speed. For better atmosphere quality, the value of VC is high i.e., the more efficiently the atmosphere is able to dispose of the pollutants [18, 25]. In contrast, the lower value of VCs leads to poor dispersal of pollutants causing stagnation and poor air quality leading to possible pollution-related hazards. A variation in the values of the ABL height and the average wind speed causes a change in the VC. VC is less than 6000 m^2/s in the afternoon hours indicating high pollution potential whereas during morning hours ABL height is less than 500 m which indicates the criteria for the occurrence of high pollution potential [24]. The VC is then computed as:

$$VC = [ABLHeight (M) * MeanWindSpeed (M/s)] \tag{1}$$

3 Result and Discussion

3.1 *Variation of ABL with Meteorological Parameters*

The ABL is positively correlated with temperature and wind speed [14]. During the day, the height of the convective boundary layer rises and falls in response to changes in surface temperature caused by the warming of the ground by solar radiation. Atmospheric convection is controlled by variations in surface temperature, and this has a significant impact on ABL height. Relative humidity, on the other hand, has a negative impact on ABL height when the ABL height drops. As shown in Table 1, the

Table 1 The daily average of meteorological parameters

Year	Day	ABL (m)	Temperature (0C)	Wind speed (m/s)	Relative humidity (%)
2014	22-Oct-14	300	27.79	0.9	61.78
	23-Oct-14	297	28.09	0.74	61.37
	24-Oct-14	327	27.99	0.76	61.7
2015	10-Nov-15	495	25.14	0.89	61.06
	11-Nov-15	660	24.98	1.06	43.49
	12-Nov-15	663	24.52	0.92	46.03
2016	29-Oct-16	286	26.0	0.58	48.04
	30-Oct-16	307	25.45	0.68	62.56
	31-Oct-16	310	24.57	0.63	71.79
2017	18-Oct-17	258	–	0.75	42.42
	19-Oct-17	263	16.06	0.53	46.36
	20-Oct-17	191	–	0.54	50.07

daily averages of meteorological parameters with ABL observed during the Diwali Season can be seen. During the post-Diwali period in 2017, ABL levels were at their lowest (191 m on 20-Oct-17) and their highest mean values in 2015 (663 m on 12-Nov-15). The motivation for the comparison of day before, after and Diwali day is to identify the contribution of crackers burning on air quality.

In addition, existing industries, control plant utilisation of vast scale vehicular exercises and habitually tidy tempest essentially contributed to high air contamination [4, 9]. Air contamination has caused eye irritation, cough, headache and respiratory problem [10]. According to Table 1, the wind speed is greatest in the year 2015 and lowest in the year 2017. Low wind speed is connected with high pollution levels [12]. If the wind direction stays consistent, the region will continue to be exposed to elevated pollution levels throughout 2016. Pollutants disseminate across a vast region when the wind direction changes. Humidity also has a significant impact on ABL height [14]. The humidity level was greatest in 2016 and lowest in 2015.

3.1.1 Determination of Pollution Loading Capacity of the Region

Assimilative capacity of the atmosphere can be determined in terms of the VC. VC of the region can be estimated by using the ABL height and average wind speed. It is an indicator of the pollution loading capacity of the region.

Figure 1 depicts the temporal variation in VC recorded during Diwali celebrations from 2014 to 2017. Figure 1 shows that the overall average value of VC is substantially lower than 6000 m^2/s for each of the four years, indicating that there is a high possibility for contamination across the region [17]. From 2014 through 2017, the year with the highest VC value is 2015. This is due to the high prevailing winds and

Ventilation Coefficient During Diwali
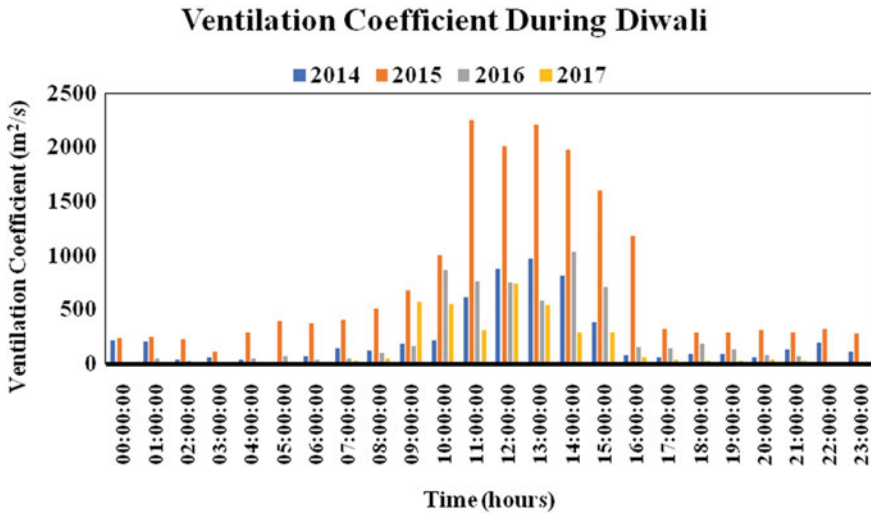
Fig. 1 VC during Diwali day

rain that happened this year. In addition, VC produced the lowest level of value in 2017. Sujatha et al. [24] stated that the dispersion of pollutants is dependent upon many meteorological parameters, the most significant being wind and ABL height that defines the volume of air through which the pollutant is mixed. Therefore, a higher value of VC is observed during the daytime and lowers in the night time, i.e. the pollution loading capacity of the atmosphere is good during daytime and poor in the night time.

3.2 Variation of ABL with Pollutants

To analyse the variation of ABL with the concentration of air pollutants during the Diwali festival period, the SODAR data for ABL and concentration of pollutants data was collected for the years 2014 (18–28 October), 2015 (6–16 November), 2016 (25 October–4 November) and 2017 (14–24 October). Round-the-year SODAR measurements were carried out at the CSIR- NPL, NewDelhi. An hourly average of ABL during Diwali day is in Fig. 2.

Burning of sulphur nitrates, magnesium, aluminium, paper, and mass of other materials contained in firecrackers has produced air pollution during Diwali. The full composition and the relative concentration of the various gaseous vapours and particulate pollutants emitted are not known. However, sulphur oxide, nitrogen oxide, and particulate matter are of special interest, as they are known to be potentially injurious to the respiratory passages and other health effects [26]. The daily average of ABL height and concentrations of $PM_{2.5}$, SO_2, CO, and NO_2 have been calculated
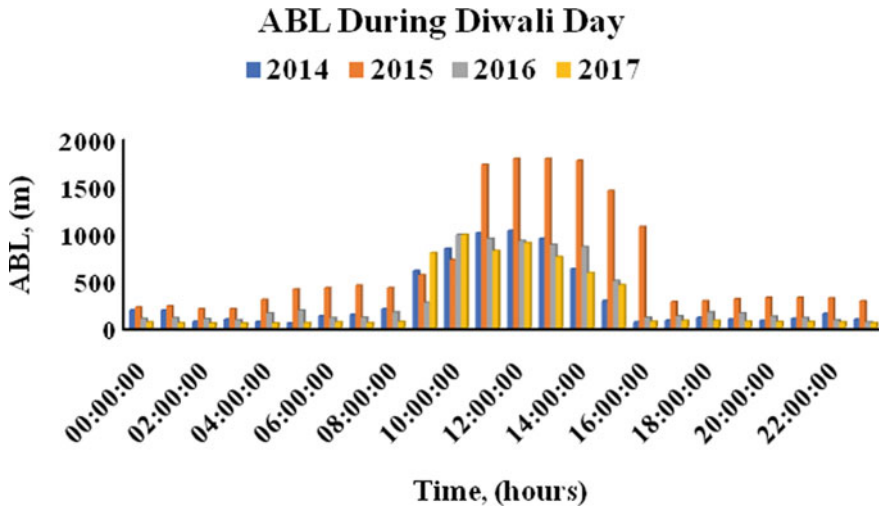
Fig. 2 Hourly average of ABL during Diwali day

for Pre-Diwali Episodes (before five days of Diwali), Diwali day and Post-Diwali Episodes (After five days of Diwali) during the year 2014–2017. The maximum variation of ABL is observed during the year 2015 and minimum variation was observed during the year 2017. On Diwali 2017, daily average values of CO, NO_2, and SO_2 were recorded at 1330, 58.24 and 66 $\mu g/m^3$ respectively, which have also been compared to other years and observed that CO has nearly 1.05, 1.94 and 0.73; NO_2 nearly 1.09, 1.13 and 0.52; and SO_2 nearly 1.43, 3.16 and 1.13 times higher in 2014–2016 respectively. The concentration of $PM_{2.5}$ was noted at 260 $\mu g/m^3$, nearly above 2.55 from 2015 and 0.45 times below from 2016 respectively. Also, the same trend has been observed in the case of Pre-Diwali and Post-Diwali.

Variety of pollutant concentration is not consistent during Diwali periods, its segment varieties demonstrate that these contaminations are influenced by the nearby source, as well as remote sources in different areas. It correlates the relationship between ABL structure and atmospheric pollutants concentration to facilitate the basis for studies to monitor and forecast urban atmospheric environment. The concentration of pollutants has shown higher value during night time when ABL has relatively low, while lower value during the daytime. The ABL has been affected by many factors such as temperature sensible and latent heat fluxes, wind speed and direction, cloud cover and relative humidity [12].

3.3 The Potential Impact of Firecracker on the Health System

The main purpose of this section is to review current literature to attempt to identify the potential differential effect of the firecracker on the respiratory health of healthy

as well as susceptible individuals. The environmental consequences of firecrackers are very serious, ranging from health hazards to human beings, birds and animals to serious accidents. Firecrackers in large amounts aggravate the level of air pollutants and cause significant short-term air quality degradation with a possible impact on human health [27]. The pollution induces disposed individuals to develop irritation and information of the respiratory tract and episodes of cough and wheezing [28].

Due to firecracker, respiratory health issues have increased, with a 30–40% increase in the cases of wheezing, exacerbation of bronchial asthma and bronchitis [29]. Also, firecrackers were found to decrease peak expiratory flow rate and increase daily symptom and medication use. Gupta et al. [30] reported the effects of air pollution on human health and practical measures for the prevention of Iron. Several types of diseases are associated with immune system dysfunction affected by poor air quality. There is a 100% rise in emergency department visits around Diwali owing to air pollution, according to publications [31]. A large increase in enrolment from both rural and urban areas was reported after Diwali. There is increasing recognition of the detrimental effect of urban air pollution as compared to rural air pollution on human health both in the long and short-term. Rizwan et al. [9], Maji et al. [10], Gouder and Montefort [28] initiated an observational study with the aim of finding out the impact of air pollution during Diwali festival in patients having respiratory illness.

3.4   Forward Selection Method

Sections 3.1 and 3.2 concludes that the ABL height is dependent on different parameters. Many authors [12, 14, 19] also mentioned the correlation between ABL height, meteorological parameters, and pollutants concentration. According to Stull [12], the diurnal cycle of temperature, humidity, pollutant concentrations, and winds is driven by ABL height physics and dynamics. In this section, the most dominant correlation between ABL height and weather parameters; and pollutants concentration is determined using a Forward Selection (FS) method.

This technique has been used effectively to create a variety of reliable prediction models [32, 33]. This method is based on a linear regression model. For a small number of sample covariates (N), a prediction model has been selected by which certain measures such as CVE (Cross Validation Error) and RMSE (Root Mean Square Error) are computed for given subgroups of predictors [34]. When N has very large, the computational content has been increased very rapidly. Therefore, to overcome this problem, one of the method is FS method, which is a well-defined step by step algorithm [35]. The following approach was used in this study to discover the optimum subsets for the relationship between ABL height and 7 input factors (meteorological and pollutants data).

Step 1: Choose an independent and dependent variable and Make correlation with independent variable and dependent variable

$$R = \frac{n(\sum xy) - (\sum x)(\sum y)}{\sqrt{\left[n(\sum x^2) - (\sum x)^2\right]}\sqrt{\left[n(\sum y^2) - (\sum y)^2\right]}} \tag{2}$$

Step 2: Find the independent variable with the highest squared correlation with the dependent variable and arrange in decreasing order

Step 3: Fit k−1 different regressions using each of the remaining variables separately

Step 4: Record the incremental changes in R2 and Select the variable with the highest R2 meeting this criterion (R2 increment is <5%)

Step 5: Stop when no variable satisfies this criterion.

A linear model is developed using the best-correlated subset of inputs. The input candidates are implemented into the model one by one according to the algorithm (Sect. 2). For evaluation of modelling goodness, correlation coefficient (R2) is used. Finally, input variables with the most significant effect on output are selected and other variables are removed. Results of FS method are presented in Table 2 where 5, 6, 3 and 5 inputs according to their importance are selected as input variables in the years 2017, 2016, 2015 and 2014 respectively. Considering the importance of daily ABL height in the atmosphere of Delhi, FS method improves the prediction capability of models. It reduces output error and calculation time due to fewer input variables.

Noori et al. [38] found that FS-based models were more accurate than gamma-based models. The burning of firecrackers is the primary source of pollutants during the Diwali season, according to the significant increase in pollutants (CO, NO_2, SO_2, and $PM_{2.5}$), while Table 2 makes it abundantly clear that the pollutants concentration and meteorological parameters are correlated with ABL height. Additionally, it has been noted that temperature is one of the most important variables influencing ABL height since it appears in every FS result year after year. Table 2a–d makes it clear that in 2017 (Temp, RH, CO, SO_2, and WS) was the most dominant subset, in 2016 (Temp, CO, RH, WS, SO_2, and NO_2) was the same, in 2015 (Temp, RH and NO_2) was the same, and in 2014 was the same (Temp, RH, CO, NO_2, and WS). An FS approach was used to identify the most affecting factors, and the most significant association between ABL height and meteorological parameters as well as pollutants concentration was found. Results of the FS method, using five input variables (temperature, relative humidity, wind speed, NO_2, SO_2) selected based on their significance in the years 2014–2017.

4 Conclusion

The biggest and most significant celebration is Diwali, which is observed across India. Fireworks are a major source of environmental pollution during celebrations, which lowers the height of the Atmospheric Boundary Layer (ABL) and harms

Table 2 Result of forward selection method

2017 Sub-table—2(a)							
Temp							0.472
Temp	RH						0.494
Temp	RH	CO					0.529
Temp	RH	CO	SO$_2$				0.534
Temp	**RH**	**CO**	**SO$_2$**	**WS**			**0.561***
Temp	RH	CO	SO$_2$	WS	PM$_{2.5}$		0.561
Temp	RH	CO	SO$_2$	WS	PM$_{2.5}$	NO$_2$	0.591
2016 Sub-table—2(b)							
Temp							0.384
Temp	CO						0.448
Temp	CO	RH					0.486
Temp	CO	RH	WS				0.517
Temp	CO	RH	WS	SO$_2$			0.561
Temp	**CO**	**RH**	**WS**	**SO$_2$**	**NO$_2$**		**0.576***
Temp	CO	RH	WS	SO$_2$	NO$_2$	PM$_{2.5}$	0.574
2015 Sub-table—2(c)							
Temp							0.522
Temp	RH						0.528
Temp	**RH**	**NO$_2$**					**0.653***
Temp	RH	NO$_2$	PM$_{2.5}$				0.654
Temp	RH	NO$_2$	PM$_{2.5}$	CO			0.652
Temp	RH	NO$_2$	PM$_{2.5}$	CO	WS		0.653
Temp	RH	NO$_2$	PM$_{2.5}$	CO	WS	SO2	0.653
2014 Sub-table—2(d)							
Temp							0.349
Temp	RH						0.35
Temp	RH	CO					0.427
Temp	RH	CO	NO$_2$				0.403
Temp	**RH**	**CO**	**NO$_2$**	**WS**			**0.464***
Temp	RH	CO	NO$_2$	WS	SO$_2$		0.466

*and _ denotes After this value, a variation of R^2 is negligible change (<5%) and thus, inputs related to this value are selected; Temp-Temperature; RH-Relative Humidity; WS-Wind Speed

human health. To understand how firecracker activity influences environmental variables during the Diwali festival in Delhi and the North Capital Region (NCR), it is required to examine the air quality and ABL height. In this study, Pre-Diwali, Diwali and Post-Diwali variations in Delhi's ABL, as well as other meteorological variables and pollutants, were analysed from 2014 to 2017. Particulate matter concentrations in

2017 were 1.14, 2.52 and 1.16 times higher than they were in 2014, 2015, and 2016. The pollution levels were found higher at night when the ABL height was low, and lower during the day when the ABL height was higher. Due to the emission and deposition of particulate matter and gas pollutants, firecrackers had a significant influence on ambient air quality during the Diwali festival. The most dominant relationship between ABL height and weather parameters, as well as pollutants concentration, was determined using the forward selection technique. The highly influencing parameter for ABL height was successfully selected. With this method, it was also possible to pinpoint exactly which parameter is to impact for the excessive pollutant loading found within ABL. As a result, this study argued for a denser network of monitoring stations in Indian cities to better quantify ABL exposure to air pollutants during the Diwali festival period.

References

1. Du C, Liu S, Yu X, Li X, Chen C, Peng Y, Dong Y, Dong Z, Wang F (2013) Urban boundary layer height characteristics and relationship with particulate matter mass concentrations in Xi'an, central China. Aerosol Air Qual Res 13(5):1598–1607
2. Peshin SK, Sinha P, Bisht AM (2017) Impact of Diwali firework emissions on air quality of New Delhi, India during 2013–2015. Mausam 68(1):111–118
3. Ambade B (2018) The air pollution during Diwali festival by the burning of fireworks in Jamshedpur city, India. Urban Clim 26:149–160
4. Tiwari S, Chate DM, Srivastava MK, Safai PD, Srivastava AK, Bisht DS, Padmanabhamurty B (2012) Statistical evaluation of PM10 and distribution of PM1, PM2.5, and PM10 in ambient air due to extreme fireworks episodes (Deepawali festivals) in megacity Delhi. Nat Haz 61(2):521–531
5. Yerramsetti VS, Sharma AR, Navlur NG, Rapolu V, Dhulipala NC, Sinha PR (2013) The impact assessment of Diwali fireworks emissions on the air quality of a tropical urban site, Hyderabad, India, during three consecutive years. Environ Monit Assess 185(9):7309–7325
6. Saxena P, Srivastava A, Verma S, Singh L, Sonwani S (2020) Analysis of atmospheric pollutants during fireworks festival 'Diwali' at a residential site Delhi in India. In: Measurement, analysis and remediation of environmental pollutants. Springer, Singapore, pp 91-105
7. National Ambient Air Quality Standards (NAAQS), Notification 18th Nov (2009) Central Pollution Control Board. SO 384(E) and SO 935(E)
8. Khafaie MA, Yajnik CS, Salvi SS, Ojha A (2016) Critical review of air pollution health effects with special concern on respiratory health. J Air Pollut Health 1(2):123–136
9. Rizwan SA, Nongkynrih B, Gupta SK (2013) Air pollution in Delhi: its magnitude and effects on health. Indian J Commun Med: Off Publ Indian Assoc Prevent Soc Med 38(1):4–8
10. Maji KJ, Dikshit AK, Deshpande A (2017) Disability-adjusted life years and economic cost assessment of the health effects related to PM 2.5 and PM 10 pollution in Mumbai and Delhi, in India from 1991 to 2015. Environ Sci Pollut Res 24(5):4709–4730
11. Kotnala G, Kumar M, Sharma AK, Dhaka SK, Gadi R, Ghosh C, Saxena M et al (2021) Variations in chemical composition of aerosol during Diwali over mega city Delhi, India. Urban Clim 40:100991
12. Stull RB (2012) An introduction to boundary layer meteorology, vol 13. Springer Business Media. eBook ISBN 978-94-009-3027-8, https://doi.org/10.1007/978-94-009-3027-8
13. Helmis CG, Sgouros G, Tombrou M, Schäfer K, Münkel C, Bossioli E, Dandou A (2012) A comparative study and evaluation of mixing-height estimation based on sodar-RASS, ceilometer data and numerical model simulations. Bound-Layer Meteorol 145(3):507–526

14. Kumar N, Soni K, Garg N, Agarwal R, Saha D, Singh M, Singh G (2017) SODAR pattern classification and its dependence on meteorological parameters over a semiarid region of India. Int J Remote Sens 38(11):3466–3482

15. Aggrawal SK, Singal SP (1980) A Study of Atmospheric Structure using Sodar in relation to Land and Sea Breezes. Bound Layer Met 18:361–371

16. Gera BS, Raghavendra T, Singh G, Ojha VK, Joginder M, Neha G, Gupta NC (2011) Instrumentation and computer capabilities for improving Sodar data acquisition. Int J Remote Sens 32(17):4807–4817

17. Mahalakshmi DV, Badarinath KV, Naidu CV (2011) Influence of boundary layer dynamics on pollutant concentrations over urban region—a study using ground-based measurements. IJRSP 40(3):147–152

18. Kumar N, Soni K, Agarwal R, Singh M (2017) SODAR as a diagnostics tool for urban air-quality and health care system. J Acoust Soc India 44(4):213–222

19. Tang G, Zhang J, Zhu X, Song T, Münkel C, Hu B, Schäfer K, Liu Z, Zhang J, Wang L, Xin J (2016) Mixing layer height and its implications for air pollution over Beijing, China. Atmos Chem Phys 16(4):2459–2475

20. Mandal P, Prakash M, Bassin JK (2012) Impact of Diwali celebrations on urban air and noise quality in Delhi City, India. Environ Monitor Assess 184(1):209–215

21. Emeis S, Schäfer K, Münkel C (2008) Surface-based remote sensing of the mixing-layer height—a review. Meteorol Z 17(5):621–630

22. Kumar N, Soni K, Agarwal R (2021) Design and development of SODAR antenna structure. Mapan 36(4):785–793

23. Singal SP, Aggarwal SK (1979) Sodar & radiosonde studies of thermal structure of the lower atmosphere at Delhi. IJRSP 8:76–81. http://nopr.niscair.res.in/handle/123456789/37079

24. Sujatha P, Mahalakshmi DV, Ramiz A, Rao PV, Naidu CV (2016) Ventilation coefficient and boundary layer height impact on urban air quality. Cogent Environmental Science 2(1):1–9

25. Saha D, Soni K, Mohanan MN, Singh M (2019) Long-term trend of ventilation coefficient over Delhi and its potential impacts on air quality. Remote Sens Appl: Soc Environ 15:100234 (1–11)

26. Kaul N, Gupta AB, Khandelwal S, Singh G, Singh V (2017) Impact of exposure to cooking-generated air pollution on human respiratory health: a case study of different microenvironments of India. Hum Ecol Risk Assess Int J 23(8):1989–2001

27. Report Central Pollution Control Board. South Zonal Office. http://cpcb.nic.in/cpcbold/upload/NewItems/NewItem_233_Firecracker%20report,%20Oct.%202017%20Final%20for%20Web%20Ebook.pdf

28. Gouder C, Montefort S (2014) Potential impact of fireworks on respiratory health. Lung India: Off Organ Indian Chest Soc 31(4):375–379

29. Karnena MK, Saritha V, Dwarapureddi BK (2017) doctrines, environmental and health impacts of Deepawali. J Basic Appl Res Int 20(2):113–121

30. Gupta S, Mittal SK, Agarwal R (2018) Respiratory health of school children in relation to their body mass index (BMI) during crop residue burning events in North Western India. Mapan 33(2):113–122

31. Adel G-A, Riahi-Zanjani B, Balali-Mood M (2016) Effects of air pollution on human health and practical measures for prevention in Iran. J Res Med Sci 21:1–12. https://doi.org/10.4103/1735-1995.189646

32. Noori R, Hoshyaripour G, Ashrafi K, Araabi BN (2010) Uncertainty analysis of developed ANN and ANFIS models in prediction of carbon monoxide daily concentration. Atmos Environ 44(4):476–482

33. Noori R, Karbassi AR, Moghaddamnia A, Han D, Zokaei-Ashtiani MH, Farokhnia A, Gousheh MG (2011) Assessment of input variables determination on the SVM model performance using PCA, Gamma test, and forward selection techniques for monthly stream flow prediction. J Hydrol 401(3–4):177–189
34. Eksioglu B, Demirer R, Capar I (2005) Subset selection in multiple linear regression: a new mathematical programming approach. Comput Ind Eng 49(1):155–167
35. Ahmadi A, Fatemi Z, Nazari S (2018) Assessment of input data selection methods for BOD simulation using data-driven models: a case study. Environ Monit Assess 190(4):190–239

Separation of Weak Signals from White Noises Using Python-Based Software

Paramita Guha and Rina Sharma

Abstract Weak signals are available from various applications like, geological explorations, biomedical sciences, military, aerospace and other fields. Detection of such signals is important for further studies. However, these signals are often mixed with high-frequency noises. These noises have very high-frequency, zero expectation value and zero average value. Various fields of control theory like, convolution time domain, frequency domain, and time domain analysis are required along with different nonlinear theoretical tools, like, chaos, stochastic resonance etc. These theoretical algorithms are used to develop an instrument called a lock-in amplifier which has a strong detection ability and high reliability of many weak signals. Before actually developing the amplifier, a simulation model is required to be developed. In this paper, the authors have developed a simulated model for the separation of weak input signals from white noises. For this process, Google Colab notebook and Python software have been used. The main advantage of this work is that the authors have used Python-based software which is open source software and takes very less computer space.

Keywords Digital lock-in amplifier · White noise · Modeling & simulation · Nonlinearity · Google Colab · Open source software

1 Introduction

A lock-in amplifier is based on the fact that the measured signal should not be correlated with the noise. A single channel analog lock-in amplifier can be schematically shown as following (Fig. 1).

Here the measured and reference signals are multiplied to achieve a spectrum after being conditioned. Then the multiplied signal is fed to a low-pass filter so that the unwanted higher frequency signals are filtered out. Finally, the required DC signals

P. Guha (✉) · R. Sharma
CSIR-National Physical Laboratory, Delhi, India
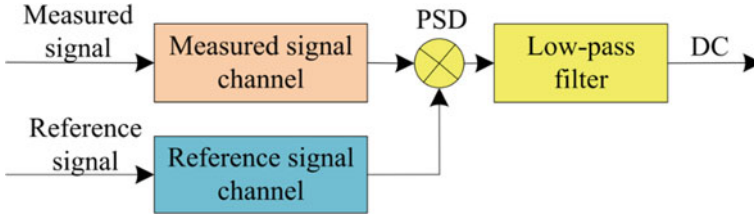e-mail: paramita.guha@nplindia.org

Fig. 1 Schematic view of single channel analog Lock-in amplifier

are obtained. This model is quite simple and highly popular. The basic principle of a typical analog lock-in amplifier is as follows.

Let the measured signal be

$$x(t) = Asin(2\pi f_1 t + \theta_1) + n(t)$$

and the reference signal is given as

$$r(t) = B\sin(2\pi f_2 t + \theta_2)$$

Here, A and B are the amplitudes of the measured and reference signals respectively, f_1 and f_2 are the respective frequencies, whereas, θ_1 and θ_2 are the initial phase angles of them. The noise in the measured signal is given as $n(t)$. The signals are multiplied by phase sensitive detector (PSD) and a by-product signal is achieved.

$$x(t).r(t) = [Asin(2\pi f f_1 t + \theta_1) + n(t)] \times [B\sin(2\pi f_2 t + \theta_2)] = n(t).r(t)$$
$$+ \frac{AB}{2}\cos[2\pi(f_1 - f_2)t + (\theta_1 - \theta_2)]$$
$$+ \frac{AB}{2}\cos[2\pi(f_1 + f_2)t + (\theta_1 + \theta_2)]$$

This signal when passed through a low-pass filter, the higher frequency signals are curtailed and the remaining signal is displayed on the output panel.

$$V(t) = \frac{AB}{2}\cos[2\pi(f_1 - f_2)t + (\theta_1 - \theta_2)] + n\prime(t)$$

Hence, smaller the frequency difference $(f_1 - f_2)$, and the residual noise $n\prime(t)$, more accurate the outputs are. Hence, this model is quite simple and easy to develop. However, there are several disadvantages of an analog lock-in amplifier. The main problems are harmonic rejection, output offsets, limited dynamic reserve, gain error etc.

In due process of time, an analog lock-in detects all of the odd harmonics which makes the system more prone to harmonics. When there is a large noise signal present, the analog PSD measures the signal with an error. The error is caused by nonlinearity

in the multiplication. This error is dependent on noise amplitude, frequency and waveform and can be quite large. This in turn causes large output uncertainty. As the analog PSD multiplies the signal by an analog reference sine wave, the variations in reference amplitude imply directly as a variation in the overall gain. Moreover, analog sine wave generators are susceptible to amplitude drift. For these reasons, a digital lock-in amplifier outperforms its analog counterpart.

2 Literature Review

Weak signals are available from various applications like, geological explorations, biomedical sciences, military, aerospace and other fields [1–3]. Detection of such signals is important for further studies. However, these signals are often mixed with high-frequency noises. Hence, an efficient detection method is required. Various fields of control theory like, convolution time domain, frequency domain, and time domain analysis are required along with different nonlinear theoretical tools, like, chaos, stochastic resonance etc. [4, 5]. These theoretical algorithms are used to develop an instrument called lock-in amplifier which has strong detection ability and high reliability of many weak signals [7, 8]. The relevant products based on these principles are discussed in detail in [9–12]. However, there are several disadvantages of analog lock-in amplifier, viz., harmonic rejection, output offsets, more gain error, limited dynamic reserve etc.

To overcome these disadvantages, digital lock-in amplifiers have been developed [13]. An automatic frequency tracking digital lock-in amplifier based on LabVIEW software has been developed in [13]. This software uses FFT to reduce the mismatch between the measured and reference signals. However, this method has disadvantages of limitations in accuracy, capturing of small discrete frequencies etc. In order to improve these disadvantages, authors in [] have proposed an improved digital lock-in amplifier such that its automatic frequency tracking ability synchronizes the frequency of reference and measured signals.

Although many digital lock-in amplifiers are available in the market, they are costly in nature. Hence, the investigators aim to develop a cost effective, efficient prototype of a digital lock-in amplifier which can be used for experimental purposes. However, before the development of any prototype, its software simulation is important to evaluate the internal parameters of the system. In this paper, a simulated model of digital lock-in amplifier is obtained using open source software.

3 Methodology

The schematic view of the proposed model is shown below (Fig. 2).

Here input voltage will be given from a photoelectric diode. The voltage output of the photo-diode will be amplified before being conditioned. The primary role of the
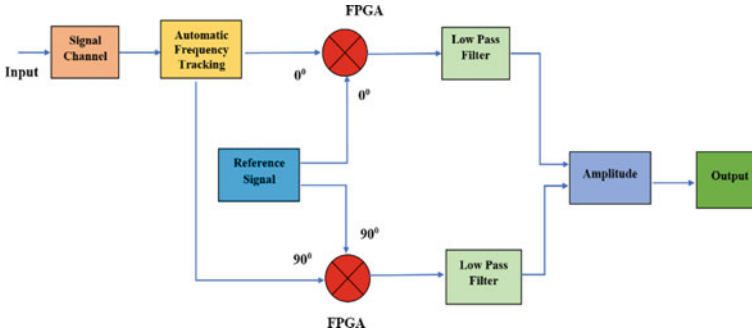
Fig. 2 Block diagram of the proposed model

conditioning circuit of the signal channel is to digitally sample the signal after which the latter is passed through an automatic frequency tracking module. The automatic frequency tracking module will track the frequency of the measured signal accurately so that a quadrature reference signal without frequency error can be generated. After that, the measured and reference signals will be multiplied using integrated circuits called Field Programmable Gate Arrays (FPGAs) to complete the frequency mixing. Then, the AC signals from FPGAs will be passed through two digital low-pass filters so that higher-order frequency signals can be eliminated. Finally, the in-phase and quadrature-phase signals will be added together to get the amplitude of the measured signal without noise.

4   Simulated Model and Results

Before actually developing the amplifier, a simulation model has to be developed using standard software. The authors have developed a simulated model and preliminary results are obtained. Here, Google Colab notebook and Python software have been used. Two signals of 100 Hz and 101 Hz are multiplied and a mixed signal is generated. They are shown in the following Figs. 3, 4, 5.

The resultant mixed signal comprises a weak signal and higher-order noises. The signal is further amplified and shown below (Fig. 6).

Then this is passed through a low-pass filter so that the higher-order noises are eliminated. The input signal without noise is given in Fig. 7. The signal is displayed in two forms, viz. amplitude and phases. They are shown in Fig. 8.

From the above figures, it can be observed that the small weak signals are efficiently separated from the higher-order noises. For implementation of this model, the noises must be white in nature with zero mean, constant variance, and uncorrelated in time. The main advantage of our method is the proposed technique uses open source software and takes very less memory space.

Fig. 3 Signal with 100 Hz frequency **a** Signal with 101 Hz frequency
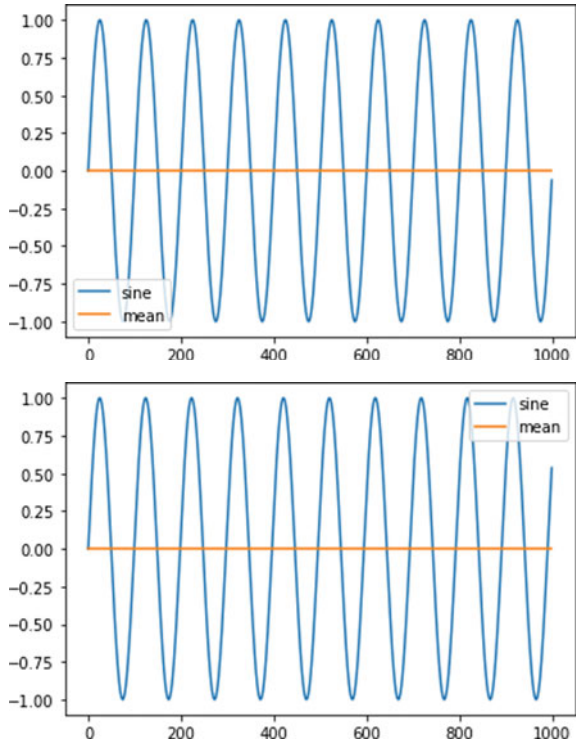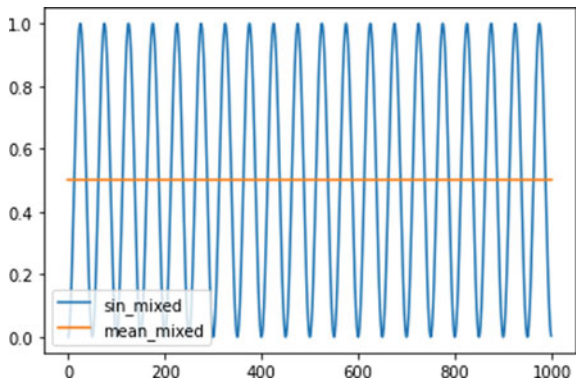
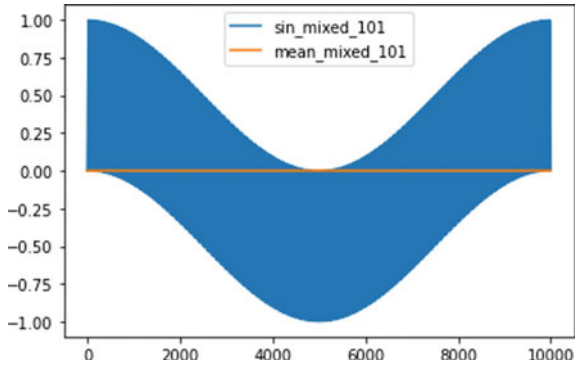**Fig. 4** Derivative of signal with 100 Hz frequency

Fig. 5 Mixed signal after multiplication
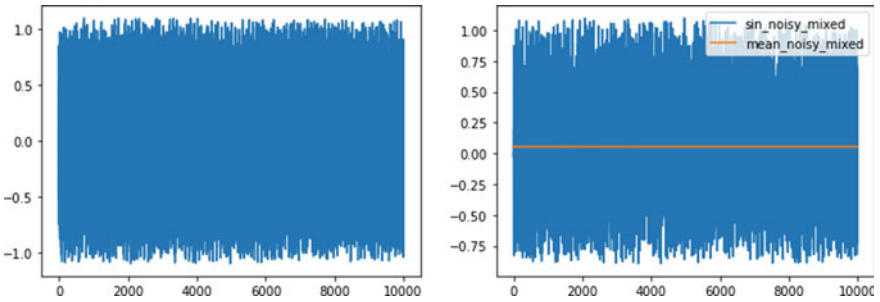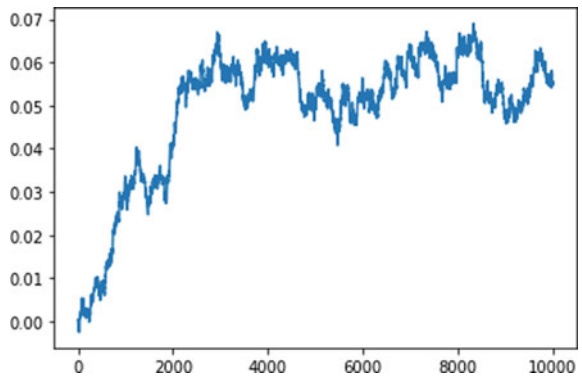

Fig. 6 Amplified signals comprise measured signals and noises

Fig. 7 Measured signal without noise
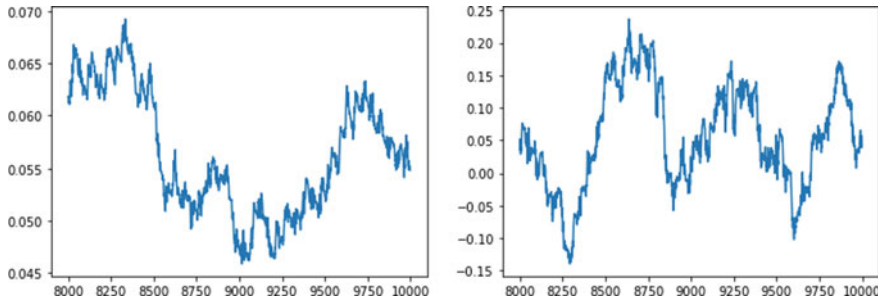
Fig. 8 In-phase and quadrature components of the measured signal without noise

5 Conclusion

In this paper, the authors have developed a simulated model so that extremely weak signals can be separated from the noises. The noises are white in nature which implies that they have zero mean, constant variances and uncorrelated in time. The model uses open source software which saves exchequers costs. For this process, Google Colab notebook and Python software have been used. Two signals of 100 Hz and 101 Hz are multiplied and a mixed signal is generated. The resultant mixed signal comprises a weak signal and higher-order noises. The signal is further amplified. Then this is passed through a low-pass filter so that the higher-order noises are eliminated. In this way, the input signal without noise is separated. The signal has been displayed in two forms, viz. amplitude and phases. The main advantage of this work is that the authors have used Python-based software which is open source software and takes very less computer space. Based on the simulated results, the hardware part of the prototype can be designed.

References

1. Cheng J, Xu Y, Wu L, Wang G (2016) A digital lock-in amplifier for use at temperatures of up to 200 °C. Sensors 16(11):1899
2. Zhang C, Dong H, Wang J, Ge J, Liu H, Yuan Z, Zhu J, Zhang H (2019) A low error rate BCH-based encoder-decoder approach for electromagnetic measurement while drilling system. IEEE Access 7:34599–34608
3. Liao C, Manhard MK, Bilgic B, Tian Q, Fan Q, Han S, Wang F, Park DJ, Witzel T, Zhong J, Wang H, Wald LL, Setsompop K 2019) Phase-matched virtual coil reconstruction for highly accelerated diffusion echo-planar imaging, NeuroImage, vol.accelerated1–302
4. Liu H, Liu Z, Dong H, Ge J, Yuan Z, Zhu J, Zhang H, Zeng X (2019) Recurrent neural network-based approach for sparse geomagnetic data interpolation and reconstruction. IEEE Access 7:33173–33179
5. Liu H, Dong H, Ge J, Liu Z, Yuan Z, Zhu J, Zhang H, (2019) A fusion of principal component analysis and singular value decomposition based multivariate denoising algorithm for free induction decay transversal data, Rev Sci Instrum, 90(3), Art. no. 035116

6. Tan C, Wang J, Li Z (2019) A frequency measurement method based on optimal multi-average for increasing proton magnetometer measurement precision. Measurement 135:418–423

7. Song H, Dong H, Yuan Z, Zhu J, Zhang H, Huang Y (2019) An EEMD based electromagnetic induction method for nondestructive testing of buried metal conductors. IEEE Access 7:142261–142271

8. Zhang R, Chu F, Ran L, Guo J (2011) Weak signal detection method under the strong noise background, In: Proc. Int. Conf. Informat., Cybern.,Comput. Eng., Melbourne, Australia, pp 417–425

9. Macias-Bobadilla G, Rodríguez-Reséndiz J, Mota-Valtierra G, Soto-Zarazúa G, Méndez-Loyola M, Garduño-Aparicio M (2016) 'Dual-phase lock-in amplifier based on FPGA for low-frequencies experiments. Sensors 16(3):379

10. Gervasoni G, Carminati M, Ferrari G (2016) FPGA-based lock-in amplifier with sub-ppm resolution working up to 6 MHz. In: Proc. IEEE Int. Conf. Electron., Circuits Syst. (ICECS), pp 117–120

11. Hu H, Zhong J (2014) The design of the new lock-in amplifier. Electron. Meas. Technol. 37(8):15–18

12. Dorrington A, Kunnemeyer R (2002) A simple microcontroller based digital lock-in amplifier for the detection of low level optical signals. In Proc. 1st IEEE Int. Workshop Electron. Design, Test Appl., pp 486–488

13. Zeng X, Yu M, Wang D (2018) A new probabilistic multi-hop broadcast protocol for vehicular networks. IEEE Trans Veh Technol 67(12):12165–12176

14. Zhang C, Huan L, Jian G, Haobin D FPGA-Based Digital Lock-in Amplifier With High-Precision Automatic Frequency Tracking, IEEE Access, 8, pp 123114–123122

Ozone Formation Potential of Volatile Organic Compounds During November 2021 at an Urban Site of Delhi

Pooja Yadav, T. K. Mandal, and S. K. Sharma

Abstract Volatile organic compounds (VOCs) are the precursor of secondary aerosols and surface ozone in the atmosphere. The present study has been carried out to understand the ozone formation potential (OFP) of different VOCs at an urban site of Delhi in November 2021. Ambient air samples were collected for VOC analysis using GC-FID. The total concentration of VOCs was (80.47 ± 38.77) ppbv. Out of 22 species of VOCs, n-butane has the highest monthly average concentration (14.47 ± 8.78) ppbv. Alkanes were the most abundant (63.80%) followed by alkenes (19.66%), aromatic hydrocarbons (11.25%), and, acetylene (5.29%) respectively. 1 hexene has the highest OFP value (56.11 ppbv) and n-nonane has the lowest OFP (0.54 ppbv) as well as the lowest concentration (0.69 ± 0.15) ppbv. Alkenes have the maximum percentage contribution (56.09%) to total OFP followed by alkanes (24.03%), aromatics (17.73%), and Alkyne (2.15%).

Keywords Surface ozone · Ozone formation potential · VOCs

1   Introduction

Delhi, India's National Capital Territory (NCT), has deteriorating urban air quality as a result of a rise in the number of motor vehicles, commercial activity, and aggressive commercialization [1] particularly post-monsoon and winter. These anthropogenic activities lead to the emission of toxic trace gases like surface ozone, volatile organic compounds (VOCs), nitrogen oxides (NO_x), Sulphur dioxide (SO_2), and carbon monoxide (CO) at an alarming rate [2]. Among all air pollutants, volatile organic compounds (VOCs) have emerged as a significant problem for urban air quality because they participated in the production of secondary aerosols and their role in the formation of surface ozone [3]. The chemical reactions of VOCs with other trace

P. Yadav · T. K. Mandal (✉) · S. K. Sharma
CSIR-National Physical Laboratory, Dr. K. S. Krishnan Marg, New Delhi-110012, India
e-mail: tuhinkumarmandal@gmail.com

Academy of Scientific and Innovative Research (AcSIR), Ghaziabad-201002, India

gases like NO_x in the presence of sunlight give rise to the secondary air pollutant surface ozone and its formation causing problems for living beings all around the world. In addition to serving as precursors for tropospheric ozone, some VOCs' oxidation products can nucleate to create new gas-to-particle phase pollutants on a local, regional, and global level [4].

The earth's atmosphere is exposed to a wide variety of VOCs, each of which reacts differently and through various mechanisms. As a result, the impact of VOCs on the generation of ozone might vary greatly. VOCs' "reactivities" is known as the variations in ozone generation by different VOCs [5].

Anthropogenic VOCs can have a wide range of chemical properties and reactivities, resulting in varying rates of ozone formation. As a result, the decrease in VOC emissions may result in a greater or lesser decrease in ozone than the decrease in another VOC's emissions. The concept of ozone-forming potential seeks to explain how various VOCs' chemical characteristics affect the ozone's photochemical production [6]. The fundamental reason for the discrepancy is the different rates at which these species react in the environment. Species that have longer lifetimes, only a small part of their emissions in urban areas undergo local reactions before being transferred elsewhere. Therefore, it makes a relatively little contribution to ozone generation in metropolitan areas. But for the species which have a shorter atmospheric lifetime, most of their part react at the site of their origin, which leads to higher Ozone formation potential [6, 7].

This study presents the ozone formation potential (OFP) of observed VOCs for the month of November 2021 to understand the role of different VOC species in the formation of surface ozone. The month of November is of special interest because Delhi faces severe air quality during this time period as it gets affected by stubble burning from the nearby states, and fireworks from the Diwali celebration.

2 Methodology

2.1 Sampling Site

The ambient sample has been collected at the CSIR- National Physical Laboratory (28°38′N, 77°10′E; 218 m mean sea level) in November 2021. The sampling location represents a typical urban setting, with heavy traffic on the surrounding highways and agricultural areas to the southwest. In the winter and summer, airmass flows from the northeast to northwest and from the southeast to southwest, respectively, have an impact on this region. Delhi's monthly average temperature ranges from 12.9 °C in the winter (December to February) to 34.8 °C in the summer (March to June) (Fig. 1).
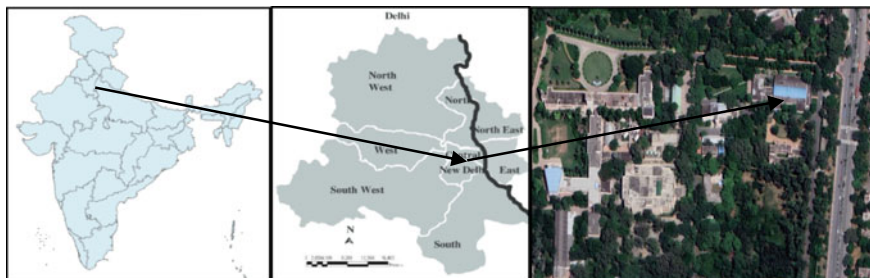
Fig. 1 Sampling site CSIR—National physical laboratory

2.2 Instrumentation

The PerkinElmer Clarus®580 Gas Chromatograph equipped with a dual flame ionization detector, a Turbo Matrix Thermal desorber, and Total Chrom Remote Control Software, was used to measure VOCs. Turbo Matrix Thermal desorber with integrated online sampling accessory is responsible for gathering the sample from the passivated canister for the flame lighting in the detector hydrogen and zero air. At the elevation of approximately 10 m above the surface of the ground, a representative sample of ambient air was collected in passivated stainless steel canisters. These canisters have a 1-L capacity and are prerinsed with nitrogen (purity: 5N). A total of 38 samples were taken during the study period.

The measured VOCs species were 25 which were categorized into 4 groups of hydrocarbons: alkanes (ethane (C_2H_6), propane (C_3H_8), iso-butane (C_4H_{10}), n-butane (C_4H_{10}), iso- pentane (C_5H_{12}), n-pentane (C_5H_{12}), n-hexane, n-heptane (C_7H_{16}), n-octane (C_8H_{18}), n-nonane (C_9H_{20}), n-decane ($C_{10}H_{22}$), n- undecane ($C_{11}H_{24}$), n-dodecane ($C_{12}H_{26}$)); Alkenes (ethylene (C_2H_4), propylene (C_3H_6), 1- butene (C_4H_8), 1- pentene (C_5H_{10}), 1-hexene (C_6H_{12}), isoprene (C_5H_8)); Aromatic hydrocarbons (benzene (C_6H_6), toluene (C_7H_8), ethyl benzene (C_8H_{10}), o- xylene (C_8H_{10}), iso-propyl benzene (C_9H_{12})) and Alkyne (acetylene (C_2H_2)). The sample collection was done during the daytime from 10 am to 5 pm.

2.3 Quantification of OFP

Ozone formation potential (OFP) was quantified to assess VOCs' ability to create O_3 [8]. The OFP was calculated using the following equation:

$$OFP = \sum_{i=1}^{n} C_i \times MIR_i$$

Here, C_i is the mass concentration of species i and MIR_i is the maximum incremental reactivity (MIR) value of species i [7].

3 Results and Discussion

3.1 Concentration of VOCs

The species with the most abundance was ethane > n-butane > isopentane > propane > ethylene > isobutane > n-pentane > 1-pentene > toluene > n-dodecane > 1-butene > n-decane > ethylbenzene > n-hexane > benzene > o-xylene > 1-hexene > n-octane > acetylene > n-undecane > isopropyl benzene > n-nonane. Out of 25 species, the least measured species isoprene, propylene, and n-heptane (presence < 25%) were taken out from the observation. The average concentration, standard deviation, and minimum and maximum values of 22 species of VOCs have been shown in Fig. 2.

Overall alkanes were the most abundant (63.80%) followed by alkenes (19.66%), then aromatic hydrocarbons (11.25%), and acetylene (5.29%). Among the alkanes, n-butane has the highest monthly average concentration (14.47 ± 8.78) ppbv, and n- nonane has the lowest monthly average concentration (0.69 ± 0.15) ppbv. In the case of alkenes, 1-hexene has the highest monthly average concentration (10.22 ± 4.22) ppbv, and 1- butene has the lowest monthly average concentration (0.77 ± 0.17) ppbv. Among alkynes, the monthly average concentration of Acetylene has a (4.49 ± 1.01) ppbv and among aromatics, toluene has the highest monthly average concentration (4.02 ± 2.63) ppbv and isopropyl benzene has the lowest monthly average concentration (0.75 ± 0.22) ppbv.
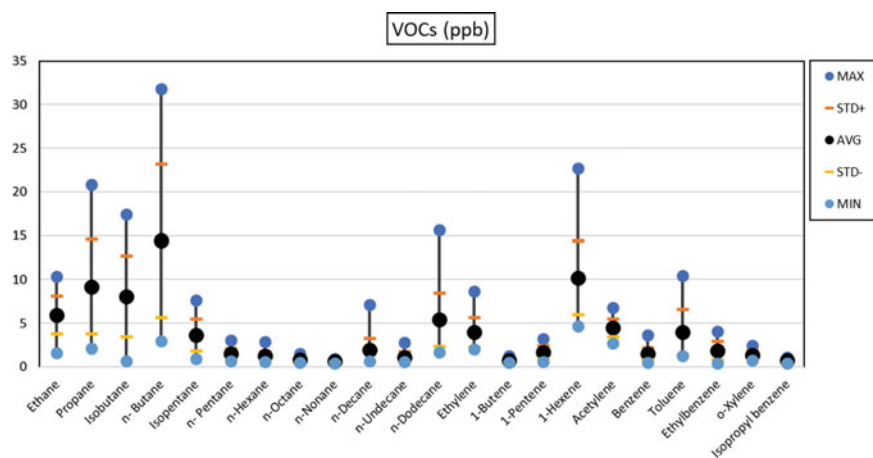

Fig. 2 Monthly average conc. with standard deviation

3.2 Assessment of Ozone Formation Potential

VOCs are recognized as the precursors of O_3 because they have the potential to take part in a number of intricate photo chemical processes in the formation of ozone. The MIR coefficient method can evaluate the near-surface O3 production potential more accurately [9]. In this study, the MIR approach was used to assess the contribution of VOCs to O3 formation in the atmosphere. Table 1 lists the MIR values and their OFP for VOC species. Among alkanes, n-butane has the highest OFP (16.64 ppb) and n-nonane has the lowest OFP (0.54 ppbv), among alkenes 1- hexene has the highest OFP (56.11 ppb) and 1-butene has the lowest OFP (7.56 ppbv) and among aromatic hydrocarbons, toluene has highest OFP (16.08 ppbv) and benzene has lowest OFP (1.09 ppbv). A similar trend of OFP of aromatic hydrocarbon was observed in Delhi [1] and Japan [10], where toluene has the highest OFP value and benzene has the lowest. Acetylene has an OFP value of 4.27 ppbv.

Among all the groups of hydrocarbons, alkenes have the highest contribution (56.09%) to the total OFP followed by alkanes (24.03%), aromatics (17.73%), and acetylene has the lowest contribution which is 2.15% as shown in Fig. 3.

The total OFP (574.47 $\mu g/m^3$) levels predicted at the study site were greater than the recommended air quality standards, which the World Health Organization (WHO) has set at 120 $\mu g/m^3$ [11]. Surface Ozone has long been regarded as one of the most dangerous gaseous air pollutants due to its range of negative impacts on human health. Numerous respiratory symptoms, such as coughing, throat irritation, infection, lung inflammation, decreased lung capacity, shortness of breath, and wheezing, may be brought on by such high levels of OFP [12].

4 Conclusion

VOCs play a very important role in the formation of ozone. VOC species have different rates of reactions and formation of ozone. In this paper, alkanes were the most abundant however, the ozone formation potential was the highest for the alkenes. In this study, the total OFP of 22 species of VOCs was 4.8 times higher than the WHO-prescribed limit of OFP value in the studied month. Such higher OFP produces very high surface ozone which ultimately harms human health and other living organisms. This study could help in the mitigation of surface ozone by removing the precursors which have high OFP values.

Table 1 Different VOCs with MIR value and their ozone formation potential

	VOC species	Average (ppbv)	MIR	OFP
Alkanes	Ethane	5.95	0.28	1.67
	Propane	9.19	0.49	4.50
	Iso-butane	8.09	1.23	9.95
	n-butane	14.47	1.15	16.64
	Isopentane	3.67	1.45	5.32
	n-pentane	1.49	1.31	1.95
	n-hexane	1.23	1.24	1.53
	n-octane	0.84	0.9	0.76
	n-nonane	0.69	0.78	0.54
	n-decane	1.93	0.68	1.32
	n-undecane	1.12	0.61	0.68
	n-dodecane	5.43	0.55	2.99
Alkenes	Ethylene	3.97	9.00	35.75
	1-butene	0.77	9.73	7.50
	1-pentene	1.70	7.21	12.29
	1-hexene	10.22	5.49	56.11
Alkyne	Acetylene	4.49	0.95	4.27
Aromatics	Benzene	1.52	0.72	1.09
	Toluene	4.02	4.00	16.08
	Ethylbenzene	1.87	3.04	5.68
	o-xylene	1.38	7.64	10.56
	Isopropyl benzene	0.75	2.52	1.88
	Total OFP (ppbv)			199.05
	Total OFP ($\mu g/m^3$)			574.47

Fig. 3 % contribution of Alkanes, alkenes, alkyne, and aromatics in ozone formation potential
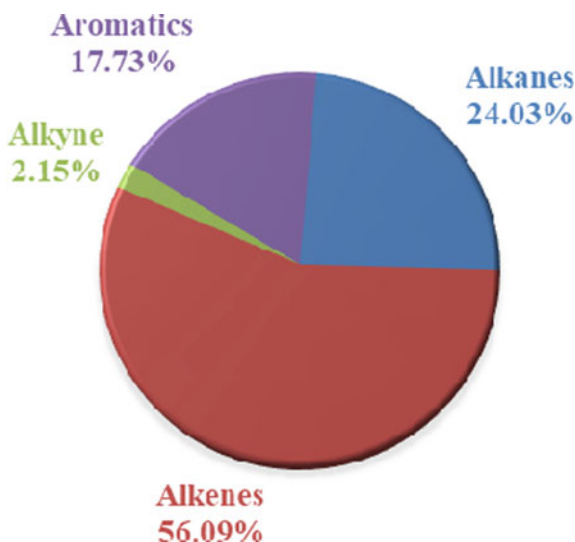
References

1. Garg A, Gupta NC (2019) A comprehensive study on Spatio-temporal distribution, health risk assessment, and ozone formation potential of BTEX emissions in ambient air of Delhi, India. Sci Total Environ 659:1090–1099
2. Sharma A, Sharma., S.K., Rohtash, Mandal, T.K., (2016) Influence of ozone precursors and particulate matter on the variation of surface ozone at an urban site of Delhi, India. Sustain Environ Res 26:76–83
3. Zhou J, You Y, Bai Z, Hu Y, Zhang J, Zhang N (2011) Health risk assessment of personal inhalation exposure to volatile organic compounds in Tianjin, China. Sci Total Environ 409:452–459
4. Jain V, Tripathi SN, Tripathi N, Sahu LK, Gaddamidi S, Shukla AK, Bhattu D, Ganguly D (2022) Seasonal variability and source apportionment of non-methane VOCs using PTR-TOF-MS measurements in Delhi, India. Atmos Environ 283–119163
5. Carter WP (1994) Development of ozone reactivity scales for volatile organic compounds. J Air Waste Manag Assoc 44:881–899
6. National Research Council (1999) Ozone-Forming potential of reformulated gasoline. Natl Acad Press, Washington, DC
7. Carter WPL (2010) Development of the SAPRC-07 chemical mechanism. Atmos Environ 44:5324–5335

8. Geng C, Yang W, Sun X, Wang X, Bai Z, Zhang X (2019) Emission factors, ozone, and secondary organic aerosol formation potential of volatile organic compounds emitted from industrial biomass boilers. J Environ Sci 83:64–72
9. Wang H, Xue S, Hao R, Fang L, Nie L (2022) Emission characteristics and ozone formation potential assessment of VOCs from typical metal packaging plants. Atmosphere 13:57
10. Tiwari V, Hanai Y, Masunaga S (2010) Ambient levels of volatile organic compounds in the vicinity of the petrochemical industrial area of Yokohama, Japan. Air Qual Atmos Health 3:65–75
11. Hajizadeh Y, Mokhtari M, Faraji M, Mohammadi A, Nemati S, Ghanbari R et al (2018) Trends of BTEX in the central urban area of Iran: a preliminary study of photochemical ozone pollution and health risk assessment. Atmos Pollut Res 9:220–229
12. Ebi KL, McGregor G (2008) Climate change, tropospheric ozone, and particulate matter, and health impacts. Environmental Health Perspective 116:1449–1455

Calibration and Analysis of Precision Capacitance Bridge and LCR Meter for Dissipation Factor Measurement

Priyanka Jain, Satish, Sachin Kumar, Ashmeet K. Uppal, Jyotsana Mandal, and J. C. Biswas

Abstract The series combination of standards resistor and capacitors is used as dissipation factor standard to calibrate precision LCR meter and capacitance bridge. The dissipation factor is measured in the range of 0.1 to 0.0001 with uncertainties in the range of 0.1% to 11%. The precision capacitance bridge and LCR meter are calibrated for dissipation factor at 1 kHz. The calibration results are compared and discussed in the presented work. It is observed that the accuracy of the dissipation factor measured with the GR1615 precision capacitance bridge is in good agreement with theoretical values.

Keywords Standards · Traceability · Dissipation factor · Capacitance · Resistance

1 Introduction

A capacitive impedance is defined as the series resistance and reactance. When a signal is applied to the capacitor, there is always a power loss. Power is absorbed by the dielectric material and dissipated through the series resistance. The dissipation factor (DF) is a measure of power loss when ac voltage is applied to the capacitor. It is defined as the ratio of series resistance and reactance of a capacitive impedance. The capacitive impedance vector is shown in Fig. 1. The DF of the capacitance is given by the ratio of the real and imaginary components of the capacitive impedance vector shown in Fig. 1 i.e., $R/(1/\omega C)$. The DF is a demanding parameter from the electrical and electronics industry. LF, HF Impedance, and DC metrology subdivision at CSIR-NPL provide calibration services for impedance [1, 2] and DC parameters. The capacitance measurement capabilities are established at CSIR-NPL from audio to radio frequencies using electrical equivalent circuit model [3].

P. Jain (✉) · Satish · S. Kumar · A. K. Uppal · J. Mandal · J. C. Biswas
Electrical & Electronics Metrology Division, CSIR-National Physical Laboratory, New Delhi, India
e-mail: jainp@nplindia.org
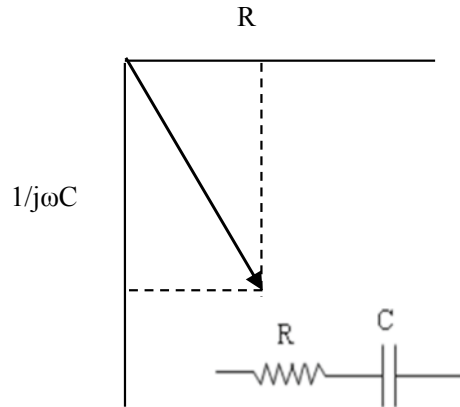
The series combination of standard capacitor and resistor can be used as a DF standard [4, 5] for precision measurements. CSIR-NPL has recently defined the DF standard from the 0.1 to 0.0001 range using the set of 4TP resistance and capacitance standards.

2 Theory

The three-terminal configuration of the series RC network has residual capacitors C_{HG}, C_{LG}, C_{RHG}, and C_{RLG}, as shown in Fig. 2a. The residual capacitance C_{LG} and C_{RHG} contribute to the DF realization. These can be measured precisely on GR1615/AH2700A capacitance bridge [5, 6]. The DF, 'D', is theoretically defined as (1), with associated uncertainty ΔD, given by (2).

$$D = 2 * \pi * f * R(C + C_{CLG} + C_{RHG}) \tag{1}$$

$$\Delta D = 2 * pi * f * \sqrt{R^2\left[\Delta C^2 + \Delta C_{LG}^2 + \Delta C_{RHG}^2\right] + \Delta R^2[C + C_{LG} + C_{RHG}]^2} \tag{2}$$

where

$R, \Delta R$: the reference resistance and associated uncertainty respectively, Ω

$C, \Delta C$: the reference capacitance and associated uncertainty respectively, F

$C_{LG}, \Delta C_{LG}$: The stray capacitance of the reference capacitor and associated uncertainty respectively, F

$C_{RHG}, \Delta C_{RHG}$: The stray capacitance of the reference resistor and associated uncertainty respectively, Ω

f: Frequency of operation, Hz.

Table 1 Measurement results

C, pF Nominal	R, kΩ Nominal	DF Nominal	DF Theoretical	$\pm u_e$, %	DF, GR1615	$\pm u_e$, %	DF, LCR meter	$\pm u_e$, %
100	100	0.1	0.099492	0.3	0.1071	0.7	0.120883	0.6
100	10	0.01	0.009914	0.3	0.0109	4.5	0.012054	0.6
100	1	0.001	0.000993	0.3	0.0011	9.4	0.001208	1.0
100	0.1	0.0001	0.000099	0.3	0.000105	10.5	0.000115	5.8

The traceability of DF measurement is linked with QHR and fused silica capacitors, as shown in Fig. 3. The combinations of four-terminal pair (4TP) resistance standards, 'R' (Model 16074A), and 4TP capacitance standards, 'C' (Model 16380A), are chosen to define the DF standard. The R, C standards and residual capacitors C_{LG} and C_{RHG} are calibrated against national standards of capacitance and resistance maintained at CSIR-NPL.

The theoretical values of the DF standards are calculated with assigned values of R, C, C_{LG} and C_{RHG} using (1). The uncertainty in measurement was computed for each range of DF according to Eq. (2). The measurement results are reported in Table 1.

3 Measurement of DF with RC Standard on GR1615 Capacitance Bridge and Precision LCR Meter

The series RC network was measured directly on the GR1615 capacitance bridge in three-terminal configurations. The residual capacitance C_{HG} is terminated with the BNC to GR874 connector to the 'H' terminal of the capacitance bridge. Similarly, C_{RLG} is terminated at the 'L' terminal of the capacitance bridge. The impact of these capacitors is eliminated with manual bridge balancing. The equivalent circuit of the DF standard is now modified to Fig. 2b.

The DF was measured directly on an Agilent E4980 LCR meter in three-terminal configurations. The uncertainties of the capacitance bridge and LCR meter for DF measurement are evaluated with repeatability in measurements, resolution of the measuring instrument, and the uncertainty 'ΔD' of the DF standard. The DF measured in the capacitance bridge and LCR meter is compared with the theoretical value of DF. The measurement results and associated uncertainties of all three methods are shown in Table 1 and Fig. 4a, b.
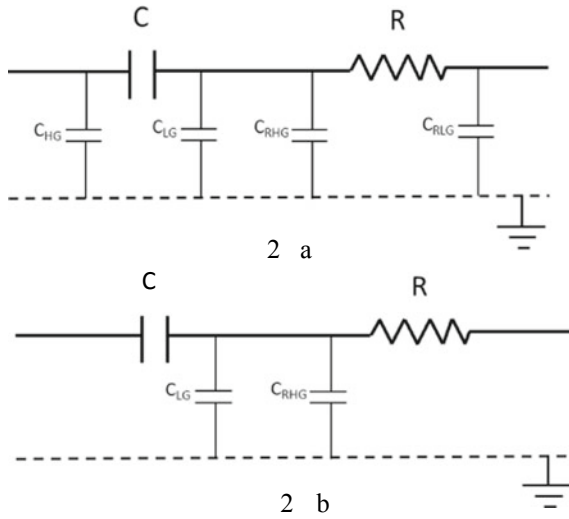
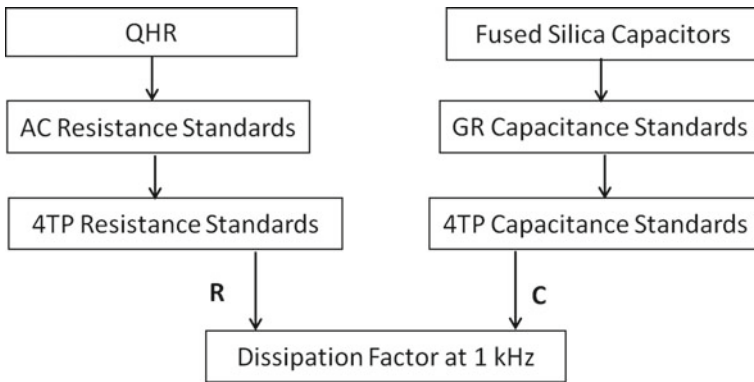**Fig. 2** **a** Three terminal configuration of series RC network **b** Equivalent circuit of dissipation factor standard

Fig. 3 Traceability chart for dissipation factor
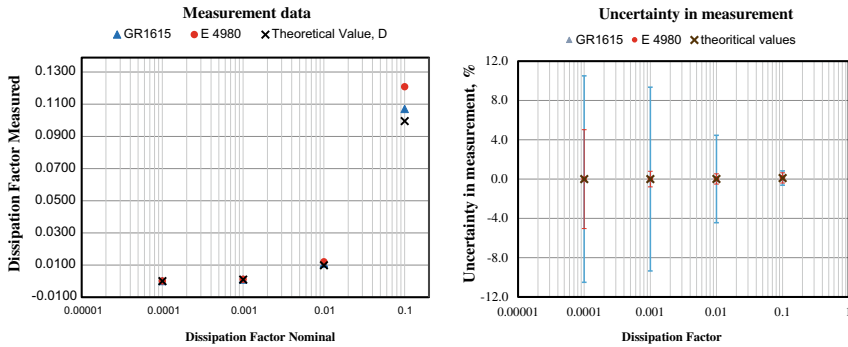
Fig. 4 **a** Dissipation factor measurement data **b** Uncertainties in measurement

4 Conclusion

This paper demonstrates that the resistance and capacitance standards could be used to define the DF precisely. The precision LCR meter and capacitance bridge are calibrated for the DF from 0.1 to 0.0001 using the series RC combination of 4TP resistance and capacitance standards at 1 kHz which are traceable to National standard of impedance at CSIR-NPL. The measurement data shows that the DF measured in GR1615 capacitance bridge is in good agreement with theoretical values. However, the uncertainties in measurement achieved in an LCR meter are comparatively better.

References

1. Dahake SL, Dhar RN, Saxena AK, Batra VK, Chandra K (1983) Progress in the Realization of the Units of Capacitance, Resistance, and Inductance at the National Physical Laboratory, India. IEEE Trans Instrum Meas 32(1):5–8. https://doi.org/10.1109/TIM.1983.4314999
2. Singh S, Kumar S, Babita, John T (2017) Realization of Four-Terminal-Pair capacitors as reference standards of impedance at high frequency using Impedance-Matrix Method. In IEEE Trans Instrum Meas, 66(8), pp 2129–2135, https://doi.org/10.1109/TIM.2017.2673098
3. Dai, Dongxue, Yang, Yan, Satish, Homklintian, Monthol. (2022). Comparison of four-terminal-pair 1 pF, 10 pF, 100 pF and 1000 pF capacitance standards at frequencies of 10 kHz, 100 kHz, 1 MHz and 10 MHz (APMP.EM-S15). Metrologia. 59. 01007. https://doi.org/10.1088/0026-1394/59/1A/01007
4. Simmon ED, FitzPatrick GJ, Petersons O (1998) Calibration of dissipation factor standards, In: 1998 Conference on Precision Electromagnetic Measurements Digest (Cat. No.98CH36254), pp 203–204, https://doi.org/10.1109/CPEM.1998.699867
5. Turhan E, Gülmez G, Erkan O, Hayirli C, Galic N, Güler NA (2018) Calibration of dissipation factor measurements of capacitance meters. In: Conference on Precision Electromagnetic Measurements (CPEM 2018), pp 1–2, https://doi.org/10.1109/CPEM.2018.8501102
6. https://www.ietlabs.com/pdf/Datasheets/1620.pdf

Elemental Analysis and Health Risk Assessment of PM$_{2.5}$ at An Urban Site of Delhi

Sakshi Gupta, S. K. Sharma, and T. K. Mandal

Abstract In order to comprehend the elemental annual contributions to PM$_{2.5}$ over Delhi's urban region from January 2021 to December 2021, this study was carried out. Elemental analysis (Na, Mg, Ca, Cr, Al, P, S, K, Fe, Cu, Zn, Cl, and Mo) of PM$_{2.5}$ was performed using a non-destructive method (Wavelength Dispersive X-Ray Fluorescence Spectrometry). During the sampling period, the observed annual average concentration of PM$_{2.5}$ was 105 ± 44 µg m^{-3}, which exceeds the National Ambient Air Quality Standards (NAAQS) limit (40 µg m^{-3}) by approximately 2.5 times. Among elements, majorly Cl (22%), S (21%), and K (19%), Fe (11%), Zn (6%), Ca (5%), Al (4%), Cr (3%) contributed to PM$_{2.5}$. Whereas Cu, Ga, Mo, Zr, Mg, Na, B, P, Mn, Pd, As, Br, Ni and Ti contributed ≤1%. The diagnostic ratios of Al/Fe, Al/Ca, and Al/Mg indicates their common source of these elements. According to enrichment factor estimation, Fe, Ca, Mg and Na contribute to crustal/ soil dust, while Mo, Cr, Zn, and Cu are likely to be emitted due to industrial activities. The health risk assessment (HRA) evaluated the non-carcinogenic risk of Cr and Pb along with the carcinogenic risk of Cr. The burning of fossil fuels and biomass, industrial pollutants, automobile emissions, and crustal or mineral dust are among the likely sources of the PM$_{2.5}$ anticipated at Delhi's urban site.

Keywords PM$_{2.5}$ · Elements · Enrichment factor · Health risk assessment · Delhi · Sources

1 Introduction

Ambient air quality and human health are negatively impacted by atmospheric particulate matter (PM)/aerosols [3]. Trace elements contribute a small fraction of PM by mass but they serve as gauges for various pollution sources [8]. In the past few

S. Gupta (✉) · S. K. Sharma · T. K. Mandal
CSIR-National Physical Laboratory, Dr. K. S. Krishnan Road, New Delhi 110012, India
e-mail: sakshi.npl21a@acsir.res.in

Academy of Scientific and Innovative Research (AcSIR), Ghaziabad 201002, India

decades, elemental pollution gained a lot of attention due to its adverse effects on atmosphere [15]. The elemental composition contains both trace &heavy metals and the heavy metal composition in PM is an important concern for human health [3, 7]. The elemental content and size distribution of these atmospheric particles are correlated, both natural and human-made sources have an impact on the emission of these aerosols [1]. The source of the origination of these trace elements involves vehicular emissions, combustion, crustal/road dust, construction activities, etc. [2, 10]. The elements such as Al, As, Cu, Ni, Pb, V, etc., are notably responsible for both cardiovascular and pulmonary disorders [4]. Therefore, identifying the sources of these heavy and trace metal emissions and quantifying them is essential for their mitigation.

Various researches have been done so far to identify the emission sources of trace and heavy metals [2, 8, 13]. Jain et al. [2] identify the natural sources i.e., crustal or road dust that dominantly contributed to the emission of major elements (Ca, Fe, Mg, Mn and Ti) while anthropogenic sources contributed to the emission of toxic elements (As, Cr, Cu, Pb and Zn). Rai et al. [8] reported the heavy elements i.e., Ba, Bi, Cl and Cu emitted from fireworks, Cl from sea salts, Ba, Cr, Cu, Fe, Mn and Zn from non-exhaust traffic related source. Wang et al. [13] reported the elements (Al, Ca, Fe, K, Na and Mg) mainly contributes to sources like soil and crustal dust and heavy elements (Co, Pb and Zn) were emitted from human-made actions.

In the current work, an effort is made to measure the elemental contents of $PM_{2.5}$ over Delhi. Also, this study includes the estimation of Enrichment Factor (EF), diagnostic ratios between various elements that correspond to the estimation of the probable sources of emission of the quantified elemental species, and health risk assessment (HRA) for various heavy metals (Al, Cr, Pb, As & Ni). The study may help to a better comprehension of annual elemental contribution and their possible sources of $PM_{2.5}$ across Delhi's urban region.

2 Methodology

2.1 Sampling Location

At the CSIR-NPL, New Delhi, $PM_{2.5}$ samples were collected from January to December 2021 (there was a complete lockdown in Delhi due to COVID-19 from May 2021–July 2021, the sampling for these 3 months was not collected). The sampling location is situated on the rooftop of the laboratory complex, 218 m above sea level (a.s.l), in central Delhi (28º38'N, 77º10'E) (Fig. 1).

The sampling site is encircled by a region with significant traffic, a residential area to the north, and an agricultural area (the Indian Agricultural Research Institute) to the south-west direction.

Fig. 1 Study site (*Source* Google Earth)
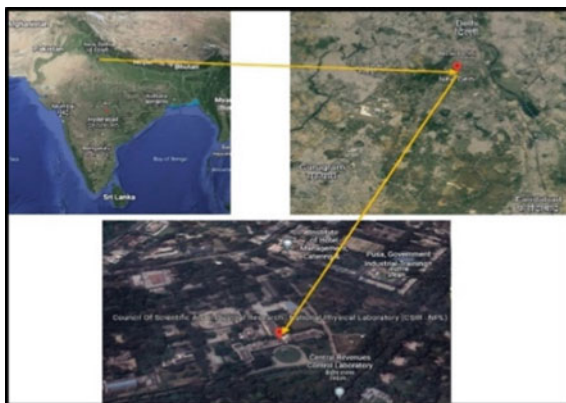
2.2 PM$_{2.5}$ Sampling

To study the annual concentration of PM$_{2.5}$, the samples were obtained using a PM$_{2.5}$ sampler (APM 550; Envirotech, India) on pre-combusted (550 ºC) quartz fiber filter. The sampler is positioned 10 m above the ground level (AGL) and the average flow rate of the sampler was 1m^{3}h^{-1} (accuracy $\pm2\%$). Following the Central Pollution Control Board's (CPCB) guidelines, 24 h sampling was carried out in Delhi, India. Before and after sampling, filters were desiccated, and microbalance with a resolution of ±10 µg was used to calculate the initial and final weights. The amount of PM$_{2.5}$ was measured gravimetrically.

2.3 Elemental Analysis

Total 59 samples (January 2021 to December 2021) were collected and examined for the study. The elemental study (Al, As, B, Br, Cl, Cr, Fe, K, Na, Mo, P, Pb, S and Zn) has been done by using non-destructive wavelength dispersive X-ray fluorescence (WD-XRF) technique (ZSX Primus, Rigaku, Japan). The analysis was done under vacuum condition having a temperature of 36 ºC and tube rating of 24 kW. Parameter method approach included in software package of WD-XRF was used to obtain quantitative results [2].

2.4 Enrichment Factor (EF)

To understand the origination of the probable source of the elemental species in the PM, the EF has been computed for PM$_{2.5}$. Taylor and McLennan [11] calculated the

EF using the Eq. (1):

$$EF = \frac{\frac{El_{sample}}{X_{sample}}}{\frac{El_{crust}}{X_{crust}}} \tag{1}$$

where, El_{sample} and X_{sample} are the mass concentrations of element (El) and reference element (X) respectively in the sample. Aluminum (Al) is considered as a reference element as it has the third highest composition in Earth's crust after oxygen (O_2) and silicon (Si). El_{crust} and X_{crust} are the mass composition of the element and reference element of the upper continental crust, respectively.

2.5 Health Risk Assessment (HRA)

HRA computation was done by using criteria suggested by USEPA and database provided by Integrated Risk Information System (IRIS) for carcinogenic and non-carcinogenic risk of Al, As, Cr, Ni, and Pbby inhalation exposure of $PM_{2.5}$. The exposure concentration ($\mu g/m^3$) (EC), Hazard Quotient (HQ) and Carcinogenic Risk (CR) was calculated by applying the following Eqs. (2–4) [12].

$$EC = \frac{C \times ET \times EF \times ED \times IR}{AT \times BW} \tag{2}$$

where, C is the composition of element in ambient air ($\mu g/m^3$), ET is exposure time (12 h/day) (h/day), EF is exposure frequency (day/year) (350 day/year), ED is exposure duration (years) (6 for children & 24 for adults), IR is the rate of air inhalation i.e., 10 m^3 day^{-1} for children and 20 m^3 day^{-1} for adults, AT is the average time (days/years) ($365 * ED$), and BW is the body weight i.e., 15 kg for children and 70 kg for adults.

For Non-carcinogenic risk assessment, Hazard Quotient (HQ) is used,

$$HQ = \frac{EC}{(Rf_c \times CF)} \tag{3}$$

where, Rf_c is reference concentration in mg/m^3, CF is the conversion factor and its value is 1000 $\mu g/mg$. $HQ \leq 1$ means no health, hazard means safe and $HQ \geq 1$ health hazard possibility is there and adverse health effects.

For Carcinogenic risk assessment,

$$CR = IUR \times EC \tag{4}$$

where IUR is inhalation unit risk and if the value of CR is greater than 10^{-4} then there is a high risk of cancer while its value between 10^{-6} to10^{-4} indicates the acceptable limit and CR value less than 10^{-6} is considered to have mild health effect [5, 6, 13, 14].

2.6 Air Mass Back Trajectory

Air mass backward trajectory analysis was performed using air resource laboratory (ARL), National oceanic and atmospheric administration (NOAA). Hybrid Single Particle Lagrangian Integrated Trajectory (HYSPLIT) model (http://ready.arl.noaa. gov/HYSPLIT.php) is used to relocate the air pathway of PM from the receptor site. Utilizing TrajStat software, the 120-h backward trajectories at 500 m AGL for sampling day were created and examined.

3 Results and Discussion

3.1 Mass Concentration and Elemental Composition

The observed annual concentration of PM$_{2.5}$ was $(105 \pm 44)\,\mu g\,m^{-3}$, which exceeds the NAAQS value $(40\,\mu g\,m^{-3})$. Among elements majorly, Cl $(2.141 \pm 1.211\,\mu g\,m^{-3})$, S $(2.050 \pm 0.709\,\mu g\,m^{-3})$, K $(1.822 \pm 0.912\,\mu g\,m^{-3})$, Fe $(1.090 \pm 0.434\,\mu g\,m^{-3})$, Zn $(0.572 \pm 0.234\,\mu g\,m^{-3})$, Ca $(0.530 \pm 0.331\,\mu g\,m^{-3})$, Al $(0.367 \pm 0.199\,\mu g\,m^{-3})$, Cr $(0.279 \pm 0.107\,\mu g\,m^{-3})$, Pb $(0.236 \pm 0.265\,\mu g\,m^{-3})$, Cu $(0.140 \pm 0.117\,\mu g\,m^{-3})$ and Ga $(0.119 \pm 0.162\,\mu g\,m^{-3})$ contributed to PM$_{2.5}$. These elements might originate from biomass burning, combustion, crustal dust and other anthropogenic activities that occurred during the study period [2, 10]. The other quantified elements Mo, Zr, Mg, Na, B, P, Mn, Pd, As, Br, Ni and Ti contributed less than 1%. The average annual elemental composition of all the estimated elements during study time is given in Fig. 2.

3.2 Diagnostic Ratio and Correlation Plot

The diagnostic ratio of Al/Ca (r = 0.97), Al/Mg (r = 0.97) and Al/Fe (r = 0.63) indicates their common source i.e., crustal or soil dust [2] (Fig. 3). Also, there is a significant correlation among Zn, Pb and Cu corresponding to their common source of origin i.e., through vehicular and industrial emissions [8] (Fig. 4).
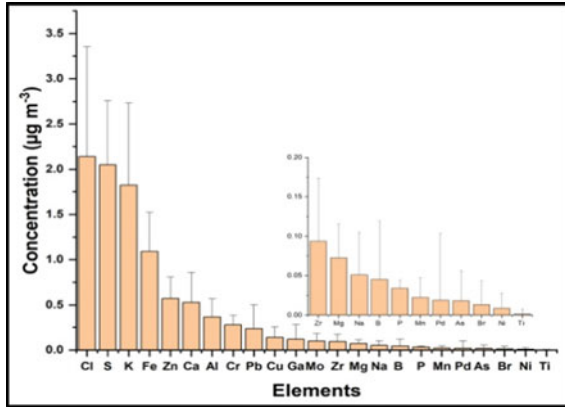
Fig. 2 Annual elemental concentration of PM$_{2.5}$
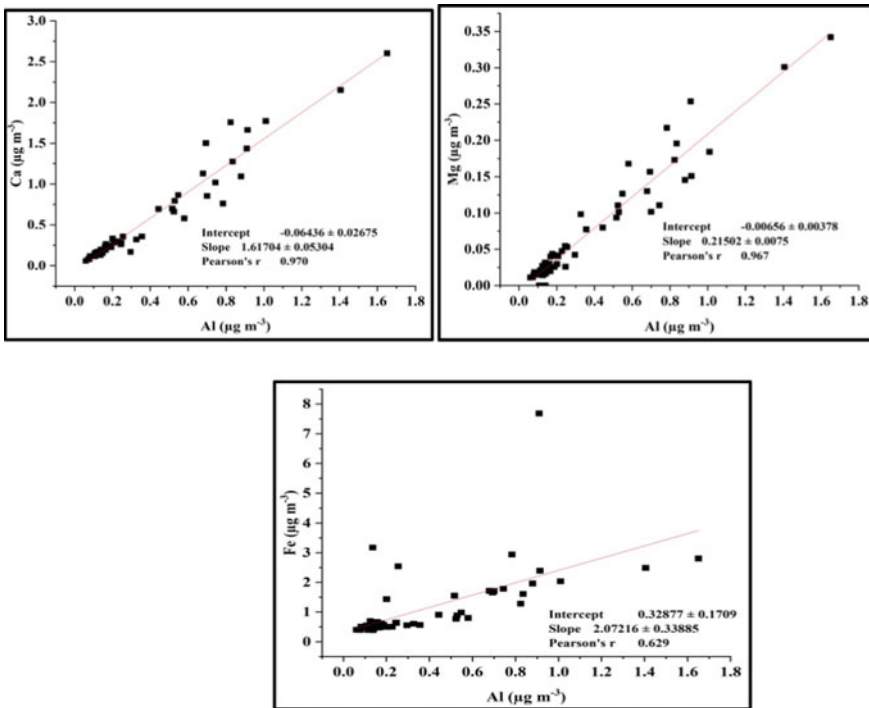
Fig. 3 Scatter plots between Al with Fe, Al with Ca and Al with Mg of PM$_{2.5}$

Fig. 4 Correlation plot of all
the elements
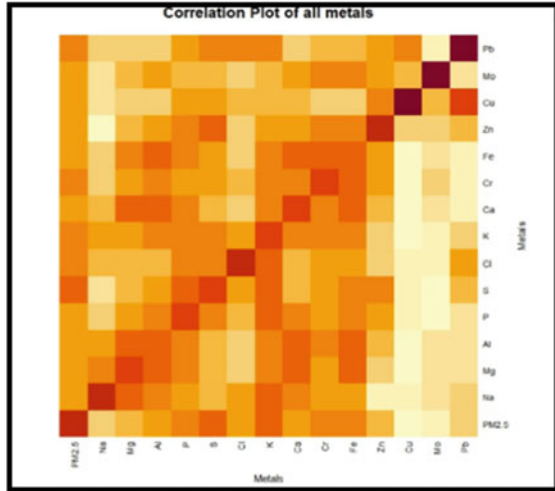
3.3 Enrichment Factor (EF)

EF explains the contrast between natural and anthroprogenic sources, as the element
having EF less than 5 will be considered as natural or crustal origin, whereas EF in
between 5 to 10 corresponding to the mixed i.e., both natural and anthroprogenic
origin and EF > 10 dominantly shows the anthroprogenic source of origin [9]. The
results specify the metals (Na, Mg, Ca and Fe) have EF less than 5, thus these elements
might have crustal or natural sources of origin. P and K have EF between 5–10, hence
have both natural and anthroprogenic sources. Both these elements might originate
from agricultural and combustion activities. The elements Cu, Zn, Cr and Mo have
EF greater than 10, thus they have anthroprogenic source of origination i.e., most
probably industrial emissions (Fig. 5).

Fig. 5 Enrichment factor
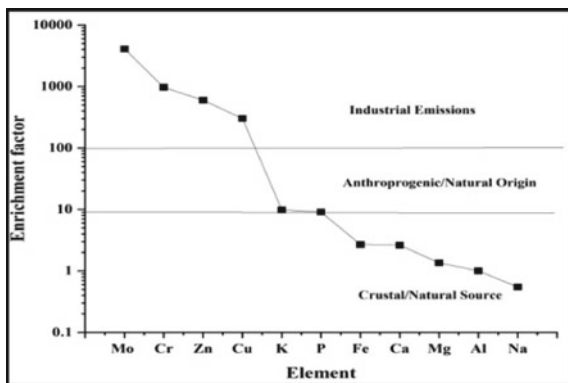
Table 1 Annual exposure concentration (EC), hazard quotient (HQ) and carcinogenic risk (CR) of heavy elements of $PM_{2.5}$ in Delhi

	Adults			Children		
Elements	EC ($\mu g\ m^{-3}$)	HQ	CR	EC ($\mu g\ m^{-3}$)	HQ	CR
As	6.01×10^{-2}	2.00×10^{-1}	1.29×10^{-5}	1.40×10^{-1}	4.68×10^{-1}	$6.03 10^{-5}$
Cr	9.17×10^{-1}	9.17×10^{0}	5.50×10^{-4}	2.14×10^{0}	2.14×10^{1}	2.57×10^{-3}
Pb	7.74×10^{-1}	1.80×10^{1}	–	1.81×10^{0}	4.20×10^{1}	–
Ni	2.85×10^{-2}	1.43×10^{-3}	–	6.66×10^{-2}	3.33×10^{-3}	–
Al	1.21×10^{0}	6.36×10^{-1}	–	2.82×10^{0}	1.48×10^{0}	–

3.4   Health Risk Assessment

The EC, HQ & CR assessment of five heavy elements (As, Cr, Pb, Ni and Al) for both adults and children are given in Table 1. The HQ values for Cr (21.4) and Pb (42.0) is beyond the safe limit i.e., greater than 1 in children whereas HQ for Cr (9.17) and Pb (18.0) is higher than the safe limit in adults. Hence these elements have non-carcinogenic health risks. Also, the element Cr has carcinogenic risk in both adults and children as its value exceeds from the permissible limit i.e., greater than 10^{-4}. Hence, children are more prone to the adverse effects of the heavy metal concentration present in $PM_{2.5}$. The HQ of As, Ni and Al are within the safe limits, therefore there is no health hazard for these elements.

3.5   Trajectory Analysis

To know the air traffic path of the sampling site throughout the sampling period, air mass annual backward trajectory at 500 m AGL is plotted (Fig. 6). The long-range transport of air traffic at the study site mainly from Pakistan, Afghanistan, Turkmenistan, North-East India, Bay of Bengal (BoB), Arabian sea and pass over IGP region.

Fig. 6 120 h air mass backward trajectories at the sample site
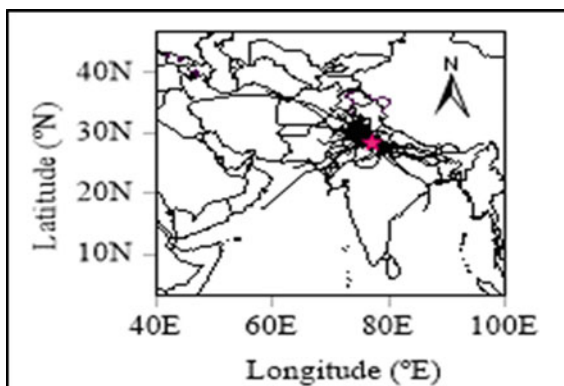
4 Conclusion

- The observed annual level of PM$_{2.5}$ was (105 ± 44) μg m^{-3} during 2021.
- EF and correlation analysis of elements indicate that Fe, Ca, Mg and Na arise from crustal/soil dust, while Mo, Cr, Zn, and Cu are likely to be coming from industrial activities.
- The HRA evaluated the non-carcinogenic risk of Cr and Pb along with carcinogenic risk of Cr.
- The long-distance transit that brings the approaching air mass traffic to the study location is mostly from Pakistan, Afghanistan, Turkmenistan, North-Eastern India, BoB, and the Arabian Sea, and it passes across the IGP region.
- The burning of fossil fuels and biomass, industrial pollutants, automobile emissions, and crustal/mineral dust are among the likely sources of the pollutants anticipated at Delhi's urban site.

References

1. Acosta JA, Faz A, Kalbitz K, Jansen B, Martínez-Martínez S (2011) Heavy metal concentrations in particle size fractions from street dust of Murcia (Spain) as the basis for risk assessment. J Environ Monit 13:3087–3096
2. Jain S, Sharma SK, Vijayan N, Mandal TK (2020) Seasonal characteristics of aerosols (PM$_{2.5}$ and PM$_{10}$) and their source apportionment using PMF: A four-year study over Delhi, India. Environ Pollut

3. Joshi P, Dey S, Ghosh S, Jain S, Sharma SK (2022) Association between acute exposure to $PM_{2.5}$ chemical species and morality in megacity Delhi, India. Environ Sci Technol 56:7275–7287

4. Kelly FJ, Fussell JC (2012) Air pollution and airway disease. Clin Exp Allergy 41:1059–1071

5. Ma W, Tai L, Qiao Z, Zhong L, Wang Z, Fu K et al (2018) Contamination source apportionment and health risk assessment of heavy metals in soil around municipal solid waste incinerator: a case study in North China. Sci Total Environ 631–632:348–357

6. Prakash J, Lohia T, Mandariya AK, Habib G, Gupta T, Gupta SK (2018) Chemical characterization and quantitative assessment of source-specific health risk of trace metals in $PM_{1.0}$ at a road site of Delhi, India. Environ Sci Pollut Res 25:8747–8764

7. Rabha S, Subramanayam KSV, Sawant SS, Saikia BK (2012) 2022 Rare–earth elements and heavy metals in atmospheric particulate matter in an urban area. ACS Earth Space Chem 6:1725–1732

8. Rai P, Furger M, Slowik JG, Canonaco F, Frohlich R, Prevot ASH (2020) Source apportionment of highly time-resolved elements during a firework episode from a rural freeway site in Switzerland. Atmos Chem Phys 20:1657–1674

9. Sharma SK, Mandal TK, Saxena M, Sharma A, Gautam R (2014) Source apportionment of PM_{10} by using positive matrix factorization at an urban site of Delhi India. Urban Clim 10:656–670

10. Shukla AK, Lalchandani V, Bhattu D, Dave JS, Rai P et al (2021) Real- time quantification and source apportionment of fine particulate matter including organics and elements in Delhi during summer time. Atmos Environ 261:118598

11. Taylor SR, McLennan SH (1985) The continental crust: its composition and evolution, p 312. Blackwell, Oxford

12. US EPA (2011) Exposure factors handbook 2011 edition (final report). U.S. Environmental Protection Agency, Washington, DC (EPA/600/R-09/052F)

13. Wang W, Chen C, Liu D, Wang M, Han Q, Zhang X, Feng X, Sun A, Mao P, Xiong Q, Zhang C (2022) Health risk assessment of $PM_{2.5}$ heavy metals in county units of northern China based on Monte Carlo simulation and APCS-MLR. Sci Total Environ 843:156777

14. Zhang J, Zhou X, Wang Z, Yang L, Wang J, Wang W (2018) Trace elements in $PM_{2.5}$ in Shandong Province: source identification and health risk assessment. Sci Total Environ 621:558–577

15. Zhi M, Zhang X, Zhang K, Ussher SJ, Lv W, Li J, Gao J, Luo Y, Meng F (2021) The characteristics of atmospheric particles and metal elements during winter in Beijing: size distribution, source analysis, and environmental risk assessment. Ecotoxicol Environ Saf 211:111937

Roundness of a Flick Standard and Analyzing Effects of Different Filters While Using Least Squares Reference Circle Method of Roundness Measurement

Sandeep Kumar, Jokhan Ram, Mukesh Jewariya, Rina Sharma, and Yogesh Mishra

Abstract It's imperative to ascertain and specify the roundness of mechanical components, otherwise, they could fail in the real world. In this paper, an attempt is made to analyze the roundness of a flick standard with Least Squares Reference Circle method using different filtration techniques. This analysis will help us understand the effect of these filters during measurements and the results thus obtained will be compared against each other to optimize the filters for roundness measurements.

Keywords Roundness · Filters · LSCI · Flick standard · Dimensional metrology · Traceability

1 Introduction

Roundness in general, is the measurement of the shape/form of an object which draws closeness to a mathematically perfect circle. The roundness measurement of an object/artefact requires 360º traces of the object with the help of a turn table type device/instrument or a stylus-type instrument [4]. The method of rotational datum is the most accurate and widely used method for the assessment of the roundness of any component. In this method, the variation of radius is measured from an accurate rotational datum with the help of a scanning type probe and the probe remains in contact with the surface of the object in question while measuring roundness and generates so many data points [11, 12]. To analyze this data, one must fit a reference circle to this data [5–10]. Accordingly, the roundness of the object can be calculated from the center of the reference circle.

S. Kumar (✉) · J. Ram · M. Jewariya · R. Sharma
CSIR-National Physical Laboratory, New Delhi, India
e-mail: kumars2@nplindia.org

Y. Mishra
NRI Institute of Information Science and Technology, Bhopal, India

Fig. 1 High precision form tester RA 2200, Make: Mitutoyo

Fig. 2 The deviation of flick standard
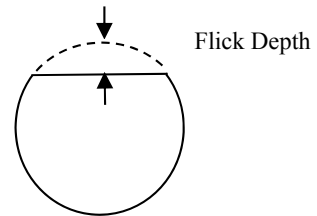
At CSIR-NPL, a high precision form tester RA 2200 (Make: Mitutoyo) is used to perform the measurements [16–18]. It is shown in Fig. 1.

Flick Standard and its Roundness

A flick standard is an easy to use standard for measuring the roundness of your instrument. A typical flick standard has a very round shape with a flat groove on one side which can be termed as the flick depth [3, 20]. The depth of this flick specifies the roundness of flick standard. As shown in Fig. 2, a flick standard has a very round ground cylinder and a nominal depth from that cylinder diameter is provided with a flick depth. When it is measured for the roundness, we could see the deflection when the probe transverses the standard.

2 Methodology and Different Filters Used for Measurement

At CSIR-NPL, a high precision form tester RA 2200 (Make: Mitutoyo) shown in Fig. 1 is used to perform the measurements.

Least Squares Reference Circle (LSCI)

In this reference circle, we fit a circle to the acquired data in any such way that the square sum of the deviation of this data from that circle is minimum [1, 2, 12]. This circle, when observed, divides the whole profile into equivalent minimum areas. LSCI is the most widely used Reference Circle by the metrologists. As shown in Fig. 3, total Roundness RONt is shown as the profile's maximum deviation from LSCI reference circle or in other words it is the sum total of the highest peak and lowest valley from the reference circle [7–13].

The method of measurement analysis is designed keeping in view the effect of spectral wave number using UPR on different filters [14, 19, 21] viz a viz 2 CR, Gaussian and robust spline. Evaluation is also done in the absence of filters and compared with the aforementioned conditions.

Following conditions are selected for the measurements of the flick standard:

Method of Measurement (reference circle algorithm)

Least Squares Reference Circle (LSCI) is the most widely used Reference Circle by the metrologists. Therefore it is decided to use LSCI as the reference circle algorithm for the study.

Fig. 3 Least square reference circle
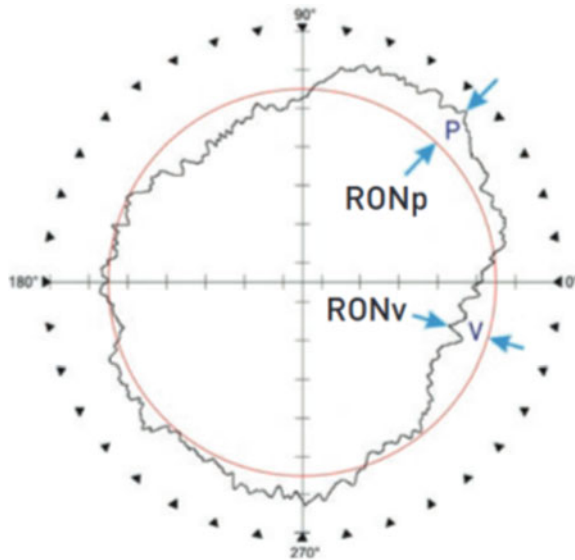
RONt = distance P + V
Least Squares Circle (LSCI)

Filters Used

Without Filter: First, we will measure the roundness of the flick standards without using any filter, be it undulation or phase correction. Such observed data will be compared against the data using a combination of various undulations and digital as well as analogue filters.

Earlier, measurement instruments were using analogue filters. These filters are known as 2CR filters. These 2CR represent two resistors and two capacitors. This electronic filter, albeit is still acceptable and recognized by international standards, suffers from phase distortion due to the nature of its electronic components. To overcome this problem, we have phase correct filters which do not suffer such issues due to the phase distortion of their electronic components.

Modern measuring instruments use phase correct filters, like the Gaussian filter. This type of filter significantly reduces filter distortion, though they can only be applied where filtering is done by mathematical algorithms as in computer based processing.

Similarly, there is a robust spline filter, which is also recommended by International Organization for Standardization (ISO) but differs from Gaussian filter in terms of algorithms and filtering characteristics [16] (Table 1).

2CR 50

This has the same attenuation characteristics as a pair of R–C circuits with an identical time constant are connected in series. The attenuation characteristic is -12 dB/oct and the amplitude transmittance at the cutoff value is 50%.

Characteristics of 2 CR 50 filter

Attenuation characteristics:

$$H(\lambda) = \frac{1}{1 + \left(\frac{\lambda}{\lambda c}\right)^2}$$

Gaussian

The attenuation characteristic is approximately -11.6 dB/oct and the amplitude transmittance at the cutoff value is 50%.

Table 1 Filter types for roundness measurement

Filter name	Amplitude characteristics	Phase characteristics	Amplitude transmittance at the cut-off wavelength
2CR 50	2CR	No	50%
Gaussian	Gaussian	Linear	50%
Robust spline	Non-linear $\frac{1}{1+16\cdot\alpha\cdot\sin^4\left(\frac{\pi\cdot\Delta x}{\lambda}\right)}$	Non-linear	Non-linear (50%)

Attenuation characteristics of Gaussian filter

Attenuation characteristics:

$$H(\lambda) = 1 - e^{-\pi\left(\frac{a\lambda c}{\lambda}\right)^2}$$

Attenuation characteristics of the low-pass filter:

$$H(\lambda) = e^{-\pi\left(\frac{a\lambda c}{\lambda}\right)^2}$$

where

$$\alpha = \left(\frac{\ln 2}{\pi}\right)^{\frac{1}{2}} = 0.4697$$

Robust Spline

The robust spline filter's transfer function cannot be given because the filter is a non-linear filter. The algorithm of this filter is based on the weighted spline filter. Therefore the output of this filter is the same as that of the spline filter for an outlier free input data.

The spline filter's transfer function is given by the following formula:

$$H(\lambda) = \frac{1}{1 + 16 \cdot \alpha \cdot \sin^4\left(\frac{\pi \cdot \Delta x}{\lambda}\right)}$$

where,

$$\alpha = \frac{1}{16 \cdot \alpha \cdot \sin^4\left(\frac{\pi \cdot \Delta x}{\lambda c}\right)}$$

This filter is a phase compensation filter and its gain at the cutoff wavelength is 50%.

UPR (undulations per revolution are the number of surface-profile deviations from a true circle in one revolution)

As we know, the roundness profile is a closed profile and is measured by a scanning probe while the component is fitted on the rotating spindle, therefore a round component can be considered to have multiple surface wavelengths or harmonics superimposed over it. Such harmonics are nothing but the information providing fingerprints about the process of manufacturing through which the component is manufactured and such irregularities can affect the function of such components when in operation. Hence, it is important to divide the roundness profile into separate harmonic regions to understand the processes and operational function in a better

way. These harmonics are stated in respect of Undulations per revolution (UPR).

$$\text{Wavelengths on the Surface} = \text{Harmonics} = \text{UPR}$$

3 Results and Discussion

In this part of the paper, measurement results of the flick standard are shown and compared with each other. We have also provided some graphs for reference given below and plotted RONt without filter data (Fig. 4).

Method of Measurement (reference circle algorithm): Least Squares Reference Circle (LSCI); Filters Used: Without Filter.

The effect of different filters on total roundness (RONt) is tabulated in Table 2 and graph is plotted in Fig. 5 to understand the same.

The uncertainty of measurement [15] of RONt for all the measurements is given below:

Uncertainty of Measurement of RONt : $\pm \mathbf{0.030}\,\mu\mathbf{m}$

The reported uncertainty is at coverage factor $k = 2$, which corresponds to a coverage probability of approximately 95% for a normal distribution.

We have also deduced the flick depth using Length Measuring Machine (LMM). Flick depth for the same is explained below:

Diameter of the Flick neck (D): 20.0127 mm.

Diameter with flick depth (D–h): 19.9966 mm.

Hence

$$
\begin{aligned}
\text{Flick Depth(h)} : &D - (D - h) \\
&= 20.0127 - 19.9966 \\
&= 0.0161 \text{ mm} \\
&= 16.1 \,\mu\text{m}
\end{aligned}
$$

Uncertainty of Measurement of Flick Depth(h) : $\pm \mathbf{0.12}\,\mu\mathbf{m}$

The reported uncertainty is at coverage factor $k = 2$, which corresponds to coverage probability of approximately 95% for a normal distribution.

The experiments show that the total roundness measurement results vary with the type of filters chosen for the measurement such as undulations per revolutions, analogue or electronic filters as discussed earlier in the report. From our results, we have observed that around 150 UPR upto 500 UPR, we close towards the

Roundness<Round_1> : 15.194µm

90.0 deg

180.0 deg

0.0 deg

270.0 deg

x665(15.028µm/ cm)

Roundness<Round_1> : 15.174µm

90.0 deg

180.0 deg

0.0 deg

270.0 deg

x664(15.057µm/ cm)

Roundness<Round_2> : 16.125µm

90.0 deg

180.0 deg

0.0 deg

270.0 deg

x589(16.969µm/ cm)

Roundness<Round_2> : 16.116µm

90.0 deg

180.0 deg

0.0 deg

270.0 deg

x589(16.964µm/ cm)

RONt without filter, µm

RONt, micron

16.5

16

15.5

15

14.5

1   2   3   4

Number of measurement
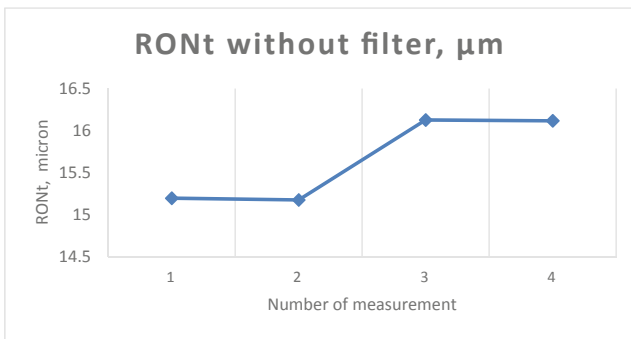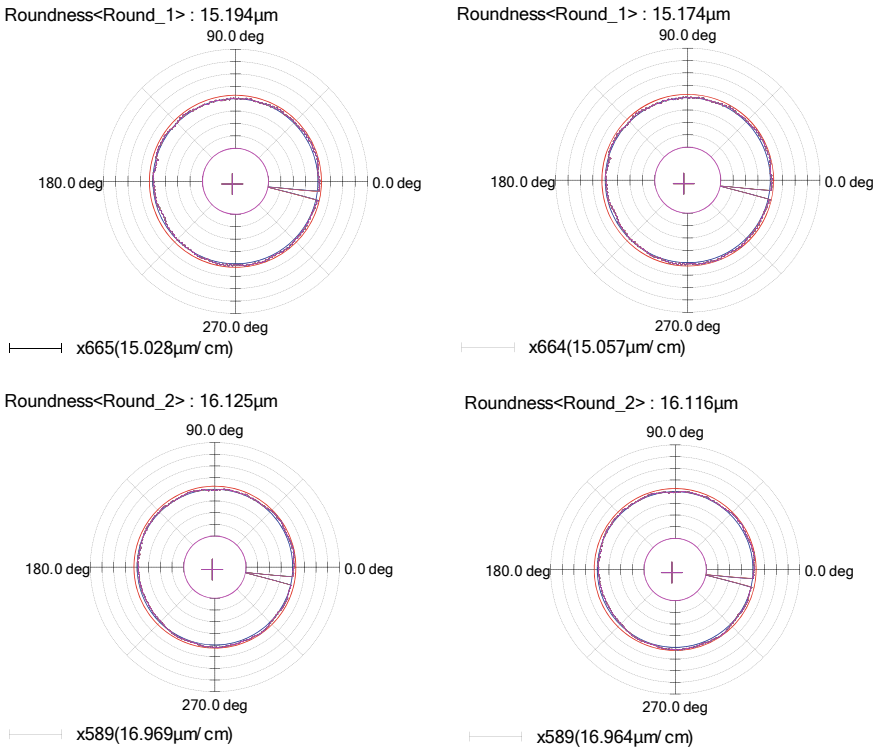
Fig. 4 RONt plot (Without Filter)

required accuracy of the results. We have compared our results with the diameter measurements done on LMM.

Table 2 Effects of different filters on total roundness (RONt)

Filter type	RONt, μm			
Unfiltered	15.194	15.174	16.125	16.116
Gaussian (average)	6.138 @ 15 UPR	13.635 @ 50 UPR	16.191 @ 150 UPR	16.553 @ 500 UPR
2 CR (average)	7.075 @ 15 UPR	14.065 @ 50 UPR	16.720 @ 150 UPR	17.216 @ 500 UPR
Robust spline (average)	5.816 @ 15 UPR	15.381 @ 50 UPR	17.212 @ 150 UPR	17.277 @ 500 UPR
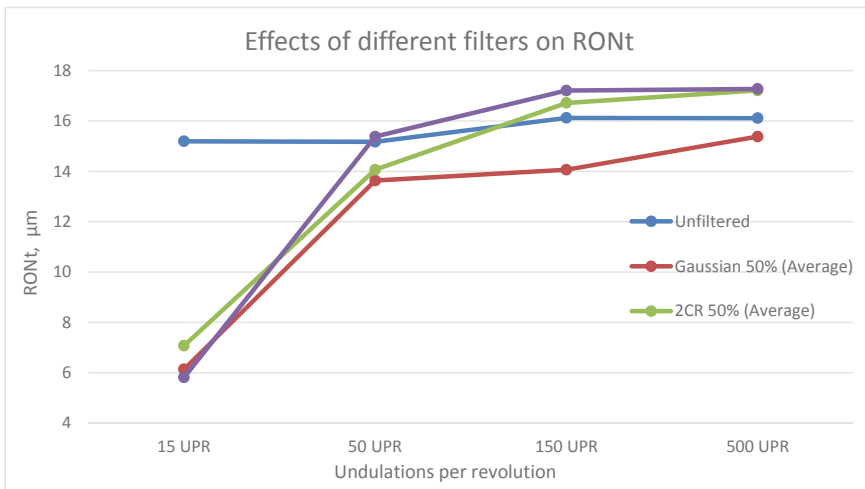
Fig. 5 Effects of different filters on total roundness (RONt)

4 Conclusion

In this work, the roundness of a flick standard is measured and analyzed using different filters viz various undulations per revolutions to represent the harmonic component of the roundness profile, without filter, analogue filter such as 2 CR filter, Electronic filters as Gaussian and Robust Spline Filters over Least Squares Reference Circle.

It is observed that lower undulation per revolution generally loses significant information about the roundness and misses the accuracy of the results. However Gaussian filter with higher UPR shows consistent and accurate results which are desired by the metrologists. It is recommended to use Gaussian filter with higher UPR, at least 150 UPR, for roundness measurement of flick standards.

References

1. Thalmann R (2006) Basic of highest accuracy roundness measurement. Simposio de Metrología
2. Thalmann R, Spiller J (2005) A primary roundness measuring machine. In: Proceedings of the recent developments in traceable dimensional measurements III, vol 5879. SPIE
3. Thalmann R, Spiller J, Küng A, Jusko O (2012) Calibration of Flick standards. Meas Sci Technol 23:094008
4. Roundness measurements, https://www.itl.nist.gov
5. ISO 12181-1:2003 (2003) Geometrical product specifications (GPS)–roundness part vocabulary and parameters of roundness. International Organization of Standardization
6. ISO 4291:1985: Methods for the assessment of departure from roundness-Measurement of variations in radius
7. Whitehouse DJ, Reason RE (1963) The equation of the mean line of surface texture found by an electric wave filter. Rank Organization, UK, London
8. Whitehouse DJ (1967) An improved type of wave filter for use in surface finish measurement. Proc Inst Mech Eng Part B J Eng Manuf 192:306–318
9. Whitehouse D (2002) Surfaces and their measurement
10. Hobson T, Roundness filters and harmonics. www.taylor-hobson.com
11. ISO 11562 (1996) Surface texture: profile method metrological characteristics of phase correct filters
12. Hobson T, Exploring roundness: a fundamental guide to the measurement of cylindrical form. www.taylor-hobson.com
13. Hobson T, What is roundness|methods of roundness measurement in metrology. www.taylor-hobson.com
14. Reason RE (1961) Report on reference lines for roughness and roundness. CIRP Ann Manuf Technol 2:95–104
15. ISO guide to the expression of uncertainty in measurement
16. Handbook/manual of surface roughness tester Mitutoyo CS-5000 CNC
17. Undulations per revolution (UPR) data in the roundness graphs. https://www2.mitutoyo.co.jp
18. Jewariya M, Ram J, Moona G, Singh G, Singh A, Kumar S, Sharma R (2022) Calibration of glass hemisphere and traceability at CSIR-National Physical Laboratory-India. Mapan. https://doi.org/10.1007/s12647-022-00562-5
19. Ali SHR (2015) Method of optimal measurement strategy for ultra-high-precision machine in roundness nanometrology. Int J Smart Sens Intell Syst 8(2):896–920
20. Kondo Y, Bitou Y, Sato O, Abe M, Calibration and uncertainty evaluation of flick standard using coordinate-measuring machine. National Metrology Institute of Japan (NMIJ), National Institute of Advanced Industrial Science and Technology (AIST). IMEKO-TC14-2014-59
21. Seewig J (2006) Linear and robust Gaussian regression filters. J Phys Conf Ser 13:254–257

Analysis of Effect of Seasonal Variations on the Environmental Noise Levels in Urban Zones

S. Kumar, N. Garg, and C. Gautam

Abstract The paper presents the effects of seasonal variations on environmental noise levels and also discusses the correlation of different meteorological factors with the ambient noise levels. The present study is conducted for two major cities of India–Delhi and Mumbai. The day and night equivalent levels of different seasons for ten sites of each of the two cities were analysed. No specific trend was observed for the seasonal variation of the noise levels for different seasons. It was observed that day, night, and 24 h equivalent levels show the highest values in the summer season.

Keywords Seasonal variation · Environmental noise · Noise pollution · Temporal trend

1 Introduction

Numerous health issues are continuously exacerbated by noise pollution, including hearing loss at a young age, high blood pressure, insomnia, lack of concentration, decreased productivity at work, various cardiovascular diseases, annoyance, etc., [1–3]. Unregulated traffic, industrial machinery, loudspeakers, and construction site activities, etc. are the major sources of elevated ambient noise levels. According to several studies, the ambient noise levels are also influenced by several other factors like variations in meteorological conditions. Ovenden et al. [4] demonstrated a 10–20 dB of variation in noise levels because of the meteorological conditions at significant distances from the highways [4]. According to Singh et al. [5], wind velocity and low relative humidity attenuate the ambient noise while the increase in temperature enhances the noise levels [5]. Chowdhury et al. [6] also reported a positive correlation of relative humidity and wind speed with respect to the noise levels

S. Kumar (✉) · N. Garg · C. Gautam
CSIR-National Physical Laboratory, New Delhi 110012, India
e-mail: saurabh.npl20a@acsir.res.in

Academy of Scientific and Innovative Research (AcSIR), Ghaziabad 201002, India

and a negative correlation of air temperature with the noise levels for Kolkata city [6]. Even the wind characteristics were observed to have convincing effects on the ambient noise [7]. Also, an increase of 0.4–1.9 dB in sound pressure levels has been reported when the wind velocity is increased by 1 m/s [8]. In addition, the meteorological parameters vary temporally with the seasons and weather conditions of an area, and various studies have shown the temporal variability of the ambient noise levels with different months and different weather conditions. Also, Jagniatinskis and Fiks [9] reported an increment in the standard deviation of monthly L_{DEN} from 1.3 dB to 5 dB when seasonal weather conditions were introduced [10]. Furthermore, Bjork [11] concluded that spring and autumn were the seasons with the highest noise levels while winter was the season with lowest noise levels [12]. In a recent study by Munir et al. [13], the variation of various noise descriptors in different seasons of the year and the correlation of noise levels with various meteorological parameters have been discussed and the summer season was identified as the season with the highest ambient noise levels in Peshawar city, Pakistan [14].

The present study is primarily focussed on the effects of different seasons on the environmental noise pollution in Indian scenario, seeking the pattern of variation of the noise levels with the change in seasons. This study has been conducted for the two major cities of India, i.e. Delhi, and Mumbai for the year 2020 with the following prime objective of investigating the effects of seasonal variations on the ambient noise levels in urban areas of the major cities of India.

2 Materials and Methods

Two metropolitan cities of India, Delhi and Mumbai were considered for the present study for the year 2020. In India, five seasons are mainly observed throughout the year: Winter (December and January), Spring (February and March), Summer (April to June), Monsoon (July to September), and Autumn (October and November). In the present study, the continuous monitoring of the ambient noise levels was conducted at ten sites of both cities by the noise monitoring stations installed by CPCB India. The technical details and working methodology of these noise monitoring stations are provided in an earlier study by Garg et al. [12]. The average day and night equivalent noise levels of each of the seasons were calculated by considering the peak month of every season—January was considered for the winter season, March was considered for the spring season, May was considered for the summer season, July was considered for the monsoon season, and October was considered for the autumn season [15]. The difference of the seasonal averages with respect to the annual average for each season is considered for the study and it is calculated as follows:

$$L_{\text{diff}} = L_{\text{annual,avg}} - L_{\text{season,avg}}$$

where, $L_{\text{annual,avg}}$ is the annual average of the noise levels of a particular site in dB(A) and $L_{\text{season,avg}}$ is the average noise level of a particular site for a season in dB(A).

3　Results and Discussion

3.1　Delhi City

It is observed from Table 1 that for the daytime, L_{diff} was recorded as highest at 4 out of 10 sites in the summer season and minimum at 4 sites in the winter season while for the nighttime, L_{diff} was observed to be highest at 4 sites in the summer season. In addition, it can be seen from Table 2 that the maximum L_{day}, L_{night}, and $L_{\text{Aeq,24 h}}$ were observed in summer season and minimum L_{day} was observed in monsoon season, L_{night} in the winter season, and $L_{\text{Aeq,24 h}}$ in the autumn season. It is observed from Fig. 1a and b that the highest seasonal day and night equivalent levels were recorded in autumn season at 4 sites and summer season at 4 sites respectively while the lowest seasonal day equivalent levels were recorded in the summer season at 4 sites and lowest night equivalent levels were recorded in spring and summer seasons at 3 sites each.

3.2　Mumbai City

It is observed from Table 1 that L_{diff} was recorded as highest at 6 sites in the summer season for the daytime and 5 sites in the summer season for the night time while L_{diff} was observed to be minimum at 5 sites in the autumn season for the daytime and 4 sites in monsoon season for the night time. Table 2 shows that the maximum L_{day} and L_{night} were observed in the summer season and the maximum $L_{\text{Aeq,24 h}}$ was observed in monsoon season while the minimum L_{day} was observed in the monsoon season and minimum L_{night} and $L_{\text{Aeq,24 h}}$ were observed in the summer season. From Fig. 2a and b, the highest seasonal day and night equivalent levels were observed in the autumn season at 5 sites and in monsoon season at 4 sites respectively. In addition, the lowest seasonal day and night equivalent levels were observed in the summer season at 7 and 5 sites respectively.

　　Although no specific trend was observed for the seasonal noise levels of both cities it has been observed that the day, night, and 24 h equivalent noise levels appeared to be maximum in the summer season in both the cities. The reason could be the fact that the speed of sound increases with the rise in atmospheric temperature, which causes listeners to perceive higher ambient noise levels [14].

Table 1 Summary of L_{diff} of 20 noise monitoring sites in each of the five seasons for two major cities of India for the year 2020

Parameters (in dB(A)) for eqv. sound levels	Noise monitoring sites in Delhi city									
	ANAND VIHAR		CIVIL LINES		CPCB		DCE		DILSHAD GARDEN	
	Day	Night	Day	Night	Day	Night	Day	Night	Day	Night
Site Zone	Commercial		Commercial		Commercial		Silence		Silence	
$L_{annual,\ avg}$	65.5	60.6	60.6	57.3	64.5	67.4	57.2	54.8	70.4	70.6
Std. Dev.	4.9	5	0.5	0.4	2	3.1	3.3	3.1	3.6	3.8
$L_{diff,\ Winter}$	−3	−3.1	−0.6	−0.6	−2.4	−0.6	0	−1.4	4.7	4.6
$L_{diff,\ Spring}$	1.6	−1	0	0.3	−0.7	0.8	−1.8	−2.7	3.2	3.9
$L_{diff,\ Summer}$	5.1	6.7	0.4	−0.1	3.1	3	−3.8	−2.2	2.7	2.2
$L_{diff,\ Monsoon}$	4.2	5.2	−0.6	0.3	0.3	−1.2	3.2	2.8	2.7	3.3
$L_{diff,\ Autumn}$	−6.5	−4.3	0.3	0.1	−0.8	−5.4	4.1	3.9	−4.6	−4.7

Parameters (in dB(A)) for eqv. sound levels	Noise monitoring sites in Mumbai city									
	ACWORTH HOSPITAL		AMBASSADOR HOTEL		BISLERI ANDHERI		BANDRA		MPCB HEAD QUARTERS	
	Day	Night	Day	Night	Day	Night	Day	Night	Day	Night
Site Zone	Silence		Commercial		Industrial		Commercial		Commercial	
$L_{annual,\ avg}$	71.7	69.8	74.2	69.6	80.1	79.6	74.7	74.4	72.9	64.1
Std. Dev.	3.9	4.4	3.3	2.1	5.1	4.3	4.1	4.2	4.2	5.5
$L_{diff,\ Winter}$	4.8	4.2	−1.9	−1.5	1	0.7	4.4	4.4	4.8	−2.7
$L_{diff,\ Spring}$	−1.2	7.2	1	0.9	5.1	3.7	5.4	7.9	4.2	−3.3

(continued)

Table 1 (continued)

Parameters (in dB(A)) for eqv. sound levels	Noise monitoring sites in Delhi city									
	ANAND VIHAR		CIVIL LINES		CPCB		DCE		DILSHAD GARDEN	
	Day	Night	Day	Night	Day	Night	Day	Night	Day	Night
$L_{diff, Summer}$	4.8	4.9	6.1	2.1	−6.8	−5.5	7.8	7.6	−3.5	6.2
$L_{diff, Monsoon}$	4.5	−0.6	−2.2	−2.8	0.6	1.6	−3.3	−2.5	6.4	7.6
$L_{diff, Autumn}$	−3.4	−3.6	0.1	1.3	5.9	5.9	3.1	5.2	7	7.1

Parameters (in dB(A)) for eqv. sound levels	Noise monitoring sites in Delhi city									
	ITO		MANDIR MARG		NSIT		PUNJABI BAGH		RK PURAM	
Site Zone	Commercial		Silence		Silence		Residential		Residential	
	Day	Night	Day	Night	Day	Night	Day	Night	Day	Night
$L_{annual, avg}$	79.8	75.6	58.3	56.6	57.4	54.3	57.3	51.7	63.3	59.2
Std. Dev.	5.3	3.4	3	5.4	2.1	1.4	0.8	1.5	2.5	1.3
$L_{diff, Winter}$	3.8	3.1	3.9	7.2	−2.7	−1.2	−0.6	0.2	1.8	4.6
$L_{diff, Spring}$	6.2	2.5	−0.3	5.5	−0.5	0	0.6	0.8	2.5	1.8
$L_{diff, Summer}$	−6.7	−5.3	−3.8	−5.6	3	2.6	0	−2.4	0.7	4.8
$L_{diff, Monsoon}$	−2.2	−1	2.3	7	0.4	−0.4	0.2	−0.8	6.1	2.5
$L_{diff, Autumn}$	3.3	0.3	−0.8	5.1	0.4	−0.2	1.6	1.3	−0.4	3.3

Parameters (in dB(A)) for eqv. sound levels	Noise monitoring sites in Mumbai city									
	LT POWAI		MM KANDIVALI		PEPSICO CHEMBUR		TMCO		VASHI HOSPITAL	
	Day	Night	Day	Night	Day	Night	Day	Night	Day	Night

(continued)

Table 1 (continued)

Site Zone	Industrial		Industrial		Residential		Commercial		Silence	
$L_{annual, avg}$	62.2	60	60.8	53.8	76.5	75.4	67.9	68.6	69.4	69.1
Std. Dev.	2.3	2.1	3.2	1.5	3.7	4	0.9	1.3	4.8	4.9
$L_{diff, Winter}$	4.6	5.4	0.8	0.7	−2.3	2.9	−1.9	−1.9	1.3	0.6
$L_{diff, Spring}$	3.4	7.8	1.9	1.6	-0.1	3.9	0.2	−0.7	3.5	2.9
$L_{diff, Summer}$	2.8	4.6	5.2	3.6	3.4	6.6	−0.3	1.5	7.6	7
$L_{diff, Monsoon}$	1.5	1.9	−0.2	−0.3	−1.7	3.1	0.3	0.2	2.8	3
$L_{diff, Autumn}$	−1.5	4	−3.5	2	−6.7	−4.1	0.5	0.5	−5.6	−6.3

Table 2 Maximum and minimum noise levels in different seasons

Seasons	Delhi						Mumbai					
	L_{day}		L_{night}		$L_{\text{Aeq,24 h}}$		L_{day}		L_{night}		$L_{\text{Aeq,24 h}}$	
	Max	Min	Max	Min	Max	Min	Max	Min	Max	Min	Max	Min
Winter	83.8	48	81.1	42	82.6	47.2	83.9	42.1	84.9	44.7	83.6	45.7
Spring	80.2	50.7	76.4	44	79.1	49.9	80.7	43.6	79.9	44.6	79.7	44.8
Summer	89.5	45	86.3	42.1	89.5	48.7	89.1	41.8	89.6	40.3	88	40.1
Monsoon	87.8	44.3	82.7	43.7	86.4	47.8	89	40.7	89.3	40.7	88.6	41.2
Autumn	85.2	47.2	81	43.8	83.9	46.5	86.9	46.1	86.6	43.5	86.8	45.6

4 Conclusions

The ambient noise levels of two metropolitan cities of India have been studied for different seasons throughout the year 2020 and the following conclusions can be derived from the present work:

- There is no specific pattern observed for the seasonal average of noise levels for different seasons for the ten locations of both cities. A possible reason for this result could be the fact that the traffic flow in Indian cities is heterogeneous and due to the heterogeneity of the traffic flow, the traffic noise dominates over the effects of seasonal impact on the noise levels, and thus no specific pattern is observed for the same.
- The maximum L_{day}, L_{night}, and $L_{\text{Aeq,24 h}}$ levels are observed in the summer season. The reason could be the fact that the speed of sound increases with the rise in atmospheric temperature, due to which higher noise levels were recorded in summer.
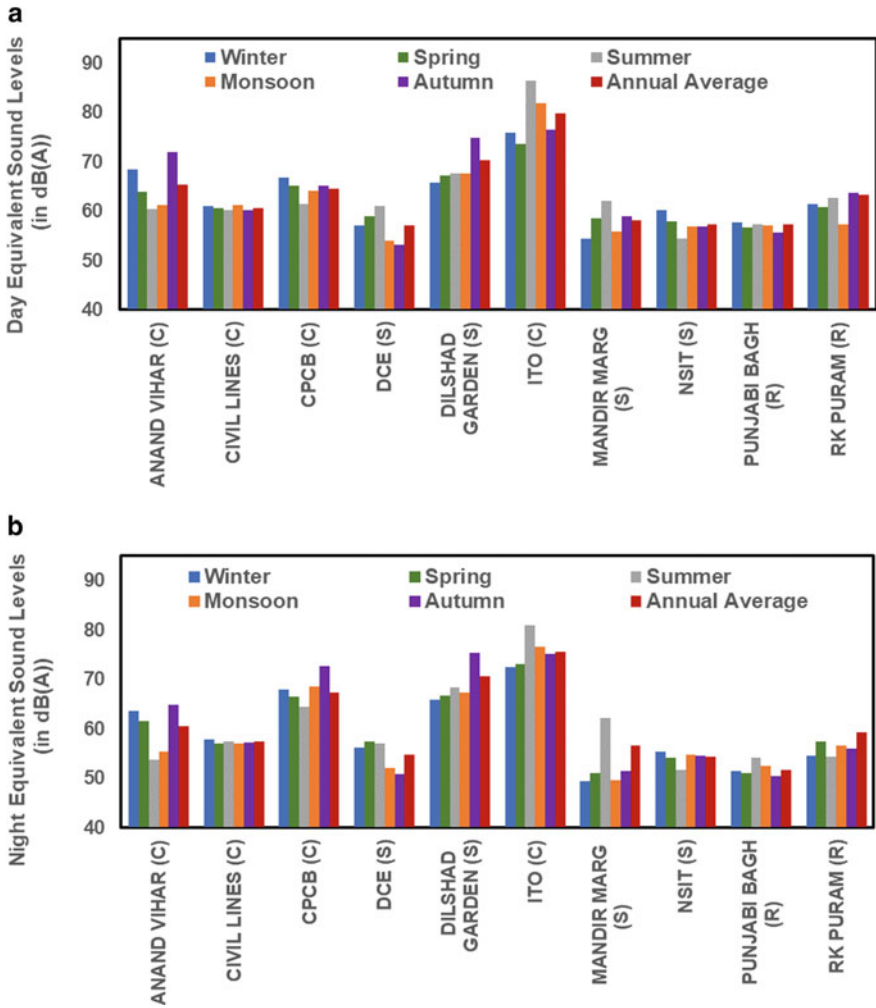
a

b

Fig. 1 **a** Day equivalent sound levels of ten sites of Delhi city in all seasons for the year 2020.
b Night equivalent sound levels of ten sites of Delhi city in all seasons for the year 2020
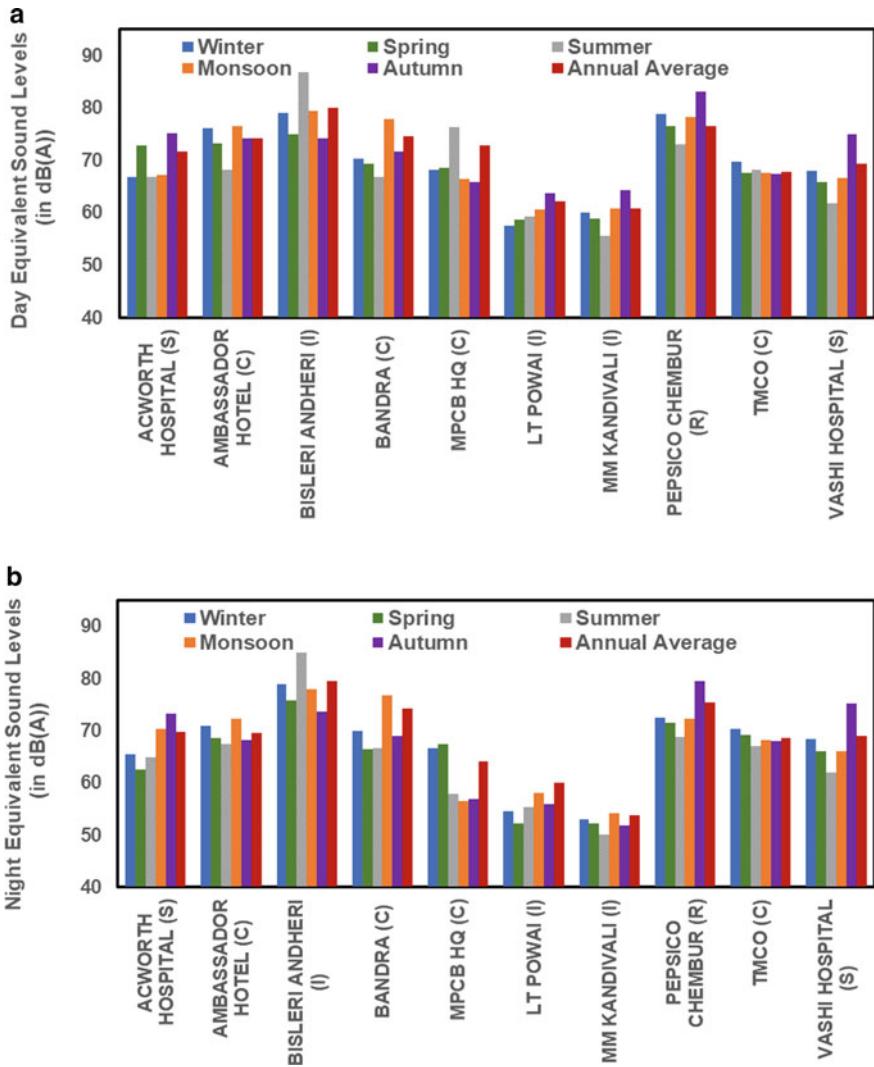
Fig. 2 a Day equivalent sound levels of ten sites of Mumbai city in all seasons for the year 2020. **b** Night equivalent sound levels of ten sites of Mumbai city in all seasons for the year 2020

References

1. Hahad O, Prochaska JH, Daiber A, Muenzel T (2019) Environmental noise-induced effects on stress hormones, oxidative stress, and vascular dysfunction: key factors in the relationship between cerebrocardiovascular and psychological disorders. Oxidative Med Cell Longev 2019:4623109. https://doi.org/10.1155/2019/4623109

2. Fritschi L, Brown A, Kim R, Schwela D, Kephalopoulos S (eds) (2011) Burden of disease from environmental noise: quantification of healthy life years lost in Europe. WHO Regional Office for Europe, Copenhagen, Denmark. JRC64428

3. Münzel T, Gori T, Babisch W, Basner M (2014) Cardiovascular effects of environmental noise exposure. Eur Hear J 35(13):829–836. https://doi.org/10.1093/eurheartj/ehu030

4. Ovenden NC, Shaffer SR, Fernando HJS (2009) Impact of meteorological conditions on noise propagation from freeway corridors. J Acoust Soc Am 126(1):25–35

5. Singh D, Prakash A, Srivastava AK, Kumar K, Jain VK (2013) The effects of meteorological parameters in ambient noise modelling studies in Delhi. Environ Monit Assess 185(2):1873–82

6. Chowdhury AK, Debsarkar A, Chakrabarty S (2015) Critical assessment of day time traffic noise level at curbside open-air microenvironment of Kolkata City, India. J Environ Heal Sci Eng 13(1):1–6. https://doi.org/10.1186/s40201-015-0219-6. (Internet)

7. Ayanlade A, Oyegbade EF (2016) Influences of wind speed and direction on atmospheric particle concentrations and industrially induced noise. Springer Plus 5:1898. https://doi.org/10.1186/s40064-016-3553-y

8. Trikootam SC, Hornikx M (2019) The wind effect on sound propagation over urban areas: experimental approach with an uncontrolled sound source. Build Environ 149(August 2018):561–70. https://doi.org/10.1016/j.buildenv.2018.11.037

9. Jagniatinskis A, Fiks B (2014) Assessment of environmental noise from long-term window microphone measurements. Appl Acoust 76:377–85. https://doi.org/10.1016/j.apacoust.2013.09.007

10. Garg N, Sinha AK, Gandhi V, Bhardwaj M, Akolkar AB (2016) A pilot study on the establishment of national ambient noise monitoring network across the major cities of India. Appl Acoust 103(Part A):20–29

11. Björk EA (1994) Community noise in different seasons in Kuopio Finland. Appl Acoust 42(2):137–150

12. Garg N, Sinha AK, Sharma MK, Gandhi V, Bhardwaj RM, Akolkar AB, Singh RK (2017) Study on the establishment of a diversified National Ambient Noise Monitoring Network in seven major cities of India. Curr Sci 113(7):10

13. Munir S, Khan S, Nazneen S, Ahmad SS (2021) Temporal and seasonal variations of noise pollution in urban zones: a case study in Pakistan. Environ Sci Pollut Res. https://doi.org/10.1007/s11356-021-12738-8

14. Riki T, Morris P (1995) Methods of environmental impact assessment. UBC Press-London, Vancouver

15. India meteorological department website. https://mausam.imd.gov.in/imd_latest/contents/seasonal_forecast.php

Importance of Cosine Response of Optical Detectors in Irradiance/ Illuminance Measurements

Vijeta, Rajeev Dwivedi, Shibu Saha, V. K. Jaiswal, and Parag Sharma

Abstract Quantification of artificial lighting is an important aspect in the field of radiometry and photometry. Optical detectors are employed for the radiometric and photometric measurements and need to be characterized in terms of linearity and angular response. This work highlights the importance of the cosine response of detectors while doing illumination measurements under different lighting conditions. It is found that the measurements under quasidirectional light sources result in erroneous values whereas the uniform distribution of illumination minimizes the measurement errors irrespective of the detector positioning. The discrepancies in the irradiance/illuminance measurements are attributed due to the cosine errors of the detectors. The analysis clearly shows the importance of ascertaining the linearity and angular response of detectors before employing them for measurement purposes. A study of angular response and corresponding measurement errors in irradiance/ illuminance is also done.

Keywords Optical detector · Linearity · Angular response · Cosine error · Illuminance

1 Introduction

In recent times, artificial lighting has become a necessary aspect of human life. It is utilized in a wide range of applications from industry to education to healthcare to home tasks etc. The measurement of artificial light can be broadly categorized in the fields of radiometry and photometry. Photometry is concerned with measuring light as

Vijeta · R. Dwivedi · S. Saha · V. K. Jaiswal · P. Sharma (✉)
CSIR-National Physical Laboratory, Dr. K.S Krishnan Marg, New Delhi 110012, India
e-mail: sharmap2@nplindia.org

Vijeta · P. Sharma
Academy of Scientific and Innovative Research (AcSIR), Ghaziabad 201002, India

R. Dwivedi
Laboratoire Hubert Curien, Université Jean Monnet, Saint-Étienne, France

perceived by the human eye, whereas radiometry encompasses measurements of the optical power of illuminations [1–3], and quantification of illumination is facilitated by optical detectors [4]. The optical detector is based on the principle of transducing the radiometric power, illuminating the detector surface, to a proportionate electrical signal. The output signal of an optical detector is proportional to the optical power irradiating a unit area of the detector is termed as irradiance in the context of radiometric measurement and illuminance, when weighed by the response of an average human eye [5]. As the detector forms the basis of photometric and radiometric measurements, hence for accurate photometric and radiometric measurements, the characterization of the detector is important [6, 7]. Establishing traceability of the measurements, to SI units, is a crucial part of the characterization process, and is achieved by calibration of the detector [4, 5]. Calibration of detectors is carried out in the laboratory under the ideal condition of normal incidence and usually at a single point. However, practical conditions are not always the same as that in the laboratory. While performing calibrations under practical conditions, the detectors may be subjected to conditions like illumination levels beyond the calibration range, and angular incidence of illumination. Hence, detector properties like linearity and angular response of detectors are required to be determined, for ensuring accuracy in the measurements [5, 8, 9]. The present article describes a study carried out to quantify the errors introduced in measurements made by commercial detectors under practical illumination conditions. An experimental setup was designed to investigate the performance of commercial detectors. The errors in measurement under three different illumination conditions were recorded. The analysis of the data shows that the angular response of detectors plays a major role in determining the reliability of their measurements. It was also observed that the non-linearity of detectors gives a misleading impression about the deviation of angular response from the ideal cosine response and needs to be verified before making measurements.

2   Experimental Procedure

2.1   *Determination of Linearity of Detectors*

The linearity of detectors is generally mentioned in their datasheet; however, it is better to verify before the measurements. For ensuring this, the response of the test detectors was compared with that of the working standard lux meter traceable to SI at different illuminance levels. The illuminance level was varied by changing the source-detector distance on an optical bench. It was verified that the range of illuminance used in the linearity study of the detectors includes the level of illuminance at which the angular responses were measured.

2.2 Determination of Angular Response of Detectors

The picture and schematic diagram of the experimental setup for determining the cosine response of detectors are shown in Fig. 1a and b, respectively. The setup was established in a dark room, simply consisting of a stable light source and the optical detectors under test mounted on a graduated rotating stage. An incandescent light source of 200W powered by a stable AC source was used for illuminating the test detectors. The test detector was made to rotate about its vertical axis in discrete steps (shown in Fig. 1c and d) keeping a constant distance between the light source and the center of the detector. This experiment was performed for the source-detector distance of 50 cm. The detector under test was mounted on a computer-controlled motorized rotary stage. Before starting the experiment, a proper alignment of the source and the test detector was ensured for normal incidence and measurements from the detectors were recorded in steps of 5° angular rotation on both sides. The angular response determined by the above setup should ideally be the same as the cosine response. However, practical detectors do not exhibit an ideal cosine response. The deviation of the angular response of detectors from an ideal cosine response is quantified by a parameter known as the integral cosine error. For determining the said parameter, angle-dependent cosine error, $f_2(\theta)$ given by the International Commission of Illumination, 1982] is calculated as [8]:

$$f_2(\theta) = \left[\frac{E(\theta)}{\mathrm{Cos}\theta\, E_0} - 1 \right]$$ (1)

where θ is the angular deviation of the incident light from the normal to the detector surface, $E(\theta)$ is the signal measured at the angle θ and E_0 is the signal measured under normal incidence. The integral cosine error $<f_2>$ (directional response index) is then evaluated as [10]:

$$< f_2 > = \int_{0°}^{85°} |f_2(\theta)| \cdot \sin 2\theta d\theta$$ (2)

The value of $<f_2>$ or performance index is zero for detectors having ideal cosine response and increases with a decrease in the angular performance of the detector.

2.3 Experimental Realization of Different Lighting Conditions Inside a Cuboidal Enclosure

To simulate actual lighting conditions inside a closed room, a cuboidal enclosure (of dimensions $50 \times 50 \times 54$ cm) was prepared as shown in Fig. 2. Five planar 3W LED sources (S, S1–S4) were placed at the roof (or top face of the enclosure) to obtain
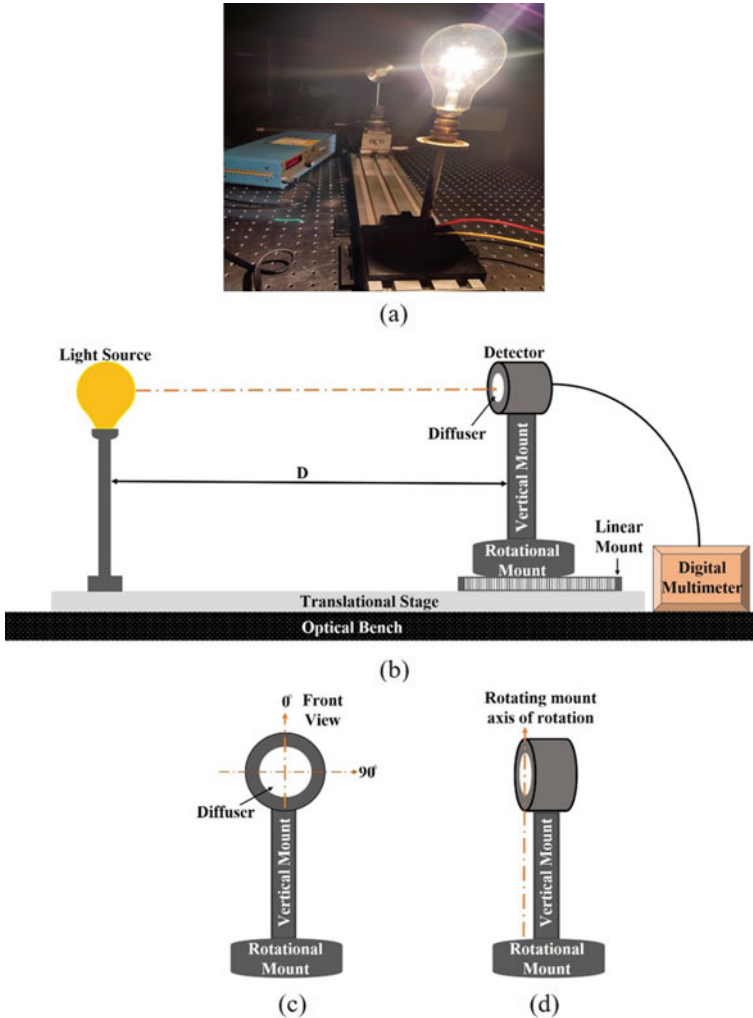
Fig. 1 a Photo of experimental setup established in the laboratory; **b** Schematic of the designed experimental setup; **c** Front view of optical detector showing the rotation of detector surface to incident light; **d** Lateral view of detector showing the axis of rotation of rotating mount

uniform distribution, as shown in Fig. 2a. The test detectors were placed at different positions on the floor for recording the illuminance measurements. To ensure precise and repeatable positioning of the detector on the floor, the box was marked to be divided into a grid of 5×5 matrix. The measurements were obtained by placing the test detectors at the center of different grids, which can be seen in Fig. 2b.

Three lighting arrangements were realized experimentally with the lights installed on the top face of the cuboidal enclosure, which is schematically shown in Fig. 3a–c [5]. The light source centered at the top face (Fig. 3a) has been considered to
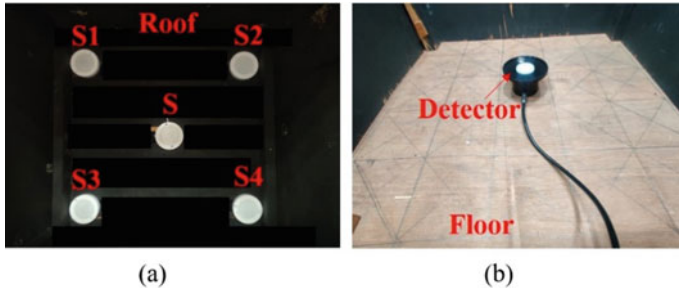
Fig. 2 **a** Photograph of the roof of the cuboidal enclosure, installed with four 3W planar LEDs at the corners and one 3W planar LED at the center; **b** Photograph of the floor of the cuboidal enclosure divided into a grid of 5 × 5 matrix and detector placed at one of the grids of the floor for the measurement
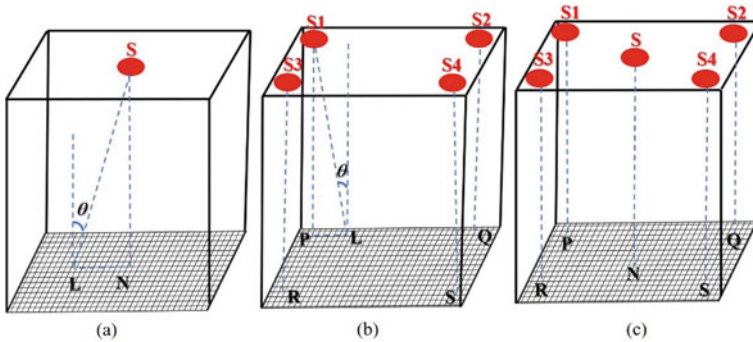

Fig. 3 Schematic of the cuboidal enclosure under different lighting conditions **a** *Sim-1*; **b** *Sim-2*; **c** *Sim-3*

simulate lighting conditions concentrated at the center of an enclosure (*Sim-1*). The configuration depicted in Fig. 3b simulates a condition of spatially apart multiple light sources placed at the far expanse of an enclosure (*Sim-2*). The schematic depicted in Fig. 3c is designed to obtain a uniformly distributed light in the enclosure (*Sim-3*).

2.4 Detectors Under Study

Six test detectors as shown in Fig. 4, were chosen for the experimental study, two were photodetectors (D1, D2), three were commercially available lux meters (D3, D4, D5), and one working standard lux meter (D6) traceable to SI. All the detectors were calibrated by a standard procedure and also tested for repeatability by subjecting them to multiple measurements under the normal incidence of illumination. The detectors D1 and D2 were found to have an uncertainty of 1.0% in their measurement; while

Fig. 4 Test detectors D1, D2, D3, D4, D5, D6 used for study

D3, D4, and D5 have an uncertainty of 0.8%. The working standard lux meter D6 has a measurement uncertainty of 0.5%.

3 Results and Discussion

3.1 Linearity of Test Detectors to Working Standard Lux Meter

The linearity study was carried out over a range of illumination achieved inside the cubical enclosure meant for the experiment. The comparison of the normalized output of the test detectors D1, D2, D3, D4, and D5 with that of a working standard lux meter (D6) under the same illumination is shown in the graphs presented in Fig. 5.

It can be inferred from the graphs in Fig. 5, that output of the detectors D1 and D2 do not vary linearly to the illuminance measured by the working standard lux meter. On the other hand, variations of the output of commercial lux meters D3, D4, and

Fig. 5 Response of detectors (D1–D5) to the illuminance measured by working standard lux meter (D6)
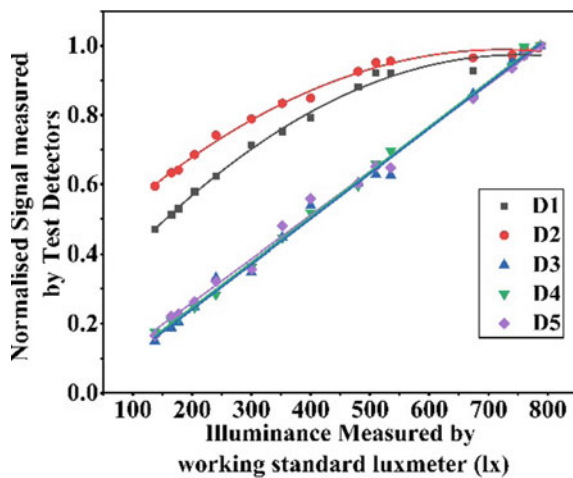
D5 vary linearly to the output of the working standard lux meter (D6) under similar illumination conditions.

3.2 Angular Response of Detectors Under Study

The angular response of the detectors under study was measured using the experimental setup depicted in Fig. 1, at an illuminance level (E_v) of 790 lx. This illuminance was chosen for ascertaining the angular responses, as the highest illumination recorded in the experimental enclosure was of a similar order. The plots of angular response obtained for the test detectors are shown in Fig. 6 along with the ideal cosine response.

It is observed that the detectors D3, D4, D5, and D6 show an angular response that is quite close to the ideal cosine response. However, the detectors D1 and D2 show a hump-type angular response that makes them prone to erratic measurement outputs in cases of oblique incidence of illumination. The error in illuminance measurement at the normal incidence position is due to the non-linear response. The quality of the detectors to their angular response can be quantified by calculating the integral cosine error ($<f_2>$), which is tabulated in Table 1.

As discussed earlier, the output signal of the detectors D1 and D2 do not vary linearly to illumination as the angular responses of the detectors deviate from the

Fig. 6 Cosine responses of the detectors (D1–D6) to detector following ideal cosine response
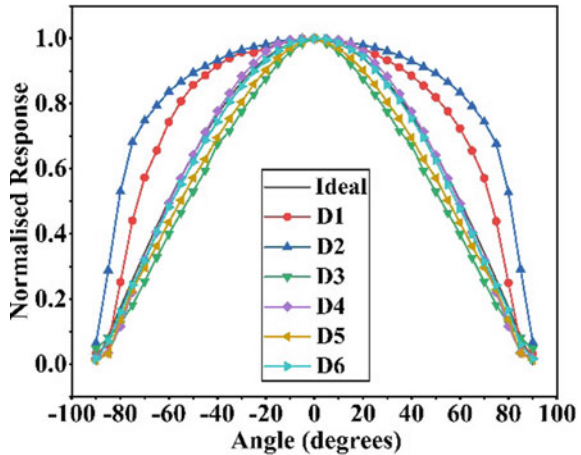
Table 1 Integral cosine error ($<f_2>$) of test detectors used for measurement

Detectors	D1	D2	D3	D4	D5	D6
$<f_2>$	14.9	28.1	8.79	2.37	6.00	1.69

ideal cosine response. Since at higher illuminations, the detector output starts saturating, hence a small fall in the illumination level with an increase in the angle of incidence (especially at angles closer to 0°), does not produce a proportional drop in the detector's output signal, leading to the flatness in angular response. On the other hand, the proximity of the angular response of the test detectors D3, D4, and D5 to the ideal cosine response may be attributed to the linear variation of the output of test detectors with illuminance in the testing range (Fig. 5). The angular response of detector D1 was again obtained, but now in lower illumination condition (E_v = 155 lx), wherein the detector response is linear. The angular response in this illumination level is quite close to the ideal cosine response curve (Fig. 7) and the corresponding integral cosine error ($<f_2>$) for detectors D1 was calculated to be 1.97.

The results indicate that the angular response of the detectors is also related to the level of illumination. Non-linearity in detector response at a particular illuminance range may adversely affect the angular response of the detector. Hence, to ascertain the usefulness of a detector in a particular illumination level (in terms of linearity and angular response), it would be advisable to verify its linearity first. The proximity of the angular response to the ideal cosine response is also indicative of the fact that the detector characteristics would be linear up to that illumination level, at which the angular response has been ascertained. However, only the linearity of a detector does not ensure a proper angular response.

Fig. 7 Cosine response of test detector D1 in lower illumination to the working standard lux meter D6
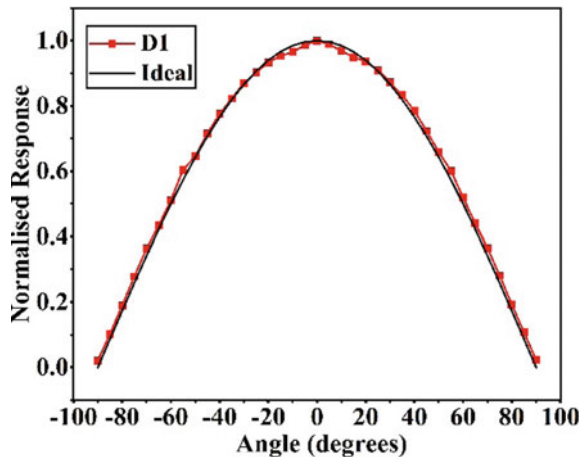
3.3 Illuminance Measurements Under Different Illumination Conditions Inside a Cuboidal Enclosure

It was observed that detectors D1 and D2 are non-linear and have flat cosine responses in higher illumination levels. Hence, illuminance measurements were done using test detectors D3-D5 and working standard lux meter, D6 having their angular responses close to the ideal cosine response. Measurements were performed under different lighting conditions as explained in Sect. 2.2.

All the experimental illuminance data were normalized to the respective illuminance measurements made by the detectors at normal incidence to the source S and compared with theoretical data (detector following ideal cosine response) as shown in Fig. 8a–c.

The relative error in the experimental measurement of each detector to the theoretical simulation was calculated. The normalized illuminance data obtained experimentally ($E_{v;N\text{-}Exp}$) was compared with the theoretical data ($E_{v;Theory}$) and the relative error due to angular response was calculated as:

$$Relative\ Error_{Angular}(\%) = \frac{E_{v;Theory} - E_{v;N-Exp}}{E_{v;Theory}} \times 100 \tag{3}$$

This relative error was calculated for illuminance measurements made by all four detectors at all twenty-five grid positions under all three illumination conditions. The
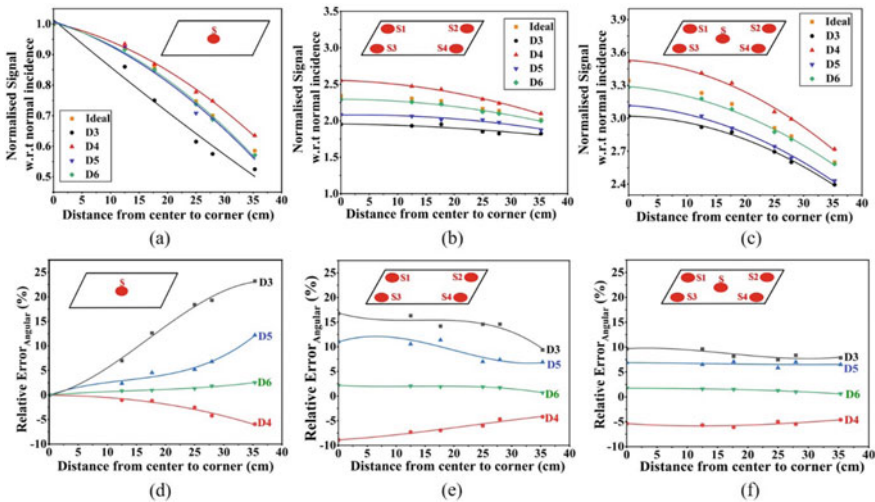

Fig. 8 Theoretical simulation of normalized illumination measurements by detectors D3-D6 and ideal detector w.r.t normal incidence position **a** *Sim-1*; **b** *Sim-2*; and **c** *Sim-3*. Relative measurement errors (%) of test detectors (D3-D6) to the detector following ideal cosine response, observed at the floor of cuboidal enclosure on moving away from central grid to the corners **d** *Sim-1*; **e** *Sim-2*; and **f** *Sim-3*

Table 2 Maximum relative errors (%) recorded by test detectors under different illumination conditions

Detectors	Sim-1	Sim-2	Sim-3
D3	23.2	16.8	9.64
D4	−5.94	−8.90	−5.37
D5	12.2	11.1	6.91
D6	2.52	2.16	1.76

Table 3 Standard deviation of relative errors (%) recorded by test detectors in different illumination conditions

Detectors	Sim-1	Sim-2	Sim-3
D3	7.92	2.39	0.83
D4	2.03	1.59	0.47
D5	3.81	1.98	0.42
D6	0.79	0.49	0.38

distance of the grids from the central grid position was evaluated. The illuminance measurements made at grid positions at the same distance from the central grid were averaged before the error calculations. The evaluated relative errors for the test detectors and working standard lux meter at different positions under different illumination conditions are graphically shown in Fig. 8.

The maximum relative errors recorded by each detector in every configuration are tabulated in Table 2. For quantifying the variation in the relative errors, the standard deviation of the relative errors was calculated as shown in Table 3.

3.3.a. Measurements under Sim-1: The measurement errors were found to be zero at the central grid due to normal incidence. The data (Table 2) shows that the maximum relative error is highest for the test detector D3 which can be attributed to the poor cosine response as compared to the other three detectors. The increase in relative errors on moving away from the central grid is much faster in detectors having larger $<f_2>$. The standard deviation of the relative errors for test detector D3 ($<f_2> = 8.79$) is calculated to be 7.92% while the measurements using working standard lux meter D6 have a minimum $<f_2>$ of 1.69 shows a standard deviation of 0.79%. The negative relative errors in the case of test detector D4 are because the response of the said detector is larger than the ideal cosine response at all angles, while the other detectors (D3, D5, D6) have a lower response to the ideal and has a positive relative error.

3.3.b. Measurements under Sim-2: The spatially apart multiple light sources create a condition wherein the detectors placed at the center will have maximum illumination but under angular incidence. However, as we move away from the central grid, the relative error starts decreasing and becomes minimum at the corners. The change in the relative errors for all four detectors (D3-D6) is quite less as the measurement position moves away from the central grid. The maximum standard deviation in relative errors is calculated to be 2.39% for detector D3, which is much lesser than illumination condition *Sim-1* (standard deviation of 7.92%).

3.3.c. Measurements under Sim-3: In this case, each point receives a higher quantity of normal illumination as compared to oblique illumination. This further leads to a much smaller deviation in relative errors due to the position of detectors, as is evident from Table 3. However, unlike the *Sim-1* configuration, the relative error is maximum at the central grid in this case and *Sim-2*. Here, it is important to point out that the deviations in angular response to the ideal cosine are maximum in the mid-angle range and lowest at both extremes of 0º and 90°. Hence, as the angle of incidence increase beyond a point, the contribution to errors due to angular response again decreases.

4   Conclusion

This manuscript presents the experimental results signifying the importance of linearity and cosine response of commercial detectors for practical field applications. It is observed that the discrepancies in photometric measurements are attributed due to the deviation of angular response from the ideal cosine response. A thorough investigation of the cosine response of detectors and their impact on the illuminance measurements under different practical lighting conditions is done. It has been found that the measurements under uniform illumination are more reliable as compared to the concentrated ones irrespective of detector positioning. Moreover, the variations in the measurement errors under uniform illuminations are very less and are quite significant for application purposes where quantified illumination is needed. It is concluded that the detectors should be calibrated for multiple illumination points rather than a single point to modify their cosine response and reduce the measurement error.

References

1. Bertenshaw D (2019) Light and photometry, the path to standardization. Bertenshaw DR" Light and Photometry, the Path to Standardisation". Die Vierte Wand, Initiative Theatermuseum Berlin, BV, vol 9, pp 152–163
2. Vijeta, Sharma P, Jaiswal VK, Saha S, Mehrotra R (2021) Study of array detector based spectrophotometer for sphere photometry. In: ICOL-2019, pp 565–569
3. Yadav S, Shivagan DD, Bapna K, Jaiswal VK, Sharma P, Saha S, …, Aswal DK (2020) Physico-mechanical metrology: part III: thermal, optical radiation and acoustic metrology. In: Metrology for inclusive growth of India, pp 307–376
4. Sharma P, Jaiswal VK, Saha S, Aswal DK (2022) Metrological traceability and crucial detector characteristics for UVC metrology in UVGI applications. MAPAN_J Met Soc India 1–13

5. Vijeta, Kapri RK, Saha S, Jaiswal VK, Sharma P (2021) Theoretical simulation for evaluating error in irradiance measurement using optical detectors having different cosine responses. MAPAN_J Met Soc India 36(3):473–480. https://doi.org/10.1007/s12647-021-00486-6
6. Wyatt C (2012) Radiometric calibration: theory and methods. Elsevier
7. Uppinakudru AP, Reynolds K, Stanley S, Pablos C, Marugán J (2022) Critical assessment of optical sensor parameters for the measurement of ultraviolet LED lamps. Measurement 196:111278
8. Mekaoui S, Zibordi G (2013) Cosine error for a class of hyperspectral irradiance sensors. Metrologia 50(3):187
9. Cahuantzi R, Buckley A (2017) Geometric optimisation of an accurate cosine correcting optic fibre coupler for solar spectral measurement. Rev Sci Instrum 88(9):095003
10. Commission internationale de l'eclairage. Characterization of the performance of illuminance meters and luminance meters. CIE Publication S023CIE S023/E:2013. (CIE 2013)

Realization of Total Spectral Radiant Flux of an Incandescent Lamp with Three Spectroradiometer Configurations

Vijeta, Shibu Saha, V. K. Jaiswal, and Parag Sharma

Abstract In an attempt to realize the total spectral radiant flux (TSRF) scale from spectral irradiance and total luminous flux, a study has been carried out to determine the suitability of the spectroradiometric configurations for sphere spectroradiometric measurements. Three spectroradiometric configurations have been studied and spectral irradiance measured from all the configurations was used to derive the TSRF scale, which has been used for the calibration of sphere-spectroradiometer system. Total luminous flux of a set of test lamps was measured under all three calibrations. Ananalysis of the measured total luminous flux has been done to ascertain the suitability of all the configurations for deriving TSRF from the spectral irradiance.

Keywords Total luminous flux · Sphere-spectroradiometer · Total spectral radiant flux · Spectral irradiance

1   Introduction

With the development, artificial lighting has become an integral part of our day-to-day life [1]. In the general lighting sector, LED (Light Emitting Diode) sources have totally replaced conventional light sources like incandescent and fluorescent lights. In developing countries, nearly 20–25% of the electric energy is used in illumination which is about 5% of the consumption of total energy [2]. LEDs are the most energy-efficient light sources used for illumination and are best suited for commercial purposes due to their environment-friendly nature. This has made LED lighting immensely popular for general illumination. Hence, the measurement and calibration of LED sources have become important.

Vijeta · S. Saha · V. K. Jaiswal · P. Sharma (✉)
CSIR-National Physical Laboratory, Dr. K.S Krishnan Marg, NewDelhi 110012, India
e-mail: sharmap2@nplindia.org

Vijeta · P. Sharma
Academy of Scientific and Innovative Research (AcSIR), Ghaziabad 201002, India

Accurate measurements of light are very crucial in scientific and technological applications, industries, manufacturing markets, environmental surveys, and health and safety sectors [3, 4]. The measurement of artificial light sources and corresponding calibration procedures are studied in the field of radiometry and photometry. Photometry is the measurement of light taking the human eye response into consideration, while the measurement of radiant power irrespective of the human vision is covered in radiometry [5–7]. Any artificial light source meant for different illumination requirements is characterized by its photometric parameters. Total luminous flux is one of the fundamental photometric quantities that is used to quantify the luminous power/flux exuded by a light source in all directions [8]. The total luminous flux of light sources can be usually measured by two methods: goniophotometer and integrating sphere which are absolute and relative methods respectively. The testing laboratories prefer the relative method due to good turn-around-time, and low-cost of initial investment. In recent times, conventional photometer-based integrating spheres have been replaced by spectroradiometer-based integrating spheres for the photometric and colorimetric measurements of light sources [6]. The sphere spectroradiometer system is calibrated against a reference standard of known total spectral radiant flux (TSRF) [8]. However, the current standard allows the total spectral radiant flux lamp to derive its traceability from spectral irradiance and total luminous flux standards, both traceable to the SI [9].

In an effort to establish traceability of the TSRF scale from spectral irradiance and total luminous flux scale, an initial study has been done to ascertain the suitability of spectroradiometer configurations for sphere spectroradiometer system. In the present study, three spectroradiometric configurations have been studied for deriving the scale of TSRF. Total luminous flux of different test lamps was measured from sphere spectroradiometer sytem, against the calibration of TSRF scale derived from different configurations to ascertain their suitability.

2 Experimental Procedure

Three spectroradiometric configurations were used for determining spectral irradiance to derive the traceability of TSRF. The first configuration (method 1), is a double monochromator based spectroradiometer having an integrating sphere of 150 mm diameter as the input optics (Fig. 1) [10]. A handheld CCD array based spectroradiometer was used in the other two different configurations. The second configuration (method 2) consists of the CCD array based spectroradiometer connected to another integrating sphere of 80 mm diameter through a multi-mode optical fiber as shown in Fig. 2. The CCD array based spectroradiometer was integrated with a PTFE cosine diffuser through the optical fiber in the third configuration (method 3) as shown in Fig. 3.

In all the arrangements the respective spectroradiometer was firstly calibrated against a standard lamp. This was followed by the spectral irradiance measurement of a seasoned 60W tungsten halogen lamp (T1), which was taken as the working
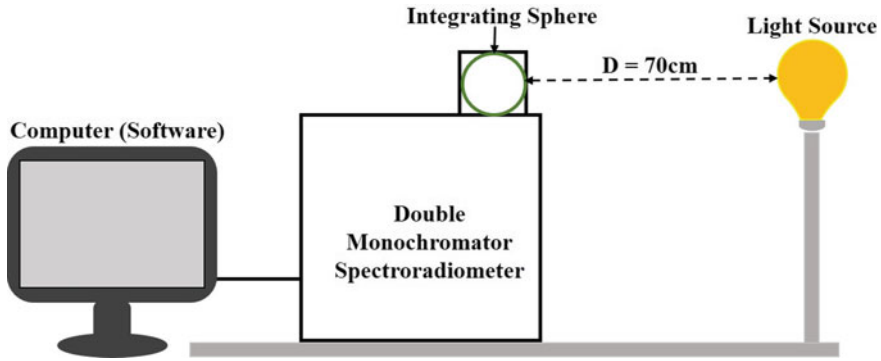
Fig. 1 Double monochromator based spectroradiometer arrangement (method 1) for spectral irradiance measurement of a light source
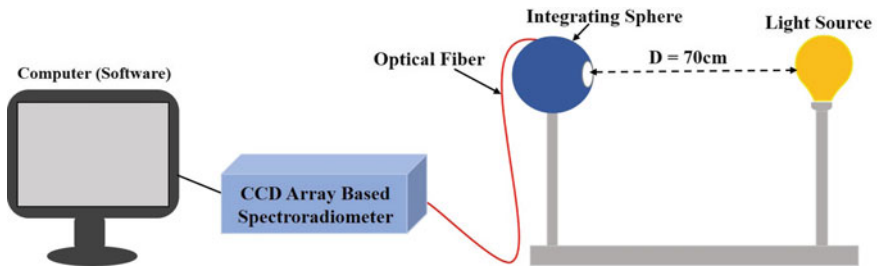

Fig. 2 CCD array based spectroradiometer integrated with integrating sphere for spectral irradiance measurement of a light source (method 2)
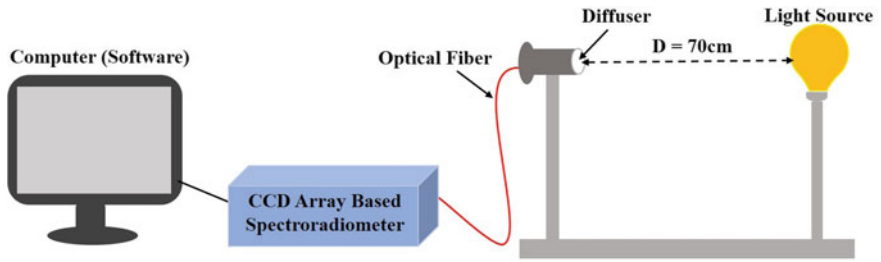

Fig. 3 CCD array based spectroradiometer integrated with a PTFE-based cosine diffuser for spectral irradiance measurement of a light source (method 3)

standard lamp for the present study. The normalized spectral density ($S(\lambda)$) was derived from the spectral irradiance data. The total luminous flux of the lamp, T1 was also derived using standard protocol. The TSRF ($\phi(\lambda)$) of the T1 lamp was derived separately from all the $S(\lambda)$ obtained from spectral irradiance measurements

made by three different configurations, and the luminous flux scale (ϕ_v), using Eqs. 1 and 2 [11]:

$$\phi = A K_m \int\limits_{380}^{780} S(\lambda) V(\lambda) d\lambda \tag{1}$$

$$A = \frac{\phi_v}{K_m \int_{380}^{780} S(\lambda) V(\lambda) d\lambda} \tag{2}$$

where, $V(\lambda)$ is the photopic spectral luminous efficiency function and K_m is the maximum spectral luminous efficiency of the human eye under light-adapted vision (683 lm/W).

The sphere-spectroradiometer system was calibrated separately against the TSRF derived from the three configurations. A set of test lamps consisting of incandescent lamps (G-1, G-2, G-3, G-4) and LED sources (LED-1, LED-2, LED-3, LED-4) of different wattages were chosen. The sphere-spectroradiometer system under different calibrations was used for the measurement of total luminous flux of the test lamps. The total luminous flux measurements were compared with the standard protocol measurements.

3 Results and Discussions

The TSRF of the reference standard lamp (T1) evaluated by obtaining spectral irradiance from the three configurations and luminous flux scale (discussed in Sect. 2), is shown in Fig. 4a.
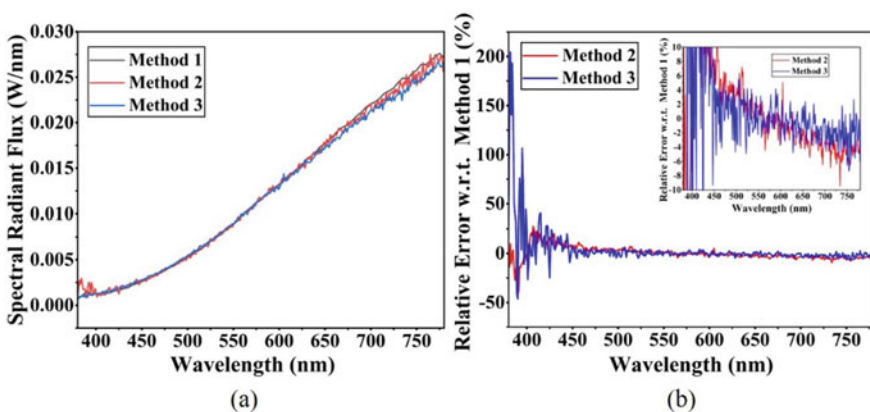

Fig. 4 a Derived TSRF of T1 using three different spectroradiometer configurations. **b** Relative error in TSRF obtained by methods 2 and 3 w.r.t method 1

The relative deviations of the TSRF obtained by the methods 2 and 3, with respect to method 1 are shown in Fig. 4b. The analysis (mean and standard deviation) of the deviation plots indicates that the derived TSRF are in correspondence to each other. However, the TSRF derived by method 1 is closer to the one obtained by method 3, as compared to that of method 2.

The total luminous flux of a set of test lamps (in the range of 300–1500 lm) was measured (Table 1) using sphere spectroradiomter system against three derived TSRF calibrations. The measured total luminous values are further tabulated along with the standard protocol measurements and the relative percentage deviation. The relative percentage deviations in the total luminous flux values are graphically represented in Fig. 5.

It can be inferred from the data that the total luminous flux values obtained using method 2 have a larger deviation as compared to the other two methods. The total

Table 1 Total luminous flux (lm) of different light sources measured by sphere-spectroradiometer system under different TSRF calibrations. The quantities in the bracket represent the relative percentage deviation with respect to the standard protocol measurements

Lamps	Standard Protocol (lm)	Method 1 (lm)	Method 2 (lm)	Method 3 (lm)
G-1	400.4	403.67 (−0.8)	409.66 (−2.3)	399.85 (0.1)
G-2	729.6	730.15 (−0.1)	734.44 (−0.6)	730.55 (−0.1)
G-3	1562.0	1565.3 (−0.2)	1599.0 (−2.4)	1563.0 (−0.1)
G-4	3110.3	3126.8 (−0.5)	3071.5 (1.2)	3144.6 (−1.1)
LED-1	636.52	643.69 (−1.1)	657.20 (−3.2)	641.87 (−0.8)
LED-2	613.27	615.00 (−0.2)	629.15 (−2.6)	616.43 (−0.5)
LED-3	1326.1	1320.7 (0.4)	1371.4 (−3.4)	1330.3 (−0.3)
LED-4	1418.1	1430.0 (−0.8)	1482.5 (−4.5)	1434.7 (−1.2)

Fig. 5 Graphical representation of relative error in total luminous flux of different test lamps measured using sphere spectroradiometer system against derived TSRF by three configurations, with respect to the measurement of total luminous flux by standard protocol
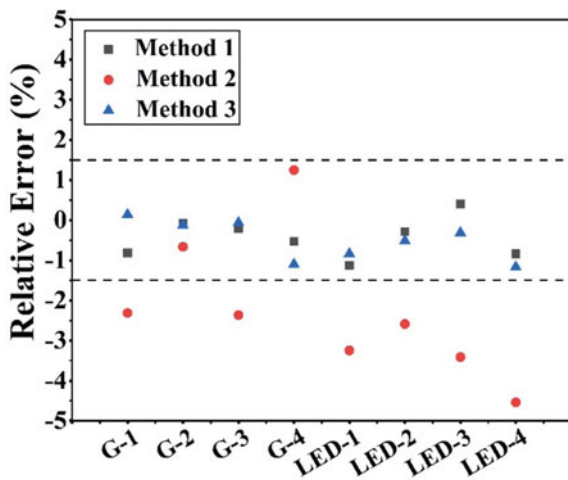
luminous flux measurements of the test lamps, made under TSRF calibration derived from spectral irradiance measurement using the configuration described in methods 1 & 3, were found to be within $\pm1.5\%$ of the standard protocol values. Method 2 uses an integrating sphere along with an array based spectroradiometer connected through an optical fiber. The larger deviations obtained in method 2 in comparison to that of the other two, may probably be attributed to the involvement of the sphere coating, which might be interfering with the true spectrum of the lamps. However, further investigations are required for a conclusive reason.

4 Conclusion

In summary, a study has been done to ascertain the suitability of spectroradiometer configuration to determine the spectral irradiance, for establishing traceability of total spectral radiant flux from spectral irradiance and total luminous flux. Three different spectroradiometric configurations were studied for deriving the scale of total spectral radiant flux. A sphere spectroradiometer system was calibrated using the three TSRF scales and measurements of a set of test lamps were made corresponding to the three different calibrations. The method for determining spectral irradiance based on array spectroradiometer with integrating sphere as the input optics, shows maximum deviations in the total luminous flux measurements made under the TSRF calibration derived from it. The total luminous flux measurements made under calibration derived from the other two methods were well within uncertainty.

The study would augment the effort for establishing traceability of the TSRF from spectral irradiance and total luminous flux, for sphere-spectroradiometeric applications. Further, the handheld CCD array based spectroradiometer can be used to establish a cost-effective sphere spectroradiometer system for the measurements of photometric parameters of artificial light sources.

References

1. Saha S, Vijeta, Jaiswal VK, Sharma P (2022) Realization of candela. In: Aswal DK, Yadav S, Takatsuji T, Rachakonda P, Kumar H (eds) Handbook of metrology and applications. Springer Nature Singapore, Singapore, pp 1–31
2. Gellings CW, Parmenter KE (2009) Building envelope efficiency measures, vol 1. Efficient use and conservation of energy-volume I

3. Bertenshaw D (2019) Light and photometry, the path to standardization. Bertenshaw DR" Light and Photometry, the Path to Standardisation". Die Vierte Wand, Initiative Theatermuseum Berlin, BV, May, vol 9, pp 152–163
4. Gorshkova TB, Sapritsky VI, Stolyarevskaya RI (2011) Metrological basis of light measurements in Russia. Light Eng 19(4)
5. Palmer JM, Carroll L (1999) Radiometry and photometry FAQ. http://www.optics.arizona.edu/Palmer/rpfag/rpfag.htm#motivation
6. Vijeta, Sharma P, Jaiswal VK, Saha S, Mehrotra R (2021) Study of array detector based spectrophotometer for sphere photometry. In: ICOL-2019, pp 565–569
7. Vijeta, Kapri RK, Saha S, Jaiswal VK, Sharma P (2021) Theoretical simulation for evaluating error in irradiance measurement using optical detectors having different cosine responses. MAPAN_J Met Soc India 36(3):473–480. https://doi.org/10.1007/s12647-021-00486-6
8. Godo K, Niwa K, Kinoshita K, Ichino Y, Zama T (2016) Realization of total spectral radiant flux scale at NMIJ with a goniophotometer/spectroradiometer. Metrologia 53(2):853
9. CIE International Standard S025/E (Vienna: International Commission on Illumination) CIE S 025/E:2015 test methods for LED lamps, LED luminaires and LED modules
10. Sharma P, Jaiswal VK, Mehrotra R, Kandpal HC (2010) Upgradation of a spectral irradiance measurement facility at National Physical Laboratory, India. Mapan 25(1):21–28
11. Sharma P, Jaiswal VK, Saha S, Mehrotra R (2021) Sphere-spectroradiometry: spectral flux evaluation. In: ICOL-2019. Springer, pp 521–524

Studies on Pressure and Temperature Dependent Dielectric Properties of Lead Magnesium Niobate -Lead Titanate Binary Relaxor to Use as a Pressure Sensing Material

Vinay Kumar

Abstract Measurement of pressure with required accuracy is important in many industries such as process, chemical manufacturing, automobile etc. The accurate pressure measurement is important not only due to quality considerations but also for safety purposes. A large number of instruments and sensors are available to measure gauge, differential, and absolute pressures. The primary standards measure the pressure using the fundamental units. The Secondary or transfer pressure standards measure pressure in terms of some other quantity like resistance, capacitances etc. Since the discovery of ferroelectricity in single crystal materials (Rochelle salts) in 1921 and its subsequent extension towards the poly-crystalline material (barium titanate, BT) during the 1940s, there has been a continued discovery of new material and technological development leading to the use of ferroelectric relaxor in a significant number of applications like multilayer capacitor, actuators, energy storage etc. The present study describes the investigation of pressure and temperature dependent dielectric properties of Lead Magnesium Niobate-Lead Titanatebinary (PMN-PT) Binary relaxor specimens. In this study, the investigator optimized the specimen's preparation method by changing PT concentration to improve the specimen's pressure sensing properties. This study adds another pressure sensing application of relaxor materials amongst many other applications.

Keywords Pressure · Relaxor · PMN · Dielectric · Sensor

1 Introduction

Pressure is one of the most important physical property needs to measure accurately. Pressure and temperatures play a major role in 'pipeline constructions', 'water supply', 'hydraulic lifts', 'hydraulic presses', 'hydraulic diggers', 'hydraulic for

V. Kumar (✉)

Jubail Industrial College, Jubail Industrial City, Al Jubail 31961, Saudi Arabia
e-mail: vinayvarsh@gmail.com

irrigation', 'thermal power', 'hydraulic power', 'aviation of flights', in flow meter, maintaining optimal pressure in tubes/tires of vehicles and in human blood, etc. The accurate measurement of pressure plays an important role in many processing industries such as automobiles, aerospace, steel, and chemical, for the synthesis of high strength materials and research etc. In the industry accurate pressure measurement is important not only due to quality considerations but also to safety requirements. No single instrument can measure the pressure in the entire range of interest with the same accuracy and reproducibility. Some types of pressure measuring devices are 'Bourdon Tube Pressure Gauge', 'Diaphragm Pressure Gauge', 'Capsule Pressure Gauge', 'Absolute Pressure Gauge', 'Differential Pressure Gauge', 'Bellows Pressure Gauge', 'Manometer Pressure Gauge', 'Piezometer Pressure Gauge' etc.

Since the discovery of the ferroelectricity in single crystal materials (Rochelle salts) in 1921 and its subsequent extension towards the poly-crystalline material (barium titanate, BaTiO3) during the 1940s, there has been a continuous discovery of new material and technological development leading to the use of ferroelectric relaxor in a significant number of applications including pressure measurement [1–13].

Relaxor ferroelectric materials are characterized by diffuse phase transition [14]. There has been extensive research activity in relaxor ferroelectric for the past few decades [15] owing to fundamental scientific interest and potential technological applications. As a result, many compounds have been discovered using relaxors till now and the work is still in progress.

A wide range of compounds having perovskite structure (ABO$_3$) exhibit relaxor ferroelectric behavior. Amongst the compounds Lead Magnesium Niobate(PMN) has been investigated extensively since its discovery, because it has high dielectric constant and fabrication of this perovskite is difficult. In past, large number of research were attributed to optimize fabrication parameter of PMN. Many theories on relaxor ferroelectrics, kinetics of formation the perovskite phase etc. were conceived with PMN [16–18] as the prototype relaxor material.

Temperature insensitiveness of the relaxor ferroelectric in the Curie region can be used to make a device, and result of that should not be affected by the temperature variation. In this context, the present investigation is directed to study the pressure effect of the Lead Magnesium Niobate -Lead Titanate (PMN-PT) relaxor material. First time, this study should lead to the development of the capacitive pressure sensing material using PMN-PT relaxor, to measure the high hydrostatic pressure independent of temperature variation.

2 Experimental

Lead Magnesium Niobate (PMN) was first synthesized by Soviet workers in the late 1950s. The dielectric properties of PMN have since been widely investigated in both single crystal and ceramic forms. The fabrication of PMN is complicated due to the formation of lead niobate-based pyrochlore phase during the initial stage of reaction between mixed oxide. The subsequent transformation of pyrochlore phase

into perovskite phase is sluggish and necessitates repeated calcination at relatively high temperature for long time. Mixed oxide process rarely results in pyrochlore free PMN and has associated problems of reproducibility and control of PbO Stoichiometry. Swartz and Shrout [16] devised a novel approach to obtaining perovskite PMN through a columbite route eliminating the intermediate pyrochlore phases. In this study, the author applied the same approach.

2.1 Specimen Preparation

Specimens with varying composition of PT in the $(1-x)$ PMN—xPT binary system where $x = 0, 0.1, 0.35$ were prepared using high purity oxides (PbO—99.9%, MgO—97%, Nb_2O_5—99.9% and TiO_2—99.9%) adopting columbite precursor technique describe as by Swartz and Shrout [16].

For preparation of specimens, all the oxides except PbO were mixed stoichiometrically and ground in agate mill for 10 to 12 h in acetone medium. Mixture was then calcined at 1273 K for 2 h. Then PbO was mixed in the calcined mixture and the resultant mixture was again calcined at 1073 K for 2 h. Calcined powder was ground finely, and few drops of poly vinyl alcohol (PVA) were added to the calcined powder and then pressed into the pellets of 18 mm in diameter and 1 to 2 mm thick by applying 5000 kg load. After burning off at 573 K for 30 min, pellets were sintered at 1373 K for a period of 2 h, in a closed alumina crucible. To minimize the lead loss during sintering, pellets were coated with lead oxide power. A flow chart for making PMN—PT specimens is shown in Fig. 1.
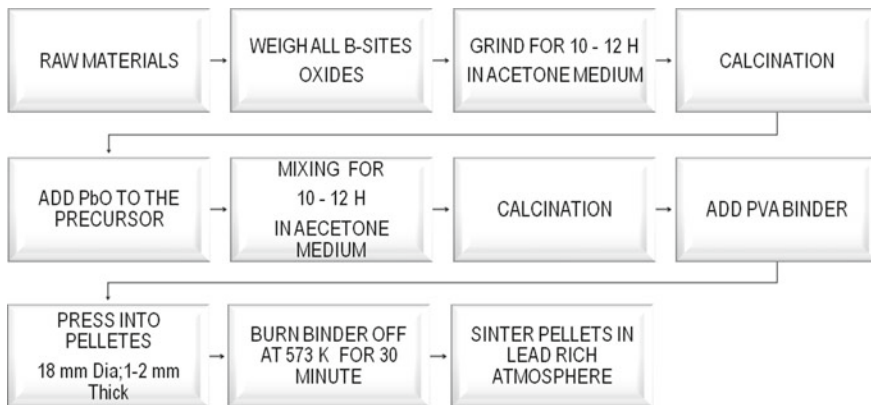

Fig. 1 Flow chart for making PMN—PT specimens

2.2 Measurement

For capacitance/dielectric measurements, the sintered pellets were polished with
1 μm Al_2O_3 powder. The guarded silver electrodes were deposited by vacuum evap-
oration, using a special mask. To eliminate fringing field effect [19] the width of
guarded electrode is chosen such that the following condition is satisfied:

$$\frac{Guardring\ width}{Specimen\ thickness} > 3$$

Capacitance and dielectric loss (Tan δ) were measured at 1 kHz fixed frequency
using auto ranging digital capacitance bridge (Andeen—Hagerling, Model 2500A,
USA) with an accuracy of 0.1 ppm in the entire capacitance range.

The schematic diagram of the high-pressure cell [4] used for the temperature
and pressure measurement is shown in Fig. 2. This specimen holder was made of
Invar[20]. Holder consists of five flanges, in the middle flange there is a hole that
can accommodates specimens of different diameters (maximum 25 mm). On both
sides of center flange there are two other flanges which have golden bellow for the
electrical contact with specimen. Three connections from bellow are given to BNC
connector, which are held outside the holder. Outer two flanges are for holding the
pressure. This holder can accommodate two specimens at a time.

Temperature for the dielectric measurement was varied using thermostatically
controlled temperature bath model RTD 8dd Nes Lab, USA. This bath is capable to
maintain the temperature of specimen within ±0.05 K. Temperature of the specimen
was measured using chromel–alumel thermocouple and a digital temperature display
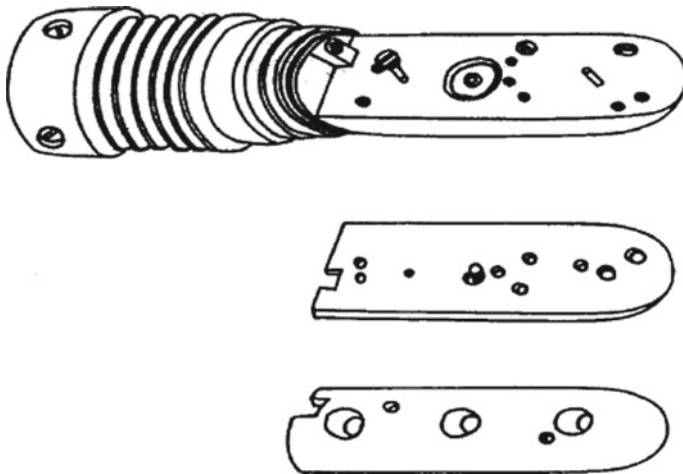of resolution 0.01 K. Range of temperature variation was chosen from 283 to323 K.
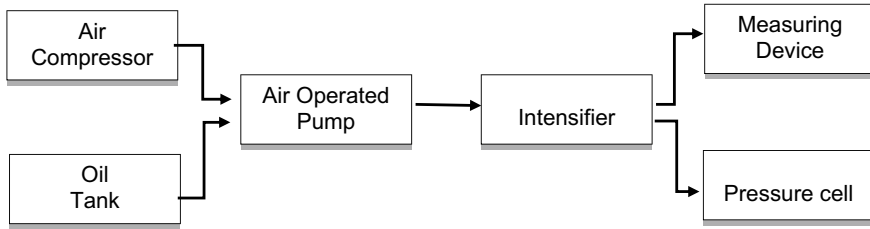

Fig. 2 High pressure cell

Fig. 3 Block diagram for pressure generating system

To measure the dielectric constant at various temperatures specimen holder was placed in copper vessel filled with ethyl hexyl sebacate fluid. As specimens were in the center of the holder therefore about 30 min time was given for stabilization of temperature whenever temperature was changed.

2.3 Dielectric Measurement at Various Pressures

To study the effect of pressure variation the specimen holder was placed in a high-pressure vessel of maraging steel which can accommodate the above said specimen holder. The pressure was generated by means of a conventional high hydrostatic pressure generating system [21] comprising pressure intensifiers and fine control valves. Block diagram for pressure generating system is shown in Fig. 3.

The pressure was transmitted through ethyl hexyl sebacate fluid as it does not react with the specimen and its viscosity does not change appreciably over the range of interest. The pressure vessel was jacketed by a copper vessel which have copper tube around it. Copper tube is connected to temperature bath to maintain the temperature. The pressure effect on chromel-alumel thermocouple was negligible, and the consequent temperature correction is quite small in the present study. The national hydraulic primary pressure standard (NPLH1) is used to measure the applied pressure. The measurement uncertainty of NPLH1 is better than 0.013%. The particulars of the NPLH1 are available elsewhere [22].

3 Result and Discussion

Capacitance of PMN, PMN + 10% PT, PMN + 35% PT measured at various temperatures 283,293, 303, 313, and 323 K increasing as well as decreasing temperatures. The dielectric constant (K)is then calculated using the standard formula from the capacitances by measuring the radius and thickness. The variation of K/K_O of PMN, PMN + 10% PT and PMN + 35% PT specimens as a function of temperature (for

both increasing and decreasing temperatures) is shown in Figs. 4, 5 and 6 respectively. Ko is Dielectric constant at 283 K and atmospheric pressure. The graphs show negligible hysteresis at lower temperature values.

Capacitance of PMN, PMN + 10% PT, PMN + 35% PT measured at various pressures 69, 138, 206, 274, 344 and 415 MPa and 302 K increasing and decreasing pressures. The variation of pressure of PMN, PMN + 10% PT, PMN + 35% PT specimens as a function of K/K_O (for both increasing and decreasing pressures) is shown in Figs. 7, 8 and 9 respectively. Ko is Dielectric constant at atmospheric pressure and 302 kelvins. The polynomial fit of 2nd order and linear fitted equations is also shown in the graph.

The Dielectric Constant, Dielectric Loss, Pressure and Temperature coefficient of PMN, PMN + 10% PT, PMN + 35% PT specimens are tabulated in Table 1. The PMN specimen has a negative temperature and pressure coefficient of dielectric constant while the PMN+10%PT and PMN+35%PT specimens have positive temperature and pressure coefficient of dielectric constant. The PMN + 10 % PT specimen have the highest dielectric constant, pressure coefficient and temperature coefficient. There is hysteresis at lower pressure points in PMN + 10%PT and PMN + 35%PT specimens but for PMN specimen hysteresis is at random pressure point.
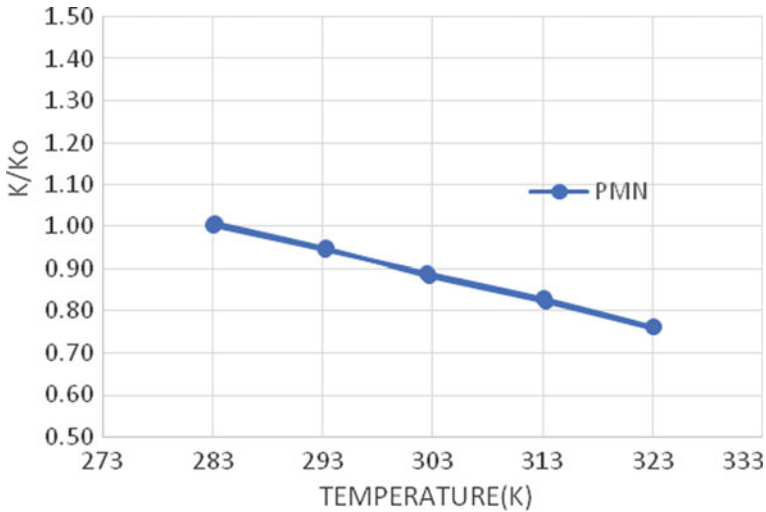

Fig. 4 The variation of K/K_O as a function of temperature of PMN specimen
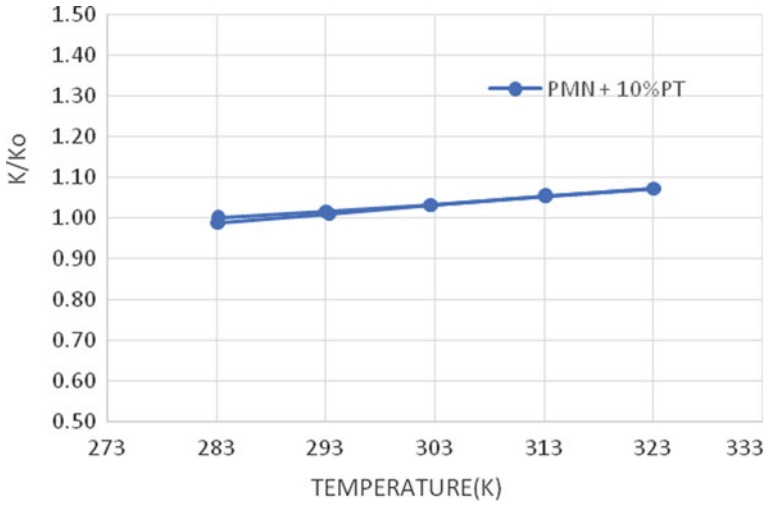
Fig. 5 The variation of K/K$_O$ as a function of temperature of PMN + 10% PT specimen
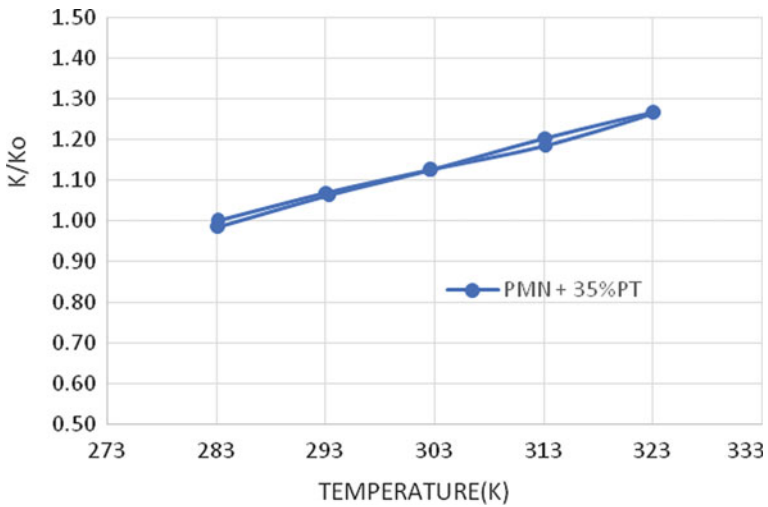

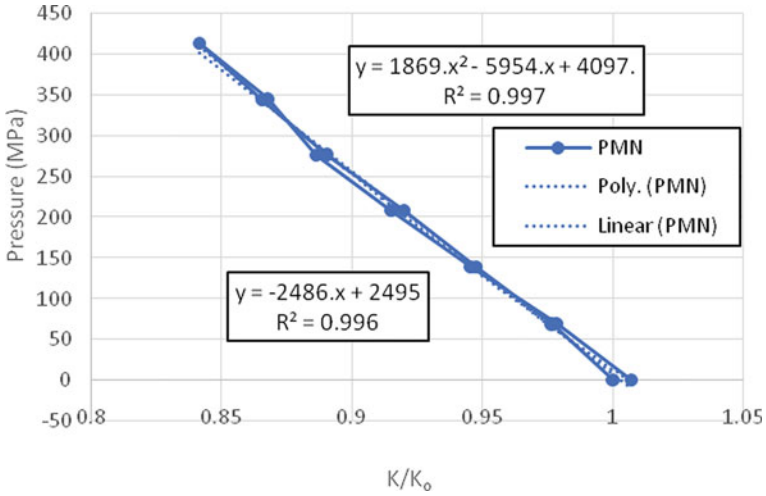**Fig. 6** The variation of K/K$_O$ as a function of temperature of PMN + 35% PT specimen

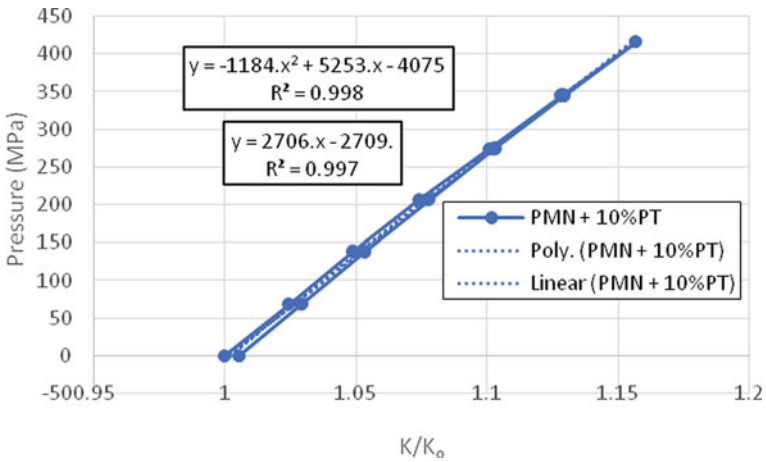**Fig. 7** The variation of pressure as a function K/K$_O$ of PMN specimen

Fig. 8 The variation of pressure as a function K/K$_O$ of PMN + 10% PT specimen
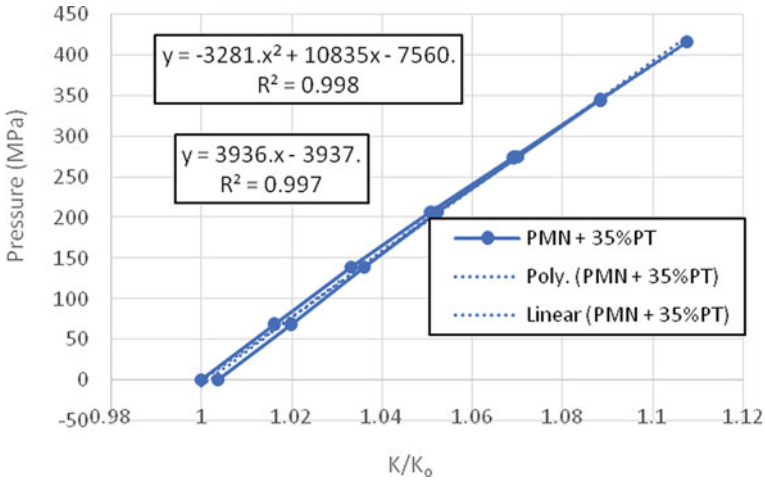
Fig. 9 The variation of pressure as a function K/K_O of PMN + 35% PT specimens

Table 1 The dielectric constant, dielectric loss, pressure and temperature coefficient of PMN, PMN + 10% PT, PMN + 35% PT specimens

Composition	Dielectric constant	Dielectric loss	Pressure coefficient (Pa^{-1})	Temperature coefficient (K^{-1})
PMN	1557.28	0.00661	-381×10^{-12}	-0.0057
PMN + 10%PT	3869.2	0.0502	$+367 \times 10^{-12}$	$+0.0164$
PMN + 35%PT	1100.55	0.0933	$+246 \times 10^{-12}$	$+0.0065$

4 Conclusion

The present investigation strongly concludes that the pure PMN or combination with PT can be used as capacitive pressure sensing material. As obvious from the fitted equation the variation of dielectric constant with pressure the 2nd order polynomial fit has less R^2 value. Therefore, second order equation can be used to calculate the pressure from dielectric constant. Furthermore, investigation is required to minimize the hysteresis, increase, and linearize the pressure coefficient and minimize the temperature coefficient. Once the processing parameters are optimized uncertainty calculation in pressure measurement is also required.

References

1. Szwagierczak D, Kulawik J (2004) Thick film capacitors with relaxor dielectrics. J Eur Ceram Soc 24(7):1979–1985
2. Jiang Y, Niu X, Liang W, Jian X, Shi H, Li F, Zhang Y, Wang T, Gong W, Zhao X, Yao Y, Tao T, Liang B, Lu S (2022) Enhanced energy storage performance in Na0.5Bi0.5TiO$_3$-based Relaxor ferroelectric ceramics via compositional tailoring. Materials 15:5881. https://doi.org/10.3390/ma15175881
3. Uchino K (1994) Relaxor ferroelectric devices. Ferroelectrics 151(1):321–330. https://doi.org/10.1080/00150199408244756
4. Vinay Kumar (2021) Studies on optimization of preparation methods of lead iron Tungstate Relaxor to use as a pressure sensing material. MAPAN-J Metrol Soc India (Springer -Nature) 36(2):305–311. https://doi.org/10.1007/s12647-021-00470-0
5. Vinay Kumar, Sanjay Yadav (2017) Studies on the use of lead iron tungstate-lead titanate relaxor binary system as a pressure sensing material. Sensors Act A Phy 258:101 -104. https://doi.org/10.1016/j.sna.2017.02.030
6. Vinay Kumar, Jain SK, Kamlesh K (2003) Jain performance of unique dielectric pressure sensor; XVII IMEKO WORLD CONGRESS June 22–27, Dubrovnik, Croatia
7. Vinay Kumar, Kamlesh K Jain, Subhash C Kashyap (2001) A novel hydraulic pressure (capacitive) gauge. Proceeding of the 17th International Conference on Force, Mass, Torque & Pressure Measurement, IMEKO -- TC3 17 -21, Istanbul Turkey, pp 394
8. Vinay Kumar, Kamlesh K Jain, Subhash C Kashyap (2001) Use of ferroelectric relaxor as a pressure gauge. MAPAN – J Metrol Soc India 16(1):77–88
9. Vinay Kumar, Kamlesh K Jain, Subhash C Kashyap (2000) Dielectric study of ferroelectric relaxor under high pressure. 43rd DAE -- Solid State Physics Symposium, Dec. 27–31, Bilaspur, MP
10. Yashwant Kumar, Vinay Kumar, Kamlesh K Jain, Subhash C Kashyap (1999) A capacitive pressure gauge as a reliable transfer pressure standard. Sens Actu B 55:217. https://doi.org/10.1016/S0925-4005(99)00088-X
11. Hsiu-Sheng Hsua, Vatcharee Benjauthrita, Fan Zhenga, Rumin Chena, Yuhong Huangc, Qifa Zhoua, K Kirk Shunga (2012) PMN-PT–PZT composite films for high frequency ultrasonic transducer applications. Sens Act A 179:121–124
12. Seoa I-T, Leeb T-G, Kima D-H, Hurb J, Kima J-H, Nahma S, Ryuc J, Choi B-Y (2016) Multilayer piezoelectric haptic actuator with CuO- modified PZT-PZNN ceramics. Sens Act A238:71–79
13. Dragan Damjanovic, Paul Muralt, Nava Setter (2001) Ferroelectric sensors. IEEE Sens J 1(3)
14. Peláiz-Barranco A, Calderón-Piñar F, García-Zaldívar O, González-Abreu Y (2012) Relaxor behaviour in ferroelectric ceramics. In Advances in Ferroelectrics. London, United Kingdom: Intech Open. https://www.intechopen.com/chapters/41273. https://doi.org/10.5772/52149
15. Bobic, Jelena D Magnetic, Ferroelectric (2018) Multiferroic metal oxides. Review of the most common relaxor ferroelectrics and their applications, pp 233–249. https://doi.org/10.1016/B978-0-12-811180-2.00011-6
16. Swartz SL, Shrout TR (1982) Fabrication of perovskite lead magnesium niobate. Mat Res Bull 17:1245–1250. https://doi.org/10.1016/0025-5408(82)90159-3
17. Jong-Gab Baek, Tetsuhiko Isobe, Mamoru Senna (1997) Synthesis of Pyrochlore-Free 0.9Pb (Mg$_{1/3}$Nb$_{2/3}$)O$_3$–0.1PbTiO$_3$ Ceramics via a soft mechanochemical route. J Am Ceram Soc 80(4):973–981. https://doi.org/10.1111/j.1151-2916.1997.tb02929.x
18. Yuichi Sato, Hideyuki Kanai, Yohachi Yamashita (1996) Effects of silver and palladium doping on the dielectric properties of 0.9Pb (Mg$_{1/3}$Nb$_{2/3}$)O$_3$–0.1 PbTiO$_3$ Ceramic. J Am Ceram Soc 79(1):261–265. https://doi.org/10.1111/j.1151-2916.1996.tb07907.x
19. Andeen C (1971) A capacitive gauge for the accurate measurement of high pressures. Rev Sci Instrum 42(4):495–496. https://doi.org/10.1063/1.1685140

20. Jain KK, Kashyap SC (1996) Pressure and temperature dependent dielectric dispersion in $Bi_{12}GeO_{20}$(100) single crystals. Bull Mater Sci 19:533–537. https://doi.org/10.1007/BF02744825
21. Sharma JKN, Jain KK (1986) Accurate measurement of pressure. Pramana - J Phys 27(3):417–434. https://doi.org/10.1007/bf02846867
22. Yadav Sanjay, Prakash Om, Gupta VK, Bandyopadhyay AK (2007) The effect of pressure-transmitting fluids in the characterization of a controlled clearance piston gauge up to 1 GPa. Metrologia 44(3):222–233. https://doi.org/10.1088/0026-1394/44/3/009

Quality Management System of BND® Development in Collaboration with RMPs at CSIR-NPL, India

Vipin Jain, Pallavi Kushwaha, S. P. Singh, and Nahar Singh

Abstract CSIR-National Physical Laboratory (NPL), India, has recently initiated the activity of development and production of CRMs in various sectors (including Water & Chemicals, Cement and Building Materials, Petroleum Products, Precious Metals, Hardness Blocks, Ores & Minerals, Organic Substances, etc.) in collaboration with recognized RMPs under the "Make-In-India" initiative of the Government of India (GoI). The aim of this joint development activity is to harmonize the Quality Infrastructure and also to boost the production and availability of indigenous CRMs in the country. The developed CRMs are available with the trade name 'BND®'. The procedure of the development and production of BNDs jointly by CSIR-NPL and concerned RMPs is controlled by the Quality Management System (QMS) of CSIR-NPL that is based on IS/ISO 17034: 2016 and IS/ISO/IEC 17,025: 2017. The 'BND Outreach' and 'BND Management' Sub-Divisions falling under the 'BND Division' at CSIR-NPL actively coordinate with numerous recognized RMPs for the joint development and production of BNDs. The 'QMS' system being followed by CSIR-NPL and concerned RMPs is being discussed in this article.

Keywords Certified Reference Material (CRM) · Bharatiya Nirdeshak Dravya (BND®) · National Metrology Institute (NMI) · Traceability · Reference Material Producer (RMP) · Quality Management System (QMS)

1 Introduction

Certified Reference Materials (CRMs) are reference materials characterized by a metrologically valid procedure for one or more specified properties, accompanied by a certificate that provides the value of the specified property, its associated uncertainty,

V. Jain (✉) · P. Kushwaha · S. P. Singh · N. Singh
CSIR-National Physical Laboratory, Dr. K.S. Krishnan Marg, New Delhi 110012, India
e-mail: vipin@nplindia.org

Academy of Scientific and Innovative Research (AcSIR), CSIR-HRDC Campus, Ghaziabad 201002, India

and a statement of metrological traceability. ISO Guide 30: 2015 very well defines various terms and definitions related to reference materials including the 'CRM' [1]. Bharatiya Nirdeshak Dravya (BND®) is a 'CRM' produced by CSIR-NPL, the National Metrology Institute (NMI) of India or a Reference Material Producer (RMP) with a well-defined traceability to CSIR-NPL established via specific criteria and protocols defined and documented by CSIR-NPL and tailored to meet the needs of the beneficiaries/clients/customers [2]. CSIR-NPL has got 'BND®' as trademark registered [TM No.- 3669341] with the Registrar of Trademark office in India in the year 2017 [3]. Under the aegis of the 'Make-In-India' initiative of the Government of India (GoI), CSIR-NPL has recently made serious efforts for the development of BNDs in collaboration with recognized RMPs in the country. These RMPs are accredited for IS/ISO 17034: 2016 [4] and/or IS/ISO/IEC 17,025: 2017 [5]. The numerous accredited RMPs having collaboration with CSIR-NPL aiming towards the joint development and production of BNDs include; AASHVI Technology LLP (ATL), Ahmedabad; National Council for Cement & Building Materials (NCCBM), Ballabhgarh; Hindustan Petroleum Corporation Ltd. (HPCL), Visakhapatnam; Bharat Petroleum Corporation Ltd. (BPCL), Mumbai; India Government MINT (IGM), Mumbai; Jalan & Company (JALANCO), New Delhi; Global PT Provider Pvt. Ltd. (GPTP), New Delhi; Pharmaffiliates Analytics & Synthetics Pvt. Ltd., Panchkula; FARE LABS Pvt. Ltd. (FARE LABS), Gurugram; SUMS Techno Labs Pvt. Ltd. (SUMS), Bellary, etc. Till date, CSIR-NPL has developed 145 NEW BNDs (About 115 nos. in association with the RMPs and 30 nos. under the 'In-House BND' activity of the laboratory) [6, 7]. This collaboration for the joint development of BNDs is in the niche areas, such as; Chemicals, Cement & Building materials, Petroleum Products, Precious Metals (Gold & Silver based), Hardness and PMMA Blocks, Ores & Minerals, etc. The procedure of the development and production of BNDs is controlled by the Quality Management System (QMS) of CSIR-NPL [8, 9] that follows the norms of international standards, i.e., IS/ISO 17034: 2016 and IS/ISO/IEC 17,025: 2017, etc. The 'QMS' system being followed by CSIR-NPL and concerned RMPs for the joint development and production of BNDs is being discussed in this article.

2   Quality Management System (QMS) of CSIR-NPL

CSIR-NPL had started working on the development of BNDs way back in the 1990s with the aim of utilizing them as economic import substitutes. However, the program has grown exponentially since 2017 after the registration of the trademark 'BND®' with the Registrar of Trademark office in India [3]. For the first time, CSIR-NPL has developed a consolidated Quality Manual for the whole laboratory that addresses all requirements of both IS/ISO/IEC 17,025: 2017 and IS/ISO 17034: 2017 [8]. This integrated Quality Manual was successfully implemented in October 2020. During November 2020, CSIR-NPL has undergone a peer review of the Quality System of twenty-three (23) Sub-Divisions through Asia Pacific Metrology Program

(APMP) [9]. Subsequently, no non-compliance was observed during the on-site assessment at CSIR-NPL. The 'QMS' of CSIR-NPL is discussed in extensive detail by Mandal et al. [9] addressing the Quality Policy of CSIR-NPL in terms of Clause 4: 'General requirements', Clause 5: 'Structural requirements', Clause 6: 'Resource requirements', Clause 7: 'Process requirements' and Clause 8: 'Management System requirements' based on IS/ISO/IEC 17,025: 2017 and IS/ISO 17034: 2016. This 'QMS' system plays an important role in maintaining the Quality System of CSIR-NPL for reporting accurate measurement results and production/development of BNDs 'In-House' and also in alliance with numerous recognized RMPs in India. Effective implementation of 'QMS' is supervised in all Sub-Divisions covered under the 'QMS' through internal audits effectively being conducted annually (once in a year) followed by management review known as 'Steering Committee'. CSIR-NPL has sufficient number of trained and qualified Assessors for conducting internal audits for its own purpose. The selection of auditors is made as per the guidelines proposed in ISO 19011 [10]. Internal audits are essentially conducted as per the guidelines/procedure set by the 'QMS'. As an apex body, APMP monitors the activities of different NMIs through numerous technical committees by the presentation of annual reports and discussions in APMP annual meetings.

3 Bharatiya Nirdeshak Dravya (BND) Division at CSIR-NPL

CRMs are important for the calibration of all analytical equipment for accurate and precise measurement of data. In order to harmonize the whole process of the BND activities, CSIR-NPL has set-up a new division entitled 'Bharatiya Nirdeshak Dravyas (BND)' also known as Indian Reference Materials Division in the year 2017. The division was further segmented into four Sub Divisions; namely, In-House BND, BND Outreach, Chemical and Food BND and BND Management. The In-House BND Sub-Division is involved in the preparation of In-House BNDs in the field of alloys and minerals, powders, liquid suspension, etc. The Sub-Division also maintains high end sophisticated analytical instruments such as, SEM & EDS, FE-SEM & EDS, XRD, XRF, HRTEM, etc. All these instruments are covered under the quality system of CSIR-NPL as per IS/ISO/IEC 17,025: 2017 [5]. The Chemical and Food BND Sub-Division focuses on the BNDs in the field of water and chemicals, trace elements, etc. This sub-division has developed several BNDs for the calibration of equipment like AAS, ICP-OES, ICP-MS, etc. as per the norms of IS/ISO 17034: 2016 [4]. It has also been providing support for chemical characterization of materials as per the requirements of CSIR-NPL and stakeholders like Delhi Jal Board, Election Commission of India, etc. This Sub-Division also maintains sophisticated equipment like ICP-HR-MS, F&GA-AAS, IC, UFLC, UV–VIS spectrophotometer, etc. as per IS/ISO/IEC 17,025: 2017. The BND Outreach Sub-Division is engaged in coordinating with numerous RMPs working in different sectors in the country

and also makes arrangements with them for signing of Agreement/MoU with CSIR-NPL for the BND development and production as per IS/ISO 17034: 2016. Finally, the BND Management Sub-Division facilitates the distinguished RMPs associated with CSIR-NPL for the BND certification (as per the guidelines of IS/ISO 17034: 2016 and CSIR-NPL 'QMS'). This Sub-Division also coordinates with different Sub-Divisions of CSIR-NPL towards certification under the In-House BND program of the laboratory. In fact, BND Outreach and BND Management Sub-Divisions collectively coordinate with different RMPs accredited for IS/ISO 17034: 2016 towards the objective of joint development of BNDs for the dire need of the country. The BND Management Sub-Division is also actively involved in the development of Nano-material based BNDs for Spectrophotometers using UV–VIS Spectroscopy, AFM, etc. In the following section, the Document Structure of CSIR-NPL that is implemented in October 2020 [9] for the joint development and production of BNDs in collaboration with RMPs is discussed.

4   Document Structure of CSIR-NPL for BND Development and Production

The 'QMS' of CSIR-NPL prepared for the BND development and production has three level Document Structure [9] as shown in Fig. 1 (a & b as per IS/ISO/IEC

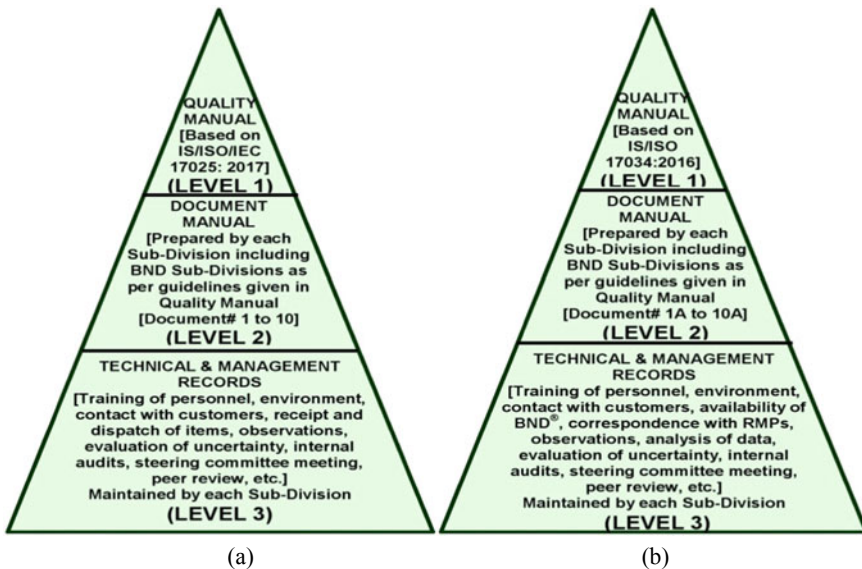(a)   (b)

Fig. 1 Document structure of CSIR-NPL for BND development and production based on **a** IS/ISO/IEC 17025: 2017 and **b** IS/ISO 17034: 2016 [9]

17,025: 2017 and IS/ISO 17034: 2016, respectively). The first level (Level-1) documentation is 'Quality Manual' of various objectives, policies, and procedures of CSIR-NPL as per IS/ISO/IEC 17,025: 2017 and IS/ISO 17034: 2016 as discussed in Sect. 2 [8]. This document has set-up guidelines for preparing Document Manual by various Sub-Divisions. The second level of documentation (Level-2) is 'Document Manual' prepared by each Sub-Division including the BND Sub-Divisions as per the guidelines given in the Quality Manual. There have been total of ten (10) documents (Doc.#1 to Doc.#10 identified for testing and calibration activities and Doc.#1A to Doc.#10A defined for the BND activities). The third level of documentation (Level-3) is relevant 'Technical and Management Records' and maintained by each sub-division at CSIR-NPL.

The 'Document Manual' (Level-2) of the four BND Sub-Divisions namely, In-House BND, BND Outreach, Chemical and Food BND and BND Management is prepared independently according to the formats and guidelines available in the CSIR-NPL Quality Manual. Hence, the structure of Level-2 documentation for each BND Sub-Division has an identical resemblance. The documentation for testing/calibration activity is as per IS/ISO/IEC 17,025: 2017 and for BND development activity is as per IS/ISO 17034: 2016. The BND Outreach and BND Management are the two Sub-Divisions that jointly coordinate with registered RMPs and their concerned 'Technical Teams' at CSIR-NPL along with the Business Development Group (BDG) of CSIR-NPL towards the development and production of BNDs. The BND Outreach and BND Management Sub-Divisions primarily look after the BND program as per IS/ISO 17034: 2016 and the structure of their Document Manual is depicted in Fig. 2 [11] and discussed in Sect. 5.

The 'Technical and Management Records' (Level-3) maintained by each BND Sub-Division primarily include Record of Training of personnel, Environment, Contact with customers, Availability of BNDs, Correspondence with RMPs, Observations, Analysis of data, Evaluation of uncertainty, Internal audits, Steering committee meeting, Peer review, etc. This is as per the guidelines of the Quality Manual of CSIR-NPL [8]. More specifically, BND Outreach and BND Management Sub-Divisions maintain Records; such as, (i) Copy of Safety Manual of CSIR-NPL, (ii) Record of Agreements with RMPs and relevant correspondences, (iii) Record of Consent by the CSIR-NPL 'Technical Teams' appointed by the Head-BND Div. for concerned RMPs, (iv) Record of Invoices with RMPs, (v) Record of Payment & GST Filing, (vi) Record of BNDs developed/produced through RMPs, (vii) Record of receipt/dispatch of RM/CRM material from/to RMPs and Record of Witness Testing conducted by concerned Technical Team/s at RMP's site [including Value Assignment data, Procedure and Production Report (PPR) of BND, Uncertainty calculation, etc.], (viii) Record of BND certificates, (ix) Record of Internal Audits as well as Peer Review and corrective action taken, (x) Record of Training of scientific/technical staff of concerned Sub-Division, and (xi) Miscellaneous documents; such as, Laboratory Layout Diagram, Record of Complaints [usually issued twice in a year by the Center for Calibration & Testing (CFCT) section at CSIR-NPL], Record of Non-conforming work and follow up action and Copy of Office Memorandums (OMs), etc.

Fig. 2 Structure of 'Document Manual' (Level-2) for BND Sub-Divisions at CSIR-NPL

5 Document Manual (Level-2) of BND Sub-Divisions

The first level (Level-1) documentation, i.e., 'Quality Manual' for various objectives, policies, and procedures of CSIR-NPL as per IS/ISO/IEC 17,025: 2017 and IS/ISO 17034: 2016 is prepared as discussed in brief in Sect. 2 [8]. The 'Document Manual' (Level-2) of the four BND Sub-Divisions; namely, In-House BND, BND Outreach, Chemical and Food BND and BND Management is prepared independently as per the formats and guidelines available in the CSIR-NPL Quality Manual. In the following sub-sections, 'Document Manual' (Level-2) maintained by the BND Outreach and BND Management Sub-Divisions is discussed. Documentation of 'Technical and Management Records' (Level-3) is already discussed briefly in Sect. 4.

5.1 Guidelines of Procedure for Traceability of BND (Doc.#2A)

According to IS/ISO 17034: 2016 [4], clause 7.9, the metrological traceability of the certified values of a 'CRM' is demonstrated in compliance with the relevant requirements of IS/ISO/IEC 17,025: 2017 [5]. Accordingly, "The laboratory shall establish and maintain metrological traceability of its measurement results by means of a documented unbroken chain of calibrations, each contributing to the measurement uncertainty, linking them to an appropriate reference" [clause 6.5.1 of IS/ISO/ IEC 17,025: 2017]. The RMP shall ensure to deliver evidence of the metrological traceability of the certified value to a stated reference. The clause 7.14 of IS/ISO 17034: 2016 briefly discusses the content of the certificate of a 'CRM' in which it is emphasized that certified property value should be mentioned with the relevant measurement uncertainty and a statement of metrological traceability and how that is established. The 'Traceability' of the property value of BNDs developed jointly by CSIR-NPL and concerned RMP is obtained through calibration and/or testing following primary method/using CRMs linking to SI units or through international key comparisons organized by BIPM, APMP, etc. Where such comparisons are not available, bilateral comparisons are conducted and degree of equivalence is ensured.

5.2 Procedure for BND Development/Production (Through RMP) [Doc.#3A(ii)]

The procedure for BND Development/Production (Through RMP) involves the following sequential steps [8, 11]:

RMP Registration: Any RMP interested in developing collaboration with CSIR-NPL for the joint development and production of BNDs shall register on CSIR-NPL website (www.nplindia.org). An online form maintained by the BND Division has to be filled up for this purpose.

BND Outreach Sub-Div. gets connected with the registered RMP in online/offline mode.

BND Outreach Sub-Division collects the scope of the RMP and calls a meeting of Heads, BND Sub-Divisions under the chairmanship of Head, BND Division for reviewing the scope/request of the RMP.

Technical Team: Head, BND Division reviews and discusses the feasibility and defines a 'Technical Team' accordingly.

Agreement/MoU: Draft of the Agreement along with scope of the RMP is prepared jointly by BND Outreach Sub-Div., BND Management Sub-Div. and concerned 'Technical Team'. The draft of the agreement is submitted to the Head, BDG at CSIR-NPL for further processing. Recently; CSIR-NPL has constituted a committee named 'BND Committee for Agreements with RMPs' to recommend the terms and conditions for signing of New/Renewal of Agreements with RMPs. Therefore, prior

to sending to Head, BDG, the draft agreement is sent for discussions in the above BND Committee. After recommendation of the BND committee, the agreement is sent to Head, BDG for necessary approval of the competent authority. Agreement signing ceremony is organized by the Head, BND Div. along with all BND Head, Sub-Divisions, Technical Team and Head, BDG. The Agreement/MoU is signed by the Director, CSIR-NPL or Head, BDG with the concerned Head, RMP.

Head, BDG is responsible to maintain the record of the signed original Agreements with RMPs; however, a copy is shared with Head, BND, Head, BND Outreach and Head, BND Management.

Planning for BND Preparation: The respective RMP does the planning of BND preparation for the desired parameter/s along with the concerned 'Technical Team' at CSIR-NPL. Clause 7.2 of IS/ISO 17034: 2016 addresses RMP's requirements for production planning of RMs including CRMs [4]. A schematic flowchart of different steps involved in the planning of BND is given elsewhere [12].

'Technical Consent' on RMP's Request: Head, RMP or its representative sends request to BND Outreach for the 'BND Registration' and for the desired parameters. Head, BND Outreach forwards the RMP's request to the concerned 'Technical Team' for its consent. This request has to be sent through the concerned Head, Sub-Division of the members of the technical team. After receipt of the approval from the 'Technical Team', Head, BND Outreach further processes the RMP's request.

Head, BND Outreach Sub-Div. further sends the request to Head, BND Management Sub-Div. for generating BND® number and invoice for the agreed parameters as per Agreement along with the name of associated 'Technical Team' members.

BND Registration and Invoice Preparation: BND Management Sub-Div. registers and allocates a unique BND number for the agreed parameter. Different series are defined based on the category of the BND. For example, series 1000, 2000, 3000, 4000, 5000, 6000, 7000, 8000 and 9000 are defined for Water & Chemical BNDs, Instrument Calibration BNDs, Food and Beverages BNDs, Metals & Alloys BNDs, Cement & Building Materials BNDs, Gas BNDs, Petroleum Products BNDs, Ores and Minerals BNDs and Biomaterial BNDs, respectively. Head, BND Management generates 'Proforma Invoice' for the new BNDs registered as well as for the successive batches of BNDs and sends to BND Outreach for further processing.

Payment & GST Filing: Head, BND Outreach Sub-Div. takes care of processing of BND invoice/s for receiving payment/s from the concerned RMP/s and subsequently for the GST filing through Head, BDG.

BND Development/Production and Value Assignment: BND development/ production by the concerned RMP is carried out as per the procedure described in the CSIR-NPL Quality Manual on pages 141–144 [8]. Concerned 'Technical Team' from CSIR-NPL will collect test material samples for validation/value assignment (at CSIR-NPL) along with required documents as per the approved checklist. Validation and value assignment may also be conducted by the technical team at RMP's site as mutually agreed. The approved checklist of documents (No. 1–6) to be provided by the RMP and/or technical team to the BND Outreach Sub-Div. includes (1) Agreement copy, IS/ISO 17034: 2016 and IS/ISO/IEC 17025: 2017 accreditations of RMP,

(2) Procedure and Production report (PPR), (3) Property value assigned by RMP and CSIR-NPL technical team with associated uncertainty, (4) Draft copy of BND certificate and label approved by the 'Technical Team' (along with certificate number and label size to be printed), (5) MSDS Report (if applicable), and (6) other relevant document (if any). Head, BND Outreach Sub-Div. reviews all the documents and submits to Head, BND Management Sub-Div. for further processing.

In the case of production of *successive batches* of BNDs of same properties by using similar starting materials and by applying the same procedures, information obtained from the previous batches remains applicable for the new/successive batches (clause A7.2.4 of CSIR-NPL Quality Manual [8]).

Certification and BND Release: BND Management Sub-Div. receives certificate and sticker draft and conducts final formatting along with size and number of labels and certificates to be printed. All the BND-CRM and BND-RM certificates are prepared as per the guidelines of IS/ISO 17034: 2016 [4] and CSIR-NPL Quality Manual [8]. BND Management Sub-Div. takes necessary approval of the Head, BND Div. for the release of the BND certificate. Final certificates and labels as per the approved number are printed by the concerned RMP/BND Management Sub-Division and record is maintained for the same.

Stock Verification of BND® Sale: A committee approved by Head, BND Management Sub-Div. & Head, BND Div. has to perform BND® stock and sale verification of all RMPs, minimum once in a year. After expiry of BNDs, BND Management Sub-Div. witnesses the destruction of expired BNDs as per IS/ISO 17034: 2016 at the concerned RMP's site. The unused certificates, labels and BNDs are destroyed after necessary approval of the Head, BND Div. and the concerned Head, RMP.

Traceability and Dissemination Charges: All RMPs have to submit record of BND® Sale minimum once in a year to Head, BND Division. After verification of the sale record by the BND Outreach and BND Management Sub-Divs., 'Proforma Invoice' is generated by the latter. The invoice is processed by BND Outreach Sub-Div. for receipt of the payment and subsequently for the GST Filing through Head, BDG.

5.3 Doc.#4A(ii), Doc.#5A(ii), Doc.#6A, Doc.#7A, Doc.#8A, Doc.#9A(ii) and Doc.#10A(ii)

Format of Authorized Signatories for BND Development/Production (Through RMP) [Doc.#4A(ii)]: The document is maintained as per the format prescribed on page 146 in the CSIR-NPL Quality Manual [8].

Labels/Stickers for BND Development/Production (Through RMP) [Doc.#5A(ii)]: Format of Labels/stickers for (i) BND (CRM) and (ii) BND (RM) developed through RMPs is given on page 148 in the CSIR-NPL Quality Manual [8].

Format of Record of Personnel Working in Sub-Division [Doc.#6A]: The document is maintained as per the format prescribed on pages 75–77 &149 in CSIR-NPL Quality Manual [8].

Procedure for Record, Storage, Handling and Use of BND Developed/Produced (Through RMP) [Doc.#7A]: The document is maintained as per the instructions given on pages 150 &151 of CSIR-NPL Quality Manual [8].

Format of Record of BND Developed/Produced (Through RMP) [Doc.#8A]: Record of BNDs developed/produced by CSIR-NPL jointly with different RMPs is maintained by the concerned Head, Sub-Div. as per the format given on page 152 of CSIR-NPL Quality Manual [8].

Format of Certificate of BND (CRM) Produced (Through RMP) [Doc.#9A(ii)]: Format of the Certificate of BND (CRM) produced by CSIR-NPL jointly with RMP is given on pages 155 & 156 in the CSIR-NPL Quality Manual [8].

Format of Product Information Sheet of BND (RM) Produced by RMP [Doc.#10A(ii)]: Format of the Product Information Sheet for BND (RM) produced by RMP jointly with CSIR-NPL is available on pages 159 & 160 in the CSIR-NPL Quality Manual [8].

6   Conclusion

CRMs are an essential requirement for the purpose of calibration of all the analytical equipment for accurate and precise measurement results. For a long time, the Indian industry was dependent on the imports of CRMs. To develop economic indigenous substitutes of imported CRMs, CSIR-NPL had initiated the program of development of CRMs with the trade name BND way back in the 1990s; however, the program has grown exponentially since 2017 after the registration of the BND® trademark. Since then, CSIR-NPL has collaborated with numerous recognized RMPs for the development and production of BNDs in the fields of Water & Chemicals, Cement & Building Material, Petroleum Products, Precious Metals, Hardness Blocks, Organic Substances, Ores & Minerals, etc. The process of development and production of BNDs by CSIR-NPL in association with RMPs is controlled by the 'QMS' system of CSIR-NPL which is a 3-Level structure that is addressed in this article.

References

1. ISO Guide 30: 2015 (2015) Reference materials-selected terms and definitions. International Organization for Standardization
2. Yadav S, Mandal G, Shivgan D, Sharma P, Zafer A, Aswal DK (2020) Chapter 3 in Metrology for Inclusive Growth of India. D.K. Aswal (Eds.). Springer
3. Indian Reference Material (Bharatiya Nirdeshak Dravya, BND) (2017) CSIR. TM Application No. 3669341, Registrar of Trademark Office Mumbai (India), 20 April 2018
4. IS/ISO 17034: 2016 (2016) General requirements for the competence of reference material producers. International Organization for Standardization
5. IS/ISO/IEC 17025: 2017 (2017) General requirements for the competence of testing and calibration laboratories. International Organization for Standardization
6. Singh SP, Kushwaha P, Singh S (2020) BND® Coffee Table Book.https://www.nplindia.in/sites/default/files/BNDCoffeeTableBook_Sep2020_4.pdf
7. Karar N, Jain V (2022) Alloys as Certified reference Materials (CRMs). In Aswal DK, Yadav S, Takatsuji T, Rachakonda P, Kumar H (eds) Handbook of metrology and applications. Springer, Singapore
8. Quality Manual (Metrological Activities) (2020) CSIR-National Physical Laboratory, New Delhi (India), 11 May 2020
9. Mandal G, Ansari MA, Aswal DK (2021) Quality management system at NPLI: transition of ISO/IEC 17025 from 2005 to 2017 and implementation of ISO 17034: 2016. Mapan-J Metrol Soc India 36(3):657–668
10. ISO 19011: 2018 (2018) Guidelines for auditing management systems. International Organization for Standardization
11. Document Manual (As per ISO 17034: 2016) of BND Outreach Sub-Division (#5.02) (2021) CSIR-NPL, New Delhi (India), September 2021
12. Pant RP, Tripathy SS, Misra DK, Singh VN, Gautam A, Vijayan N, Basheed GA, Maurya KK, Singh SP, Nahar Singh SP (2020) Chapter 19 in Metrology for Inclusive Growth of India. In Aswal DK (ed). Springer